ISSN 0915-6348

NATIONAL INSTITUTE FOR FUSION SCIENCE

Proceedings of
The Japan-US Workshop on Plasma Polarization Spectroscopy
and
The Fourth International Symposium on
Plasma Polarization Spectroscopy

(Eds.) T. Fujimoto, P. Beiersdorfer

(Received - June 15, 2004)

NIFS-PROC-57 July 2004

RESEARCH REPORT
NIFS-PROC Series

TOKI, JAPAN

Proceedings of
The Japan-US Workshop on Plasma Polarization Spectroscopy
and
The Fourth International Symposium on
Plasma Polarization Spectroscopy

(Supported partly by The 21st Century COE Program for Research and Education on Complex Functional Mechanical Systems)

February 4 – 6, 2004, Kyoto

Edited by

Takashi Fujimoto

Peter Beiersdorfer

Abstract

The international meeting on Plasma Polarization Spectroscopy (PPS) was held at Kyoto University during February 4-6, 2004. This Proceedings book includes the summaries of the talks given in that meeting. Starting with the Overview talk by Csanak, the subjects cover: x-ray polarization experiments on z-pinches (plasma foci), and an x-pinch, a laser-produced plasma in a gas atmosphere, an interpretation of the polarized $1 \leftarrow 0$ x-ray laser line, polarization observation from various laser-produced plasmas including a recombining phase plasma, a report on the on-going project of a laser facility, several polarization observations on magnetically confined plasmas including the Large Helical Device and an ECR plasma, a new laser-induced fluorescence diagnostic method. On atomic physics side given are: various polarization measurements on EBIT, precision spectroscopy on the TEXTOR, user-friendly atomic codes. Instrumentation is also a subject of this book.

Preface

The Japan-US Workshop on Plasma Polarization Spectroscopy and the Fourth International Symposium on Plasma Polarization Spectroscopy was held during February 4 – 6, 2004, at Kyoto University. This was the fourth meeting of the series: The first US-Japan Workshop, was held February 1-3, 1994, at the Los Alamos National Laboratory organized by D. Cartwright, The second was in January 26 – 28, 1998, in Kyoto organized by T. Fujimoto, and the third was in June 18 – 21, 2001, at the Lawrence Livermore National Laboratory organized by P. Beiersdorfer. These Workshops were held jointly with international meetings, and the present meeting was also The Fourth International Symposium on Plasma Polarization Spectroscopy. The meeting was attended by 5 participants from the US, 4 from Russia, 1 from Korea, 1 from France, 1 from Poland and more than 15 from Japan.

Plasma spectroscopy is one of the disciplines of plasma physics, and it has played an important contributing role to the development of plasma physics through plasma diagnostics by providing important information on electron density and temperature, and on transport of plasma particles in a plasma. Plasma spectroscopy is characterized by its strong relationship to, or basis of, atomic physics. This is because the object which emits spectral lines are atoms or ions, and their behavior in a plasma is controlled by a collection of processes that are the realm of atomic physics. Plasma Polarization Spectroscopy (PPS) is a new branch of plasma spectroscopy, which provides information on electric and magnetic fields and electron distribution functions. The strong relationship with atomic physics is even more true for PPS. In developing PPS, it is essential to have close cooperation between plasma spectroscopists and atomic physicists. This series of meetings has been the forum of exchanging information from both sides, and served to benchmark past developments and the present status of PPS at the time of a meeting.

The above tradition was followed in this meeting, and all the participants were impressed by the past developments and the perspective of a bright future. These Proceedings summarize the papers presented at this meeting. The editors hope that the reader can sense the excitement felt by the participants and will gain insight into the prospects of the field.

May 2004

Takashi Fujimoto

Peter Beiersdorfer

List of Participants

E. Baronova: RRC Kurchatov Institute, Moscow, Russia; baronova@fusion.ru

P. Beiersdorfer: Lawrence Livermore National Laboratory, P.O. Box 808, L-260, Livermore, California 94551-9900 USA; beiersdorfer@llnl.gov

G. Csanak: Los Alamos National Laboratory, Los Alamos, NM, 87545, USA; gc@t4.lanl.gov

H. Chen: Lawrence Livermore National Laboratory, P.O. Box 808, L-260, Livermore, California 94551-9900 USA; chenhui@llnl.gov

J. Dubau: LIXAM, Université Paris-Sud, 91405, Orsay, France; jacques.dubau@lixam.u-psud.fr

T. Fujimoto: Department of Engineering Physics and Mechanics, Graduate School of Engineering, Kyoto University, Kyoto 606-8501, Japan; a53080@sakura.kudpc.kyoto-u.ac.jp

M. Goto: National Institute for Fusion Science, Gifu, 509-5292, Japan; goto@nifs.ac.jp

M. Hasuo Department of Engineering Physics and Mechanics, Graduate School of Engineering, Kyoto University, Kyoto 606-8501, Japan; hasou@kues.kyoto-u.ac.jp

H. Hayakawa: Department of Engineering Physics and Mechanics, Graduate School of Engineering, Kyoto University, Kyoto 606-8501, Japan;

A. Iwamae: Department of Engineering Physics and Mechanics, Graduate School of Engineering, Kyoto University, Kyoto 606-8501, Japan; iwamae@kues.kyoto-u.ac.jp

L. Jakubowski: The Andrej Soltan Institute for Nuclear Studies (IPJ), 05-400 Otwock-Swierk n. Warsaw, Poland; jakubowski@ipj.gov.pl

T. Kagawa: Dept. of Physics, Nara Women's University, Nara 630-8506, Japan. kagawa@ec.nara-wu.ac.jp

T. Kai: Miyazaki University, Faculty of Engineering, Dept Applied Physics, Miyazaki 889-2192, Japan; takeshi@phys.miyazaki-u.ac.jp

Y. Kato: Kansai Research Establishment, Japan Atomic Energy Research Institute, 8-1 Umemidai, Kizu-cho, Souraku-gun, Kyoto 619-0215, Japan;

T. Kawamura: Institute for Laser Technology, Osaka, Japan

Koike: Kansai Research Establishment, Japan Atomic Energy Research Institute, 8-1 Umemidai, Kizu-cho, Souraku-gun, Kyoto 619-0215, Japan;

D.E. Kim: Pohang University of Science and Technology, San 31 Hyoja-Dong, Namku, ohang, Kyoungbuk 790-784, Rep. of KOREA; kimd@postech.ac.kr

Y.-W. Kim: Department of Physics, Lewis Laboratory 16, Lehigh University Bethlehem, PA 18015, USA and School of Physics, Seoul National University, Seoul, Korea; ywk0@lehigh.edu

R. Mizutani: Department of Engineering Physics and Mechanics, Graduate School of Engineering, Kyoto University, Kyoto 606-8501, Japan;

K. Moribayashi: Kansai Research Establishment, Japan Atomic Energy Research Institute, 8-1 Umemidai, Kizu-cho, Souraku-gun, Kyoto 619-0215, Japan; kengo@aprms.apr.jaeri.go.jp

M. Nimura: Department of Engineering Physics and Mechanics, Graduate School of Engineering, Kyoto University, Kyoto 606-8501, Japan;

H. Nishimura: Institute of Laser Engineering (ILE), Osaka University, 2-6 Yamada-oka, Suita, Osaka 565-0871, Japan; nishimu@ile.osaka-u.ac.jp

D. L. Robbins: Department of Physics, Morehouse College, Atlanta, GA 30314: robbins13@llnl.gov

A. Sasaki: Kansai Research Establishment, Japan Atomic Energy Research Institute, 8-1 Umemidai, Kizu-cho, Souraku-gun, Kyoto 619-0215, Japan; sasaki@apr.jaeri.go.jp

T. Sato: Department of Engineering Physics and Mechanics, Graduate School of Engineering, Kyoto University, Kyoto 606-8501, Japan;

K. Takiyama: Graduate School of Engineering, Hiroshima University,1-4-1, Kagamiyama, Higashi-Hiroshima,739-8527, Japan: takiyam@hiroshima-u.ac.jp

S. Tojo: Department of Engineering Physics and Mechanics, Graduate School of Engineering, Kyoto University, Kyoto 606-8501, Japan;

I.Yu. Tolstikhina: P.N.Lebedev Physical Institute, Russian Academy of Sciences Moscow, Russia: inga@sci.lebedev.ru

A.M. Urnov: P. N. Lebedev Physics Institute, Russian Academy of Sciences Moscow, Russia; urnov@sci.lebedev.ru

L.A. Vainshtein: P.N.Lebedev Physical Institute, Russian Academy of Sciences Moscow, Russia

Japan-US Workshop on Plasma Polarization Spectroscopy

and

The Fourth International Symposium on Plasma Polarization Spectroscopy

Symposium Schedule

Wednesday, February 4th, 2004

9:00- 9:10 Opening: Fujimoto

9:10-10:00 Overview: Csanak

10:00-10:15 <Break>

Session I

10:15-10:55 Baronova

10:55-11:35 Jakubowski

11:35-12:05 (Hakel and Mancini) presented by Beiersdorfer

12:05-13:30 <Lunch>

Session II

13:30-13:50 Beiersdorfer

13:50-14:30 Nishimura

14:30-15:00 (Shlyaptseva and Ouart) presented by Beiersdorfer

15:00-15:40 Y.W. Kim

15:40-16:00 <Break>

Session III

16:00-16:40 Urnov

16:40-17:00 Hayakawa

17:00-17:40 Goto

Thursday, February 5th, 2004

Session I

9:00- 9:40 Beiersdorfer

9:40-10:10 Chen

10:10-10:30 <Break>

Session II

10:30-11:10 Robbins

11:10-11:50 Kagawa

11:50-13:30 <Lunch>

Session III

13:30-14:00 Tolstikhina and Vainshtein

14:00-14:40 Csanak

14:40-15:15 Chen

15:15-15:30 <Break>

Session IV

15:30-16:00 Nimura

16:00-16:40 Takikama

16:40-17:00 Sato

17:00-17:40 Iwamae

18:30- <Party>

Friday, February 6th, 2004

9:00- 9:40 Dubau

9:40-10:20 D.-E. Kim

10:20 - Summary and Discussion "Achievements and Challenges": Fujimoto

List of Talks

Wednesday

Overview

"Plasma Polarization Spectroscopy: Past, present and future—A subjective view"
George Csanak, Los Alamos National Laboratory, USA

Session I

"On polarization study of ArXVII and FeXXV lines in z-pinches"
Elena Baronova, RRC Kurchatov Institute, Russia

"Time-resolved dependence of high-ionized Ar-lines observed within MAJA-Plasma-Focus device"
Lech Jakubowski, The Andrzej Soltan Institute for Nuclear Studies, Poland

"X-ray line spectroscopic signatures of plasmas driven by ultra-short laser pulses "
Peter Hakel and Robert Mancini, University Nevada, Reno, USA
(Presented by P. Beiersdorfer)

Session II

"X-ray polarization measurements at relativistic laser intensities"
Peter Beiersdorfer, Lawrence Livermore National Laboratory, USA

"Polarization spectroscopy for hot electron transport in ultra-high intensity laser plasma"
Hiroaki Nishimura, Institute of Laser Engineering, Osaka University, Japan

"Spectrapolarimetry of high-temperature plasmas"
Alla Shlyaptseva and Nicholas Ouart, University Nevada, Reno, USA
(Presented by P. Beiersdorfer)

"Toward 3-D E-field visualization in laser-produced plasma by polarization-spectroscopic imaging"
Yong W. Kim, Lehigh University, Bethlehem, PA USA

Session III
"Verification of accuracy for atomic data needed in PPS employing K-spectra emitted by the tokamak TEXTOR"
Alexander M. Urnov, P.N.Lebedev Physics Institute, Russia

"Plasma polarization spectroscopy on the LHD"
Masayuki Hayakawa, Kyoto University, Japan

"Influences of optical elements on the polarization measurement"
Motoshi Goto, National Institute of Fusion Science, Japan

Thursday

Session I

"Polarization of beam-excited K-shell and L-shell x-ray lines: application in line identification"

Peter Beiersdorfer, Lawrence Livermore National Laboratory, USA

"Polarization measurements for the 2p-3d and 2p-3s transitions in Ne-like and F-like iron"

Hui Chen, Lawrence Livermore National Laboratory, USA

Session II

"Measurement of the polarization of the K-shell resonance line emission of helium-like and lithium-like sulfur at relativistic electron beam energies"

Darron L. Robbins, Morehouse College / Lawrence Livermore National Laboratory, USA

"Theoretical analysis for X-ray spectra from Ne-like Xe observed by EBIT"

Takashi Kagawa, Nara Women's University, Japan

Session III

"Level alignment in CIII ions: R-matrix calculations of m-resolved excitation cross section"

Inga Yu. Tolstikhina and Leonid A. Vainshtein, P.N.Lebedev Physical Institute, Moscow, Russia

"Alignment creation by elastic electron scattering: a review and new developments"

George Csanak, Los Alamos National Laboratory, USA

"Polarization calculations using the Flexible Atomic Code"

Hui Chen, Lawrence Livermore National Laboratory, USA

Session IV

"Relaxation of atomic polarization by radiation re-absorption"
Masanori Nimura, Kyoto University, Japan

"Observation of interference between Stark and electric quadrupole transitions in LIF from He atoms in plasmas"
Ken Takiyama, Hiroshima University, Japan

"Plasma polarization spectroscopy on the ECR helium plasma in a CUSP field"
Takeshi Sato, Kyoto University, Japan

"Polarization of ECR helium plasma and Population-Alignment Collisional-Radiative model"
Atsushi Iwamae, Kyoto University, Japan

Friday

"Progress report on the polarization of J=0-1 X-ray laser"
Jacques Dubau, LIXAM, Universite Paris-Sud, France

"Study of anisotropy of electron energy distribution of optical-field ionized oxygen plasma by using polarization spectroscopy"
Dong Eon Kim, Pohang University of Science and Technology, Korea

Contents

Contents contd.

Plasma Polarization Spectroscopy: Past, Present, and Future - A Subjective View

G. Csanak
Los Alamos National Laboratory, Los Alamos, NM, 87545, USA

Abstract

I describe how I got into the field of plasma polarization spectroscopy (PPS), how the PPS Workshops started, and how the whole field got consolidated and strengthened. Subsequently I describe what kind of present theoretical and experimental activities I am aware of. Finally I explain why I think that the future of PPS is bright.

1. Introduction

First and foremost, I would like to recall the memory of Professor Douglas H. Sampson.

Professor Sampson, who passed away on December 8, 2002, has made an immense contribution to atomic physics, atomic collision physics, and astrophysics in general and plasma polarization spectroscopy (PPS) in particular. The codes developed under his supervision in fact form the backbone of electron-ion collisional- and PPS calculations [1 – 17]. These codes were used for PPS applications at The Pennsylvania State University [18 – 21], at Lawrence Livermore National Laboratory [22 – 63], at the Naval Research Laboratory [64], at Los Alamos National Laboratory and Kyoto University [65, 66] and at other places [67, 68]. These codes are now also being incorporated into the Los Alamos suite of atomic data codes. In the person of Professor Sampson the PPS community has lost a magnificent theoretician but his immense legacy will be with us for a long time to come.

Here I would like to give an "Overview": the past, present, and future of PPS the way I see it now and the way I experienced it in the past.

I heard about PPS before (from Professor Fujimoto), but I really got involved with PPS during the Sept 1991 - Aug 1992 period when I spent my sabbatical in Japan. During that time in Japan there was already a group of plasma physicists, atomic physicists, and atomic collision physicists who had regular meetings and were discussing issues related to PPS. I attended two of those meetings in Nagoya. One of the outcomes of those meetings was the report entitled "Atomic Processes

Relevant to Polarization Plasma Spectroscopy" [69]. As of today this report remains a fundamental compendium on PPS and a great help for a scientist working in this field.

Simultaneously, I started to work with Professor Fujimoto on PPS which meant in part reading the manuscript of what later became the report by Fujimoto *et al.* [70]. This report formulates the population alignment collisional radiative (PACR) model based on the impact and the impact parameter approximations and formed the basis of much future work. I also started work with Professor Fujimoto on a complete quantum-mechanical formulation of the relaxation rate equations for cylindrically symmetric baths, based on the work of Fano [71] and Ben-Reuven [72]. This work still remains unfinished [73]. After having returned from Japan to Los Alamos I started to read the fundamental review articles of Professor Kazantsev and collaborators on PPS [74, 75] and many of the references quoted there. I learned about the massive amount of experimental work that had already been done in Professor Kazantsev's laboratory (mainly on discharge plasmas) and the significant work in France and Russia on the PPS of the sun (especially solar flares). Shortly afterwards the first U.S. - Japan Workshop was held at Los Alamos organized by D.C. Cartwright and T. Fujimoto. This workshop was attended by four scientists from Japan, including Professors Fujimoto and Y. Kato, by Professors Kazantsev, Cornille, Dubau, and Kieffer, and numerous scientists from the U.S. This workshop, which was extended to be the International Workshop on PPS, was held subsequently in Kyoto in 1998 (organized by Fujimoto and Beiersdorfer), in Livermore in 2001 (organized by Beiersdorfer and Fujimoto) and now in Kyoto again (organized by Fujimoto and Iwamae). The PPS workshops, all of which I had the opportunity to attend, brought together the principal participants, both theoreticians and experimentalists, working on PPS, from all over the World. Throughout these years there occurred a consolidation and strengthening of this field. This was documented by two books published on PPS by Kazantsev and Henoux [76] and by Kazantsev, Petrashen, and Firstova, [77], as well as by the joint review of Fujimoto and Kazantsev [78].

Turning now to the recent past and to the present, PPS appears to be teeming with activities. In the theoretical area (which is my area) I am aware of the following major activities:

1. The development, testing, and implementation of the population-alignment collisional- radiative (PACR) model for a variety of systems by Iwamae, Fujimoto and associates and collaborators. First results from the PACR model were reported by Iwamae *et al.* for beryllium-like oxygen [65] . Subsequently detailed calculations were performed for helium-like carbon [66] and current work deals with helium itself [79].

2. The development of the magnetic-sublevel population time-dependent collisional radiative atomic kinetics code by Hakel, Mancini and collaborators, and linking it to hydrodynamics and radiation transport codes and implementing it for

the interpretation of polarization spectra of laser-produced plasmas [80].

3. Development and implementation of a theoretical scheme for the use of X-ray spectropolarimetry to measure weak magnetic fields by Kazantsev, Petrashen, Shlyaptseva and collaborators [81, 82].

4. The use of the Zhang-Sampson-Clark code for the interpretation of polarization experiments on the EBIT machine at the Lawrence Livermore National Laboratory and the study of various physical effects in the polarization by Reed and M.H. Chen [83], by Smith [84], and by H. Chen [85] and collaborators.

5. Development of a fully relativistic approach for incorporating resonance contributions to the electron impact induced magnetic sublevel excitation cross sections of ions by Zhang and Sampson [17].

6. Quantum-mechanical formulation of the problem of alignment creation by elastic scattering by Csanak, Kilcrease and collaborators [86].

The following major experimental activities came to my attention:

1. Polarization measurements on an ECR Plasma by A. Iwamae, T. Fujimoto and collaborators [79].

2. PPS on the Large Helical Device by M. Hayakawa, A. Iwamae, and T. Fujimoto [87].

3. PPS of recombining plasmas produced by ultra-short laser pulses, by T. Kawachi, N. Hasegawa, A. Iwamae, T. Fujimoto and collaborators [88].

4. PPS measurement on the laser-produced recombining Al plasma by D.E. Kim and J. Kim [89].

5. X-ray line polarization measurements on the EBIT Machine: principal interest was recently L-shell X-ray lines. These include the 2-3 lines in Fe XVII and in Fe XVII [90]. PPS was also used to diagnose the thermal energy distribution in the Livermore EBIT machine [91].

6. X-ray spectropolarimetry on the pulsed power Z-pinch device at the Nevada Terawatt Facility by Shlyaptseva and collaborators [92].

This concludes the list of those theoretical and experimental activities in PPS in the recent past and currently which I was aware of just before the Workshop. For updated information the reader should consult the Table of Contents of these Proceedings and for details the individual articles.

And now to the future!

It is known to be difficult to make predictions for the future, but I see the future of PPS is bright!

My optimism is based on the following facts:

1. In astrophysics, especially in the physics of solar flares, PPS is a solidly established technique. In fact one of the reasons Kazantsev, Petrashen, and Firstova [77] wrote their book was to give the theoretical foundation of PPS for astrophysicists as well as collect PPS's successes in astrophysics. Their main interest was directed to solar physics, but it is known that neutron stars and white dwarfs have very high magnetic fields on their surfaces and therefore radiation emanating from

their surfaces should be polarized too [93].

2. There are now well established PPS laboratories all over the world (Kyoto University, NIFS, JAERI-Kansai, Livermore, Reno, Pohang, Lehigh University, Moscow).

3. There are well established collaborations between various research groups (Kyoto-Los Alamos-Perth, Livermore-Reno-Meudon-St.Petersburg, Kyoto-Pohang, Kyoto-Toki, Kyoto-JAERI-Kansai). Professors Vainshtein, Urnov, and Dubau have collaborated with several experimental groups in the past.

4. There are experimental-theoretical efforts directed at the same problem: the experimentally obtained data are being interpreted theoretically (Kyoto-Los Alamos-Perth, Livermore, Reno).

I am sure that in the future the field of PPS will undergo further consolidation as the most important technical and scientific problems surface and get solved. Thus we can look forward to the next PPS Workshop with anticipation.

I would like to thank to Drs. A. Iwamae, P. Beiersdorfer, A. Shlyaptseva, P. Hakel, J. Weisheit, H.L. Zhang and D.P. Kilcrease for providing input to this "Overview".

This work was performed under the auspices of the U.S. Department of Energy.

References

[1] D.H. Sampson, H.L.Zhang, A.K. Mohanty and R.E.H. Clark, *Phys. Rev. A* **40**, 604 (1989).

[2] H.L. Zhang, D.H. Sampson and A.K. Mohanty, *Phys. Rev. A* **40**, 616 (1989).

[3] H.L. Zhang, D.H. Sampson and R.E.H. Clark, *Phys. Rev. A* **41**, 198 (1990).

[4] H.L. Zhang and D.H. Sampson, *Phys. Rev. A* **42**, 5378 (1990).

[5] D.H. Sampson and H.L. Zhang, *Phys. Rev. A* **45**, 1657 (1992).

[6] H.L. Zhang and D.H. Sampson, *Phys. Rev. A* **47**, 208 (1993).

[7] C.J. Fontes, D.H. Sampson and H.L. Zhang, *Phys. Rev. A* **47**, 1009 (1993).

[8] C.J. Fontes, D.H. Sampson and H.L. Zhang, *Phys. Rev. A* **48**, 1975 (1993).

[9] C.J. Fontes, D.H. Sampson and H.L. Zhang, *Phys. Rev. A* **49**, 3704 (1994).

[10] H.L. Zhang and D.H. Sampson, *Phys. Rev. A* **52** 3827 (1995).

[11] D.H. Sampson and H.L. Zhang, *J. Quant. Spectrosc. Radiat. Transfer* **54**, 345 (1995).

[12] D.H. Sampson and H.L. Zhang, *J. of Phys. B* **30**, 1449 (1997).

[13] H.L. Zhang, *Phys. Rev. A* **57**, 2640, (1998).

[14] C.J. Fontes, H.L. Zhang and D.H. Sampson, *Phys. Rev. A* **59**, 295 (1999)

[15] H.L. Zhang and D.H. Sampson, *Phys. Rev. A* **61**, 21707, (2000).

[16] H.L. Zhang, D.H. Sampson and Mokhtar K. Inal, *Phys. Rev. A* **63**, 52713, (2001).

[17] H.L. Zhang and D.H. Sampson, *Phys. Rev. A* **66**, 042704 (2002).

[18] M.K. Inal, H.L. Zhang and D.H. Sampson, *Phys. Rev. A* **46**, 2449 (1992).

[19] M.K. Inal, D.H. Sampson, H.L. Zhang and J. Dubau, *Physica Scripta* **55**, 170 (1997).

[20] D.H. Sampson, H.L. Zhang, M.K. Inal and C.J. Fontes, in *Proceedings of the 3rd US-Japan Plasma Polarization Spectroscopy Workshop*, Livermore, California June 18-21, 2001 (Edited by P. Beiersdorfer and T. Fujimoto), University of California Lawrence Livermore National Laboratory Report UCRL-ID-146907, p.271.

[21] M.K. Inal, H.L. Zhang, D.H. Sampson, and C.J. Fontes, *Phys. Rev. A* **65**, 32727 (2002).

[22] P. Beiersdorfer et al., *Phys. Rev. Lett.* **65**, 1995 (1990).

[23] P. Beiersdorfer et al., in ICPEAC XVII, Brisbane, July 1991 section 7.

[24] P. Beiersdorfer, M.H. Chen, R.E. Marrs, M.B. Schneider and R.S.Walling, *Phys. Rev. A* **44**, 396 (1991).

[25] K.J. Reed, M.H. Chen and D.L. Moores, *Phys. Rev. A* **44**, 4336 (1991).

[26] P. Beiersdorfer, *Nucl. Instrum. Methods Phys. Res. B* **56-7**, no. AY, p. 1144 (1991).

[27] K.J. Reed and M.H. Chen, *Phys. Rev. A* **45**, 4519 (1992).

[28] M.H. Chen and K.J. Reed, *Phys. Rev. A* **45**, 4525 (1992).

[29] S. Chantrenne, P. Beiersdorfer, R. Cauble and M.B. Schneider, *Phys. Rev. Lett.* **69**, 265 (1992).

[30] P. Beiersdorfer, T.W. Phillips, K.L. Wong,R.E. Marrs and D.A. Vogel, *Phys. Rev. A* **46**, 3812 (1992).

[31] K.L. Wong, P. Beiersdorfer, R.E. Marrs, B.M. Penetrante, K.J. Reed, J.H. Scofield, D.A. Vogel and R. Zasadzinski, *Nucl. Instrum. Methods Phys. Res. B* **72**, 234 (1992).

[32] M.H. Chen and K.J. Reed, *Phys. Rev. A* **47**, 1874 (1993).

[33] K.L. Wong, P. Beiersdorfer, M.H. Chen, R.E. Marrs, K.J. Reed, J.H. Scofield, D.A. Vogel and R. Zasadzinski, *Phys. Rev. A* **48**, 2850 (1993).

[34] K.J. Reed and M.H. Chen, *Phys. Rev. A* **48**, 3644 (1993).

[35] B.J. Wargelin, P. Beiersdorfer and S.M. Kahn, *Phys. Rev. Lett.* **71**, 2196 (1993).

[36] M.H. Chen and K.J. Reed, *Phys. Rev. A* **50**, 2279 (1994).

[37] K.L. Wong, P. Beiersdorfer, K.J. Reed and D.A. Vogel, *Phys. Rev. A* **51**, 1214 (1995).

[38] P. Beiersdorfer, A. Osterheld, S.R. Elliott, M.H. Chen, D. Knapp, and K. Reed, *Phys. Rev. A* **52**, 2693 (1995).

[39] R.E. Marrs, P. Beiersdorfer, S.R. Elliott, D.A. Knapp and T. Stoehlker, *Physica Scripta* **T59**, 183 (1995).

[40] P. Beiersdorfer et al., *Phys. Rev. A* **53**, 3974 (1996).

[41] A.J. Smith, P. Beiersdorfer, V. Decaux, K. Widman, K.J. Reed and M.H. Chen, *Phys. Rev. A* **54**, 462 (1996).

[42] K.J. Reed and M.H. Chen, *Phys. Rev. A* **54**, 2967 (1996).

[43] D.W. Savin, P. Beiersdorfer, J.C. Lopez-Urrutia, V. Decaux, E.M. Gullikson, S.M. Kahn, D.A. Liedahl, K.J. Reed, K. Widmann, *Astrophys. J.* **470**, L73 (1996).

[44] P. Beiersdorfer, J.C. Lopez-Urrutia, V. Decaux, K. Widmann, P. Neill, *Rev. Sci. Instrum.* **68**, 1073 (1997).

[45] A.S. Shlyaptseva, R.C. Mancini, P. Neill, P. Beiersdorfer, J.R. Crespo Lopez-Urrutia, K. Widmann, *Phys. Rev. A* **57**, 888 (1998).

[46] G.V. Brown, P. Beiersdorfer, D.A. Liedahl, K. Widmann, S.M. Kahn, *Astrophys. J.* **502**, 1015 (1998).

[47] P. Beiersdorfer, G.V. Brown, S. Utter, P. Neill, K.J. Reed, A.J. Smith, R.S. Thoe, *Phys. Rev. A* **60**, 4156 (1999).

[48] D.W. Savin, B. Beck, P. Beiersdorfer, S.M. Kahn, G.V. Brown, M.F. Gu, D.A. Liedahl, J.H. Scofield, *Physica Scripta* **T80B**, 312 (1999).

[49] M.F. Gu, S.M. Kahn, D.W. Savin, P. Beiersdorfer, G.V. Brown, D.A. Liedahl, K.J. Reed, C.P. Bhalla and S.R. Grabbe, *Astrophys. J.* **518**, 1002 (1999).

[50] D.W. Savin, P. Beiersdorfer, S.M. Kahn, B.R. Beck, G.V. Brown, M.F. Gu, D.A. Liedahl and J.H. Scofield, *Rev. Sci. Instrum.* **71**, 3362 (2000).

[51] A.J. Smith, P. Beiersdorfer, K.J. Reed, A.L. Osterheld, V. Decaux, K. Widmann, M.H. Chen, *Phys. Rev. A* **62**, 012704 (2000).

[52] J.M. Laming, I. Kink, E. Takacs, J.V. Porto, J.D. Gillaspy, E.H. Silver, H.W. Schnopper, S.R. Bandler, N.S. Brickhouse, S.S. Murray, *Astrophys. J.* 2000 **545**, L161 (2000).

[53] R. Radtke, C. Biedermann, T. Fuchs, G. Fussmann, P. Beiersdorfer, *Phys. Rev. E* **61**, 1966 (2000).

[54] G.V. Brown, P. Beiersdorfer, and K. Widman, *Phys. Rev. A* **63**, 032719 (2001).

[55] P. Beiersdorfer, S. von Goeler, M. Bitter, D.B. Thorn, *Phys. Rev. A* **64**, 032705 (2001).

[56] G.V. Brown, P. Beiersdorfer, H. Chen, M.H. Chen, and K.J. Reed, *Astrophys. J.* **557**, L75 (2001).

[57] M.F. Gu, S.M. Kahn, D.W. Savin, E. Behar, P. Beiersdorfer, G.V. Brown, D.A. Liedahl, and K.J. Reed , *Astrophys. J.* **563**,462 (2001).

[58] G.V. Brown, P. Beiersdorfer, K.R. Boyce, K.C. Gendreau, M.F. Gu, J. Gygax, S.M. Kahn, R. Kelley, F.S. Porter, D.W. Savin, *Physica Scripta* **T92**, 130 (2001).

[59] H. Chen, P. Beiersdorfer, J.H. Scofield, K.C. Gendreau, K.R. Boyce, G.V. Brown, E.L. Kelley, F.S. Porter, C.K. Stahle, A.E. Szymkowiak, *Astrophys. J.* 2000 **567**, L169 (2002).

[60] P. Beiersdorfer, E. Behar, K.R. Boyce, G.V. Brown, H. Chen, K.C. Gendreau, M.F. Gu, J. Gygax, S.M. Kahn, R.L. Kelley, F.S Porter, C.K. Stahle and A.E. Szymkowiak, *Astrophys. J.* **576** L169 (2002).

[61] P. Beiersdorfer, M. Bitter, D. Hey, K.J. Reed, *Phys. Rev. A* **66**, 032504 (2002).

[62] P. Beiersdorfer, H. Chen, D. Hey, A.J. May, A.L. Osterheld, K.J. Reed, J.H. Scofield, D.B. Thorn, A. Bitter, K.R. Boyce, *AIP Conference Proceedings* v.**635**, p.135-144 (2002).

[63] P. Beiersdorfer, B. Beck, J.A. Becker, J.K. Lepson, K.J. Reed, electron beam in the SuperEBIT electron beam ion trap", *AIP Conference Proceedings* v.**652**, p.131-140 (2003).

[64] A. Dasgupta, K.G. Whitney, H.L. Zhang and D.H. Sampson, *Phys. Rev. E* , **55**, 3460 (1997).

[65] A. Iwamae, A. Tanaka, T. Inoue, T. Fujimoto, H.-L. Zhang, D. Kilcrease and G. Csanak, *Polarization Emission Lines from Beryllium-like oxygen OV: Analysis based on the Population-Alignment Collisional-Radiative model*, in *Proceedings of the 3rd US-Japan Plasma Polarization Spectroscopy Workshop*, Livermore, California June 18-21, 2001 (Edited by P. Beiersdorfer and T. Fujimoto), University of California Lawrence Livermore National Laboratory Report UCRL-ID-146907, p.165

[66] A. Iwamae, T. Fujimoto, H. Zhang, D.P. Kilcrease, G. Csanak and K.A. Berrington, *Population Alignment Collisional Radiative Model for Helium-like Carbon: Velocity Distribution Function in Plasmas*, Research Report, NIFS-DATA Series, NIFS-DATA-78, Aug.2003

[67] M.K. Inal and R Bensaid, *Hyperfine Interactions* v.**127**, 263 (2000).

[68] U. Kentsch, G. Zschornack, F. Grossann, V.P. Ovsyannikov, F. Ullmann, Fritzsche, Surzhykov, *Nucl. Instrum. Methods Phys. Res. B* **187**, no. AY, p. 1144 (2002).

[69] T. Fujimoto, F. Koike, K. Sakimoto, R. Okasaka, K. Kawasaki, K. Takiyama, T. Oda and T. Kato, *Atomic Processes Relevant to Polarization Plasma Spectroscopy*, Research Report, NIFS-DATA Series, NIFS-DATA-16, Apr. 1992

[70] T. Fujimoto, H. Sahara, G. Csanak and S. Grabbe, *Atomic States and Collisional Relaxation in Plasma Polarization Spectroscopy: Axially Symmetric Case*, Research Report, NIFS-DATA Series, NIFS-DATA-38, Oct. 1996

[71] U. Fano, *Phys. Rev.* **131**, 259 (1963)

[72] A. Ben-Reuven, *Phys. Rev.* **145**, 7 (1966)

[73] G. Csanak, *Two Notes on Atoms in Dense Plasmas*, LA-UR-93-0034

[74] S.A. Kazantsev, *Usp.Fiz.Nauk* , **139**, 621 (1983), (English translation: *Sov.Phys.Usp*, **26**, 328 (1983))

[75] S.A. Kazantsev, N.Ya. Polynovskaya, L.N. Pyatnitskii, and S.A. Edel'man, *Usp.Fiz.Nauk*, **156**, 3 (1988) (English translation: *Sov.Phys.Usp.*, **31**, 785 (1988)

[76] S.A. Kazantsev and J.-C. Henoux, *Polarization Spectroscopy of Ionized Gases*,Kluwer Academic Publishers, Dodrecht, 1995

[77] S.A. Kazantsev, A.G. Petrashen, and N.M. Firstova, *Impact Spectropolarimetric Sensing*, Kluwer Academic/Plenum Publishers, New York,1999

[78] T. Fujimoto and S.A. Kazantsev, *Plasma Phys. Control. Fusion*, **39**, 1267 (1997)

[79] A. Iwamae, T. Sato, Y. Horitomo and T. Fujimoto, *Polarization of ECR helium plasma and Population-Alignment Collisional-Radiative model* (This Workshop, 2004)

[80] P. Hakel, R.C. Mancini, J.-C. Gauthier,E. Minguez, J. Dubau, and M. Cornille, *X-Ray line Polarization of He-like Si Satellite Spectra in Plasmas Driven by High-Intensity Ultra-Short Pulsed Lasers*, Accepted for publication in Phys. Rev. E, 2003

[81] S.A. Kazantsev and A.G. Petrashen, Opt.Spekt. **92**, 533 (2002), (English translation: Optics and Spectroscopy **92**, 483 (2002))

[82] V.L. Kantsyrev, A.G. Petrashen, and A.S. Shlyaptseva, Opt. Spek. **94**, 377 (2003), (English translation: Optics and Spectroscopy, **94**, 338 (2003))

[83] K.J. Reed and M.H. Chen, *Relativistic effects on the Polarization of line radiation emitted from He-like and H-like ions following electron impact Excitation*, in *Proceedings of the 3rd US-Japan Plasma Polarization Spectroscopy Workshop*, Livermore, California June 18-21, 2001 (Edited by P. Beiersdorfer and T. Fujimoto), University of California Lawrence Livermore National Laboratory Report UCRL-ID-146907, p.305

[84] A.J. Smith, P. Beiersdorfer, K.L. Wong and K.J. Reed, *Measurement of the Polarization of the K 2 Line of heliumlike* V^21+, in *Proceedings of the 3rd US-Japan Plasma Polarization Spectroscopy Workshop*, Livermore, California June 18-21, 2001 (Edited by P. Beiersdorfer and T. Fujimoto), University of California Lawrence Livermore National Laboratory Report UCRL-ID-146907, p.299

[85] H. Chen, *Effect of Polarization on the measurements of Electron Impact Excitation Cross-Section of L-shell Fe in an Electron Beam Ion Source* , in *Proceedings of the 3rd US-Japan Plasma Polarization Spectroscopy Workshop*, Livermore, California June 18-21, 2001 (Edited by P. Beiersdorfer and T. Fujimoto), University of California Lawrence Livermore National Laboratory Report UCRL-ID-146907, p.319

[86] G. Csanak, D.P. Kilcrease, D.V. Fursa, and I. Bray, *Alignment Creation by Elastic Electron Scattering* (This Workshop, 2004)

[87] M. Hayakawa, A. Iwamae, T. Fujimoto, M. Goto, and S. Morita,*Plasma polarization spectroscopy on Large Helical Device* (This Workshop, 2004)

[88] T. Kawachi, N. Hasegawa, A. Iwamae, Y. Horitomo, and T. Fujimoto, *Plasma polarization spectroscopy on recombining plasmas produced by ultrashort laser pulses* (This Workshop, 2004)

[89] J. Kim and D.-E. Kim , Phys. Rev. E **66**, 017401 (2002)

[90] H. Chen,*Polarization measurements for the 2p-3d and 2p-3s transitions in Ne-like and F-like iron*, (This Workshop, 2004)

[91] P. Beiersdorfer and M. Slater, Physical Review E, **64**, 066408 (2001)

[92] A.S. Shlyaptseva, D.A. Fedin, S. Hamasha, S. Hansen, C. Harris, V.L. Kantsyrev, P. Neill, N. Ouart, P. Beiersdorfer, U. Safranova, Rev. Sci. Instr. **74**, 194, (2003)

[93] J. Weisheit, Private communication, 2004

Review of X-ray polarization measurements on Z-pinches in Russia and Poland

Baronova E.O., Stepanenko M.M., Sholin G.V., Jakubowski[1] L., Fujimoto[2] T.
RRC Kurchatov Institute, Moscow, Russia
[1] Soltan Institute of Nuclear Study, Poland, Warsaw
[2] Kyoto University, Japan

1. Introduction

With regard to the light emission, polarization is the second characteristic next to the photon energy. In the optical region polarization is rather straightforward to measure and it is contributing to understanding the characteristics of plasmas [1]. However, polarization of x-rays is difficult to measure, and many x-ray spectra are presented in the literature even without an explicit mention about the polarization effects. Exceptions are *e.g.*, polarized He-like x-rays from the electron beam ion trap [2], solar flares [3], vacuum sparks [4], plasma foci [5], and laser-produced plasmas [6].

One difficulty in spectroscopy of the plasmas produced by lasers and from Z-pinches is that they radiate emissions from a small region, which is called the hot spot, the bright spot or the plasma point [7]. These plasmas vary too rapidly in space and time to be followed by the conventional instrumentation. The measurements are then averages over space and time, but these averages do not necessarily reflect the average of the plasma state.

Interpretation of the spectra in terms of single plasma parameters suffers further problems, which are difficult to solve or poorly known. These problems include the use of polarized x-rays for calibration without recognizing that, or a possible angular dependence of the intensity of polarized radiation from the plasma. Original polarization may be affected by hyperfine interactions, or by the opacity since photons diffuses through the various plasma regions to reach the instrument outside.

Radiation from a plasma is polarized only if the radiation comes from excited ions that are aligned at the time that they radiate. Aligned excited states may be due to a preferential orientation of the ions in electromagnetic fields. Those macroscopic fields can be generated in plasma or just created by electrons responsible for excitation of ions.

When the plasma electrons are in random directions, the x-rays from the different ions are also polarized in random directions, and the radiation from the plasma is unpolarized. However, if the electrons that are energetic enough to excite the ions are anisotropic, with their velocities mostly in a particular direction, the x-rays from the plasma could be polarized. Usually only the electrons in the high energy tail of a Maxwellian energy distribution are responsible to excite helium-like ions, for example. In addition various kinds of fast electrons are expected in hot dense plasma of Z-pinches [8]. Therefore, polarized x-rays are very sensitive diagnostic means for electrons in the anisotropic tail of a basically Maxwellian energy distribution.

Interpreting the polarization measurement in terms of an anisotropic electron distribution assumes that the electron's electric field determines the orientation of the ion during the time needed to radiate the polarized x-ray. This is true for isolated ions, or for

ions in a relatively tenuous plasma. Then the only electric field that can orient the excited ion comes from the electron that did the excitation.

Since the plasmas treated in this review are dense the electric field produced in the plasma becomes more important in orienting the electron orbit in the excited ion, as first suggested by Sholin [9]. Then the polarization reflects not only the anisotropic electrons, but also the plasma electric field. However details are not known yet about the plasma size, the spatial extent of the electron beam and electromagnetic fields, their duration, and the interaction of spatially anisotropic hot electrons and electromagnetic fields with multicharged ions.

In conventional spectroscopy x-ray spectrum is interpreted in terms of the plasma density and temperature on the basis of the ratio between specific lines. However, some lines can be polarized while others are not, so that ignoring polarization could give substantially different estimates from the correct plasma density, for example. On the other hand, if we have a proper theoretical understanding the observed polarization could give information about anisotropic electrons or strong electric and/or magnetic fields. To the best of our knowledge, the necessary theoretical understanding of polarized x-ray emission from a dense plasma is still being developed; for isolated ions the line spectrum and its polarization are understood, at least in principle [2].

In this paper we review the experimental results of the He-like lines of iron and argon emitted from vacuum spark plasmas from the standpoint of polarization study. These include the plasma focus at the discharge current 500 kA and the Z-pinch with current of 3 MA [10,11], which is discussed for the first time here. The He-like lines are favored for diagnosing plasmas because they have substantial intensities over a large temperature range, and they can be resolved well with modern spectrometers.

Despite many publications on polarized radiation from plasmas over the last few decades, it is not yet possible for us to use the various theoretical approaches in a quantitative interpretation of the observed x-ray polarization in terms of the two effects that have received much attention: anisotropic energetic electrons and the strong electric and/or magnetic fields. Both the effects should be characteristic of the pinch plasma, which has a definite axis defined by the electrodes. At present we have to restrict ourselves within the qualitative discussions as presented below.

2. Experimental results.

I. *Vacuum spark —discharge current 150 kA*

A 150 kA vacuum spark machine [4] with iron electrodes produced iron plasmas which usually contained one or more plasma points. These localized plasma regions are responsible for all the plasma's radiation in helium-like x-rays. The x-rays were observed by two focusing Johann spectrometers with high resolution of $d\lambda/\lambda \sim 5 \times 10^{-4}$. The dispersive element was a spherical quartz crystal ($2d$=0.85 nm, R_{cr}= 0.5 m), which was placed at about 0.14 m away from the plasma. A 20 micron thick beryllium filter protected the spectrometers from the visible light.

The film was exposed to the radiation from 500 shots. Then the electrode was replaced and the same film was further exposed to the x-rays from an additional 500 shots. Ten of these shot sequences were necessary to obtain reproducible spectra. The reproducibility was verified with a second series of 5000 shots. These spectra are averages: they are sum of the features of the thousands of plasma points produced in

5000 shots, not the characteristics of an individual plasma point. We are confident that both devices observed the same region, *i.e.*, the entire vacuum spark. In an independent experiment it was confirmed that two spectrometers with dispersion planes oriented in the same direction with respect to the pinch axis gave an identical spectra (in the second order).

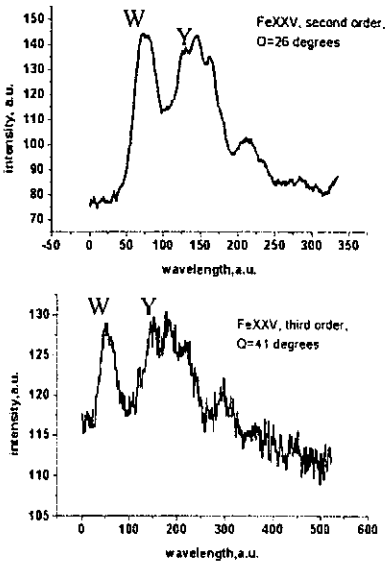

Fig.1a,b. Spectra FeXXV in second and third orders

Figure 1a is the FeXXV lines obtained with the first spectrometer in the second order, and Figure 1b is the same lines obtained with the second spectrometer in the third order. In both cases the crystal dispersion plane is oriented perpendicular to the discharge axis. The only line that is more or less isolated is the Fe XXV $1s2p(^1P_1)$-$1s^2(^1S_0)$ resonance line (marked with Gabriel's notation, **w**). The other three main FeXXV lines are unresolved: a peak at the position of the $1s2p(^3P_1)$-$1s^2(^1S_0)$ intercombination line (marked **y**) is visible as part of the broad structure which contains two additional lines, the $1s2p(^3P_2)$-$1s^2(^1S_0)$ magnetic-quadrupole transition and the $1s2s(^3S_1)$-$1s^2(^1S_0)$ forbidden line. All the lines are heavily broadened, which are due to different plasma positions, satellite transitions in the lithium-like ions, and other well known effects. We try a qualitative interpretation of these spectra below.

It is obvious that Figures 1a and 1b differ substantially; in the second order of reflection, Figure 1a, the **w**-line produces the larger film density than the broad structure. In the third order, in Figure 1b, the **w**-line is less intense than the broad structure. In other words, the w line can be weaker or stronger than other lines in FeXXV, depending on the diffraction order. The relative intensity of the **w** and **y** lines is commonly used to estimate the plasma density. Using these different **w/y** line ratios from these different spectra would give substantially different density estimates, even though the spectra come from the same plasma. This difficulty is resolved if we take x-ray polarization into account explicitly and correct the crystal reflectivity for different polarizations.

For the λ=0.185 nm (6.7 keV) iron line diffracted off our quartz crystal with $2d$=0.85 nm in the second order of reflection (n=2) the Bragg angle (given by $2d \sin\theta = n\lambda$) is θ = 26 degrees, and in the third order (n=3) the angle is θ = 41 degrees. For the spectrum of Figure 1b, the crystal is close to the Brewster angle for x-rays (45 degrees), and reflection of the p-polarized x-rays is virtually zero. As a result, Figure 1b is a spectrum that contains only x-rays with polarization whose electric field is parallel to the crystal surface. Figure 1a contains both polarizations, parallel and perpendicular to the crystal. In a further quantitative interpretation, we may have to take into account the opacity effects.

II. ***Plasma focus, Mather type —discharge current 500 kA***

Two X-ray spectrometers A, B with spherical quartz crystals (2d = 0.668 nm, R_{cr} = 0.5 m) with mutually perpendicular dispersion planes were used to obtain spectra of ArXVII in one shot [13]. The spectrometer arrangement is given in Fig.2. Dispersion

plane of device B is perpendicular to the discharge axis and it incorporates a 300μm slit. The plasma to crystal distance was 0.5 m, and Kodak DEF was detector. A typical plasma image is shown in the central part of Fig. 2. Plasma consists of a few (1-10) hot spots with diameter 0.3-0.5 mm.

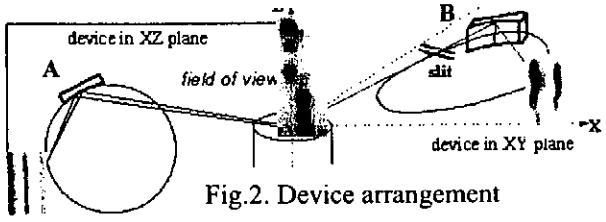

Fig.2. Device arrangement

For polarization analysis the only shots with a single hot spot were considered which provided the same field of view for both the spectrometers [14]. An example of spectra from both the spectrometers and the corresponding plasma image are presented in Fig.3. The spectrum from spectrometer A with the dispersion plane parallel to the discharge axis exhibits the **w** line much stronger than **y** while the spectrum taken by B shows less dramatic difference in the intensities of those lines. That is understandable if the **w** line is polarized in the direction perpendicular to the discharge axis.

According to the theory [9] the **w** line is polarized by up to 60% if the excitation is by fast electrons just above the excitation threshold and a degree of polarization up to 50% can be expected due to the presence of electric fields.

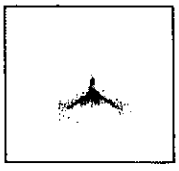

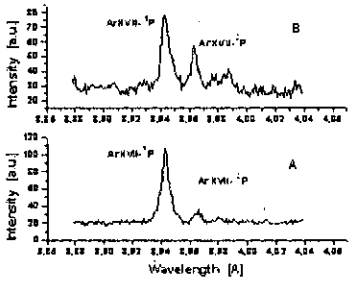

Fig.3. Spectra and plasma image

Within the accuracy of the present measurements the other lines are unpolarized, in accordance with the prediction from the simple theories. The degree of polarization could be even lower owing to such effects as depolarizing collisions with low-energy electrons or opacity. Still, the measurements here indicate an appreciable polarization in the **w**-line.

Although the **w** lines from the vacuum spark and plasma focus indicate polarization, the relatively large line widths, opacity effect, etc make it more difficult to reach definite conclusions about the velocity distribution or electromagnetic fields.

III. *Angara-5-1 —discharge current 3 MA*

An x-ray spectrometer with a convex mica crystal (2d = 1.9989 nm, R_{cr} = 0.025 m) was used to observe the x-ray spectra emitted from Angara-5-1 machine. The plasma to crystal distance was 2.2 m, and the dispersion plane of the spectrometer was perpendicular to the discharge axis. Kodak DEF was used as detector. An example of the spectra is shown in Fig.4a. The H- and He-like lines of Ar are registered in the second, third and forth orders. Figure 4b shows the corresponding densitograms. These spectra were kindly provided by the researchers from Angara-5-1 and detailed discussions are further planned in [10, 11].

The two spectra in Fig. 4b show no obvious difference in relative intensities of the **y** and **w** lines. Even if these lines were polarized, the polarization degrees are lower than those of the lines emitted from the machines with a smaller discharge current. This very preliminary conclusion needs to be confirmed in future experiments.

Fig.4a. Ar XVIII, Ar XVII-spectra in II,III, IV orders of reflection.

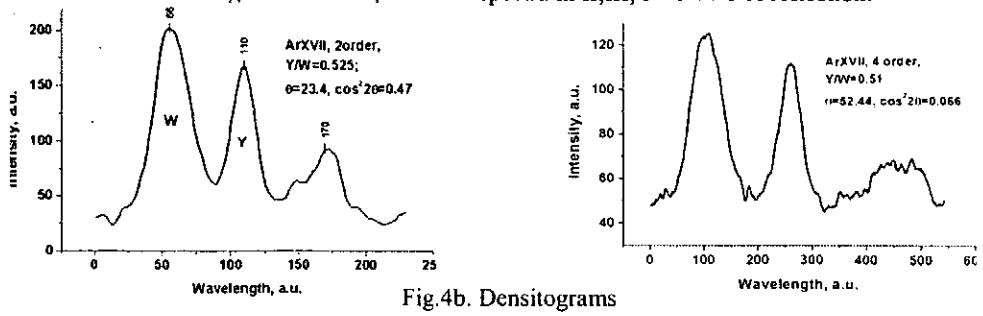

Fig.4b. Densitograms

The degree of polarization would be interpretable in terms of interesting plasma parameters if it were known how the plasma affects the x-ray polarization. Some related aspects of the given problem are considered in section 3 of this paper.

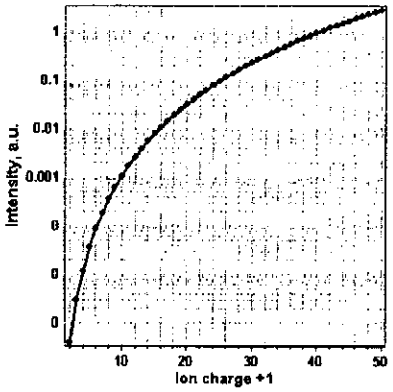

Fig.4c. Calculated relative intensity of y to w

Summarizing the results from sub-section I-III we emphasize the important features of the presented time integrated spectra:

i) The width of the resonance line is larger than that of the intercombination line for all the studied elements at the current 500 kA, 3 MA (y line is not resolved enough at the current 150 kA to make such a conclusion).

ii) Relative intensity of the intercombination line is higher than expected; see Fig.4c.

iii) The apparent intensity of the resonance line to the intercombination line intensity might indicate polarization at the discharge current of 150 and 500 kA.

We further consider the problems, mentioned in i)-iii).

3. Spectrum analysis — line width and intensity.

I. *Measured width of lines*

The experimental width of the resonance line of Ar XVII at the discharge current 3 MA is 10 mÅ. The measured width $\Delta\lambda_m$ consists of several components:

$$\Delta\lambda_m = (\Delta\lambda_{dev}^2 + \Delta\lambda_p^2 + \Delta\lambda_{rad}^2 + \Delta\lambda_{ukn}^2)^{1/2}, \qquad (1)$$

where $\Delta\lambda_{dev}$ – the broadening due to apparatus function, $\Delta\lambda_p$ – the line broadening due to the plasma, $\Delta\lambda_{rad} \cong 0.1$ mÅ – the natural width, $\Delta\lambda_{ukn}$ – broadening from unknown reasons. The first two components can be estimated as follows:

$$\Delta\lambda_{dev}^2 = \Delta\lambda_{geom}^2 + \Delta\lambda_{diffr}^2 + \Delta\lambda_{foc}^2 + \Delta\lambda_{det}^2 + \Delta\lambda_{size}^2, \qquad (2)$$

where $\Delta\lambda_{geom}$ – the geometrical component: for focusing crystals it includes optical aberrations and errors in manufacturing, $\Delta\lambda_{diffr}$ – the diffraction component, which

corresponds to HWRC = 40 arcseconds for our quartz crystals, $\Delta\lambda_{foc}$ – the component due to incorrect positioning of the detector on the Rowland circle (for Johann, Johansson, Cauchois and Cauchois-Johansson spectrometers), $\Delta\lambda_{det}$ – the broadening due to the detector itself (an example is the double layer film when used at a small grazing angles [15], $\Delta\lambda_{size}$ – the broadening caused by a finite size of the plasma; this type of broadening is negligibly small in the case of focusing spectrometers of Johann or Cauchois type and vanishes on the middle plane of an ideally manufactured Johansson or Cauchois – Johansson spectrometer. $\Delta\lambda_{dev}$ = 5 mÅ for the spectra at the current 3 MA.

$$\Delta\lambda_p^2 = \Delta\lambda_D^2 + \Delta\lambda_{Stark}^2 + \Delta\lambda_{Zeeman}^2, \qquad (3)$$

where $\Delta\lambda_D$ – the Doppler broadening, $\Delta\lambda_{Stark}$ – the Stark broadening, $\Delta\lambda_{Zeeman}$ – the broadening due to the Zeeman effect.

It should be noted that, in optically thick plasmas, the line width is further disturbed by opacity and the measured width can be even larger than that described by equation (1).

II. ***Doppler component of the w-line width***

The line broadening caused by the thermal motion of radiating ions (atoms) is:

$$\frac{\delta\lambda_D}{\lambda} = 2.44\cdot 10^{-3}\sqrt{\frac{T_i}{A}}. \qquad (4)$$

Here T_i is the ion temperature in keV, A is the ion mass in atomic units, $\delta\lambda_D$ is the total width at half-maximum. Substituting the argon mass one obtains for the w-line of the helium-like argon (λ=3,947 mÅ)

$$\delta\lambda_{D/Ar} = 1.53\sqrt{T_i}\ \text{mÅ}. \qquad (5)$$

If T_i = 1 keV then $\delta\lambda_{D/Ar}$ = 1.53 mÅ. In Z-pinches the typical situation is $T_e \cong 1$ keV and $T_e \cong T_i$, so that the experimental width of w (10 mÅ) cannot be explained by the Doppler effect.

III. ***Stark component of the w-line width***

Figure 5 shows the displacement of upper levels of the ArXVII resonance line 2 $^1P_1 - 1^1S_0$ and the intercombination line $2^3P_1 - 1^1S_0$ versus the strength E of the plasma macroscopic electric field (Stark effect). Calculations are made for stationary electric field in the LS-coupling scheme. This approximation gives the upper bound of the actual displacement of the levels.

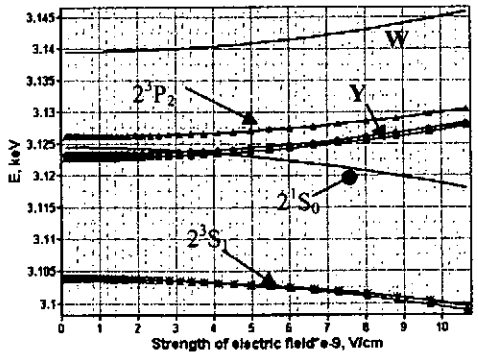

Fig.5. n=2 levels is electric field, ArXVII

In plasma dynamics the following situation may arise: an electric field generated by the plasma collective processes grows up to a substantial strength during the lifetime of the He-like ions. The displacement of upper level of corresponding lines would then be a measure of line broadening due to the Stark effect.

It is seen from Fig.5 that $\Delta\lambda_{Stark} \cong 1$ mÅ for $E = 4 \times 10^9$ V/cm. Stark broadening would be comparable with the measured width (10 mÅ) of the w-line only if $E > 10^{10}$ V/cm. To our knowledge no experimental evidence exists that confirms the presence of such an electric fields with $E > 10^{10}$ V/cm. In section V below in this paper, we will discuss the time-dependent electric fields as estimated theoretically.

IV. *Zeeman component of the w-line width*

A possible maximum value of a magnetic field on the boundary of plasma column (radius r) is expressed as $B = 0.2I/r$, where r is in cm, B is in Gauss, and I is the current in amperes. For the case of $r = 1$ mm, $I = 3 \times 10^6$ A, $B = 6 \times 10^6$ Gs. $\Delta\lambda_{Zeeman} \cong \Delta\lambda_{rad} \cong 0.1$ mÅ is two orders of magnitude smaller than the measured width of the w-line.

IV. *Intensity of intercombination line and forbidden line*

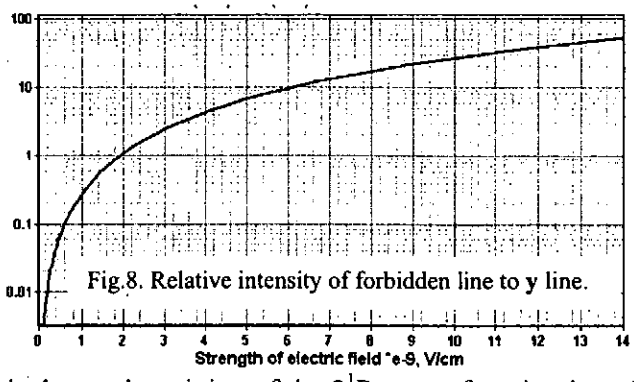

Fig.8. Relative intensity of forbidden line to y line.

The forbidden line $2^1S_1 - 1^1S_0$ lies in close vicinity to the intercombination line $2^3P_1 - 1^1S_0$ for all the elements; see Fig.6. According to selection rules the intensity of the forbidden line is zero. But the situation is changed under strong electric fields. Figure 7 shows the relative intensity of $2^1S_0 - 1^1S_0$ to $2^1P_1 - 1^1S_0$ versus E. Since this increase is due to the mixing of the 2^1P_1 wave function into the 2^1S_0 state, the w line decreases by the same amount as the increase in the y line intensity. Figure 8 shows the relative intensity of the $2^1S_0 - 1^1S_0$ line to the intercombination line y. The intensity of the forbidden line can be larger than that of the intercombination line if $E > 2 \times 10^9$ V/cm.

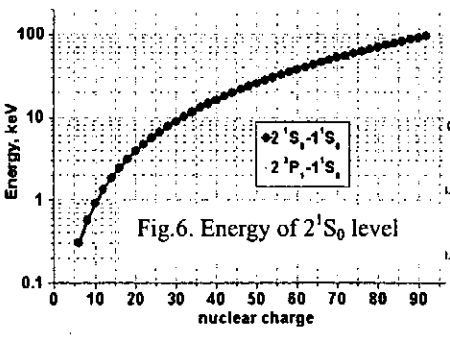

Fig.6. Energy of 2^1S_0 level

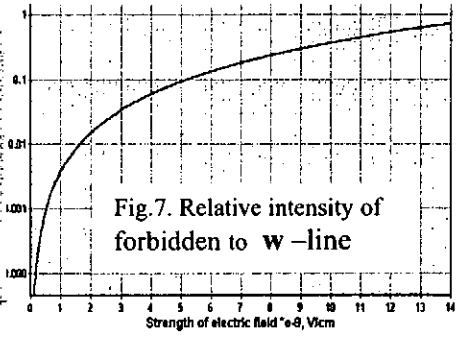

Fig.7. Relative intensity of forbidden to w –line

For time integrated measure-ments the actual yield of the for-bidden line depends on the strength of the electric fields in plasma dynamics: i.e. how long electric fields coexist with the He-like ions. Since the forbidden line lies in the close vicinity of y, the measured intensity of the y-line can be enhanced due to the yield of the forbidden line. This point has to be taken into account in plasma diagnostics, where the ratio y/w is widely used to determine the plasma electron density. In this case, the width of the intercombination line y includes contributions both from the forbidden line and the adjacent satellites.

V. *MHD calculations of electric fields and electron beams*

MHD calculations for the argon discharges were carried out, which included the magnetic field pressure, the plasma outflow in the z-direction, anomalous Joule heating,

radiation losses and the generation of an electron beam. The detailed description of the physical model is given in [16]. High ohmic electric fields is generated in the z-direction due to anomalous plasma resistivity and an even higher Hall electric field is generated in the radial direction. Figure 9 shows an example of the strength of the radial electric field E_r, the axial electric field strength E_z in MV/cm, the plasma temperature T_e in keV, the plasma density N_e in cm^{-3}, the plasma radius r, the electron beam current I_{beam} in kA, together with the intensities of the resonance lines of He- and H-like ions (arbitrary units) versus time. The discharge current is 500 kA. In the final stage of plasma expansion T_e is kept constant in >90 nsec. It is seen that the maximum value of is E_r is 2 MV/cm, and this is higher than the maximum value of E_z = 0.6 MV/cm. The maximum value of the beam current is 20 kA. This figure suggests that **time-integrated** intensities of the resonance H-like line can be more affected by the electric fields or/and the electron beam than the He-like resonance line.

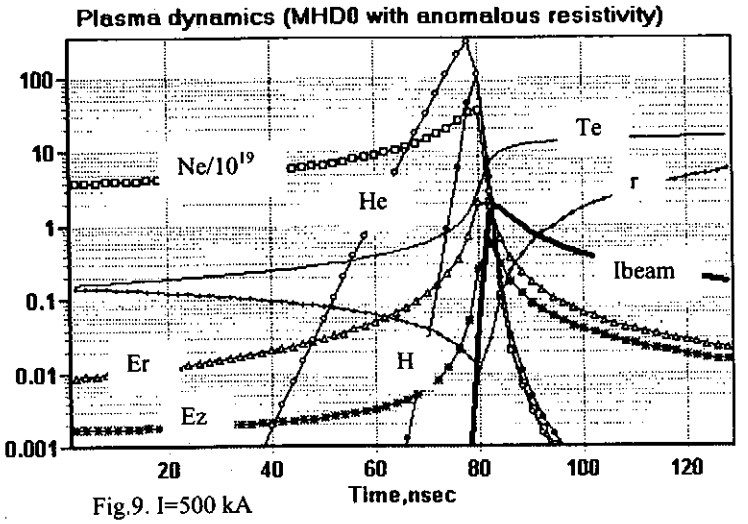

Fig.9. I=500 kA

Figure 10 shows the same parameters as Fig. 9 at the discharge current 2 MA, and

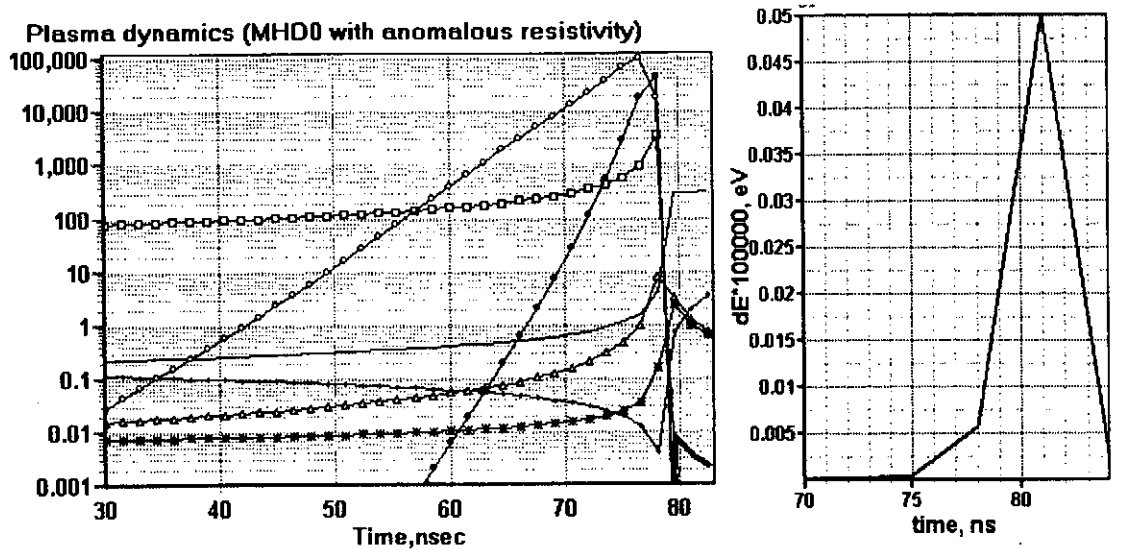

Fig. 10. I = 2 MA. The displacement of the $^1P_1$ level of He-like argon.

the corresponding displacement of upper level of the resonance line w versus time. Figures 9 and 10 testify that He and H-like ions coexist in time with fast electrons and high electric fields in the same plasma volume. The electron beam (and also the generation of electrons with a few keV) is thought to come from the hot spot and its

neighborhood at the time of its breakdown, when the density of hot ions is still sufficient to emit substantial radiation. In these models the electron beam has an energy distribution from many keV up to many hundreds of keV, and the motion of low energy (a few keV) electrons emanating from the beam is determined by the complicated electromagnetic fields inside the plasma. Our conclusions are: the higher is the discharge current

i) the higher is the strength of the generated electric fields, and the shorter is the lifetime of electric fields;
ii) the less is the percentage of electrons in the electron beam, and the shorter is the beam lifetime;
iii) the shorter is the plasma lifetime; and
iv) the shorter is the interaction time of the He-like ions with electron beams and electric fields.

Figure 9 suggests that, even for the small discharge current, the space and time averaged degree of plasma anisotropy may be small and so is the observed polarization. However, time and/or space resolved data could reveal high degree of polarization at some instant.

In our MHD model we did not take into account the turbulent magnetic fields, which might change the plasma dynamics. Its influence on plasma dynamics as well as on the x-ray emission are described in [9]. Another theoretical approach, given in [17], predicts the electric field strength $E = 10^{10}$ V/cm.

VI. ***Estimation of opacity effect***

The absorption range L_w for resonance photons (**w**-line) on the assumption of the Doppler line shape is: $L_w \cong (\delta\lambda_D / \delta\lambda_{rad}) / N / 3.14 / \lambda \cong 2\times 10^{15}/N$ cm, where N is the concentration of the He-like ions. If $N \cong 10^{19}$ cm^{-3} then $L_w \cong 2\mu$. For the 3MA plasma we do not have experimental data on the size d of the hot spots, radiating the **w**-line. Typical plasma size is 0.1-1 mm. Thus we may conclude that $L_w \cong 2\mu$ is much smaller than the plasma size.

The absorption coefficient for the **w**-line is $k_w = 1/ L_w$ and $k_d = d/L_w > 50$. So the plasma is optically thick to the **w**-line radiation. The broadening of the **w**-line due to the plasma opacity for a Doppler line shape can be roughly estimated as

$$\delta\lambda_D^* \cong \delta\lambda_D \times (\ln k_w^* d)^{1/2} \cong 4\delta\lambda_D \qquad (6)$$

The apparent broadening of the w line in Figs. 3 and 4 may be due to this effect. It is noted that, even the opacity effect modifies the line profile, the integrated intensity over the line is unchanged, because under our experimental conditions, the population balance of the upper level, 2 $^1P_1$, is excitation and the radiative decay, i.e., corona equilibrium. More correct estimation (within the pinch dynamics) is now being considered and will be published.

4. Concluding remarks

It is noted that difficulties in doing a more complete analysis on polarization are partly experimental. It would be desirable if we can have a crystal which gives lower order reflection angle that coincides with the Brewster angle for x-rays (45°).

Careful quantitative interpretation of polarization phenomena in hot dense plasmas needs a theory that takes into account important details of the processes involved.

The theoretical prediction of the degree of polarization of the w and y lines can be done in the framework of the time dependent collisional-radiative model, which includes: generation of fast electrons and atomic rates integrated over a nonmaxvellian distribution function, the opacity effect, the cascade feeding, the fine structure of appropriate levels, generation of high electromagnetic fields and their influence on energy levels, including forbidden lines, etc. A more satisfactory and quantitative interpretation of the results presented here is underway.

Acknowledgements.
We are grateful to Dr. M.Goto for fruitful discussions on this paper.
Three of us are partially supported by RFFI grant no 02-02-16832.

References

1.T.Fujimoto, Journal of Plasma and Fusion research,v.78,no 8, p.731-737, 2002.
2. J. R. Henderson, P. Beiersdorfer, C. L. Bennett, S. Chantrenne, D. A. Knapp, R. E. Marrs, M. B. Schneider, K. L. Wong, G. A. Doschek, J. F. Seely, C. M. Brown, R. E. LaVilla, J. Dubau, M. A. Levine, Phys. Rev. Lett 65 705 (1990).
3. Korchak A.A. Sov. Phys. Dokl., 12, 92 (1967).
4. Baronova E.O., Vikhrev V.V. et.al. Proc. Eleventh Col. on UV and X-Ray Spectr., Nagoya, Japan, pp. 465-467, (1995) and Plasma Physics reports v.24,n.1,25,1998.
5. Jakubowski L, et al, Proceedings of the 4-th z-pinch Conference, AIP Conf. Proc 409 (1997).
6. J.C.Kieffer., J.P.Matte, M.Chaker, Y.Beaudoin, C.Y. Chein, S.Coe, G. Mourou, J.Dubau and M.K. Inal, Phys. Rev. Letters, 68, 480 (1992).
7. K. N. Koshelev and N. R. Pereira, J. Appl. Phys. 69, R21 (1991).
8. Vikhrev V.V.,Baronova E.O., Proc of Beams Conf, editted by M. Marcovitz and J.Shiloh, vol. 2, p. 666-669,1998.
9. Sholin G.V. Docl. Acad of Science, 175, 1256, (1967).
10. Baronova E.O., Stepanenko M.M., Vikhrev V.V., Sholin G.V., Fujimoto T., will be presented on Beams 2004 Conference, Saint-Petersburg, Russia .
11. Volkov G.V., Zaitsev V.I, etc, will be presented on Beams 2004 Conference, Saint Petersburg, Russia.
12. Inal M.K., Dubau J. J. Phys. B: At. Mol. Phys. 20, 4221, (1987). The first computation is Oppenheimer J.R., Z. Phys. a, 43, 27 (1927): see also e.g., N. F. Mott and H. S. W. Massey, "The theory of atomic collisions," third edition, p 510 (Oxford, 1985) .
13. L.Jakubowski, M.Sadowski, E.O.Baronova, Nucl.Fusion, 2004.
14. Baronova E.O, Stepanenko M.M., Jakubowski L., Tsunemi H., Journal of Plasma and Fusion research,v.78,no 8, p.759-766, 2002.
15. Baronova E.O., Takasugi K., Vikhrev V.V., Miyamoto T., "X-ray spectra of Argon and Iron ions in a gas-puff Z-pinch", Beams Conference, June, 2000, Niigata, Japan, p. 364.
16. Baronova E.O., Vikhrev V.V., all-Russian Seminar on Z-pinches, April 2004.
17. Gordeev A.V., Loseva T.V., Plasma physics reports, 2003, v.29, no 9, p.809-817.

Time-Resolved Studies of Highly Ionized Ar-Lines within MAJA Plasma Focus Device

L.Jakubowski, M.J.Sadowski, E.O.Baronova[1)]

The Andrzej Soltan Institute for Nuclear Studies (IPJ),
05-400 Otwock-Swierk n. Warsaw, Poland
[1)] NRC "Kurchatov Institute", Institute of Fusion Research, Moscow, Russia
E-mail: jakubowski@ipj.gov.pl

Abstract: The paper concerns studies of highly-ionized argon spectral lines measured with spatial- and temporal-resolution. In plasma-focus devices operated with a deuterium-argon mixture, there are often observed several (up to a dozen) high-temperature plasma micro-regions (so called hot-spots), which are formed near the pinch axis. The appearance of several micro-sources of X-rays makes the determination of some important plasma characteristics e.g., the polarization of the emitted X-ray lines, difficult and questionable. Time-resolved measurements of the selected spatial lines enable the temporal correlation of the analyzed phenomena to be performed. The paper presents also studies of pulsed electron beams measured along and perpendicularly to the z-axis, as well as other characteristics of plasma-focus discharges. It has been found that the emission of highly ionized argon lines is well correlated with the appearance of successive hot-spots. On the basis of X-ray measurements there were determined temporal changes of the electron concentration and temperature within the observed hot-spots.

1. Introduction

In pulsed discharges of the plasma-focus (PF) type, the accelerated current sheath (after reaching the electrode ends) undergoes the radial collapse and it forms a dense plasma pinch column [1-2]. Inside this column one can observe numerous micro-regions of an increased X-ray emission, which are called hot-spots. It was observed that the hot-spots are formed successively, starting from the electrode outlet and developing along the z-axis [3-4]. It makes difficult to determine some characteristics of PF discharges, e.g. the polarization of X-ray spectral lines cannot be measured unanimously because there are several micro-sources of their emission.

Since different hot-spots are formed along the *z*-axis in various instants, in order to determine accurate values of the electron concentration and temperature it is necessary to perform measurements of the chosen X-ray lines as a function of space and time. Such measurements can also facilitate identification of other objects (plasma regions) emitting similar X-ray lines, e.g. regions of Rayleigh-Taylor instabilities which appear within the moving current sheath. Therefore, simultaneously with the registration of the selected X-ray spectrum lines, we studied their correlation with pulsed electron beams emitted perpendicularly to the discharge axis as well as in the upstream direction (towards the anode). There were also investigated X-rays in various directions, as well as time-integrated X-ray images taken by means of an X-ray pinhole camera.

Precise measurements of time instants, when the observed spectral lines are emitted from individual hot-spots, should enable the accurate determination of the polarization of those lines to be performed. The aim was to carry out time-resolved measurements of the X-ray lines recorded by means of two crystal spectrometers with mutually perpendicular dispersion planes, to correlate the selected spectral peaks with corresponding hot-spots, and to determine the polarization of the X-ray emission from the investigated hot-spots.

2. Experimental set-up and diagnostic techniques

Time-resolved measurements of X-ray spectra, and particularly of highly-ionized argon lines, were performed within the MAJA-PF device operated up to 45 kJ. The device was equipped with two coaxial electrodes with diameter 130 mm and 70 mm, respectively. The main insulator, which embraced the inner electrode, was made of pyrex tube. Discharges were powered from a condenser bank charged up to 35 kV, and the maximum discharge current amounted to about 500 kA. The PF-type discharges were initiated by a break-down along the main insulator surface, and the current sheath was accelerated within the inter-electrode tubular gap. At the electrode outlet the radial collapse of the current-sheath formed a dense pinch column (called the plasma-focus). This plasma column was usually non-uniform and it demonstrated different instabilities. Inside the PF pinch column, under given experimental conditions, there are formed micro-regions of relatively high electron concentration ($>10^{21}$ cm^{-3}) and temperature (~ 1 keV). These dense plasma micro-regions (hot-spots) constitute sources of intense visible and X-ray emission, pulsed electron beams and fast ion beams [7-8]. If such discharges are performed with the deuterium filling there are also observed fast neutrons originating from D-D fusion reactions.

The X-ray emission has been investigated within the MAJA-PF device for many years. The X-ray spectra in the wavelength range of 3.8 – 4.2 Å were measured by means of a crystal spectrometers of the Johann type. In this wavelength range one can observe intense lines of highly ionized argon, and particularly Ar-XVII – $1s2p(^1P_1) - 1s^2(^1S_0)$ - resonance line, $1s2p(^3P_1)$- $1s^2(^1S_0)$ - intercombination line, as well as Li-like (Ar-XVI) satellite lines belonging to 1s213L transitions. Therefore, the recent studies have been performed at the deuterium filling with a small (several per cent) argon admixture.

During previous experiments with the MAJA-PF device particular attention was paid to spectral measurements of X-rays emitted from different hot-spots [5]. It was performed by

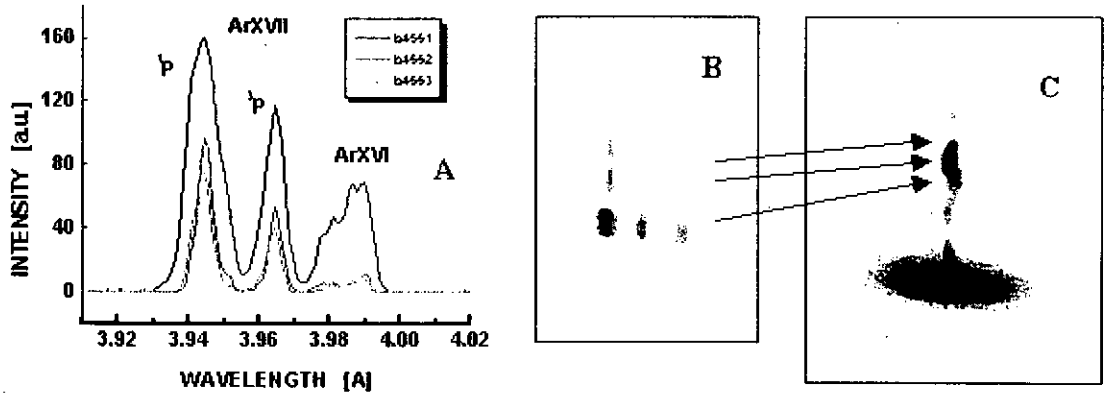

Fig. 1. X-ray lines intensities (A) and corresponding X-ray spectra (B), as obtained from highly ionized argon-ions, in a comparison with the X-ray pinhole picture (C), which shows the spatial distribution of hot spots in the investigated PF discharge.

means of a narrow slit place in front of the crystal spectrometer, which ensured the same spatial resolution along the discharge axis. Some examples of the recorded X-ray spectra are presented in Fig.1 [6]. Taking into account intensity ratio of the selected X-ray lines, as recorded for individual hot-spots, it was possible to estimate values of the electron concentration and temperature within the observed micro-regions.

Measurements of the polarization of the chosen X-ray lines have been carried out by means of two spectrometers equipped with almost identical crystals, but oriented in such a way that their dispersion planes were mutually perpendicular [9-10]. In order to record the selected X-ray lines as a function of time, the detection systems of the spectrometers were modified so that the X-ray films were replaced by sets of miniature scintillators of the NE102A type. These scintillation detectors could record the chosen spectral lines separately. Due to spatial limitations it was necessary to place the neighbour scintillators with some shift

along the observed spectral lines. All the detectors were coupled with fast photomultipliers through thin optical cables. The whole detection system has been tested and the measured differences in the signal transmission times have been set below 1 ns. Amplification factors of the investigated signals have also been determined. The time-resolved measurements of the X-ray lines were correlated with measurements of "soft" (1-4 keV) and "hard" (8-30 keV) X-ray emission as well as of pulsed ion streams emitted along the discharge axis. The use was made of a multi-channel digital analyzer operated at 1 GHz probing frequency. There were also measured pulsed electron beams, emitted perpendicularly to the z-axis (at 90°) as well as those emitted towards the anode (at 180°). To investigate electrons emitted in the upstream direction, the anode was equipped with a special opening (of 10 mm in diameter), which enabled the e-beams to be recorded behind the main collector plate, at a distance of about 50 cm from the PF pinch region. These e-beams were recorded by means of Čerenkov–type detectors [11] equipped with special radiators made of rutil. The Čerenkov effect appears when electrons have energies higher than a given threshold value, which depends on a refractive index of the radiator material. The rutil crystals enabled electrons of energy >40 keV to be observed, but to eliminate the visible radiation it was necessary to apply additional cooper-foil filters, which increased the detection threshold to about 70 keV. In order to record fast electrons emitted perpendicularly (of 90°) to the z-axis the applied Čerenkov detectors were placed at a distance of 50 cm from this axis.

3. Experimental results

3.1. Study of fast electrons emitted perpendicularly to the discharge axis

As it was reported in previous papers [3,4,6] fast electron beams are emitted mostly towards the anode (at the angle of 180°) during the radial collapse of the PF pinch column at

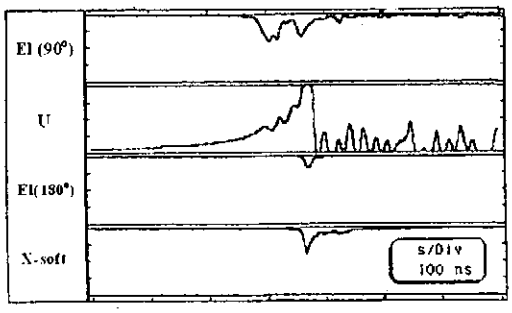

Fig,2. Correlation of electron pulses observed perpendicularly to the z-axis - El (90°) with other discharge waveforms, i.e. inter-electrode voltage - U, fast electron beams emitted along the z-axis - El (180°) and "soft" X-rays measured at the z-axis - $X_s(0°)$

the z-axis. In particular,the intense electron pulses correspond to the appearance of the hot-spots. These electron peaks are combined with peculiarity (dip) of the main discharge current and they usually correspond to the maximum of the induced over-voltage pulse. At the same time there appears the emission of "soft" X-rays and accelerated primary ions (emitted mostly along the z-axis).

In order to understand differences in the polarization of X-ray lines observed side-on the motion of electrons in radial directions is of primary importance. The electron measurements, as performed in the direction perpendicular to the discharge axis (under conditions when the Čerenkov detector did not see the electrode ends), have shown that the pulsed electron beams appear about 100 ns, before the voltage spike, as shown in Fig.2. This corresponds to an instant when the current sheath appears in front of the electrode outlet. The emission of an intense electron pulse of energy > 80 keV, in the radial direction, can be induced by some instabilities developing in the current sheath, e.g. those of the Rayleigh-Taylor type. Such instabilities have also been observed in other experiments with the coaxial electrodes [12]. It should be reminded that the emission of fast electrons in the direction perpendicular to the discharge axis has already been observed in the previous experiments within MAJA-PF device [13]. It has also been recorded in the large (1 MJ) PF-1000 facility [14].

3.2. Time-resolved studies of highly-ionized argon lines

Typical examples of oscillograms, as obtained from a PF-type discharge performed with 5% admixture of argon, are shown in Fig.3. One can easily see that the main emission of the

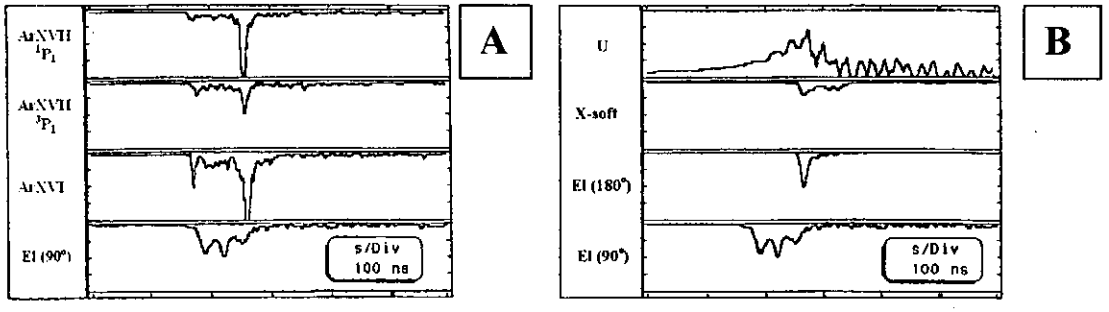

Fig.3. Correlation of time-resolved signals corresponding to the highly ionized argon lines with those showing the electron emission at the angle of 90° to the z-axis (A), as well as with other characteristics of the investigated discharge (B). The total neutron yield from this shot was 3×10^8.

considered spectral lines, i.e. the ArXVII-$^1P_1$ - resonance line, the ArXVII-$^3P_1$ intercombination line, and the averaged ArXVI satellite line, appears during the over-voltage peak (U). This effect is accompanied by the peculiarity (dip) of the discharge current and the

emission of the "soft" X-rays - X-soft as well as fast electrons directed towards the anode – El (180°). It should be noted that the beginning of the emission of the investigated X-ray lines correlates well with the appearance of pulsed electron beams emitted at the angle of 90° to the discharge axis. The considered spectral lines and the radially oriented electron beams appear about 100 ns before the main current dip. In this instant the current sheath is pushed from inter-electrode gap into the region in front of the electrode ends. The emission of the X-ray lines as well as fast electrons at this time is probably induced by Rayleigh-Taylor instabilities developing inside the moving current sheath, as observed in similar experimental facilities [12]. Evidently, theoretical studies on the modeling of discharges and instabilities in MAJA-PF device should be continued, especially for the radial collapse phase.

3.3. Study of correlation of highly-ionized argon lines with appearing hot-spots

During the radial collapse the current sheath undergoes the compression at the z-axis. The maximum concentration region moves along this axis with a velocity of the order $2x10^7$ cm/s. Inside the dense pinch column there appear high-temperature micro-regions (hot-spots) with an increased emissivity of the electromagnetic and corpuscular radiation. The hot-spots are formed successively along the z-axis and they exist about 10 ns [4]. Also in the emitted X-ray spectral lines it possible to see correlation with successive hot-spots.

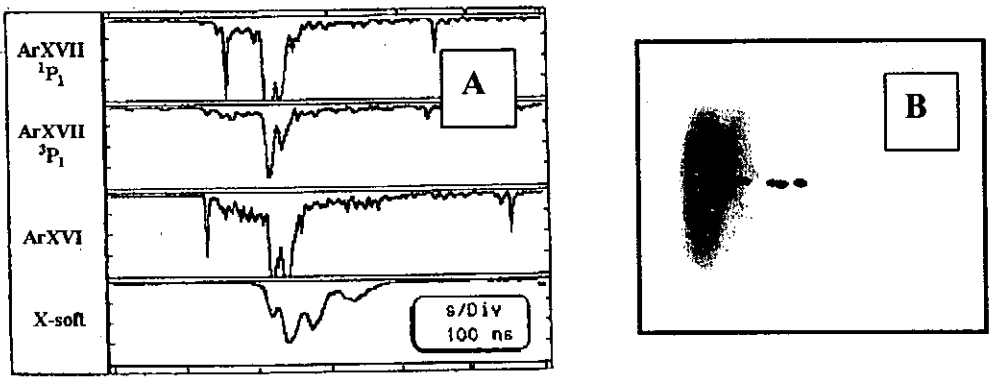

Fig.4. Temporal correlation of the emission of the investigated X-ray lines (A) with the appearance of the hot spots (B) recorded by means of an X-ray pinhole camera.

Typical traces of the analyzed spectral lines with distinct peaks corresponding to the recorded hot-spots, are presented in Fig.4. The observed peaks of the X-ray spectral lines correspond also to peaks of the total X-ray emission within energy range of 1-4 keV (see trace "X-soft" in Fig.4A). Upon the recorded X-soft trace there are also visible some late peaks, induced in the scintillation detector by fast ion pulses, which were emitted simultaneously

with the X-rays and recorded after their time-of-flight at a distance 70 cm from the PF pinch. Temporal shifts between successive peaks of the spectral line intensity and real spatial distances between successive hot-spots are consistent, provided that the velocity of motion of the maximum concentration region along the z-axis is equal to $2x10^7$ cm/s, as estimated in the previous paper [4]. On the basis of numerous recorded traces it was estimated that an average life-time of the hot-spots, as well as the half-width value of the X-ray spectral lines, amounts to about 10 ns.

The emission of the X-ray spectral lines occurs not only at the instant when the pinch is formed, but it starts when the current sheath reaches the electrode ends. This emission lasts (with varying intensity) until the maximum collapse, and it depends on appearing instabilities, which are microscopically irreproducible. An excellent example of three recorded hot-spots, which were formed after 30 ns and 40 ns, respectively, is presented in Fig.5. It can be seen that for the first and second hot-spot there were recorded all the considered spectral lines, while for the third hot-spot it was possible to record the resonance line only. It was probably caused by the fact that observation regions for the resonance and intercombination lines were different along the z-axis [15].

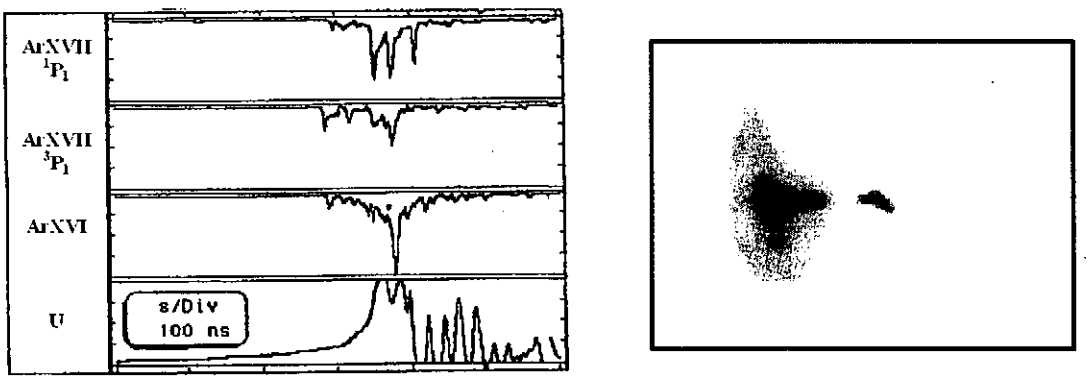

Fig.5. Correlation of the emission of X-ray spectral lines and the spatial X-ray pinhole image of three distinct hot-spots.

It should be noted that for different hot-spots one can measure various values of the ratio of the resonance, intercombination and satellite lines. This is of course connected with different values of the electron concentration and temperature in individual hot-spots. Some found were performed in the previous experiments [5]. For the considered case it was estimated that the electron concentration in the first hot-spots was $5.9*10^{21}$ cm^{-3}, while that in second hot-spot was $7.5*10^{20}$ cm^{-3} only. It should also be noted that the emission of the satellite lines starts first and it lasts the longest time.

3.4. Study of temporal changes in the electron concentration and temperature of individual hot-spots.

The electron concentration of plasma can be estimated from the ratio of intensities of the resonance and intercombination lines [16]. Since in the applied diagnostic system the radiation originated from the whole line width, the amplitude of the recorded peak correspond to the integral over the line profile for the considered instant. Hence, a comparison of amplitudes of signals for the resonance and intercombination lines enables to estimate the electron concentration to be performed for the chosen instants. Using this technique for different instants it is possible to determine temporal changes in the electron concentration during the appearance and development of different hot-spots.

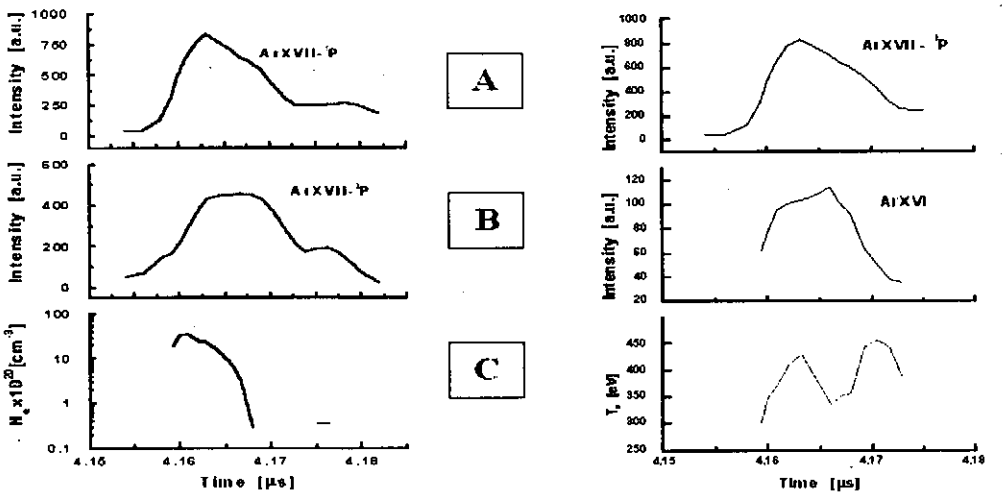

Fig.6. Oscillograms of the measured spectral lines of highly-ionized argon (A,B) and corresponding temporal changes in the electron concentration and temperature (C).

Some examples of oscillograms of the chosen spectral lines emission and computed changes in the electron concentration, as a function of time (time is counted from the beginning of the main discharge current), are presented in Fig.6. It should be noted that the computations were performed under an assumption that the electron velocity distribution was maxwellian. Therefore, the results should be treated as approximated ones. In order to determine these parameters accurately one should know more about directions of the electron beams propagation and their influences on the population of ion energetic levels.

Using a similar technique and the ratio of intensities of the satellite and resonance lines, one can also estimate [17] temporal changes in the electron temperature for different hot-spots. The results of such computations as performed on the basis of traces shown in Fig. 6A and 6B,

are presented in Fig.6C. Results of analogous computations, carried out for a discharge with several hot-spots, are given in Fig.7.

4. Summary and conclusions

The temporal changes in the emission of highly ionized argon lines were recorded in MAJA-PF device by means of a relatively simple measuring technique. These changes were correlated with hot-spots formed inside the pinch column, as well as with the emission of pulsed electron beams towards the anode and perpendicularly to the z-axis.

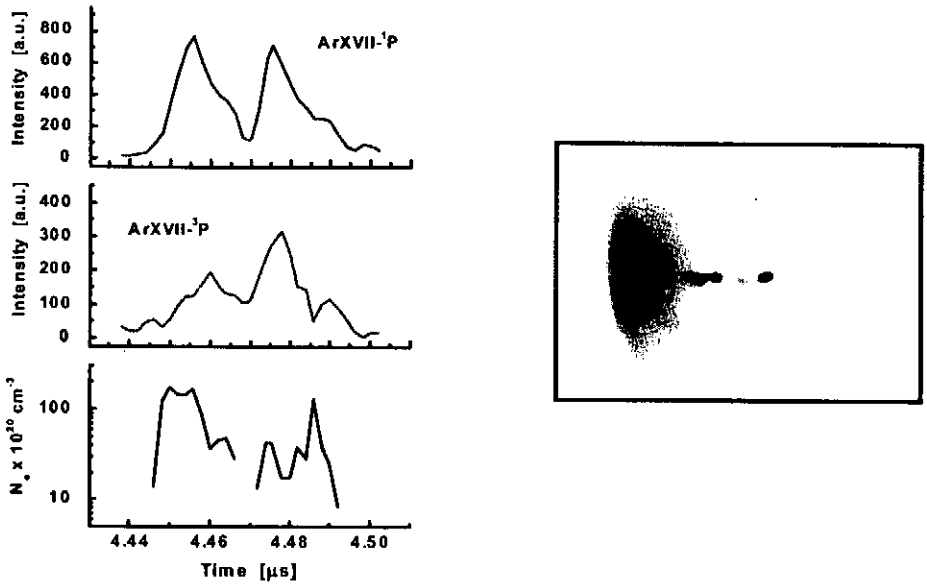

Fig.7. Oscillograms of the highly-ionized argon lines and computed changes in the electron concentration N_e in a comparison with an integrated X-ray pinhole picture, taken from a discharge with several hot-spots.

The most important results can be summarized as follows:

1. The electron beams, as observed along the z-axis through the anode, are emitted from plasma regions (hot-spots) formed inside the PF pinch column at (or nearby) the discharge axis. It was observed that the pulsed electron beams are also emitted perpendicularly to this axis, especially from the region close to the electrode outlet. Such radially-oriented beams appear about 100 ns before the distinct dip in the discharge current. It can be explained by the emission of the electron beams from strong instabilities, which develop in the current sheath when it leaves the interelectrode region.

2. It was found that the emission of highly-ionized argon lines originates from the observed hot spots. The maximum emission of the investigated spectral lines is well correlated with the appearance and life-time of hot-spots formed during the discharge.

3. The emission of the X-ray spectral lines starts about 100 ns before the current peculiarity (dip) and it is correlated with pulsed electron beams emitted perpendicularly to the discharge axis. It is possible that these effects are caused by Rayleigh-Taylor instabilities developing within the current sheath.

4. Time-resolved measurements of the chosen spectral lines make possible to determine changes in the electron concentration and temperature as a function of time, and particularly during the formation and development of individual hot-spots.

References

1. N.V. Filipov, T.I. Filipova, V.P. Vinogradov, Nuclear Fusion, Suppl., part 2, 577 (1962).
2. J.W. Mather, Phys. Fluids 8, 366 (1965).
3. L.Jakubowski, M. Sadowski, Proc. 22nd EPS Conf. on Controlled Fusion and Plasma Physics, Bournemouth 1995, Part II, p.161
4. L. Jakubowski, M. Sadowski and E.O. Baronova, Proc. Int. Conf. on Plamsa Physics Nagoya, vol. II, pp. 1326-1329 (1996).
5. L.Jakubowski, M.Sadowski and E.O.Baronova, Czech. J. Phys. **50**, Suppl. S3 (2000), pp. 173-178.
6. L.Jakubowski, M.J.Sadowski, Brazilian Journ. of Phys. **32**. 1; 187 (2002).
7. W. Neff, et al., Phys. Lett. **79A** 165-172 (1980).
8. G. Decker et al., Plasma Sources Sci. Technol. **5** 112-118 (1996).
9. L. Jakubowski, M. Sadowski, E.O. Baronova, and V.V. Vikhrev., BEAMS'98, 12th Intern. Conf. on High Power Particle Beams, Heifa, Israel, June 8-12, 1998.
10. E.O.Baronova, G.V.Sholin, L.Jakubowski, Journ. Tech. Phys 40, 1157-160 (1999).
11. L. Jakubowski, M. Sadowski, J. Żebrowski; Journ. Techn. Phys., **38**, 1, 141-150, (1997).
12. M. Rabinski, K. Zdunek, Surface and Coatings Technology 173-174, 964-967 (2003).
13. L.Jakubowski, M.Sadowski, 26th EPS Conference on Controlled Fusion and Plasma Physics, Maastricht, June 1999; ECA Vol. 23J 589-592 (1999).
14. L. Jakubowski, A. Banaszak, M.J. Sadowski, M. Scholz, Proc. Intern. Conf. on Plasma Research and Applications PLASMA-2003, Warsaw, Poland, September 9-12, 2003.
15. L.Jakubowski, M.Sadowski and E.O.Baronova, Nuclear Fusion (2004), in print.
16. A.V. Vinogradov, et al., Kvantovaya electronika (in Russian) **2(6)** 1165 (1975).
17. E.V. Aglickiy, et al., Kvantovaya electronika (in Russian) **1(3)** 579 (1974).

Magnetic-Sublevel Atomic Kinetics Modeling for Line Polarization Spectroscopy

Peter Hakel* and Roberto C. Mancini
Department of Physics, University of Nevada, Reno, NV 89557, USA
*current address: T-4 group, Los Alamos National Laboratory, NM 87545, USA

Abstract

We discuss the mechanism of polarized X-ray line emission in plasmas, its connection to plasma anisotropy, and introduce an atomic kinetics model and code (POLAR) [1] based on the population kinetics of magnetic sublevels. POLAR represents a multi-level, multi-process approach to the problem of polarized spectra in plasmas, and hence it is well suited for plasma applications where cascade effects and alignment transfer can become important. Polarization degrees of X-ray spectral lines computed with POLAR were successfully benchmarked against calculations done with other formalisms, and experimental results obtained at the EBIT facility of Lawrence Livermore National Laboratory. We also investigated the polarization of He-like Si X-ray satellite lines as spectral signatures of anisotropy in the electron distribution function. A comprehensive modeling study was performed taking into account hydrodynamics and electron kinetics. We find that two satellite lines connecting singlet states develop a noticeable polarization while the triplet lines remain unpolarized. These results suggest a scenario where triplet lines could be used as a reference while the singlets could be used as polarized markers of plasma anisotropy.

I. Introduction

Plasma spectroscopy has been a valuable tool for the determination of plasma characteristics in astrophysical as well as laboratory plasmas. Observed spectral line intensity ratios are yardsticks for measuring plasma temperature; Stark-effect-induced broadening of line profiles contains information about plasma density. Theoretical modeling of synthetic spectra requires calculation of populations of the plasma ion species that are in their ground as well as excited states. In non-LTE plasmas, the populations often strongly deviate from the Boltzmann/Saha-equilibrium values. In order to address this issue multi-level collisional-radiative atomic kinetic models are constructed. Energy level populations are then calculated as the result of combined effects of many atomic processes. Many energy levels may need to be included in a model of spectral data, which in turn leads to large sizes of atomic databases. The size and complexity of a particular atomic kinetic model is

determined by the level of detail used in the description of energy level structure and the number of atomic processes linking them. Since polarized line radiation emerges from collections of ions with unequal populations of magnetic sublevels within individual fine-structure levels, development of fundamental, magnetic-sublevel atomic kinetic models is warranted. Such models must be complemented with a way of calculating polarized line emissions based on magnetic sublevel populations. Previous work in this direction has been done by Inal and Dubau using the photon density-matrix formalism [2]. We present another approach based on properties of multipole radiation fields, which agrees with this previous work and is consistent with results of the density matrix method adopted for EBIT measurements [3-6]. With our technique the more traditional (line-intensity oriented) atomic kinetics modeling is naturally extended to the area of line polarization.

This is implemented in the code POLAR, a collisional-radiative atomic kinetics code aimed at calculation of magnetic sublevel populations. This model extends more conventional atomic kinetic modeling by considering alignment-creating anisotropic atomic processes driven by non-thermal electrons. In Section II we present the development of POLAR and Section III contains the results of application of POLAR to steady-state, low-density situations in which detailed experiments and independent calculations have been carried out. The experiments were done at the EBIT facility of Lawrence Livermore National Laboratory. Experimental conditions in EBIT are ideal for polarization studies, which makes EBIT very well suited for fundamental studies and tests of X-ray line polarization models. To this end we have applied POLAR to calculations of polarized K-shell emissions from He-like Fe ions based on a complex sublevel kinetics model that includes cascade effects. Thus, the above mentioned experiments and calculations represent a test bed for the magnetic-sublevel atomic kinetics code POLAR. Next, we applied a fully time-dependent version of POLAR to modeling of polarized X-ray emissions from laser-produced plasmas. The results of those investigations are contained in Section IV.

II. POLAR – collisional-radiative atomic kinetics of magnetic sublevels

We present a method for calculation of polarization-dependent line radiation that is based on a fundamental atomic kinetics modeling of magnetic sublevel populations. Magnetic sublevels are quantum states characterized by parity π, energy E, total angular momentum J, and its projection M_J. We complement these quantum numbers by the dominant configuration and LS energy-term labels. We construct the rate equations for

populations of magnetic sublevels using sublevel-to-sublevel electron-impact excitation cross sections, rates of electron capture, spontaneous radiative decay and other atomic processes.

Having obtained magnetic sublevel populations from atomic kinetics we then calculate polarization-dependent line intensities. For this purpose we use the multipole expansion of the radiation field rather than the photon density matrix. It has been customary to experimentally observe polarized emissions in a direction perpendicular to the chosen quantization axis and record intensities of radiation that is linearly polarized in the parallel and perpendicular directions with respect to the quantization axis. In general, the polarization of line emissions from sublevel-to-sublevel transitions is determined by the multipole type of the transition and the absolute difference in M_J values of the upper and lower levels. This is a manifestation of angular momentum conservation of the ion and field system during ion's decay by photon emission. A fine structure line transition $J_i \rightarrow J_f$ consists of sublevel emissions polarized in both directions, which overlap due to degeneracy with respect to M_J [7]. In the optically thin approximation we calculate polarization-dependent fine-structure line intensities by,

$$I_{\parallel,\perp} \propto h\nu\, A(J_i \rightarrow J_f) \times$$

$$\times \sum_{M_i=-J_i}^{J_i} f(M_i) \sum_{M_f=-J_f}^{J_f} MI_{\parallel,\perp}(\Delta M, \theta = 90°) \times \left(J_f \quad q \quad M_f \quad -\Delta M \quad \middle| J_i \quad M_i\right)^2 \qquad (1)$$

where hν is the transition energy, $A(J_i \rightarrow J_f)$ is the transition's radiative decay rate, $f(M_i)$ are populations of upper level's sublevels, θ the angle between the quantization axis and the line of sight, q is the multipolarity of the transition, $\Delta M = M_f - M_i$, and () is a Clebsch-Gordan coefficient. $MI(\Delta M, \theta)$'s are relative multipole intensities based on the angular parts of wave-zone multipole fields that are also known as vector spherical harmonics [8]. The two polarization-dependent line intensities observed at θ = 90° then yield the linear polarization,

$$P = \frac{I_{\parallel} - I_{\perp}}{I_{\parallel} - I_{\perp}} \qquad (2)$$

Under isotropic conditions (Maxwellian plasmas, for instance) populations of magnetic sublevels within a fine-structure level are the same, which results in unpolarized (i.e., isotropic) line emissions. Polarization may therefore arise only from lines whose upper levels are aligned, i.e., the population is distributed unequally among their sublevels. Alignment can be created by anisotropic processes such as collisional excitation or electron capture due to a beam of energetic electrons.

III. Application of POLAR to steady-state line emissions from He-like Fe

Our atomic kinetic model for He-like Fe consists of 17 J-levels from configurations $1s^2$, 1s 2l, and 1s 3l which results in a total of 53 magnetic sublevels. In order to assess the effects of 1s 3l → 1s 2l' radiative cascades we calculated polarization of the four 2-to-1 lines w, x, y, and z at electron beam energies 6.8 and 8.0 keV. The 1s 3l excitation threshold is 7.9 keV, hence at 6.8 keV the 1s 3l states acquire only negligible populations by stepwise excitation via 1s 2l states. Therefore only cascades within the 1s 2l states may play a role at 6.8 keV. At 8.0 keV the 1s 3l states become accessible to direct excitation from the ground state which turns on the n=3 cascades. Considering the low electron density of the beam (10^{12} cm^{-3}) it is sufficient to include only electron-impact excitation and spontaneous radiative decay processes. Using the suite of Los Alamos codes [9-11] we constructed a database of 50 rates of electric dipole transitions between J-levels. Our model also includes the rates of three higher-order transitions, namely those associated with lines x and z [12] and the two-photon decay 1s 2s $^1S_0 \rightarrow 1s^2\ ^1S_0$ [13]. Inclusion of these processes is necessary, because the upper levels of these three transitions lack dominant electric dipole decay channels. Sublevel radiative decay rates are then calculated from the J-level rates by the well-known formula based on the Wigner-Eckart theorem,

$$A(J_i M_i \rightarrow J_f M_f) = A(J_i \rightarrow J_f) \times \left(J_f \quad q \quad M_f \quad M_i - M_f \quad | J_i \quad M_i\right)^2 \qquad (3)$$

Electron-impact excitations are represented by a database of 1296 sublevel excitation cross sections created with the Los Alamos code ACE. Since the results of kinetic models heavily depend on the quality of the employed atomic database, we also obtained another collection of cross sections independently calculated by a fully relativistic code [14]. This allows us to investigate the sensitivity of our results with respect to various collections of atomic data produced under different methods and approximations. The comparisons between these two collections of data show that the relativistic corrections play only a small role.

For an electron energy of 8.0 keV radiative cascades from n=3 singly excited states turn on. Adding more energy levels to our model is not necessary because this energy is still below the 8.2 keV threshold for the n=4 singly excited states. Lines w and x do not undergo any major changes but line z exhibits interesting properties. Since the "2-level" polarization of line z is remains zero at 8.0 keV, and a calculation at this energy with the n=3 states excluded yields a value around –0.08, the significant increase of polarization up to –0.15 is caused by cascades from 1s 3l. We pinpointed the most significant feeding channels of 1s 2s $^3S_1$ and constructed a 5-level model in which these effects on line z can be illustrated. This

five-energy-level subset is: $1s^2\ ^1S_0$, 1s 2s $^3S_1$, 1s 2p $^3P_0$, 1s 2p $^3P_2$, and 1s 3p $^3P_2$. Our results show that the cascade from 1s 3p $^3P_2$ further enhances the negative polarization value seen also at 6.8 keV that was attributed to the cascade from 1s 2p $^3P_2$. The line emission associated with this cascade is itself noticeably polarized (P = + 0.29) which demonstrates that alignment transfer from 1s 3p $^3P_2$ to 1s 2s $^3S_1$ is indeed taking place. On the other hand, these two cascades compete with the isotropic cascade from 1s 2p $^3P_0$ level. These findings are consistent with earlier calculations of Inal and Dubau [15], who accounted for cascades by calculating effective collision strengths for the $1s^2$ - 1s 2l excitations at several energies, of which the one closest to our calculations is 7.9 keV (582 Ry). Fig. 1 shows the most dominant atomic processes in the kinetics of the upper level of line *z*. The "population×rate" values are the measure of influence of a particular atomic process on the population of the 1s 2s $^3S_1$ level. The fact that several feeding channels are of comparable importance and that the direct excitation from the ground state is not even the most dominant among them illustrates the critical importance of considering complex cascade effect patterns. Hereby presented magnetic-sublevel kinetic modeling addresses these issues by definition. This is an improvement with respect to previous efforts that start with a "2-level" type modeling and add cascades on a case-by-case basis.

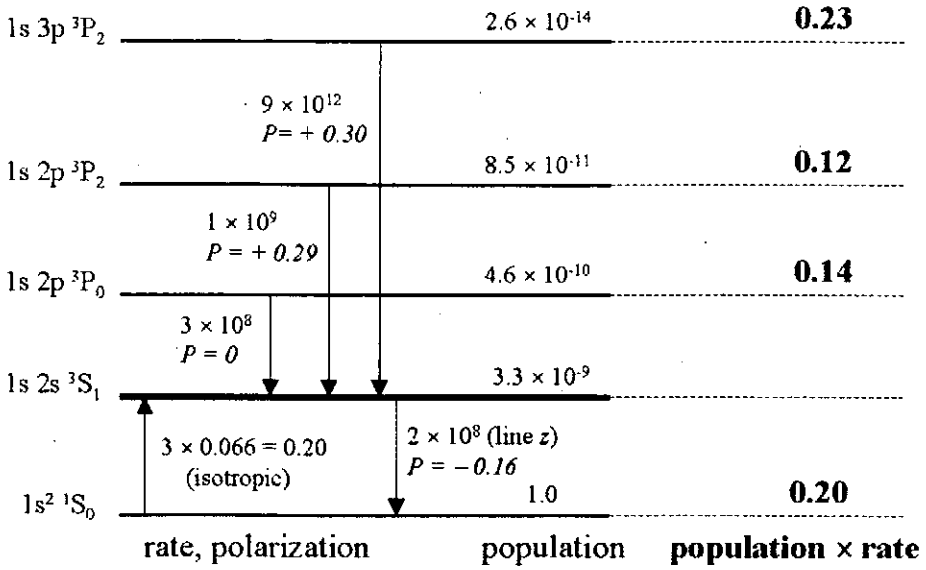

Fig. 1. Dominant feeding channels for upper level of line *z* (1s 2s $^3S_1$) at 8.0 keV.

IV. Polarized Ly-α satellite emissions from laser-produced Si plasmas

In an effort to produce a realistic modeling study, in this case the magnetic-sublevel atomic kinetics computation is fed with temperature and density time histories from a hydrodynamic simulations of laser-produced plasma (code FILM), and electron beam generation due to laser-plasma interaction calculated with an electron kinetics model and code (EUTERPE). Both isotropic and anisotropic atomic processes are considered in POLAR and hence the creation of alignment in the plasma will result from the competition of alignment creating and destructing processes.

Our calculations of He-like Si X-ray polarization-dependent spectra are based on a suite of codes run in succession according to the scheme in Fig. 2. The laser pulse intensity is a variable input parameter. FILM is a 1-D Lagrangian hydrocode that simulates the overall target behavior as it is heated by the laser. The energy distribution of the electron beam is obtained from a 1 and ½ particle-in-cell code EUTERPE that models the production of a beam of energetic electrons by the laser-target interaction [16,17]. In our model we account for both groups of electrons by splitting the electron pool of density N_e (calculated by FILM) into a thermal (Maxwellian) part $f_{Maxw}(T_e,E)$ of density $(1-\alpha)N_e$ and a beam part described by a time-dependent energy distribution $f_B(E)$ and density αN_e. The fraction of non-thermal electrons α ($0 \leq \alpha \leq 1$) is a constant free parameter in our model and we tested several α values that produced the expected rise of polarization with increasing α and vanishing polarization for $\alpha = 0$. Having obtained the electron kinetics characteristics from FILM and EUTERPE we then calculate the overall ionization balance using the M3R code. M3R is a comprehensive atomic kinetics code [18] that calculates the time-dependent populations of 514 LS-terms ranging from Ne-like Si to the fully stripped ion. The time histories of He and H-like ions' ground state populations calculated with M3R serve as input for POLAR, a detailed time-dependent collisional-radiative magnetic-sublevel atomic kinetics code. Databases of atomic data needed for M3R and POLAR were constructed using the Los Alamos suite of codes [9-11] and the UCL code [19]. POLAR then calculates the time-dependent magnetic sublevel populations in the He-like ion, which are then converted to time histories of polarization-dependent line intensities through Eq. 1. This procedure is repeated for several fluid elements at various depths in the target. An example of time- and space-integrated polarization-dependent spectrum is shown in Fig. 3. The collection of triplet lines in the center remains unpolarized while the two singlet lines develop a noticeable polarization effect. This result suggests that polarized singlet lines could be useful as markers of plasma anisotropy while the triplets could serve as unpolarized reference.

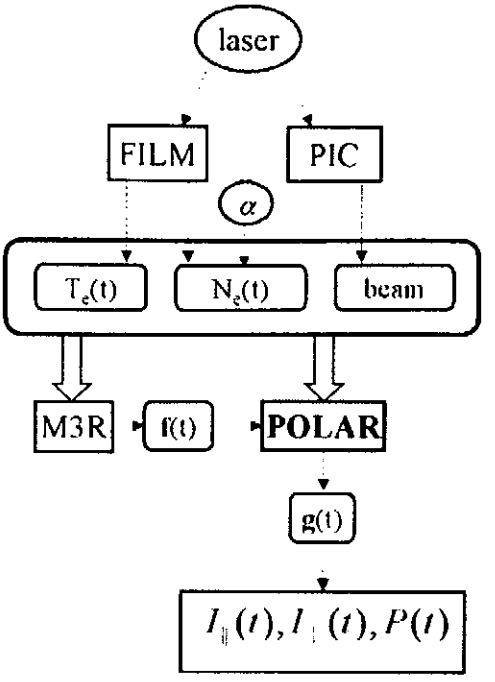

Fig. 2 Suite of codes used in modeling of polarized X-ray satellite emissions driven by high-intensity, ultrashort-duration lasers.

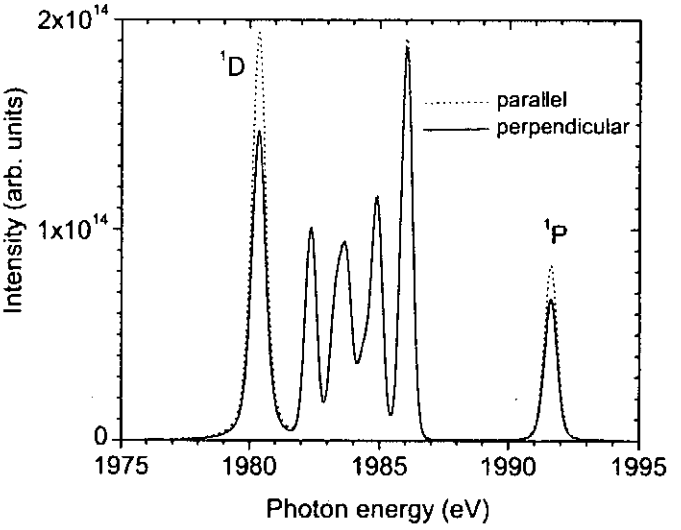

Fig. 3. Time- and space-integrated polarization-dependent spectra, for laser intensity 2×10^{16} W/cm^2, $\alpha = 0.2$. (^{1}D: $2p^2\ ^1D_2 \rightarrow 1s\ 2p\ ^1P_1$; ^{1}P: $2s\ 2p\ ^1P_1 \rightarrow 1s\ 2s\ ^1S_0$)

V. Conclusions

We presented an overview of a magnetic-sublevel atomic kinetics model and code POLAR aimed at modeling of polarized line emissions. We showed how our model predictions compare with previous calculations based on density-matrix formalisms and Electron Beam Ion Trap (EBIT) experiments performed at Lawrence Livermore National Laboratory (LLNL). We addressed the importance of cascade effects on polarized X-ray line emissions by studying the polarized K-shell emission in He-like Fe. With POLAR we find that alignment transfer can indeed significantly alter polarization of certain lines. It is therefore important to move beyond "two-level" models that have been considered in most previous work in this area. With the foundation and validation of the POLAR model we constructed a fully time-dependent version of POLAR and performed a comprehensive modeling study of polarized He-like Si satellite line emissions driven by femtosecond-duration lasers [20]. We observe that the He-like Si satellite lines of interest fall into two groups. Two lines connecting singlet states develop a noticeable polarization while the triplet lines remain unpolarized. This results from the competition between anisotropic processes driven by beam electrons versus the depolarizing influence of isotropic processes driven by thermal electrons. We conclude that the triplets could be used as unpolarized reference while the singlets show potential as polarized markers of plasma anisotropy.

Acknowledgements

This work was supported by LLNL contracts B336460 and B503614, NATO Grant CRG 971588, and the University and Community College System of Nevada. We also thank Peter Beiersdorfer for presenting this work at this Symposium.

References:

1. P. Hakel, X-ray Line Spectral Signatures of Plasmas Driven by High-Intensity Ultra-Short Laser Pulses, Ph.D. dissertation, University of Nevada, Reno (2001).
2. M.K. Inal and J. Dubau, J. Phys. B, **20**, 4221 (1987).
3. R.M. Steffen and K. Alder, in The Electromagnetic Interaction in Nuclear Spectroscopy, edited by W.D. Hamilton, 505, North-Holland (1975).
4. P. Beiersdorfer, D.A. Vogel, K.J. Reed, V. Decaux, J.H. Scofield, K. Widmann, G. Hölzer, E. Förster, O. Wehrhan, D.W. Savin, and L. Schweikhard, Phys. Rev. A, **53** (6), 3974 (1996).

5. A.S. Shlyaptseva, R.C. Mancini, P. Neill, P. Beiersdorfer, J.R. Crespo López-Urrutia, and K. Widmann, Phys. Rev. A, **57** (2), 888 (1998).
6. A.S. Shlyaptseva, R.C. Mancini, P. Neill, and P. Beiersdorfer, J. Phys. B, **32** (4), 1041 (1999).
7. U. Fano, J. Opt. Soc. Am., **39** (10), 859 (1949).
8. B.W. Shore and D.H. Menzel, Principles of Atomic Spectra, Wiley (1968).
9. J. Abdallah Jr., R.E.H. Clark, and R.D. Cowan, Los Alamos National Laboratory report LA-11436-M vol. I (1988).
10. R.E.H. Clark, J. Abdallah Jr., G. Csanak, J.B. Mann, and R.D. Cowan, Los Alamos National Laboratory report LA-11436-M vol. II (1988).
11. R.E.H. Clark, J.B. Mann, G. Csanak, and A.L. Merts, Los Alamos National Laboratory report LA-UR-89-2675, Vol. 2 (1989).
12. A.S. Shlyaptseva, P. Hakel, and R.C. Mancini, poster paper at the 11th APS Topical Conference on Atomic Processes in Plasmas, Auburn (1998).
13. C.D. Lin, W.R. Johnson, and A. Dalgarno, Phys. Rev. A, **15** (1), 154 (1977).
14. H.L. Zhang, D.H. Sampson, and R.E.H. Clark, Phys. Rev. A, **41** (1), 198 (1990).
15. M.K. Inal and J. Dubau, Phys. Rev. A, **47** (6), 4794 (1993).
16. G. Bonnaud and G. Reisse, Nucl. Fusion, **26** (5), 633 (1986); E. Lefebvre, Ph.D. dissertation, Université de Paris XI-Orsay, 1996 (unpublished).
17. Th. Schlegel, S. Bastiani, L. Grémillet, J.-P. Geindre, P. Audebert, J.-C. Gauthier, E. Lefebvre, G. Bonnaud, and J. Delettrez, Phys. Rev. E, **60** (2), 2209 (1999).
18. R.C. Mancini and E. Mínguez, "M3R: a NLTE atomic kinetics model for plasmas." First International NLTE Atomic Kinetics Workshop, Gaithersburg, MD, August 12-16, 1996.
19. J. Dubau, private communication; calculations based on W. Eissner, Comp. Phys. Commun., **114** (1-3), 295 (1998) and H.E. Saraph, Comp. Phys. Commun., **15** (3-4), 247 (1978).
20. P. Hakel, R.C. Mancini, J.-C. Gauthier, E. Mínguez, J. Dubau, and M. Cornille, Phys. Rev. E (2004), in print.

X-ray Polarization Measurements at Relativistic Laser Intensities

P. Beiersdorfer[1], R. Shepherd[1], R. C. Mancini[2], H. Chen[1], J. Dunn[1], R. Keenan[1], J. Kuba[1], P. K. Patel[1]
Y. Ping[1], D. F. Price[1], K. Widmann[1]
[1] *Lawrence Livermore National Laboratory, Livermore, CA 94550, USA*
[2] *University of Nevada, Reno, NV 89557, USA*

An effort has been started to measure the short pulse laser absorption and energy partition at relativistic laser intensities up to 10^{21} W/cm^2. Plasma polarization spectroscopy is expected to play an important role in determining fast electron generation and measuring the electron distribution function.

I. INTRODUCTION

Plasma polarization spectroscopy (PPS) has been employed to verify and study the existence of non-thermal, fast electrons in laser-plasma interaction since the first experiments by Kieffer *et al.* [1–3]. The laser intensity in these measurements has been in the range $10^{14} - 10^{16}$ W/cm^2. Measurements of laser absorption at higher intensities $\leq 10^{18}$ W/cm^2 have been made [4] but without employing x-ray polarimetry. Theoretical studies of fast-electron generation and their effect on the x-ray linear polarization have been made [5,6], which considered laser intensities as high as 10^{18} W/cm^2.

Here we describe a planned effort to use PPS as a diagnostic for determining fast electron generation and energy partition of short pulse lasers interacting with matter at relativistic laser intensities up to 10^{21} W/cm^2.

II. PHYSICS LASERS AT LLNL

The Physics and Advanced Technologies Directorate at the University of California Lawrence Livermore National Laboratory operates four powerful multi-purpose laser facilities used for experiments in high-energy density physics, x-ray laser development, and material science. These facilities are used in collaborative experiments with many non-LLNL user, and new collaborations are always welcome. In fact, the planned PPS experiment respresents a collaboration between LLNL and the University of Nevada in Reno.

The first of these lasers is the Compact Multipulse Terawatt (COMET) laser operating at 1.054 μm. A schematic of the facility is shown in Fig. 1. The laser consists of a Ti:sapphire oscillator with glass amplifiers that can generate and probe plasmas with up to four beams. One or two long pulse beams (Δt = 600 ps) with 15 and 4 J, respectively, are available together with two or three short pulse beams (Δt = 500 fs) with 1 or 7.5 J. One of the short pulse beams is equipped for operation frequency doubled or tripled laser light. A summary of the parameters of the COMET laser is given in Table I.

The COMET laser has been used mainly for developing efficient x-ray laser schemes [7,8]. The multi-pulse capability has been used to generate an additional plasma on a slab that in turn is probed with the x-ray laser pulse generated by the other COMET laser beams [9].

TABLE I. Parameters of the COMET laser.

Beam type	Energy (J)	Pulse Length (ps)
Long pulse	15	600
Short pulse	7.5	0.5
Beam 3	1	0.5
Beam 3	4	600
Probe beam		0.5[a]

[a] At 2ω or 3ω emission, i.e., 527 nm and 351 nm, respectively.

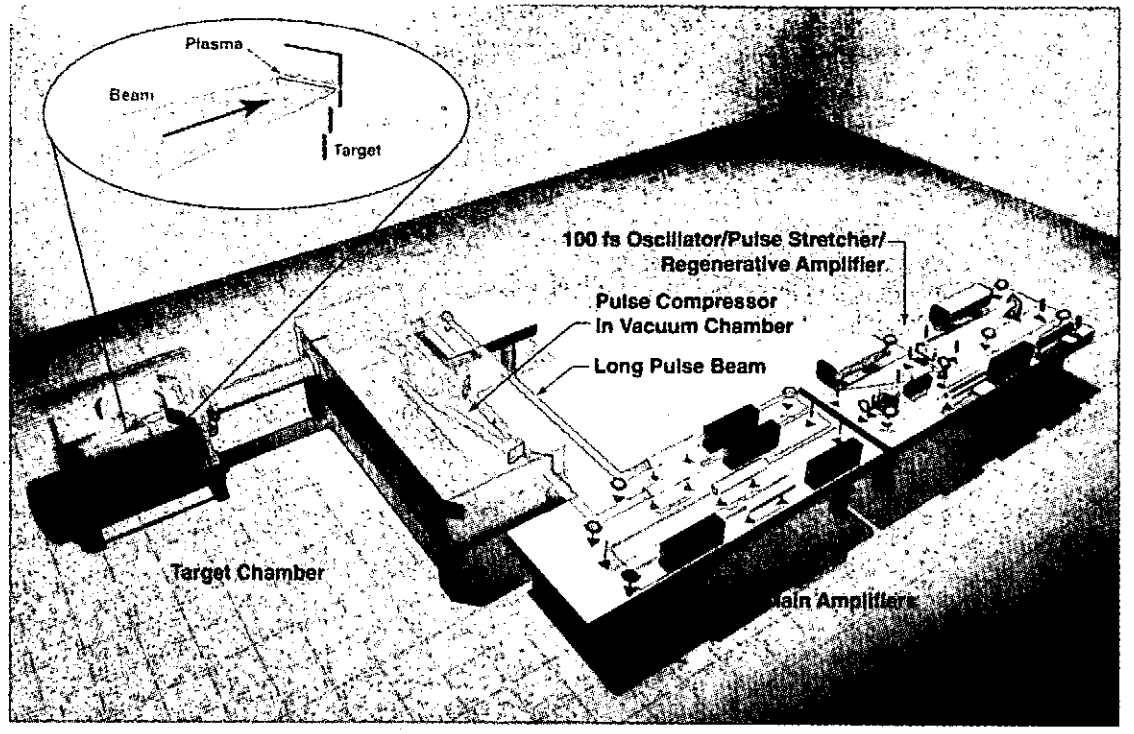

FIG. 1. Schematic of the COMET laser.

The second of the physics lasers is the Ultra Short Pulse (USP) laser, shown schematically in Fig. 2. USP is a Ti:Sapphire laser operating either at 800 nm with an energy of 1 J or at 400 nm with an energy of 0.35 J. The pulse width of the USP laser is $\geq$ 80 fs; the spot size is less than three times the diffraction limit, i.e., about 1–2 μm at 400 nm (about 3 μm at 800 nm). As a result, USP has an intensity as high as 5×10^{19} W/cm^2. The contrast between prepulse and main pulse is 10^5 at 1ω and 10^7 at 2ω. Short pulse laser energy of 100–120 mJ is available at 10 Hz repetition rate and at about 20/hour at higher energies. A summary of the parameters of the USP laser is given in Table II.

TABLE II. Parameters of the USP laser.

Wavelength (nm)	Energy (J)	Pulse Length (fs)	Spot Size μm
800	1	$\geq$ 80	3
400	0.35	$\geq$ 80	1–2

Currewntly, the USP laser is being used for atomic physics studies of hot, high-density plasma [10] and equation of state related conductivity studies of warm-dense matter [11,12].

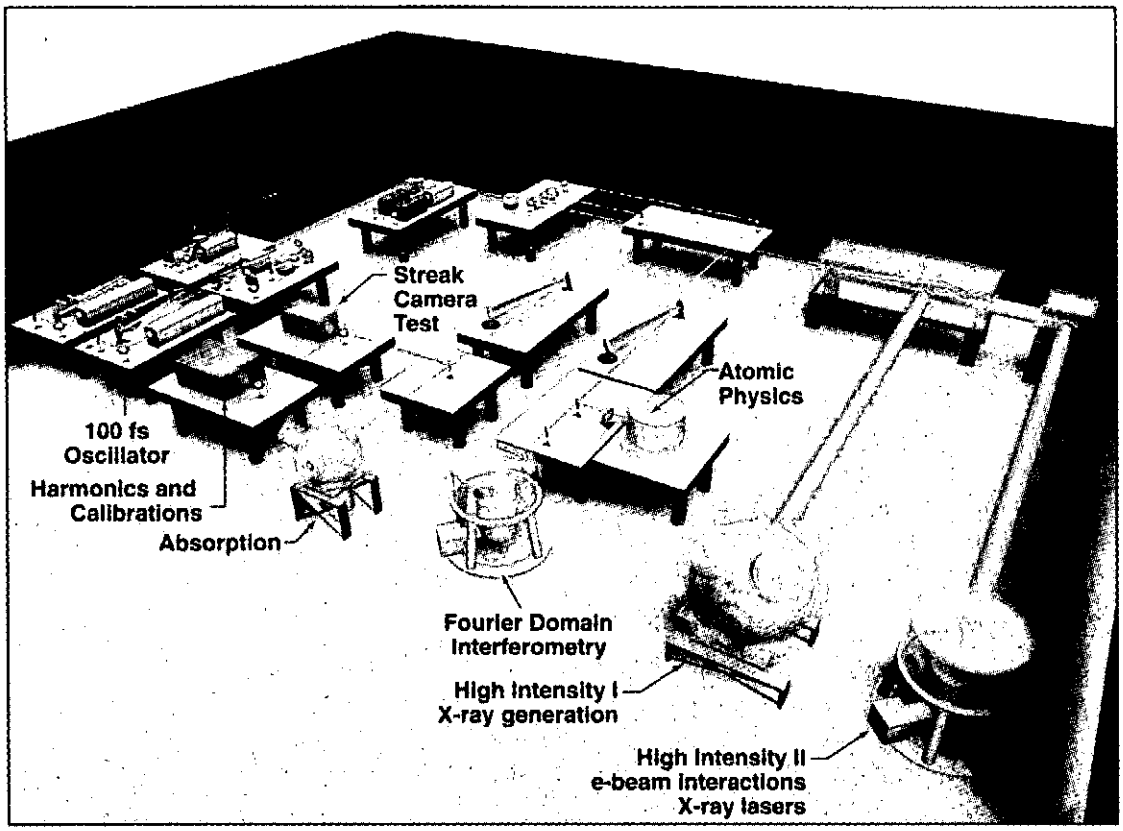

FIG. 2. Schematic of the USP laser.

The third laser is the Janus laser, which is shown schematically in Fig. 3. This facility has been operating since the early 1970s when it was commissioned for studies of inertial confinement fusion (ICF). Janus is a two-beam laser (hence its name), providing 300 J per beam on target. When the primary ICF studies on Janus were replaced with studies on the Argus laser and later on the Shiva and Nova lasers, the emphasis of the Janus facility was shifted to ICF support studies and ICF diagnostics development. It has also been used for x-ray laser studies [13]. Like these subsequent lasers, Janus can operate at 1064 nm as well as the double and triple frequency, as summarized in Table III. The pulse width can be varied from 100 ps to greater than 6 ns. Beam smoothing was added in 1999. The spot size is 17 μm, and up to three shots per hour can be accomodated. An upgrade to 1000 J per beam is currently under way.

TABLE III. Parameters of the Janus laser.

Parameter	Value
Wavelength	1064 nm, 532 nm, 366 nm
Energy	300 J at 1064 nm
Pulse width	0.1 – 6 ns
Spot size	17 μm
Repetition rate at rod shot energies (2–20 J)	20 shots per hour
Repetition rate at maximum energy	2 per hour

An important feature is that one of the Janus beams (at 532 nm) can be used to pump a second ultra short pulse laser. The ultra short pulse laser pumped by Janus has been dubbed JanUSP [14]. A schematic of JanUSP is shown in Fig. 4.

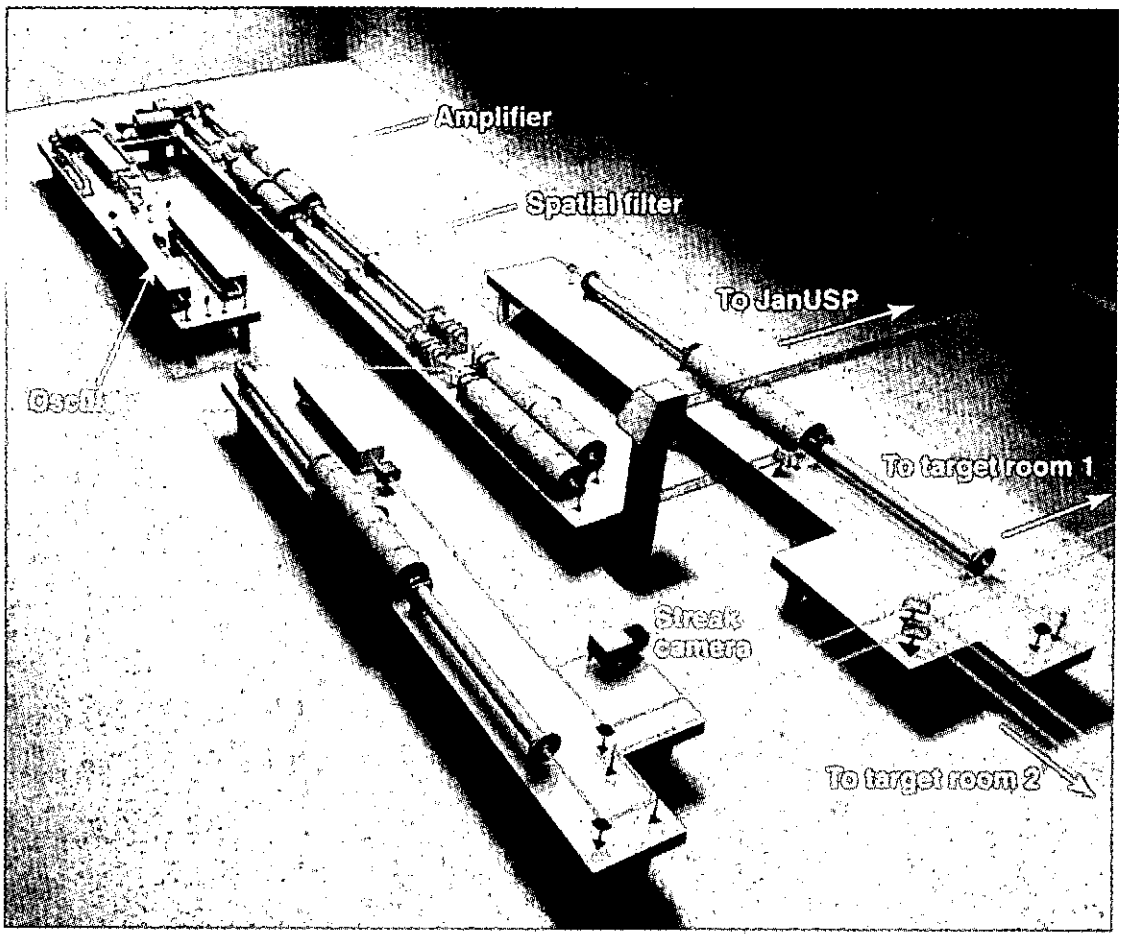

FIG. 3. Schematic of the Janus laser.

TABLE IV. Parameters of the Janus-pumped ultra short pulse laser JanUSP.

Parameter	Value
Wavelength	800 nm
Energy	15 J
Pulse width	$\geq$ 80 fs
Spot size	$\leq$ 3 μm
Repetition rate in low-power mode (300 mJ)	10 Hz
Repetition rate at maximum energy	2 per hour

Like USP, JanUSP is a Ti:Sapphire laser. But being pumped by Janus it can reach energies of 15 J at 800 nm and high peak power in excess of 150 TW. The focussing spot of JanUSP is two times the diffraction limit ($\lesssim 3\mu$m), which is better than that of the USP laser; the pulse width is about the same at $\geq$ 80 fs. As a result of these operating parameters the JanUSP laser can focus up to 10^{21} W/cm^2 on target. The contrast between the prepulse and the main pulse is in the range of 10^9 and may be improved by implementing a frequency doubling crystal. The repetition rate is 2 shots per hour. Parameters of the JanUSP laser are given in Table IV.

JanUSP can also be operated in a low-energy mode with 300 mJ per shot at a repetition rate of 10 Hz. This capability is currently being used to develop high repetition rate x-ray laser schemes [15].

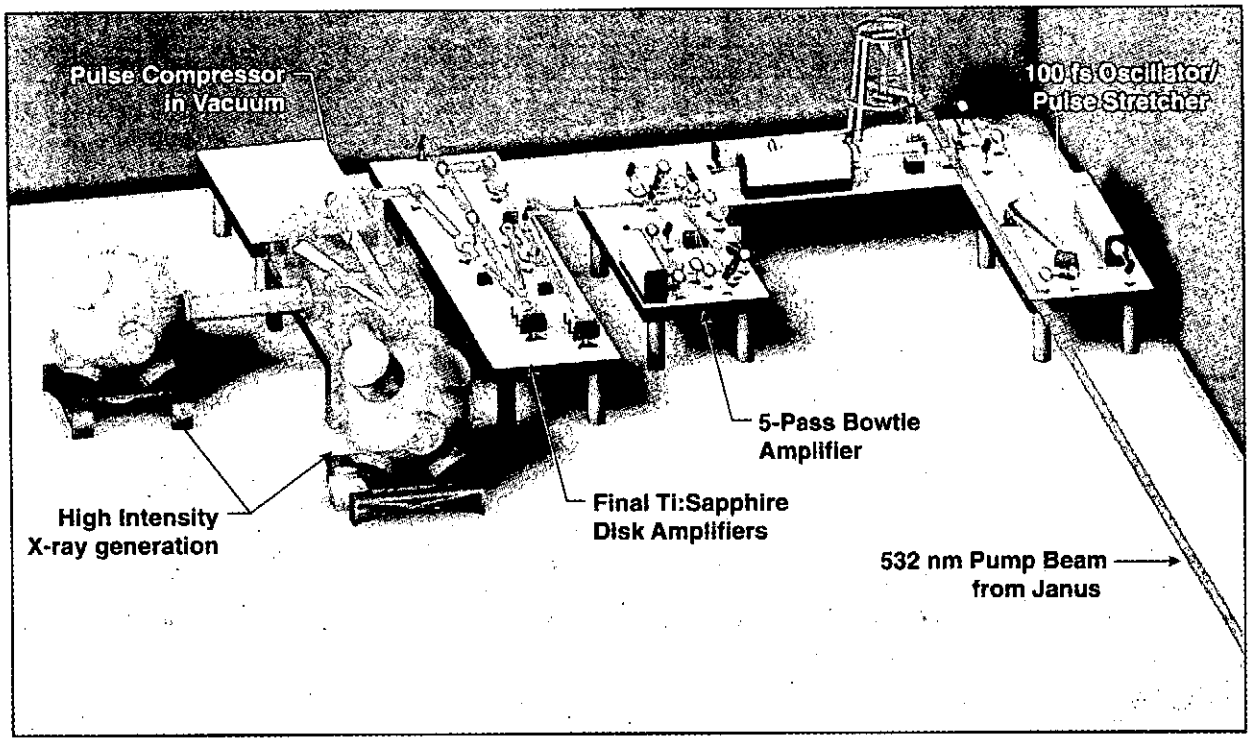

FIG. 4. Schematic of the JanUSP laser.

JanUSP has been used for beam generation experiments. In particular, it has been used for energy partition and γ-ray beam generation experiments [16,17]. About one to two percent of the laser energy can be converted into a proton beam emanating from the back surface of a thin (10–20 μm) aluminum foil propagating at energies up to 20–25 MeV [16]. Detection of the proton beam was by radiochromatic film.

Electron beam generation from the back (and front) side of foil targets has also been observed [18]. For this an electron spectrometer was built utilizing permanent magnets for energy analysis and a charge couple device camera for read out that can measure electrons with energies between 100 keV and 60 MeV [18]. It is possible that up to half of the total laser energy is converted to fast electrons at the high intensities possible with JanUSP.

III. PLANNED EXPERIMENTS

Laser absorption at intensities close to 10^{18} W/cm^2 was studied by Price et al. employing the USP laser [4]. They showed that absorption by inverse bremsstrahlung is replaced by relativistic $J \times B$ heating at a laser intensity near 10^{17} W/cm^2. As the intensity is increased further additional absorption mechanisms may play an important role such as ion shock formation and vacuum (Brunel) heating. Moreover, there is a relativistic increase in the electron's mass making the electron response to the oscillating laser field more sluggish and thus allowing the laser to penetrate deeper by increasing the critical density. The pondermotive pressure will steepen the density profile above the target surface and thus will affect the electron and ion transport. Also, ultra-high electric and magnetic fields can be generated that change the absorption at very high intensities. The magnetic field may reach values as high as 3 gigagauss; the electric field may reach values of 10^{12} V/cm. The interplay of all of these processes has not been systematically studied at high laser intensities, but it needs to be known as petawatt lasers are being put in use for physics studies.

We are planning to study laser absorption in a sytematic and controlled way, and PPS will play an important role. X-ray emission measurements are planned to determine the relative fraction of the hot electron component relative to the thermal component. These will involve studies of K-alpha generation by fast electrons as a function of plasma density. The experimental scheme to perform such experiments is shown in Fig. 5.

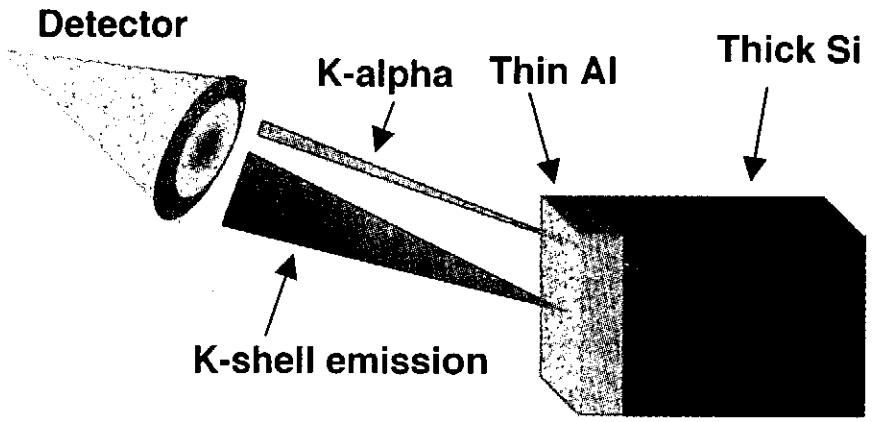

FIG. 5. Schematic of the setup to measure the K-alpha emission of silicon produced by fast electrons from the laser-heated aluminum target.

Moreover, time-dependent measurements of the x-ray emission are planned that are sensitive to the collisional dynamics of thermal and hot electrons, as shown schematically in Fig. 6. For such measurements fast streak cameras are needed. We have developed x-ray cameras with 500 fs time resolution [19]. These measurements will also resolve the polarization of the x-ray lines by operating our cylindrically bent crystal spectrometers near the Brewster angle.

IV. ACKNOWLEDGEMENT

This work was performed under the auspices of the U.S. DOE by the University of California Lawrence Livermore National Laboratory under contract W-7405-Eng-48.

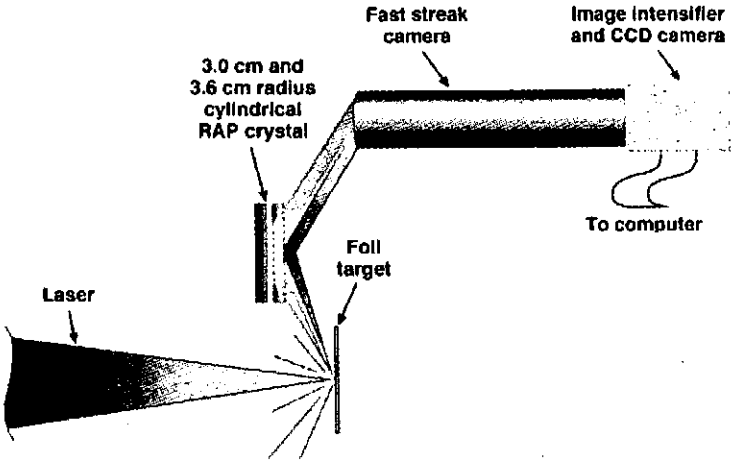

FIG. 6. Schematic of the setup to measure the x-ray spectra using high-resolution von Hámos-type crystal spectrometers and fast streak cameras.

[1] J. C. Kieffer, J. P. Matte, H. Pépin, M. Chaker, Y. Beaudoin, T. W. Johnston, C. Y. Chien, S. Coe, G. Mourou, and J. Dubau, Phys. Rev. Lett. **68**, 480 (1992).

[2] J. C. Kieffer, J. P. Matte, M. Chaker, Y. Beaudoin, C. Y. Chien, S. Coe, G. Mourou, J. Dubau, and M. K. Inal, Phys. Rev. E **48**, 4648 (1993).

[3] H. Yoneda, N. Hasegawa, S. ichi Kawana, and K. ichi Ueda, Phys. Rev. E **56**, 988 (1997).

[4] D. F. Price, R. M. Moore, R. S. Walling, G. Guethlein, R. L. Shepherd, R. E. Stewart, and W. E. White, Phys. Rev. Lett. **75**, 252 (1995).

[5] P. Hakel, R. C. Mancini, J.-C. Gauthier, E. Mínguez, J. Dubau, and M. Cornille, Rev. Sci. Instrum. **72**, 1245 (2001).

[6] P. Hakel, R. C. Mancini, J.-C. Gauthier, E. Mínguez, J. Dubau, and M. Cornille, Phys. Rev. E in press, .

[7] J. Dunn, R. F. Smith, J. Nilsen, H. Fiedorowicz, A. Bartnik, and V. N. Shlyaptsev, J. Opt. Soc. Am. B **20**, 203 (2003).

[8] R. F. Smith, J. Dunn, J. R. Hunter, J. Nilsen, S. Hubert, S. Jacquemot, C. Remond, R. Marmoret, M. Fajardo, P. Zeitoun, L. Vanbostal, C. L. S. Lewis, M. F. Ravet, and F. Delmotte, Opt. Lett. **28**, 2261 (2003).

[9] R. F. Smith, J. Dunn, J. Nilsen, V. N. Shlyaptsev, S. Moon, J. Filevich, J. J. Rocca, M. C. Marconi, J. R. Hunter, and T. W. Barbee, Phys. Rev. Lett. **89**, 065004 (2002).

[10] P. Audebert, R. shepherd, K. B. Fournier, O. Peyrusse, D. Price, R. Lee, P. Springer, J.-C. Gauthier, and L. Klein, Phys. Rev. Lett. **89**, 265001 (2002).

[11] K. Widmann, G. Guethlein, M. E. Foord, R. C. Cauble, F. G. Patterson, D. F. Price, F. J. Rogers, P. T. Springer, R. E. Stewart, A. Ng, T. Ao, and A. Forsman, Phys. Plasmas **8**, 3869 (2001).

[12] K. Widmann, T. Ao, M. E. Foord, D. F. Price, A. D. Ellis, P. T. Springer, and A. Ng, Phys. Rev. Lett. in press, .

[13] J. Dunn, A. L. Osterheld, R. Shepherd, W. E. White, V. N. Shlyaptsev, and R. E. Stewart, Phys. Rev. Lett. **80**, 2825 (1998).

[14] J. D. Bonlie, F. Patterson, D. Price, B. White, and P. Springer, Appl. Phys. B **70**, S155 (2000).

[15] R. Keenan, J. Dunn, V. N. Shlyaptsev, R. F. Smith, P. K. Patel, and D. F. Price, Proc. SPIE Int. Soc. Opt. Eng. **5197**, 213 (2003).

[16] P. K. Patel, A. J. Mackinnon, M. H. Key, T. E. Cowan, M. E. Foord, M. Allen, D. F. Price, H. Ruhl, P. T. Springer, and R. Stephens, Phys. Rev. Lett. **91**, 125004 (2003).

[17] M. Allen, P. K. Patel, A. Mackinnon, D. F. Price, S. Wilks, and E. Morse, Phys. Rev. Lett. submitted, .

[18] H. Chen, P. K. Patel, D. F. Price, B. K. Young, P. T. Springer, R. Berry, R. Booth, C. Bruns, and D. Nelson, Rev. Sci. Instrum. **74**, 1551 (2003).

[19] J. Kuba, R. Shepherd, R. Booth, R. E. Stewart, E. C. W. Lee, P. Audebert, J. K. Crane, R. R. Cross, J. Dunn, and P. T. Springer, Proc. SPIE Int. Soc. Opt. Eng. **5194**, 183 (2004).

X-ray Spectropolarimetry of high temperature and high density plasma supported by LLNL Electron Beam Ion Trap experiments

A. S. Shlyaptseva, V. L. Kantsyrev, N. D. Ouart, D. A. Fedin, P. Neill, C. Harris, S. M. Hamasha, S. B. Hansen, U. I. Safronova, *University of Nevada, Reno, USA*

P. Beiersdorfer, *Lawrence Livermore National Laboratory, USA*

A.G. Petrashen, *St. Petersburg Institute of Fine mechanics and Optics, Russia*

Abstract

Plasma polarization spectroscopy work done by our group since the 3rd US-Japan PPS Workshop is overviewed. Theoretically, the polarization dependence on various electron distribution functions for He-like, Ne-like, and Ni-like x-ray transitions for a wide range of Z has been investigated. In particular, this study was focused on the polarization dependence for monoenergetic and steep electron distribution functions. The diagnostically important spectral lines and features of K-, L-, and M-shell ions were identified which can be used in x-ray spectropolarimetry of plasma. Importance of polarization-sensitive LLNL Electron Beam Ion Trap data is emphasized. The results of the UNR polarization-sensitive Ti and Mo x-pinch experiments are discussed.

I. Introduction: overview of our polarization spectroscopy work done since the 3rd US-Japan PPS Workshop

The results of theoretical and experimental studies of anisotropic plasma sources such as x-pinch plasmas were reported in [1]. They are based on x-ray line spectropolarimetry, a powerful new tool for investigating anisotropy of high-temperature plasmas. This new diagnostic involves spectroscopic monitoring and modeling of polarization-sensitive x-ray line spectra recorded simultaneously by two spectrometers with different sensitivities to polarization. The difference in these polarization-sensitive spectra indicate polarization of lines caused by anisotropic electron beams and can be used to diagnose the parameters of such beams in plasmas.

Theoretically, the polarization dependence on various electron distribution functions for He-like, Ne-like, and Ni-like x-ray transitions for a wide range of Z has been investigated [2]. The degree of polarization by a monoenergetic electron beam was calculated for all lines using the newly developed, relativistic, multiconfigurational atomic package by M.F. Gu [3]. In particular, this study was focused on the polarization dependence for monoenergetic and steep electron distribution functions. A variety of features was discussed and illustrated such as the polarization dependence on Z, maximum positive and negative polarization near the threshold energy, and zero polarization crossings. The effects of polarization influenced by varying the values of electron temperature, fraction of hot electrons and its cutoff energy was studied. The diagnostically important spectral lines and features of K-, L-, and M-shell ions were identified and discussed. This work provided the

best candidates for x-ray spectropolarimetry of high-temperature plasmas with multiply charged ions in a very broad range of the nuclear charge Z from 10 (Ne) up to 79 (Au) [2].

Generation of electron beams in x-pinch plasmas was studied in detail and polarization of soft x-ray radiation was considered along with anisotropy of hard x-rays [4]. The results of Ti and Mo x-pinch polarization-sensitive experiments at UNR were overviewed [1]. In particular, the spectroscopic results from seven Ti and four Mo x-pinch shots were analyzed. Polarization-sensitive spectra from Ti x-pinches were also compared with the similar spectra generated by a quasi-Maxwellian electron beam at the LLNL EBIT-II electron beam ion trap [5]. The analysis of polarization-sensitive x-pinch experiments indicated x-ray line polarization in two Ti and three Mo x-pinch shots.

In general, x-ray line polarization is sensitive not only to the electron distribution function but also to the magnetic field. The magnetic fields in x-pinches were recently estimated to be of the order up to few thousands of tesla but were not measured yet. The possibility of using x-ray spectropolarimetry for measurements of magnetic field in dense hot x-pinch plasma was explored. The design of the new x-ray spectropolarimetry experiments involving the measurements of the magnetic fields was discussed. The standard two spectrometer technique was overviewed and in addition the new three spectrometer measurements were proposed [6-8].

II. Theoretical Study of the Influence of Electron Distribution Functions on X-ray Line Polarization in Plasmas

In laboratory and astrophysical plasmas, the electron distribution function (EDF) may differ from the isotropic Maxwellian distribution, due to the presence, for example, of electron beams. This will lead to the addition of a hot electron component that may be described by Gaussian (almost monoenergetic) or steep electron distribution functions. Although most of the electrons in the plasma may follow the Maxwellian distribution, the contribution of the hot electrons is essential and can affect the emission spectra and many other characteristics of the plasma. For example, beams of hot electrons can lead to polarization of x-ray lines in plasmas. In this work, we theoretically studied the polarization dependence on various electron distribution functions for He-like, Ne-like, and Ni-like x-ray transitions for a wide range of Z. This study will focus on the polarization dependence for monoenergetic and steep electron distribution functions. This work identifies and studies some of the candidates for x-ray spectropolarimetry of high-temperature plasmas with multiply charged ions in a very broad range of nuclear charge Z from 10 (Ne) up to 79 (Au).

In Fig. 1, polarization of the resonance w and intercombination y lines was calculated with a monoenergetic EDF for a broad range of mid-Z elements from Ne (Z=10) up to Mo (Z=42). The electron beam energies are given in threshold units which are listed in Fig. 1 for all considered ions. Polarization of the resonance line w has a maximum at the threshold, then monotonically decreases to zero and only slightly depends on the ion. On the contrary, polarization of the intercombination line y strongly depends on the type of the ion and electron beam energy in particular for lower-Z elements (from Ne to Ni). Specifically, polarization of y line has the minimum values at the threshold (for example, less than –50% for Ne ion), which increases with Z. The maximum value of polarization of y line also increases with Z (it is the largest for the element with the highest Z, for Mo ion) and moves closer to the threshold as Z increases. For higher-Z elements and high electron beam energies polarization of y line approaches polarization of w line.

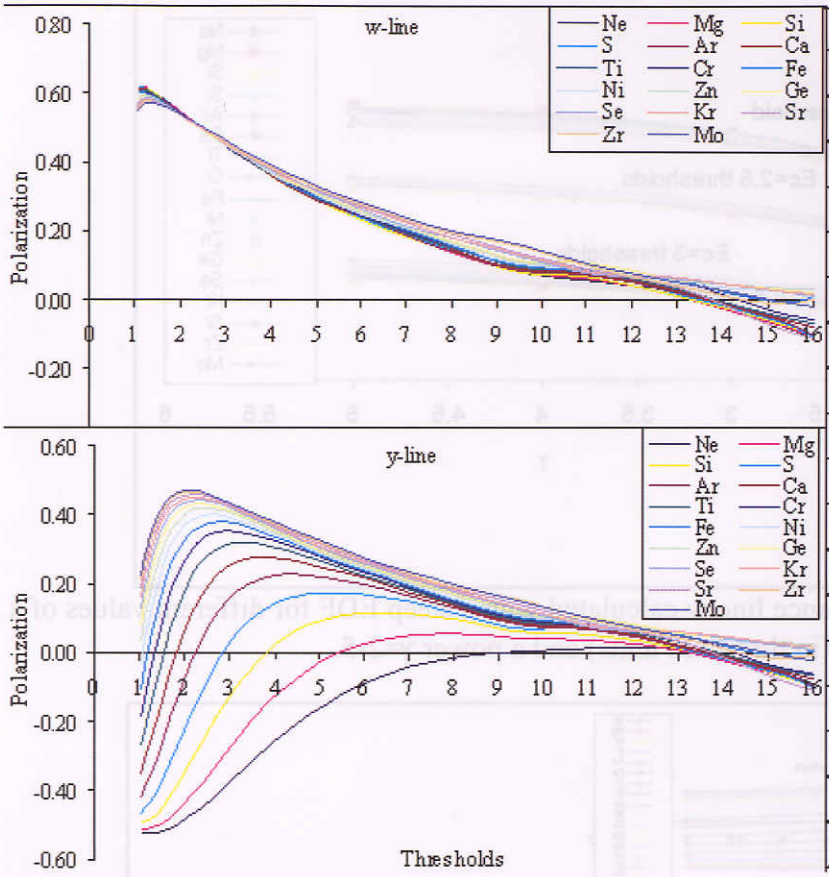

Threshold energy in eV

	Z	w	y
Ne	10	9.20E+02	9.13E+02
Mg	12	1.35E+03	1.34E+03
Si	14	1.86E+03	1.85E+03
S	16	2.46E+03	2.45E+03
Ar	18	3.14E+03	3.12E+03
Ca	20	3.90E+03	3.88E+03
Ti	22	4.75E+03	4.73E+03
Cr	24	5.68E+03	5.65E+03
Fe	26	6.70E+03	6.67E+03
Ni	28	7.80E+03	7.76E+03
Zn	30	9.00E+03	8.95E+03
Ge	32	1.03E+04	1.02E+04
Se	34	1.16E+04	1.16E+04
Kr	36	1.31E+04	1.30E+04
Sr	38	1.47E+04	1.46E+04
Zr	40	1.63E+04	1.62E+04
Mo	42	1.81E+04	1.79E+04

Fig. 1. Polarization of the resonance line w and intercombination line y of mid-Z ions (Z=10-42) calculated with a monoenergetic EDF for different electron beam energies (in threshold units). Threshold energies are given in Table on the right.

Figs. 2 and 3 illustrate the depolarization effect by a non-monoenergetic EDF, for example, a steep EDF with a cutoff energy Ec and a power γ. Specifically, polarization of line w substantially decreases with the increase of Ec, whereas it only slightly changes (increases) with increase of γ. This effect is almost independent from the type of the ion. On the contrary, with the increase of Ec polarization of line y increases from negative values for lower-Z elements to positive values, whereas polarization of higher-Z elements decreases. As a result, polarization of y line becomes less dependent on the type of the ion as Ec increases from 1 to 3 (in threshold units). Polarization of y line is almost independent from a power γ.

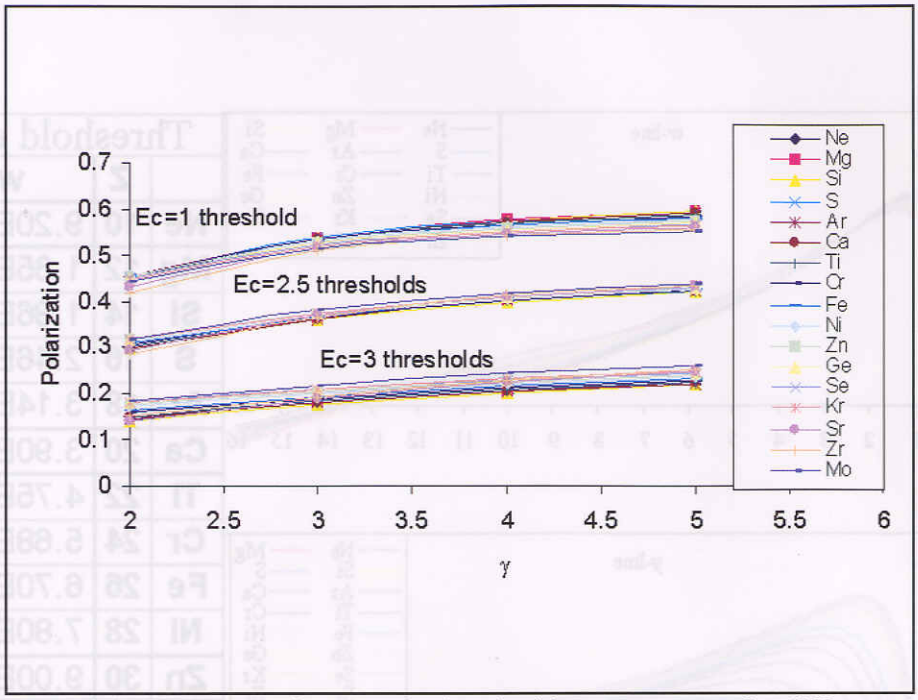

Fig. 2. Polarization of the resonance line w calculated with a steep EDF for different values of a cutoff energy Ec=1, 2.5, and 3 (in threshold units) and a power γ=2-5.

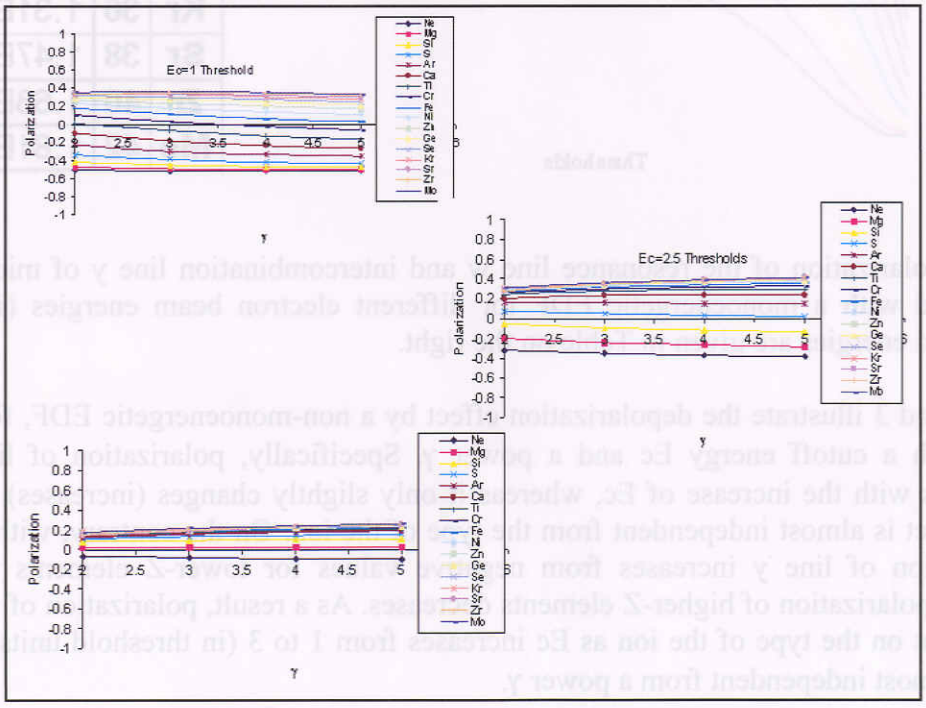

Fig. 3. Polarization of the intercombination line y calculated with a steep EDF for different values of a cutoff energy Ec=1, 2.5, and 3 (in threshold units) and a power γ=2-5.

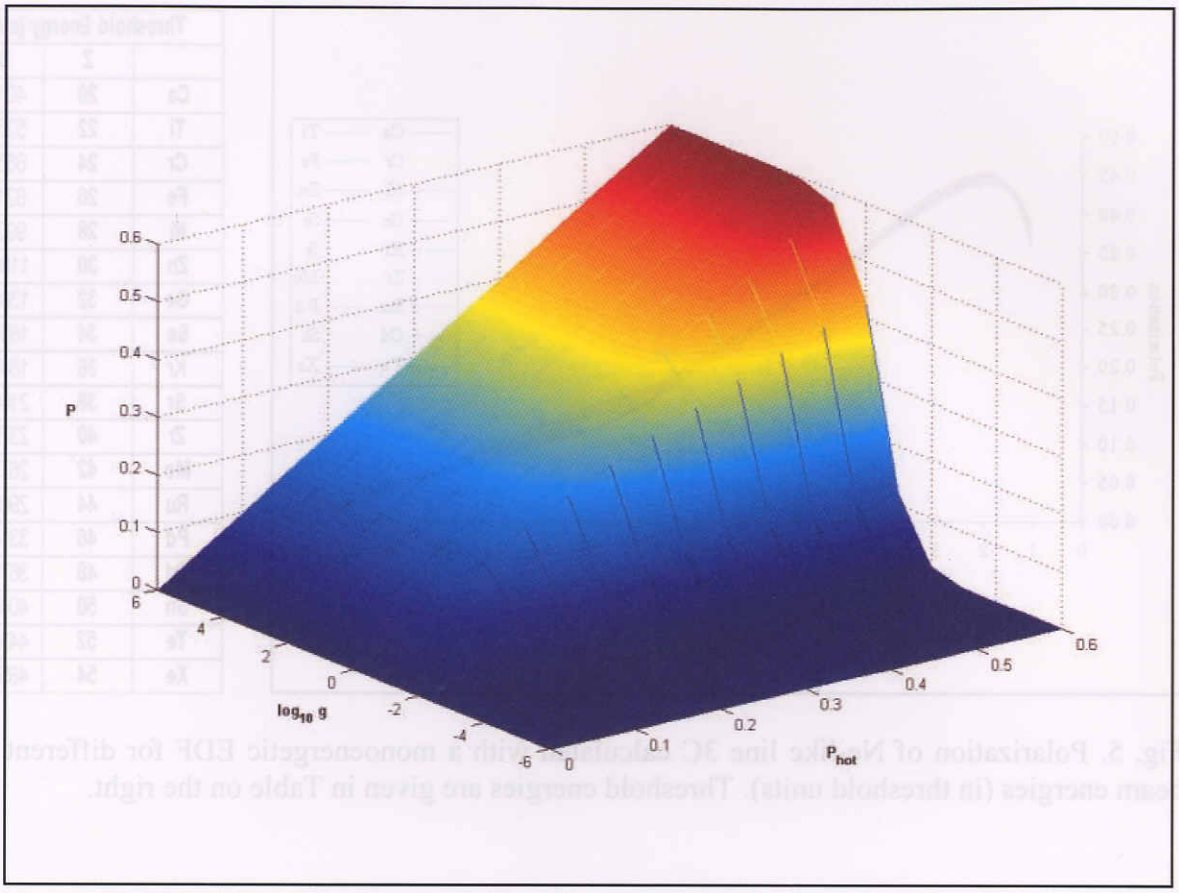

Fig. 4. Illustration of depolarization of the resonance line w by Maxwellian electrons in plasmas. P is polarization in plasma with Maxwellian and non-Maxwellian, hot electrons; Phot is polarization in plasma with only non-Maxwellian, hot electrons; and g is the ratio of the excitation rates of non-Maxwellian and Maxwellian electrons.

Fig. 4 illustrates depolarization caused by Maxwellian electrons in plasmas. Line polarization in plasmas strongly depends on the fraction of non-Maxwellian, hot electrons (with respect to the total electron density). In general, the fraction of 3-5% is sufficient to observe line polarization of 5-10% (assuming the maximum polarization more than 50%).

Figs. 5 and 6 show the results of calculations of polarization of Ne-like lines. In particular, polarization of one of the most intense Ne-like lines, 3C line calculated in threshold units for ions from Ne-like Ca (Z=20) up to Xe (Z=54) together with threshold energies for these ions are presented in Fig. 5. Polarization of diagnostically important 3A-3F lines calculated for Mo ions is given in Fig. 6. These results agree well with calculations by Zhang et al [9], which are listed up to six thresholds and with the polarization of Ne-like Fe lines produced at the LLNL EBIT [10]. The degree of polarization of 3C and 3D lines are close and smaller than for 3A, 3B, 3F, and 3G lines. The 3C and 3D lines are mostly collisionally excited and in the first approximation we can use present theoretical predictions whereas polarization of the other lines is affected by radiative cascades and requires full kinetic modeling.

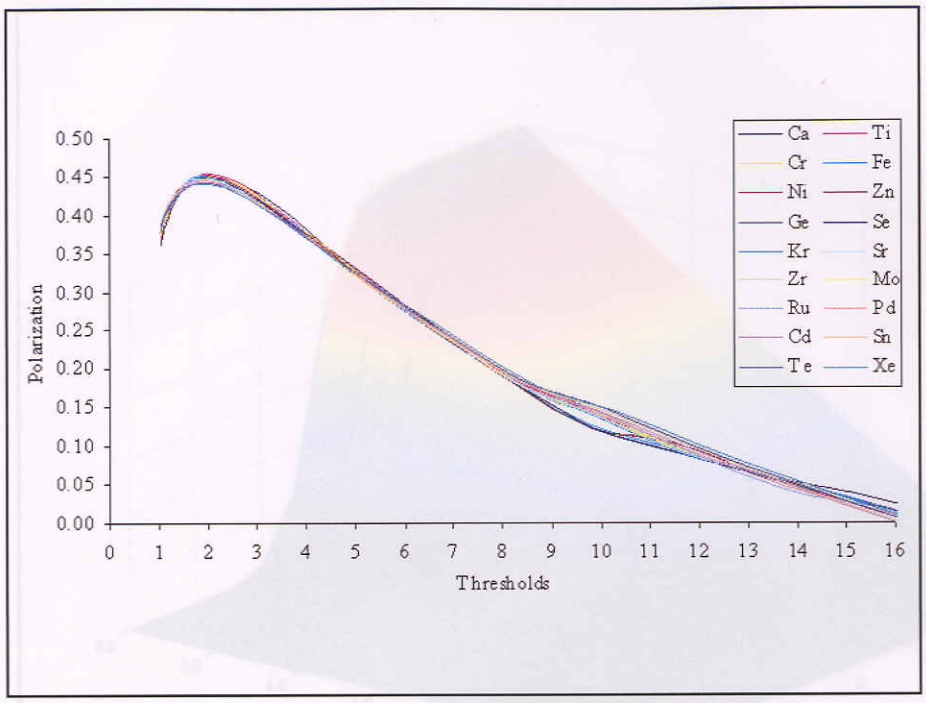

Threshold Energy [eV]		
	Z	3C
Ca	20	401.90
Ti	22	525.91
Cr	24	665.57
Fe	26	821.11
Ni	28	992.80
Zn	30	1180.90
Ge	32	1385.80
Se	34	1607.70
Kr	36	1847.00
Sr	38	2104.10
Zr	40	2379.30
Mo	42	2675.70
Ru	44	2985.80
Pd	46	3318.10
Cd	48	3670.40
Sn	50	4043.30
Te	52	4437.30
Xe	54	4853.20

Fig. 5. Polarization of Ne-like line 3C calculated with a monoenergetic EDF for different electron beam energies (in threshold units). Threshold energies are given in Table on the right.

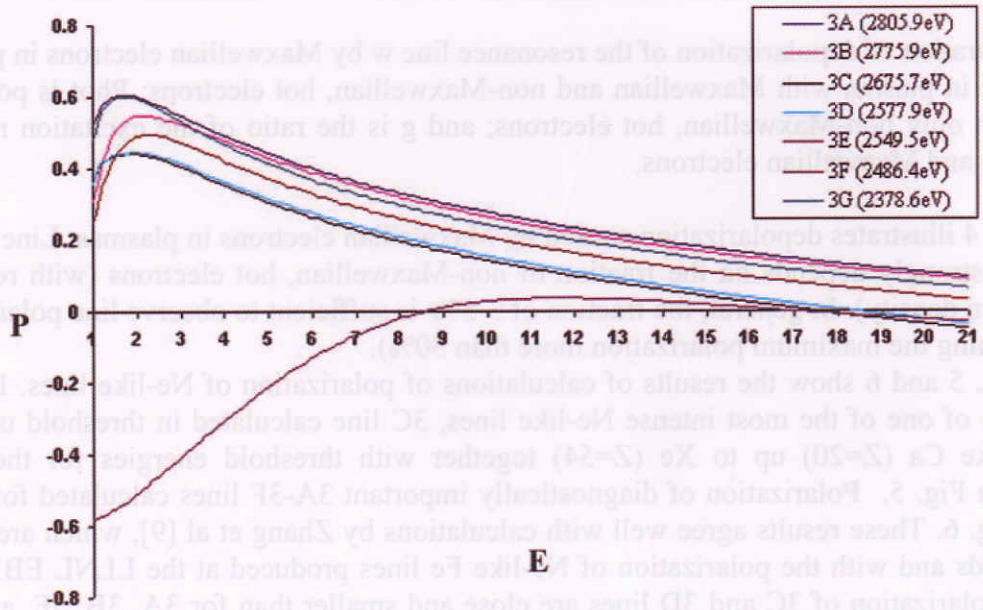

Fig. 6. Polarization of Ne-like lines 3A-3F calculated with a monoenergetic EDF for different electron beam energies (in threshold units). Threshold energies are given in a box on the right.

III. X-ray spectropolarimetry in Ti and Mo x-pinch experiments

X-pinches produce a bright, small x-ray source with a well-defined location. They can yield x-ray spectra from numerous ions with very high resolution. Currently, x-ray spectra of x-pinches are collected and studied at different types of pulsed power machines, for example, at the 1 MA pulsed power device at University of Nevada, Reno (UNR) [11]. A distinct feature of x-pinches is the existence of plasma anisotropy in the form of strong electron beams, which makes them attractive objects for spectropolarimetry. X-ray spectropolarimetry is a new diagnostic that can provide detailed information about the electron distribution function in plasmas. This diagnostic is based on spectroscopic monitoring of the plasma and modeling of the polarization-sensitive spectra. Such spectra are simultaneously recorded by two crystals with different sensitivity to polarization. The difference in line ratios from two simultaneously recorded spectra yields information on the parameters of electron beams such as a fraction of hot electrons and an energy cutoff. Polarization-sensitive experiments were performed on the 1 MA pulsed power Z-pinch device at the UNR Nevada Terawatt Facility for Ti and Mo x-pinches (see for details [1]). The scheme of the x-pinch experiments involving polarization-sensitive measurements is given below.

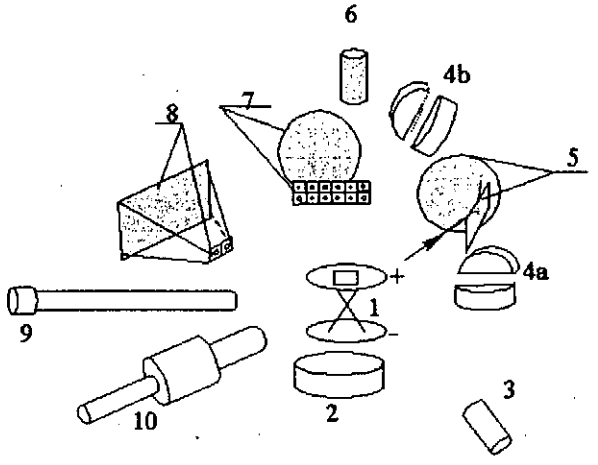

1. X-pinch load; 2. Horizontal space-resolved convex crystal spectrometer with a low resolution time-integrated pinhole camera; 3. Collimated hard x-ray *Si*- diode; 4. (a) Side-on convex crystal polarimeter; (b) End-on convex crystal polarimeter; 5. Flat crystal time-gated spectrometer; 6. Hard x-ray detector (outside vacuum chamber); 7. Time-gated pinhole camera; 8. High resolution pinhole camera; 9. PCD, XRD and Ni bolometer assembly; 10. Polychromator and transmission grating spectrometer assembly.

Fig. 7. The scheme of x-pinch experiments involving polarization-sensitive measurements.

A planar-loop configuration was used for x-pinch loads (labeled 1 in Figure 7) in which the top and the bottom wire loops were touching each other only at one central point. The polarization-dependent spectra of K-shell line radiation from Ti x-pinches and L-shell line radiation from Mo x-pinches were recorded by a polarimeter which includes so-called horizontal (H) and vertical (V) spectrometers (labeled 4a in Figure 7). The "H" spectrometer has a dispersion plane perpendicular to the discharge axis and records mostly the parallel polarization state. The "V" spectrometer has a dispersion plane parallel to the discharge axis and records mostly the perpendicular polarization

state. The crystals for Ti and Mo x-pinch measurements were selected to provide the value of a nominal Bragg angle close to 45°. For Ti x-pinches, LiF (2d=4.027Å) crystals were used with a spacing corresponding to the nominal Bragg angle of 40° at the wavelength of 2.62 Å (w line). For Mo x-pinches, α-quartz (2d=6.687Å) crystals with a spacing corresponding to the nominal Bragg angle of 46° at the wavelength of 4.8 Å (3D line) were employed.

Ti results: Earlier, preliminary results of x-ray spectropolarimetry studies of Ti x-pinches at UNR were presented in [12-13]. Recently, spectroscopic results from seven Ti x-pinch shots have been analyzed [5]. Similar K-shell Ti polarization-dependent spectra generated by a quasi-Maxwellian electron beam at the LLNL EBIT-II electron beam ion trap have been studied [5] and compared with previous LLNL EBIT studies with a monoenergetic electron beam [14]. In [14], the x-ray spectrum of He-like Ti was measured at the energy just above the electron-impact excitation threshold (4800 eV). The measured intensities were collected by the spectrometers with a crystal recording almost a pure parallel polarization state (I_1) and a crystal recording a mixture of both polarization states (I_2) [14]. In [5] we use the same technique to measure polarization-sensitive Ti spectra generated by a quasi-Maxwellian electron beam which was set to model a quasi-Maxwellian distribution function with T_M=2.3 keV in the energy range up to 11.85 keV (2.5 excitation threshold). The measured intensities simultaneously recorded by the spectrometers with a Si (220) crystal (almost a pure parallel polarization state, I_3) and a Ge (111) crystal (mixture of both polarization states, I_4) were I_3=0.212, I_4=0.335 for z/w; I_3=0.068, I_4=0.145 for x/w; and I_3=0.113, I_4=0.153 for y/w. Theoretical modeling of He-like Ti lines with Gaussian and quasi-Maxwellian electron distribution functions was performed to match less-sensitive to polarization data I_2 and I_4. The theory describes well the ratios and differences in spectra between monoenergetic and quasi-Maxwellian beams, specifically the fact that the ratio z/w does not change, but the x/w ratio decreases from 0.191 to 0.145 and the y/w ratio also decreases from 0.235 to 0.153. The comparison of polarization-sensitive ratios I_1/I_2 and I_3/I_4 for the z, x, and y lines prove that: the ratio decreases for the lines z and x and they become more negatively polarized and the ratio increases for the line y, which become more positively polarized. This agrees well with theoretical predictions.

Mo results: Modeling of experimental Mo x-pinch spectra together with the most intense and diagnostically-important L-shell spectral features including the Ne-like lines (3A-3G) are shown in Fig. 8. The results of this modeling was discussed in detail in [11]. Ne-like lines are the best candidates for L-shell spectropolarimetry because only Ne-like lines are single lines and also theoretical calculations predict strong polarization of lines 3C and 3D near the threshold. Results of modeling presented in Fig. 8 indicate the presence of hot electrons with a fraction from 3 up to 7 % which provides justification of using such Mo x-pinches for x-ray spectropolarimetry. The typical polarization-sensitive spectra from Mo X-pinches are presented in Fig. 9. Analysis of four Mo X-pinch shots shows that the H and V traces are different for shots 91, 92, and 93 and are almost identical for the shot 97. The intensities associated with different polarization states $I_{\parallel}/I_{\perp}$ for each of the spectral lines (3A, 3B, F1, 3C, and 3D) and the line ratios of the satellite lines to their resonance lines (Na2/3C) from the horizontal and vertical spectra have been analyzed. In this analysis, we used theoretical predictions discussed in a previous section. Experimental values of $I_{\parallel}/I_{\perp}$ for the line ratio 3D/ 3C was found to be close to 1 for all shots, which indicates the same polarization for the 3C and 3D lines and agrees well with theory. Experimental values of $I_{\parallel}/I_{\perp}$ for other lines are greater than 1, which gives a positive polarization compared to resonance lines using the two spectrometer technique. Analysis of four Mo x-pinch shots indicates polarization of x-ray L-shell lines was significant in three shots (91, 92, and 93) and was not significant in the shot 97.

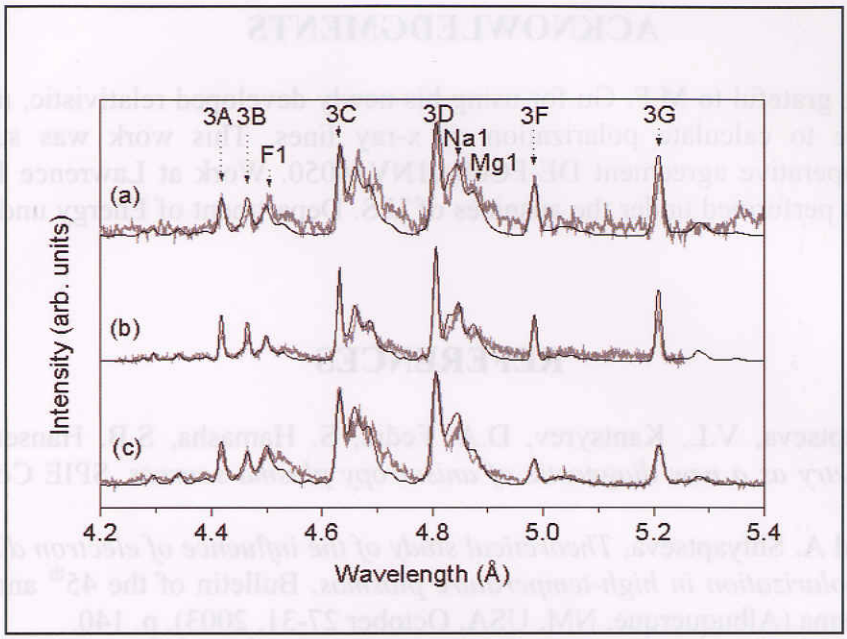

Fig. 8. Experimental spectra (gray lines) from Mo x-pinches of various wire diameters fit with modeled spectra (black lines). (a) 62 μm wire pinch and the modeled spectrum has 7% hot electrons, T_e = 850eV, and $n_e = 2.1 \times 10^{21} cm^{-3}$. (b) 50 mm wire pinch and the modeled spectrum has 4.5% hot electrons, T_e = 850eV, and $n_e = 5 \times 10^{21} cm^{-3}$. (c) 24 mm wire pinch and the modeled spectrum has 3% hot electrons, T_e = 825eV, and $n_e = 2 \times 10^{22} cm^{-3}$.

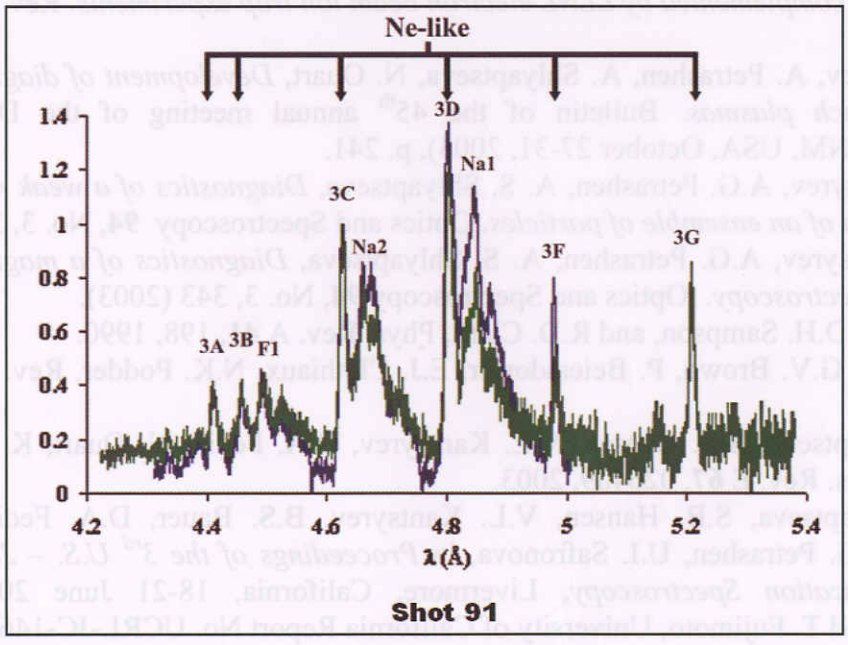

Fig. 9. X-ray polarization-sensitive spectra from a Mo X-pinch recorded by H (blue lines) and V (green lines) spectrometers.

ACKNOWLEDGMENTS

The authors are grateful to M.F. Gu for using his newly developed relativistic, multiconfigurational atomic package to calculate polarization of x-ray lines. This work was supported by DOE-NNSA/NV cooperative agreement DE-FC08-01NV14050. Work at Lawrence Livermore National Laboratory was performed under the auspices of U.S. Department of Energy under Contract No. W-7405-Eng-48.

REFERENCES

1. A.S. Shlyaptseva, V.L. Kantsyrev, D.A. Fedin, S. Hamasha, S.B. Hansen, N. Ouart, *X-ray spectropolarimetry as a new diagnostic of anisotropy plasma sources.* SPIE Conf. Proc., **5196**, 16 (2003).
2. N. Ouart and A. Shlyaptseva, *Theoretical study of the influence of electron distribution functions on x-ray line polarization in high-temperature plasmas.* Bulletin of the 45th annual meeting of the Division of Plasma (Albuquerque, NM, USA, October 27-31, 2003), p. 140.
3. M. F. Gu, Astrophys. J. **582**, 1241, 2003.
4. V.L. Kantsyrev, D.A. Fedin, A.S. Shlyaptseva, S. Hansen, D. Chamberlain, and N. Ouart, *Energetic electron beam generation and anisotropy of hard x-ray emission from 0.9 to 1.0 MA high-Z X-pinches*, Physics of Plasmas **10**, 2519 (2003).
5. A.S. Shlyaptseva, D. A. Fedin, S. Hamasha, S. Hansen, C. Harris, V. L. Kantsyrev, P. Neill, N. Ouart, P. Beiersdorfer, U. Safronova, *X-ray Spectroscopy and Spectropolarimetry of high energy density plasma complemented by LLNL electron beam ion trap experiments*. Rev. Sci. Instr. **74**, 1947 (2003).
6. V. Kantsyrev, A. Petrashen, A. Shlyaptseva, N. Ouart, *Development of diagnostics of magnetic fields of z-pinch plasmas.* Bulletin of the 45th annual meeting of the Division of Plasma (Albuquerque, NM, USA, October 27-31, 2003), p. 241.
7. V. L. Kantsyrev, A.G. Petrashen, A. S. Shlyaptseva, *Diagnostics of a weak magnetic field upon pulse excitation of an ensemble of particles*. Optics and Spectroscopy **94**, No. 3, 338 (2003).
8. V. L. Kantsyrev, A.G. Petrashen, A. S. Shlyaptseva, *Diagnostics of a magnetic field by x-ray polarization spectroscopy*. Optics and Spectroscopy **94**, No. 3, 343 (2003).
9. H.L. Zhang, D.H. Sampson, and R.D. Clark, Phys. Rev. A **41**, 198, 1990.
10. S.B. Utter, G.V. Brown, P. Beiersdorfer, E.J. Clothiaux, N.K. Podder, Rev. Sci. Instr. **70**, 284, 1999.
11. A.S. Shlyaptseva, S.B. Hansen, V.L. Kantsyrev, D.A. Fedin, N. Ouart, K. Fournier, and U.I. Safronova, Phys. Rev. E **67**, 026409, 2003.
12. A.S. Shlyaptseva, S.B. Hansen, V.L. Kantsyrev, B.S. Bauer, D.A. Fedin, N. Ouart, S.A. Kazantsev, A.G. Petrashen, U.I. Safronova, in *Proceedings of the 3rd U.S. – Japan Workshop on Plasma Polarization Spectroscopy*, Livermore, California, 18-21 June 2001, edited by P. Beiersdorfer and T. Fujimoto, University of California Report No. UCRL-JC-146907 (2001), pp. 93-120.
13. A.S. Shlyaptseva, S.B. Hansen, V.L. Kantsyrev, B.S. Bauer, D.A. Fedin, N. Ouart, S.A. Kazantsev, A.G. Petrashen, U.I. Safronova, Rev. Sci. Instr. **72**, 1241, 2001.
14. P. Beiersdorfer, G. Brown, S. Utter, P. Neill *et al.*, Phys. Rev. A **60**, 5, 4156 (1999).

Toward 3-D E-Field Visualization in Laser-Produced Plasma by Polarization-Spectroscopic Imaging

Yong W. Kim
Department of Physics, Lewis Laboratory 16, Lehigh University
Bethlehem, PA 18015
and
School of Physics, Seoul National University
Seoul, Korea

(February 28, 2004)

Abstract

A 3-D volume radiator such as laser-produced plasma (LPP) plumes is observed in the form of a 2-D projection of its radiative structure. The traditional approach to 3-D structure reconstruction relies on multiple projections but is not suitable as a general method for unsteady radiating objects. We have developed a general method for 3-D structure reconstruction for LPP plumes in stages of increasing complexity. We have chosen neutral gas-confined LPP plumes from an aluminum target immersed in high-density argon because the plasma experiences Rayleigh-Taylor instability. We make use of two time-resolved, mutually orthogonal side views of a LPP plume and a front-view snapshot. No symmetry assumptions are needed. Two scaling relations are invoked that connects the plasma temperature and pressure to local specific intensity at selected wavelength(s). Two mutually-orthogonal lateral luminosity views of the plume at each known distance from the target surface are compared with those computed from the trial specific intensity profiles and the scaling relations. The luminosity error signals are minimized to find the structure. The front-view snapshot is used to select the initial trial profile and as a weighting function for allocation of the error signal into corrections for specific intensities from the plasma cells along the line of sight. Full Saha equilibrium for multiple stages of ionization is treated, together with the self-absorption, in the computation of the luminosity. We show the necessary optics for determination of local electric fields through polarization-resolved imaging.

1. Introduction

A 3-D volume radiator such as laser-produced plasma (LPP) plumes is observed in the form of a 2-D projection of its radiative structure. The traditional approach to 3-D structure reconstruction relies on multiple 2-D projections [1] but is not suitable as a general method for structure analysis of unsteady volume radiators. A dramatic example of such unsteady radiators is a LPP plume confined in a dense neutral gas. The interface between the neutral gas and the LPP plume can become Rayleigh-Taylor unstable when the mass density disparity between the two media reaches a threshold condition at higher neutral gas densities. The consequences are irregular growths of the plume over time with the attendant loss of shot-to-shot reproducibility and the development of local electric fields due to resultant charge separation within the plasma plume.

There are two goals in this investigation. The first goal is to demonstrate the practicality and robustness of a newly developed algorithm for reconstruction of the 3-D structure of an

arbitrary LPP plume as a general method. Here, the structure is given in terms of the local specific emission intensity as radiated from individual plasma elements. The second is to map out the local electric fields by further resolving the state of polarization of the local plasma emissions.

Our approach to the goals follows the strategy of incorporating into the analysis increasing complexity in stages: a) axisymmetric LPP plumes with self-absorption; [2] b) non-symmetric but non-self absorbing LPP plumes; [3] and c) non-symmetric self-absorbing LPP plumes. We have now focussed on neutral gas-confined LPP plumes from an aluminum target immersed in high-density argon. This is because as the argon density is increased the aluminum LPP plume to argon interface becomes unstable due to emergent Rayleigh-Taylor instability. The resulting plasma plume evolves into a complex volume radiator, and this serves our interest in 3-D volume radiators of arbitrary structure as the majority of naturally occurring plasmas is. Such plasmas accommodate the goal of formulating a general method for determining the distribution of local electric fields as well.

2. Imaging by Luminosity Streaks

We present two scenarios of LPP plumes, one generated in vacuum and another confined in a dense neutral gas medium. These two cases are similar in that there exists significant self-absorption of plasma emissions in either type of plasma plumes. But they are different in that in the presence of confinement by a dense neutral gas the advancing interface of the plume suffers Rayleigh-Taylor instability, and the plasma loses its axial symmetry. We will first describe the procedure for structure reconstruction for axially symmetric LPP plumes, and then address the general case of LPP plumes without any simplifying symmetry properties.

A. Axisymmetric self-absorbing LPP plumes

Our approach for the structure reconstruction is built on two time-resolved, mutually orthogonal side views of a LPP plume and a front-view snapshot at an early moment. In one implementation, multiple sets of mutually orthogonal, lateral-view luminosity streaks are acquired, each set taken at different distances from the target surface. The front-view snapshot of the LPP plume is also taken once shortly after the onset of the LPP plume. No symmetry assumptions are needed for the full algorithm but we illustrate the important issues at hand by first considering the case of axisymmetric LPP plume. Figure 1 shows a breakdown of the

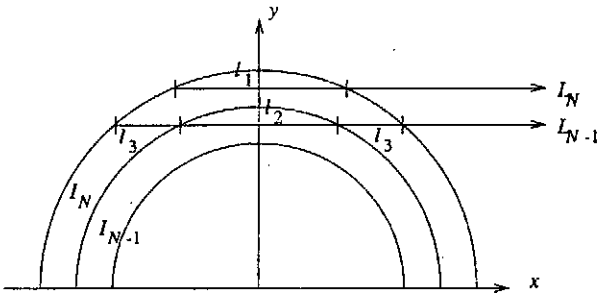

Figure 1. Coaxial shell scheme for an axisymmetric plasma plume for the calculation of plasma luminosity.

plume into N radial shells of uniform spacing about its axis of symmetry at constant thickness. This shell is imaged along the x-axis as a function of distance along the y-axis, where the axis of

symmetry lies along the z-axis. For the outermost N^{th} shell, the measured luminosity, L_N, is a result of emissions from a plasma element of path length l_1. For this case, we are able to write out the luminosity in terms of the specific emission intensity of the plasma, I_N, and the plasma absorption coefficient, k_N, according to the solution of the equation of radiative transfer: [4]

$$L_N = \frac{I_N}{k_N}(1 - e^{-k_N l_1}) \tag{1}$$

The measured luminosity at the next pixel of the imaging detector contains contributions from three different plasma elements along the line of sight. Starting from the leftmost end of the line of sight, the luminosity emerging from the plasma element of path length l_3 must suffer attenuation in two other plasma elements to the right, one with path length l_2 and the other with path length l_3. Notice that the absorption properties of the leftmost and rightmost elements are the same. The center element has its own specific intensity I_{N-1} and absorption coefficient k_{N-1}, and its luminosity suffers attenuation by the rightmost element before reaching the luminosity detector. Finally, the contribution from the rightmost element completes the luminosity, L_{N-1}. The full expression for the luminosity is given in eq. (2) below:

$$L_{N-1} = \frac{I_N}{k_N}(1 - e^{-k_N l_3})(1 - e^{-k_{N-1} l_2})(1 - e^{-k_N l_3}) + \frac{I_{N-1}}{k_{N-1}}(1 - e^{-k_{N-1} l_2})(1 - e^{-k_N l_3}) + \frac{I_N}{k_N}(1 - e^{-k_N l_3}) \tag{2}$$

The significant aspect of this line of development is that each succeeding luminosity expression contains as unknown only one shell's specific intensity and absorption coefficient; the rest have been determined from the luminosity relations of all preceding shells. The path lengths for successive plasma elements are found from the geometry of the shell scheme. Once all specific intensity values are found, we have reconstructed the full structure of the plasma, which is axially symmetric in this illustration. The large question is then: how does one find the self-absorption coefficient in each succeeding new plasma segment? We resolve the question by invoking two scaling relations, one which connects the local plasma temperature to the specific intensity and the other which ties the plasma pressure to the specific intensity:

$$T = C_T I^{\alpha} \tag{3}$$

$$p = C_p I^{\alpha+\beta} \tag{4}$$

Here we have made use of the fact that the luminosity spectrum is a continuum for a dense LPP plume from an aluminum target at early times, and the specific emission intensity also has a continuum spectrum. The scaling exponents α and β and the scaling constants C_T and C_p are undetermined constants, which can be determined after full structure reconstruction has been completed. We will return to this point later.

Eq. (1) may now be solved self consistently to find I_N. We begin by choosing a set of values for α, β, C_T and C_p, and guessing a value for I_N, which assigns values for T and p. It is noted here that the plasma of interest here has high densities such that the mean collision time is of the order of 10 fs while the plasma evolves over nanosecond time scale. This means that the plasma is in a state of local thermal equilibrium and the populations of different species are

specified by Saha equations. [4] There are altogether 13 stages of ionization for aluminum, and the respective Saha equations may be written out by using the electron pressure, p_e, as follows:

$$\frac{\alpha_1(1-\alpha_2)}{(1-\alpha_1)} = \frac{2kT(2\pi m_e kT)^{3/2}}{p_e h^3}\frac{(q_e)_{Al+}}{(q_e)_{Al}}$$
$$\vdots \qquad (5)$$
$$\frac{\alpha_{13}}{(1-\alpha_{13})} = \frac{2kT(2\pi m_e kT)^{3/2}}{p_e h^3}\frac{(q_e)_{Al13+}}{(q_e)_{Al12+}}$$

where for the first stage of ionization, for example,

$$\frac{(q_e)_{Al+}}{(q_e)_{Al}} = \frac{(q_e)^{\circ}_{Al+}}{(q_e)^{\circ}_{Al}} e^{-IP^*_{Al}/kT}$$
$$(q_e)^{\circ}_{Al\,1+} = \sum_{i=0}^{i^*} g_i e^{-E_i/kT} \qquad (6)$$
$$\Delta IP = \frac{(Z+1)e^2}{\rho_D}$$

Here α_1, α_2, ... α_{13} are the degrees of ionization for the thirteen stages of ionization, respectively. $(q_e)_{Ali+}$ denotes the single-particle canonical partition function of an ith ion for electronic degrees of freedom, and $(q_e)^o_{Ali+}$ denotes its value evaluated with the zero of the energy fixed at the ground state of the i^{th} ion of aluminum. IP^*_{Al} is the ionization potential of the neutral aluminum atom which is corrected for its lowering of the continuum edge, ΔIP, due to merging of the bound states by the Stark effect. ρ_D is the plasma Debye length, and Z is the charge number of the ion in question. m_e, k and h are the electron mass, Boltzmann constant and Planck's constant, respectively.

The Saha equations are solved self consistently by using the electron pressure, p_e, as a floating parameter, knowing that p_e is related to the plasma pressure, p, by

$$p_e = p\frac{\bar{Z}}{(1+\bar{Z})} \qquad (7)$$

Here the mean charge number is determined from the degrees of ionization as follows:

$$\bar{Z} = \alpha_1 + \alpha_1\alpha_2 + \alpha_1\alpha_2\alpha_3 + \cdots + \alpha_1\alpha_2\alpha_3\cdots\alpha_{12}\alpha_{13} \qquad (8)$$

We start with a trial value for p_e, set ΔIP to zero and solve for α_i's. Then we calculate p_e using the solutions of the Saha equations, and it is compared with the trial value for p_e. This is continued until the initial and final values of p_e are brought to agreement within a preset error range.

The self-absorption coefficient is then calculated from the imaginary part of the plasma index of refraction: [5]

$$n_i = \frac{1}{\sqrt{2}}\left[\sqrt{\left(1-\frac{\omega_p^2}{\omega^2+\upsilon_{ei}^2}\right)^2 + \left(\frac{\nu_{ei}}{\omega}\frac{\omega_p^2}{\omega^2+\nu_{ei}^2}\right)^2} - \left(1-\frac{\omega_p^2}{\omega^2+\nu_{ei}^2}\right)\right]^{1/2} \qquad (9)$$

where

$$\nu_{ei} = \frac{n_e}{(kT)^{3/2}} \frac{\bar{Z}\pi^{3/2}e^4}{m_e^{1/2}2^{5/2}\gamma(\bar{Z})} \ln(\Lambda) \tag{10}$$

$$\gamma(\bar{Z}) \approx \frac{\bar{Z}n_e}{kT} \ln\left(\frac{kT\rho_D}{\bar{Z}e^2}\right) \tag{11}$$

Λ and ω_p are the Coulomb length and plasma frequency, respectively. The absorption coefficient at frequency ω is given by $k = n_i\, \omega/c$. c is the speed of light in a vacuum.

We can now return to eq. (1) and solve for I_N, and then to eq. (2) to solve for I_{N-1}, and so on. When the structure reconstruction has been carried out for all other sections of the plasma, we obtain the entire plasma structure in terms of the specific emission intensity. The structure in terms of plasma pressure and temperature follows according to eqs. (3) and (4). This makes it possible to compute the total mass and energy contained in the plasma plume and the attenuation of an external beam transmitted through the plasma, all at a given time. Once the process has been carried out for all times, we can find the plasma mass as a function of time. When the masses are all added together, we have at hand the total mass ablated from the target surface. The total energy within the plasma can be similarly calculated. The energy in the plasma can be added up. When the radiative losses and the energy expended in heating, melting and evaporation of the ablated matter are combined, we have the total energy in the laser pulse which has been actually coupled into generating the LPP plume. This is now ready to be compared with the measured energy. It is also possible to compute the attenuation coefficient of the LPP plume for an external beam of light that is transmitted through the plasma; this beam attenuation coefficient is also measurable.

A composite error can be constructed by comparing the measurements with calculations for each set of selected values for α, β, C_T and C_p. Minimization of the composite error constitutes not only a calibration of the luminosity detectors but also an assignment of the absolute values for the scaling exponents, α and β, and scaling constants, C_T and C_p. A demonstration of the structure reconstruction algorithm has been carried out for a LPP plume of aluminum generated in a vacuum. [2]

B. **Non-symmetric self absorbing LPP plumes**

For LPP plumes that lack axial symmetry, reconstruction of the structure of a 2-D section of the plume remains a 2-D problem. An x-y section of the plume contains N^2 pixels whose specific intensities need to be found, whereas two mutually-orthogonal, time-resolved lateral-view luminosity images of the section provides only 2 N luminosity values. These are not sufficient to find a unique solution for the cross-sectional structure of the plume. To facilitate the search for a unique structure, we have incorporated a front-view snapshot along the laser beam axis of the plume at an early instant. Notice that the plume grows out of the target surface as a result of the interaction of the laser pulse with the surface. This adds N^2 new constraints to the problem at one early instant of time. A breakdown of the luminosity field in relationship to the plasma structure is given in Fig. 2. The front-view snapshot at time t_o is shown in the form of constant luminosity contours. Each luminosity value is indicated decomposed into its s- and p-polarization components. For the moment, we ignore the polarization aspect of the problem; the

sum of the two polarization-resolved components gives the full luminosity along the line of sight, terminating at one detector pixel.

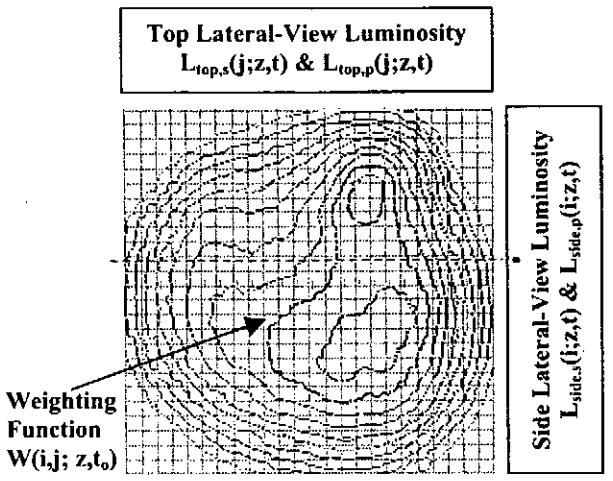

Figure 2. A scheme for plasma cells of an asymmetric LPP plume is shown for the calculation of plasma luminosity. Polarization-resolved lateral-view luminosity images are shown for both s- and p-polarization. Contributions from the plasma cells along a line of sight (broken line) define the luminosity recorded at a detector position (filled circle) at time t. The contour plots indicate the weight function formulated using a front-view snapshot.

In Fig. 3 we demonstrate the effect of self-absorption on luminosity and the degree to which the confinement of the LPP plume by argon at high density modifies the evolution of the LPP plume. The total lateral-view luminosity is shown for each of the two lateral-view directions as a function of time. In the absence of self-absorption, the two displays of total luminosity must coincide. A set of two runs is shown for each of two neutral argon pressures, one atm and 50 atm. They clearly demonstrate the existence of self-absorption; the total luminosity plots along two mutually orthogonal directions deviate from each other as the plume heats up. The discrepancy grows larger as the plume is confined more tightly at increasing neutral gas density. In addition, as the neutral gas density is increased, the discrepancy becomes increasingly less reproducible from a run to the next, as manifestations of Rayleigh-Taylor instability.

The structure reconstruction starts by proposing a trial 2-D distribution of specific emission intensity, $I_{plasma}(i, j, t)_o$ for a section of the plume at a given distance in z from the aluminum target. The luminosity is calculated along a given line of sight, such as the one shown by a broken line in Fig. 2. The plasma pressure and temperature are obtained for each of the cells along the line of sight by using the scaling relations of eqs. (3) and (4). Equilibrium Saha calculations are carried out, and a temporary value of the luminosity, $tempL_{top}(i, t)$ or $tempL_{side}(j, t)$, is calculated. Comparison with the measured luminosity for the same line of sight generates an error signal. It is here that we make use of the front-view snapshot in deciding how to allocate the luminosity error into corrections to the specific intensities in the cells along the line of sight. The weighting function is obtained by setting the global sum of the pixel values of the front-view image to unity. To find the fractions of the luminosity error to be assigned to individual line-of-sight cells, the values of the weighting function along the given line of sight is

first normalized. The product of the luminosity error and the value of the line-of-sight normalized weighting function for the cell give the correction to the luminosity emerging from a

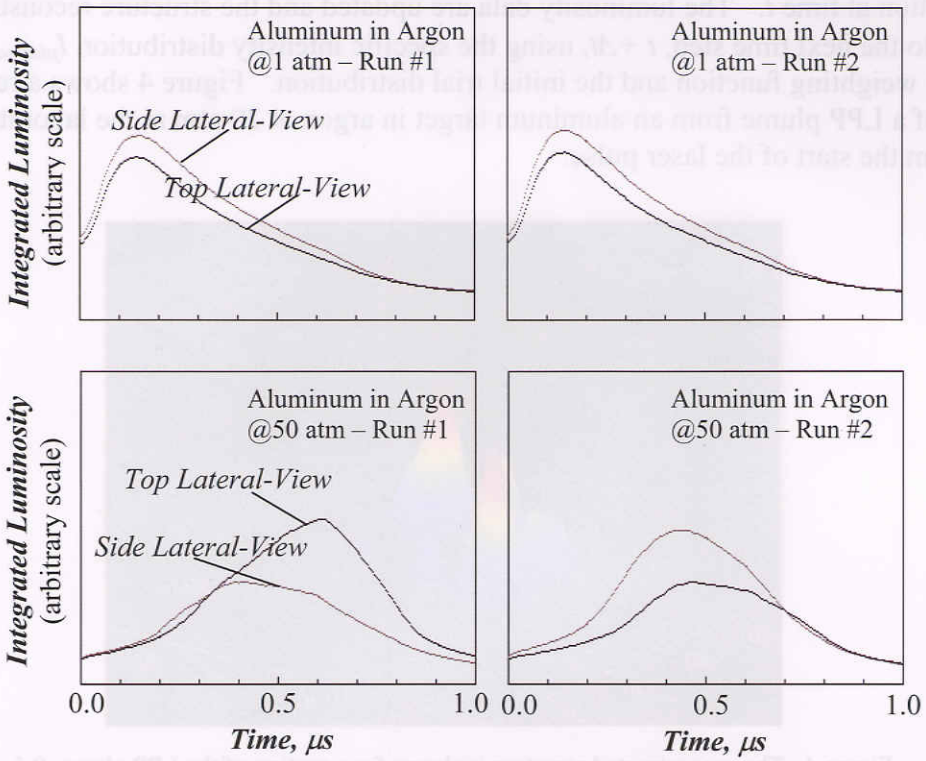

Figure 3. The total luminosity versus time plots from two mutually-orthogonal lateral-view streaks are shown for two different sets of LPP runs: a pair of runs from an aluminum target in 1 atm argon and another pair in 50 atm argon. These show direction dependence, indicative of significant self-absorption, and demonstrate a loss of shot-to-shot reproducibility due to intensifying Rayleigh-Taylor instability at higher neutral gas density.

plasma cell. The correction to the specific intensity of each plasma cell is found by solving eq. (1), which is written out for the luminosity correction for the cell. The corrected specific intensity for cell at position (i, j) is obtained when the intensity, $I_{plasma}\ (i, j, t)$, is corrected twice, once each for the two intersecting lines of sight:

$$I'_{plasma}(i,j,t) = I_{plasma}(i,j,t)_0 - \frac{k(i,j)}{(1-e^{-k(i,j)\Delta l})}[tempL_{top}(i,t) - L_{top}(i,t)]W_2(i,j,t) \quad (12)$$

$$I_{plasma}(i,j,t) = I'_{plasma}(i,j,t) - \frac{k(i,j)}{(1-e^{-k(i,j)\Delta l})}[tempL_{side}(j,t) - L_{side}(j,t)]W_1(i,j,t) \quad (13)$$

Here, $tempL_{top}\ (i, t)$ and $L_{top}\ (i, t)$ denote the calculated luminosity and the measured luminosity along the y-axis line of sight at i, respectively. Similarly, $tempL_{side}\ (j, t)$ and $L_{side}\ (j, t)$ are those along the x-axis line of sight at j, respectively. $W_2(i, j, t)$ denotes the weighting function that has bee normalized along the y-axis line of sight, whereas $W_1(i, j, t)$ is the one normalized along the x-axis line of sight. Δl denotes the distance between the cells. Notice that the plasma absorption coefficient of the cell must be found by solving the Saha equations self consistently.

The luminosity is calculated from the full $I_{plasma}(i, j, t)$ distribution for all i and j values and compared with the measured luminosity values to find the error signal.

The process is continued until the error signal is minimized. This concludes the structure reconstruction at time t. The luminosity data are updated and the structure reconstruction is advanced to the next time step, $t + \Delta t$, using the specific intensity distribution $I_{plasma}(i, j, t)$, both as the new weighting function and the initial trial distribution. Figure 4 shows a reconstructed structure of a LPP plume from an aluminum target in argon at 20 atm at the laboratory time of 355 ns from the start of the laser pulse.

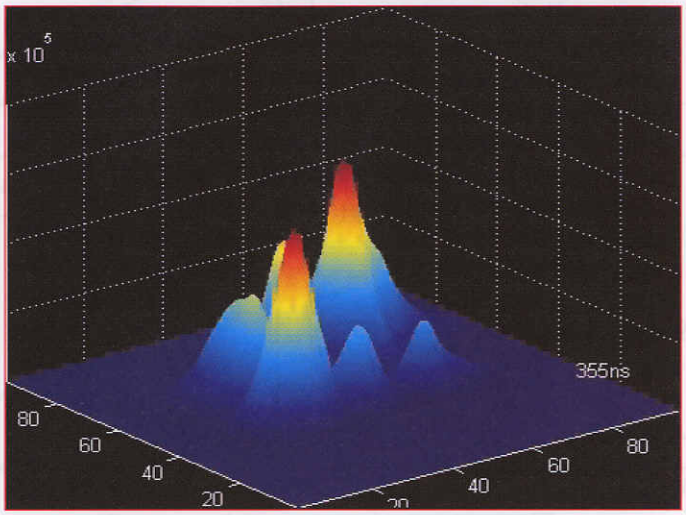

Figure 4. The reconstructed structure is shown for a section of the LPP plume, 0.5 mm from the surface of an aluminum target in 20 atm argon, at 355 ns from the start of the laser pulse. The structure is represented in terms of specific plasma emission intensity as a function of cross-sectional position given in detector pixels. Each detector pixel corresponds to a 60.4 μm square in laboratory.

3. Lateral-View Imaging at Multiple Times

The discussions in the preceding section apply to plasma structure reconstruction based on full lateral-view images, instead of the luminosity streaks. Two mutually orthogonal lateral-view images of a LPP plume may be taken at discrete time intervals. An imaging detector is needed to capture a set of lateral-view images at each selected time interval. If polarization-resolved imaging is desired, the number of detectors may have to be doubled in number. Figure 5 shows the optical arrangement suitable for polarization resolved imaging. The setup for capturing one of the needed two lateral-view images is shown. To round out the completeness of the luminosity data, a front-view snapshot of the LPP plume must be taken at an early moment of the plume's evolution.

The local E-field is deduced from the measured *degree of polarization*. For an electric dipole in an E-field, the mean dipole moment is given by

$$< \boldsymbol{M} > = \alpha_a \boldsymbol{E} + \boldsymbol{d}\ L\ (y) \qquad (14)$$

where the Langevin function is defined by

$$L\ (y) = [\ coth\ (y) - y^{-1}\ ]. \qquad (15)$$

Here $y = \boldsymbol{d} \bullet \boldsymbol{E} / k_B T$, and α_a denotes atomic polarizability. [6]

There are three major considerations for including of the distribution of local electric field in the program of plasma structure determination. First, notice that the degree of polarization for an emission line must be local, whereas the imaging gives the line-of-sight average degree of polarization, i.e., the degree of polarization for the luminosity. To find the degree of polarization for a local emission line within the plasma, the structure reconstruction needs to be carried out for the two specific intensity components of polarization in such a way that the scaling relations of eqs. (3) and (4) are satisfied for the total specific intensity. Second, we remind that the program for electric field determination relies on imaging by line emissions, not continuum emissions. The question is whether the scaling relations are appropriate for line emissions. We believe that the power-law scaling relations are good approximations, but it is useful to make a critical comparison with an alternative one based on an explicit expression for the specific emission intensity of an emission line. Third, it is necessary to rewrite the

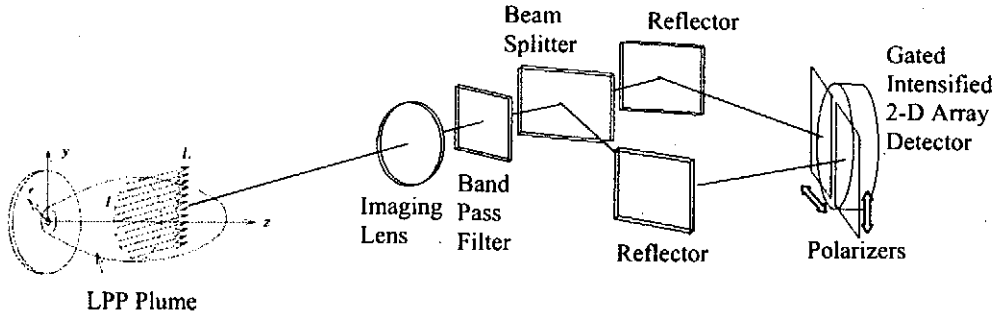

Figure 5. Schematic diagram of the optical setup for capturing polarization- and wavelength-resolved lateral-view images of a LPP plume at a selected time from the start of a laser pulse. A second identical setup is needed to capture another set of lateral-view images in a direction perpendicular to the first at the same time. Here, the image is first split into two images, and the two images are captured by a single gated, intensified 2-D array detector through two separate polarizers of mutually orthogonal polarization.

expression for the self absorption coefficient of the plasma with one for an emission line, consisting of the number density in the upper level of the transition, atomic transition probability, emission line profile function and the photon energy of the emission line. [4]

We have examined the feasibility of polarization-resolved imaging of a LPP plume from an aluminum target in low-pressure argon. Two polarization-resolved front-view images of the plume are captured using a single gated intensified CCD array detector, and a 2-D distribution of the degree of polarization has been successfully constructed for the plasma luminosity. [7] According to the general approach in our development, the luminosity polarization must now be inverted to the distribution of the polarization of specific line emissions.

4. Conclusions

We have shown that in the event of charge separation due to internal fluctuations, it is in principle possible to unfold 3-D distribution of resultant local electric fields by acquiring mutually orthogonal, polarization- and wavelength-resolved images of the LPP plume. Each of the key components of the requisite instrumentation has been investigated for simultaneous

determination of both the structure and 3-D electric field distribution, which comprise polarization spectroscopic imaging of the LPP plume from three mutually orthogonal directions.

Acknowledgement

This paper includes numerous contributions from the author's doctoral students: Conrad Lloyd-Knight, Jaechul Oh, Hedok Lee, John Labenski and Nopporn Poolyarat. The author gratefully acknowledges partial support for the research by the CTU 5-2 Consortium on Laser-Produced Plasmas, Lehigh University and Seoul National University as the author's host during the sabbatical year 2003-04 from Lehigh University.

References

[1] H. H. Burrett and W. Swindell, *Radiological Imaging* (Academic, New York, 1981), Vols. 1 and 2.

[2] Y. W. Kim and C. Lloyd-Knight, *Rev. Sci. Instr.***72**, 944 (2001).

[3] Y. W. Kim and J.-C. Oh, *Rev. Sci. Instr.* **72**, 948 (2001).

[4] Y. W. Kim, in *Laser-Induced Plasmas and Applications*, eds. L. J. Radziemski and D. A. Cremers (Dekker, New York, 1989), Chapter 8.

[5] H. Hora, *Physics of Laser Driven Plasmas,* (Wiley, New York, 1981).

[6] H. S. Robertson, *Statistical Thermophysics* (Prentice Hall, Englewood, NJ, 1992).

[7] Y. W. Kim and H.-D. Lee, *Rev, Sci, Instr.* **74**, 2123 (2003).

Plasma Polarization Spectroscopy on the LHD

M. Hayakawa, A. Iwamae, M. Goto[A], S. Morita[A] and T. Fujimoto,
LHD Experimental Groups
Graduate School of Engineering, Kyoto University
National Institute for Fusion Science [A]

Abstract

The polarization resolved H_α line has been observed on long-pulse NBI plasmas of the LHD. The Zeeman profile of H_α line yields the strength and the direction of the magnetic field, and the location of the emission regions are identified on the well-established map of the magnetic field of the plasma. It is found that the emission is localized just outside the main plasma. The Doppler width and shift of the profile indicate two temperature components and the inward atom flux with velocity of 10^3~10^4 m/s on each emission location.

1. Introduction

In fusion devices such as tokamaks and helical machines, determination of neutral particle influx from the plasma edge region to the main plasma is extremely important for the purpose of studying, e.g., the *H* mode[1, 2], the formation of density profiles[3] and the recycling neutrals[4]. In this regard, the emission line intensity is the only source of information.

Neutral helium emission lines have been observed with an array of optical fibers which covers the entire poloidal cross section of the LHD plasma[5]. The observed spectrum was interpreted as a superposition of two Zeeman profiles that originate from different locations on the same line of sight and are relatively shifted. The Zeeman profile yields a magnetic field strength, and the locations of the emission region are identified on the well-established map of the magnetic field of the plasma. The locations form a closed zone just outside the region, the so-called "ergodic layer," where the magnetic field line structure is chaotic.

When we observed a hydrogen emission line (H_α), we obtain a spectrum like Fig. 1. It is obvious that it is impractical to interpret this as a superposition of two Zeeman profiles like the case of helium. In this study, we resolve the H_α line profile into the polarized components, and determine its emission locations.

2. Experiment

Large helical device (LHD) is a heliotron type device of a double null divertor configuration. The major and average minor radii are 3.9 m and 0.6 m, respectively. The maximum magnetic field strength on the magnetic axis B_{ax} could be as high as 3 T. The map

of the magnetic surfaces and field strength are shown in Fig. 2, and the variation of the field strength along the line of sight, which is shown with the dash-dotted line, is shown in Fig. 3. The direction of the magnetic field, θ is defined as the angle from the horizontal plane. The magnetic field on the line of sight is twisted. Because of the absence of an inductive current, the magnetic field is accurately determined from the coil currents as a function of R, the distance from the center axis.

The emission from the LHD plasma was observed with the polarization separation optics (PSO), which is shown in Fig. 4. This optics consists of a 76° polarization separation prism (Halbo Optics, PBC12) and a Glan-Taylor prism (Halbo Optics, PS12) made of calcite and a pair of lens couplers, each of which focused the plasma radiation on a optical fiber for orthogonal linearly polarized light, o-ray or e-ray. The output from the fibers was fed in a line in front of a spectrograph of 1.33 m focal length *f*/9.4(McPherson M209, 1800 grooves/mm). The spectral image was recorded with a CCD (Andor DV435-BV, 1024×1024 of 13μm square pixels).

The measurement was carried out for 25 s stationary phase of a hydrogen discharge heated by neutral beam injection (NBI). The nominal field strength B_{ax} and the radius of the magnetic axis R_{ax} of the discharge were 2.75 T and 3.6 m, respectively. The NBI power was 600 kW. The gas-fueling rate was controlled so as to keep the line-averaged electron density n_e, constant. In the stationary phase n_e was 10^{19} m^{-3}. The tilt angle α of PSO, which was defined as the angle of the polarization direction of the o-ray from the horizontal plane, was −45 degrees. An example of the observed H_α line profiles is shown in Fig. 5. We calibrated the wavelength by using the spectra in the recombining phase, which are known to be unshifted. Though the H_α line is in the region of the Paschen-Back effect [6], the observed profiles show a rather complicated structure. We try to interpret these profiles as a superposition of two Zeeman profiles like the case of helium.

3. Analysis

We synthesize the H_α line profiles based on the following assumptions.

1. The H_α line is emitted from the two locations, the inner and the outer points on the line of sight.

2. On each point, there are two temperature components, and each component atoms move toward the magnetic axis with a different velocity.

3. There is a high temperature component, represented by a broad Gaussian profile.

We performed a least-squares fitting on the observed e-ray and o-ray line profiles simultaneously with four sets of Zeeman profiles plus a broad Gaussian profile. Each set of Zeeman profile has an independent intensity, Doppler width and shift. The results of the fitting are shown in Fig. 5 with the bold solid line. The adjustable parameters are shown in

Table.1. Two sets of Zeeman profiles for the inner point determine the value of the magnetic field and thus R. The other two profiles give the outer point. It is found that the emission locations were R=2.80 m and R=4.70 m.

The results of observation in the nine time spans (t = 1.0-1.5, 3.5-4.0, 6.0-6.5, 8.5-9.0, 11.0-11.5, 13.5-14.0, 16.0-16.5, 18.5-19.0, 21.0-21.5 s) are shown in Fig. 2. It is found that the H_α is emitted just outside the main plasma like the case of neutral helium and the intensity of the inner point is twice that of the outer point. At the inner point, hydrogen atoms have two temperatures, 0.286 and 3.40 eV, and inward velocity, 3.00×10^3 and 6.86×10^3 m/s, respectively. At the outer point, the hydrogen atoms have two temperatures, 0.127 and 0.837 eV, and inward velocity, -1.63×10^3 and -3.48×10^3 m/s, respectively. The warm component on each emission location (3.40 eV for the inner point and 0.837 eV for the outer point) could be identified as due to dissociative excitation of molecular hydrogen. A quantitative discussion is in progress based on a neutral particle transport code that includes molecular and molecular-ion dissociation processes.

Acknowledgements

The authors are grateful to the LHD experimental group for their excellent and helpful support.

Reference

[1] J.A. Snipes *et al.*, Plasma Phys. Controlled Fusion **38**, 1127 (1996)

[2] T. Fukuda, Plasma Phys. Controlled Fusion **40**, 543 (1998)

[3] S. Morita *et al.*, *in Proceedings of 16th International Conference on Fusion Energy, Montreal, 1996*, IAEA-CN-64/CP-3 (IAEA, Vienna, 1997).

[4] A. Kumagai *et al.*, Plasma Phys. Control. Fusion **42**, 529 (2000)

[5] M. Goto and S. Morita, Phys. Rev. E 65, 026401 (2002)

[6] P.H. Heckmann, E. Trabert 1989 Introduction to the Spectroscopy of Atoms (North-Holland)

Table. 1. The adjustable parameters and their obtained values. T_a and v_{LOS} indicate the atom temperature and the velocity along the line of sight, respectively.

	adjustable parameters	obtained value
inner component	R (m)	2.807(5)
cold	Intensity (10^4 counts)	1.83(4)
	T_a (eV)	0.299(9)
	v_{LOS} (10^3 m/s)	3.00(9)
warm	Intensity (10^4 counts)	3.0(1)
	T_a (eV)	3.3(1)
	v_{LOS} (10^3 m/s)	7.2(2)
outer component	R (m)	4.66(1)
cold	Intensity (10^4 counts)	0.35(6)
	T_a (eV)	0.11(2)
	v_{LOS} (10^3 m/s)	−1.3(2)
warm	Intensity (10^4 counts)	1.5(1)
	T_a (eV)	0.76(7)
	v_{LOS} (10^3 m/s)	−3.2(2)
broad component	Intensity (10^4 counts)	3.8(1)
	T_a (eV)	143(5)
	v_{LOS} (10^3 m/s)	33(2)

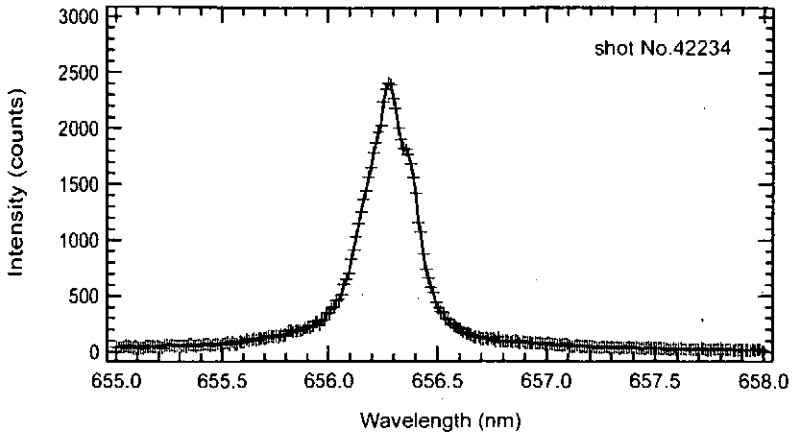

Fig. 1. An example of polarization unresolved profile of the H_α line.

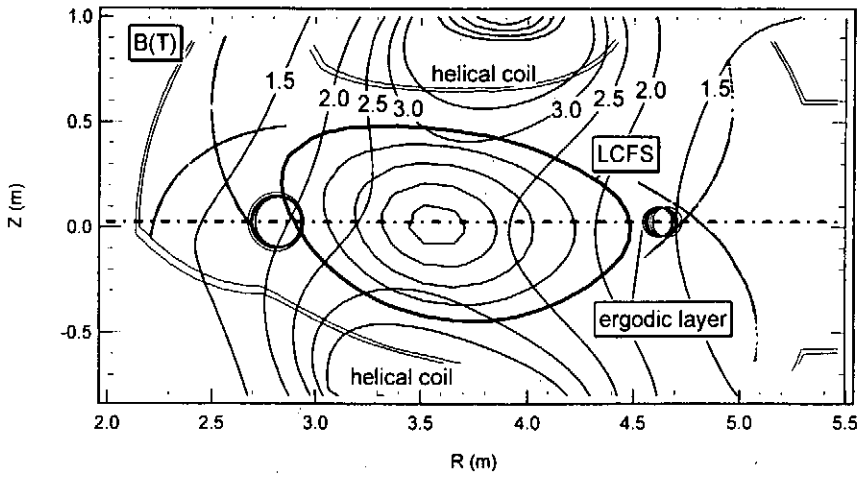

Fig. 2. Map of the magnetic surfaces and field strength for the configuration of R_{ax} = 3.6 m and B_{ax} = 2.75 T. The R and Z axes indicate the major radial direction and the direction perpendicular to the equatorial plane, respectively. The dashed line indicates the line of sight. The circles indicate the locations of the H_α line emission and their size indicates the intensity of the emission.

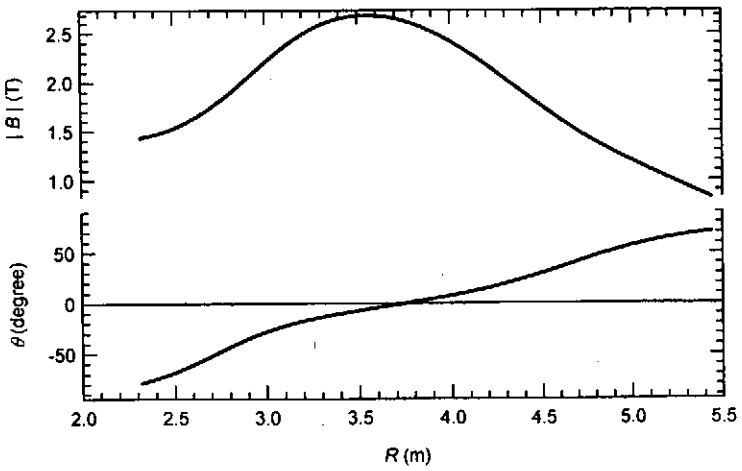

Fig. 3. The variation of the field strength and the angle of the magnetic field from the horizontal plane, θ.

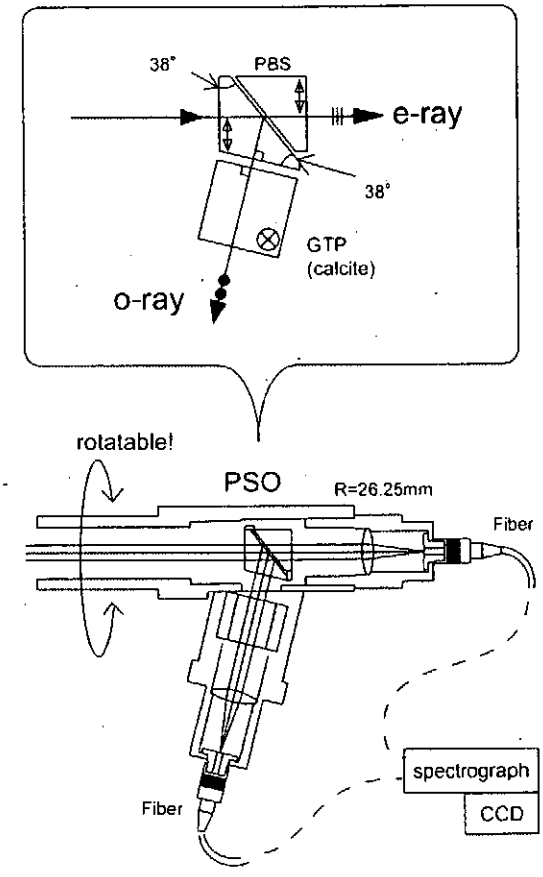

Fig. 4. The polarization separation optics (PSO).

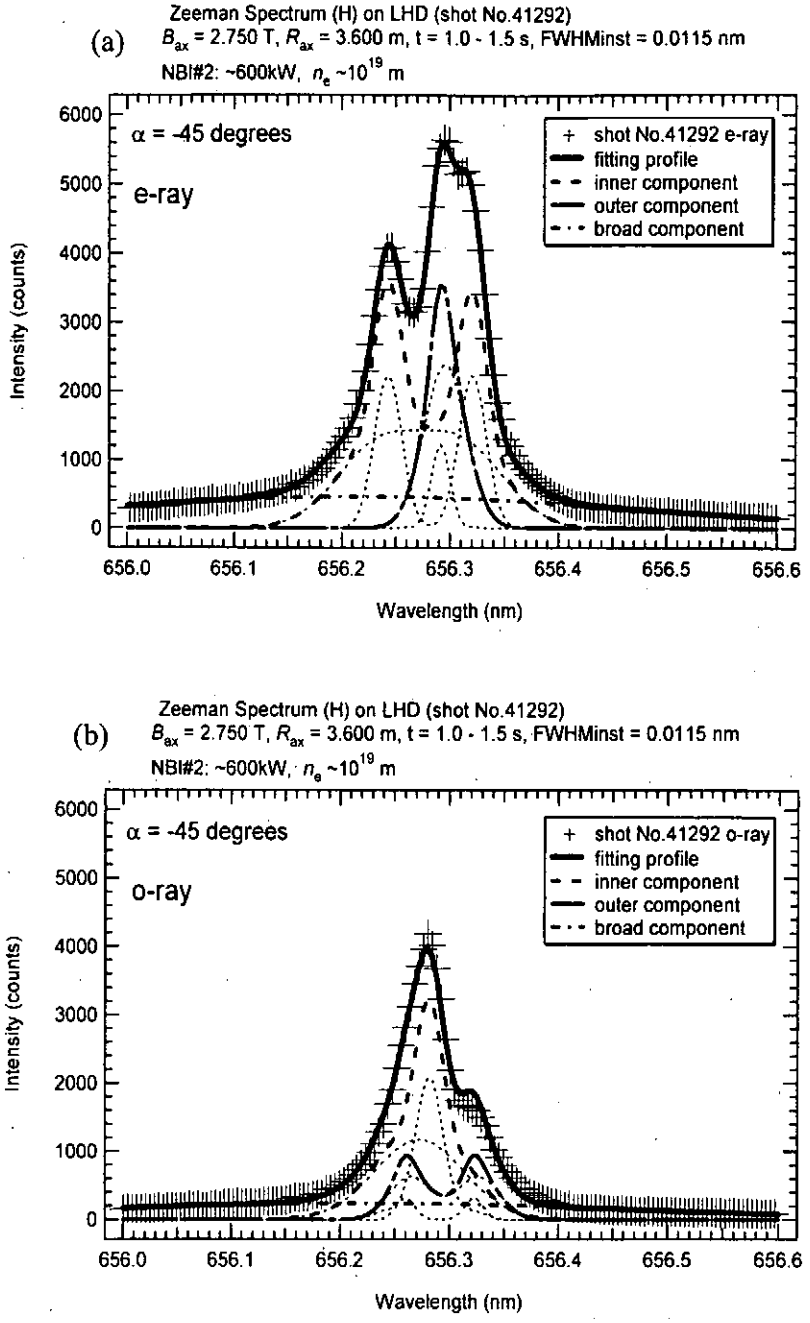

Fig. 5. The e-ray (a) and the o-ray (b) of the H_α line. The solid line is the result of the least-squares fitting with four sets of Zeeman profiles plus a broad Gaussian profile.

Influences of optical elements on the polarization measurement

M. Goto[1], M. Hayakawa[2], M. Atake[2], and A. Iwamae[2]

[1]*National Institute for Fusion Science, Toki 509-5292, Japan*
[2]*Department of Engineering Physics and Mechanics, Graduate School of Engineering, Kyoto University, Kyoto 606-8501, Japan*

abstract

An emission line of HeI λ 667.8 nm is observed in the Large Helical Device (LHD) with a polarimeter, with which two linearly polarized components of the light from the same line of sight is simultaneously measured. The emission line exhibits splittings due to the normal Zeeman effect and the π and two σ lights are respectively observed. The results indicate the polarization state of emission lines is different from our expectation. From two measurement, for the second of which the polarimeter is rotated 45 degrees from the first, the polarization ellipses of all the three polarized lights are determined. Some observations for a reversed magnetic field plasma operation, for different emission lines of different ions, and also for operations with some different magnetic field strengths suggest that the distortion of the polarization state originates not in the atomic radiation itself or the plasma condition, but in the optical window at the observation port of the vacuum chamber.

1 Introduction

In the plasma polarization spectroscopy, which aims at quantitative determination of the anisotropy of electron velocity distribution function in plasma, a high precision measurement of the polarization state of emitted light is required. If the polarization state is distorted by some reasons other than the anisotropic electron collisions, the reason of the distortion must be made clear and its affection must be removed experimentally or in the analysis.

Some polarization measurements have been carried out in the Large Helical Device (LHD) and we have found a distortion of polarization state which is not ascribed to the anisotropic electron collisions. This article introduces the method we have employed to determine the polarization state of the observed emission lines from a limited number of experimental results and seeks the origin of the distortion.

We mainly use an emission line of HeI λ 667.8 nm (2^1P–3^1D). This line clearly exhibits a normal Zeeman effect and is split into three components which respectively have different polarization states: one of them is the linearly polarized light along the magnetic field direction (*pi* light) and others are the right- and left-handed circularly polarized light on the plane perpendicular to the field direction (*sigma* light). This feature is quite useful for the present study because different types of polarization state can be simultaneously measured.

In LHD whole the magnetic field is stationary formed irrespective of plasma state. Owing to this characteristic, at the end of a discharge most of the ions and electrons in the plasma quench through volume recombination processes rather than dissipation [2] and finally show an intensive radiation on the magnetic axis. This study exploits such a strong and spatially localized radiation is used.

2 Experimental setup

Figure 1 shows a schematic top view of LHD and the line of sight which is on the equatorial plane. From the geometrical relation between the line of sight and the magnetic field direction on the magnetic axis, the polarization ellipses [1] of the π and two σ lights of the Zeeman-split HeI λ 667.8 nm line are expected to have such shapes as shown in Fig. 2. In this case, the spectrum to be observed is shown in Fig. 3. We denote the σ light having a shorter wavelength of the two as σ^+ and the other as σ^- throughout. In the same figure, actually observed data are also drawn with crosses and they show a good agreement with each other.

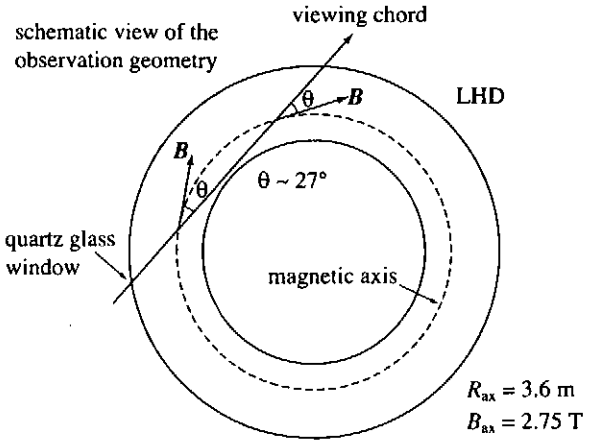

Figure 1: Schematic top view of LHD and the line of sight which is on the equatorial plane. $\boldsymbol{B}$ indicates the direction of the magnetic field for normal operations.

The magnetic field strength determines the wavelength shift of σ^+ and σ^- lights from the unshifted π light, and the angle between the line of sight and the field direction determines the intensity ratio of π to σ light. The good agreement in Fig. 3 indicates that our assumption that the line emission is localized on the magnetic axis is reasonable.

For the polarization measurement, such an optical system as shown in Fig. 4 is employed. With this polarimeter, two orthogonal components of linearly polarized light from the same viewing chord is simultaneously measurable. In addition to that, the angle of the axes of the linearly polarized light with respect to the equatorial plane can be changed by rotating the polarimeter.

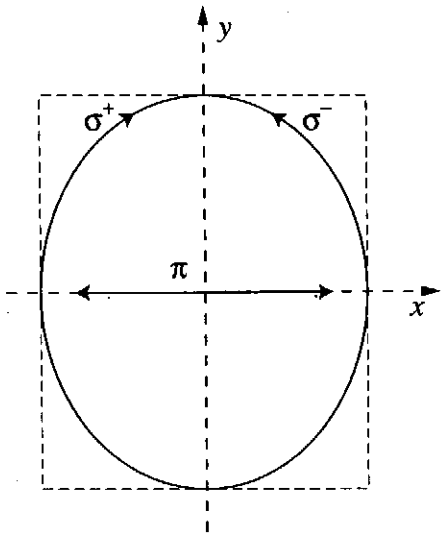

Figure 2: Expected polarization ellipses for the π and two σ lights.

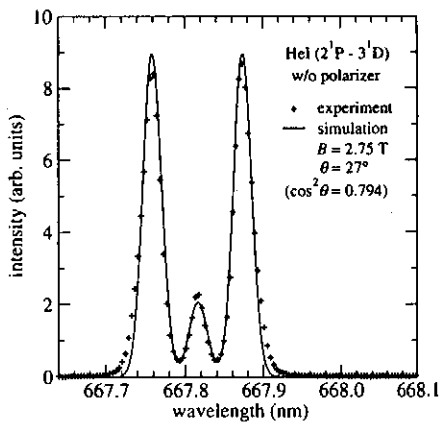

Figure 3: Observed profile of the HeI λ 667.8 nm line. Expected profile based on the polarization ellipses in Fig. 2 is also shown.

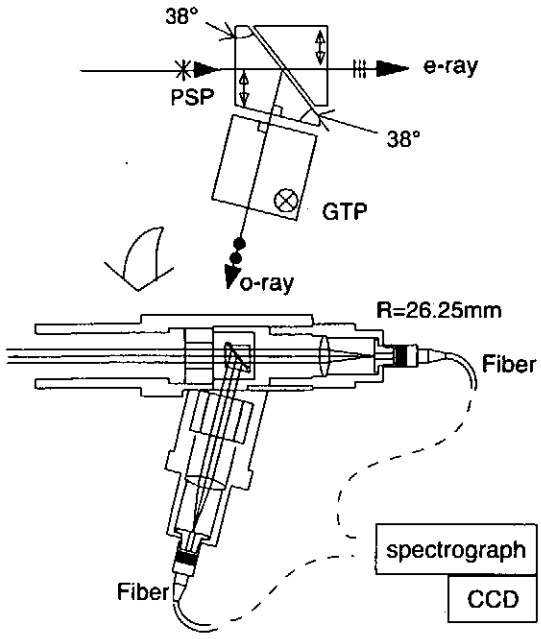

Figure 4: Optical system used for the present measurement. The axes of the linearly polarized lights to be measured can be arbitrarily determined.

3 Results

We have tried a measurement of the same emission line through a polarimeter in Fig. 4. When the two orthogonal axes of the polarimeter are aligned in the horizontal (x) and vertical (y) directions, respectively, the expected spectra are shown in Fig. 5 which is based on the polarization ellipses in Fig. 2. The x component of the π light is denoted as π_x and similarly for others in the following.

From the polarization ellipses in Fig. 2 the π light is expected to appear only in the x component. As for the σ lights the x component should be a little weaker than the y component because the line of sight has a finite angle with the magnetic field direction on the horizontal plane. What should be noted here is that there is no reason which gives rise to differences between σ^+ and σ^- lights.

The results of an actual observation, however, contradict our expectation. They are shown in Fig. 6. In the x component, the intensity of σ_x^- is higher than that of σ_x^+ and vice versa in the y component. The intensities in the x and y components in Fig. 6 can be directly compared because the relative sensitivity including the transmittance of the polarimeter is calibrated. The calibration is carried out as follows. As shown in Fig. 3, σ^+ and σ^- show equal intensities without the polarimeter. This means the summation of σ_x^+ and σ_y^+ is equal to that of σ_x^- and σ_y^-. This is written as

$$I(\sigma_x^+) + \frac{I(\sigma_y^+)}{\alpha} = I(\sigma_x^-) + \frac{I(\sigma_y^-)}{\alpha}, \tag{1}$$

where $I(\sigma_x^+)$ and others stands for the observed intensities of the respective line components, and α is the relative sensitivity of the y to x components. The coefficient α is then obtained as

$$\alpha = \frac{I(\sigma_y^-) - I(\sigma_y^+)}{I(\sigma_x^+) - I(\sigma_x^-)}. \tag{2}$$

As for π light, the x component predominates over the y component in the actual observation, and this seems reasonable here. More detailed analysis about the π component is carried out later.

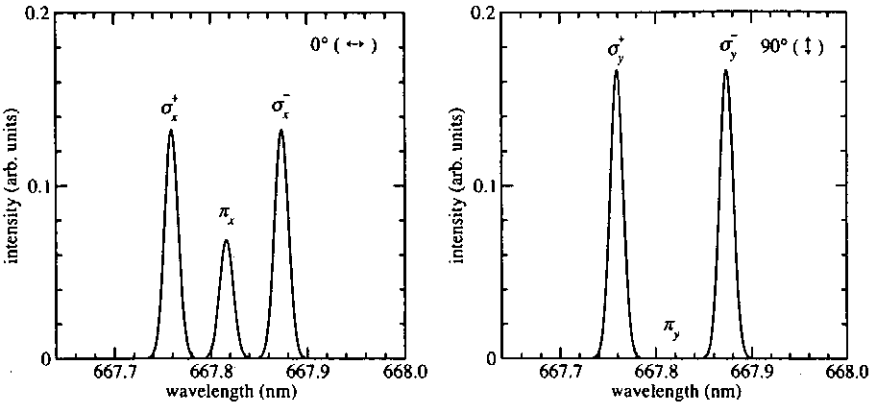

Figure 5: Expected spectra of HeI λ 667.8 nm from the polarization ellipses in Fig. 2 when the axes of the polarimeter is aligned in the horizontal (x) and vertical (y) directions, respectively.

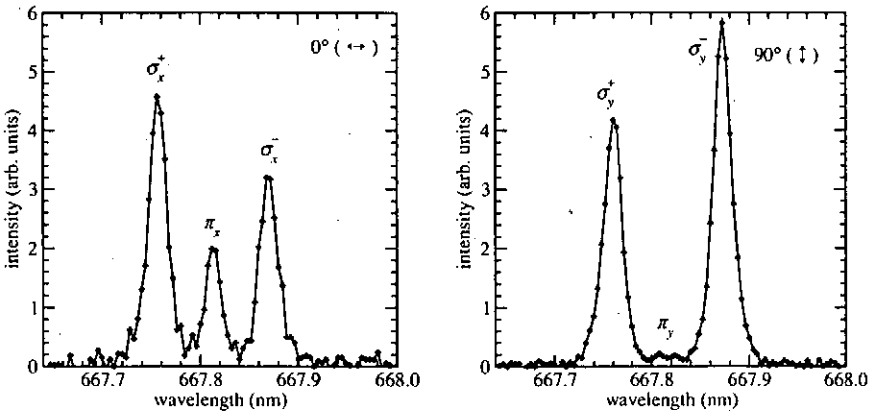

Figure 6: Observed HeI λ 667.8 nm line with the polarimeter, the polarization axes of which are aligned in the horizontal (x) and vertical (y) directions, respectively.

Then we consider the meaning of these asymmetric σ intensities. For this purpose, the polarization ellipses are also helpful. For each of the ellipses, a unique envelope rectangle

is drawn, the sides of which are parallel to either the x or y axis. The different σ intensities in the x component indicate that the length of the envelope rectangle in the x axis direction is different between for σ^+ and σ^- lights. The different y component intensities can be considered similarly. These results indicate that the two polarization ellipses, which correspond to σ^+ and σ^-, respectively, have different shapes as schematically shown in Fig. 7, though they are not yet uniquely determined at this moment. The ellipses drawn in Fig. 7 are only examples.

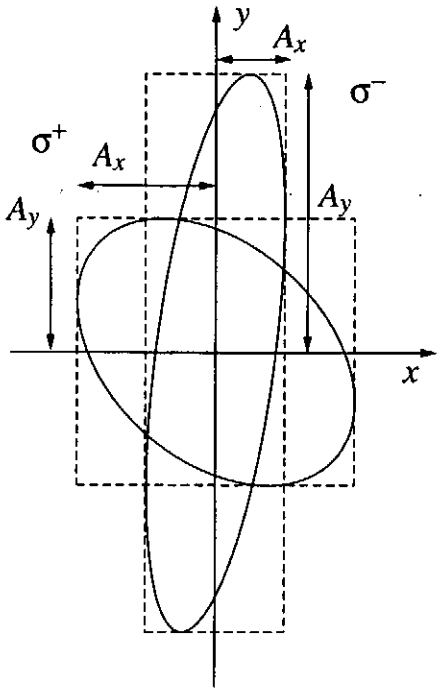

Figure 7: Relations between the observed line intensities and the polarization ellipses or the envelope rectangles when the axes of the polarimeter are aligned in the x and y directions. This figure is only for an explanation and the real observation results are not reflect on it.

In order to identify the polarization ellipses, we have rotated the polarizer 45 degrees and measured the same emission line. If the true polarization ellipses are the ones in Fig. 2, the ξ and η components should be identical as shown in Fig. 8. Figure 9 shows the result of an actual observation. In this case the intensities of the σ^+ and σ^- lights are almost the same in both of the ξ and η components. Therefore we denote their intensity just as $I(\sigma_\xi)$ or $I(\sigma_\eta)$ here.

The results in Fig. 9 are also relatively calibrated. However, a similar calibration method as in the previous case is unavailable because the two σ components have the same intensity. Instead we give attention to the intensity ratio of the σ to π lights. It is readily noticed that the ratio is different between in the ξ and η components. Since the

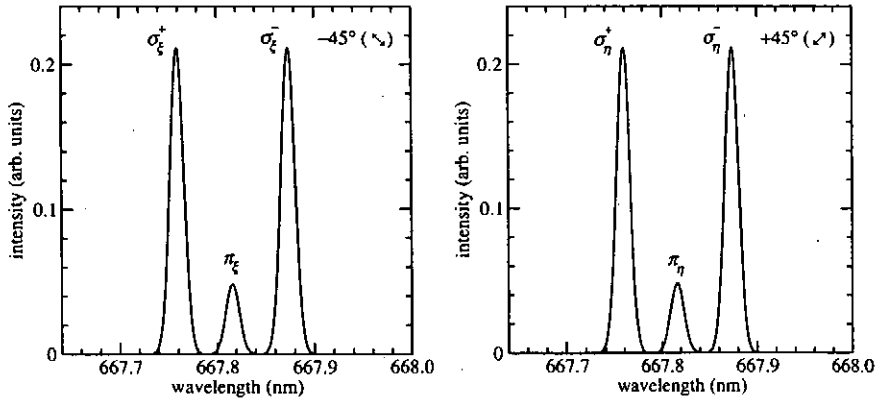

Figure 8: Expected spectra of HeI λ 667.8 nm from the polarization ellipses in Fig. 2 when the axes of the polarimeter is aligned in the −45 degrees (ξ) and +45 degrees (η) directions, respectively.

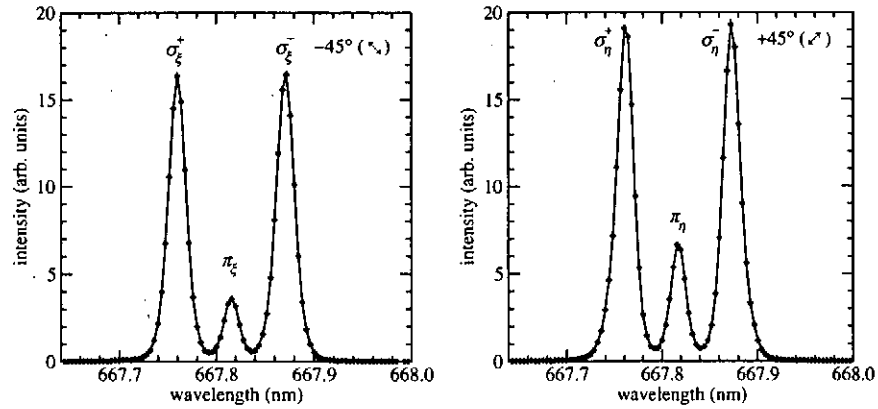

Figure 9: Observed HeI λ 667.8 nm line with the polarimeter, the polarization axes of which are aligned in the −45 degrees (ξ) and +45 degrees (η) directions, respectively.

ratio of the summation of true intensities should be equal to that of Fig. 3, the following equation must hold true,

$$\frac{I(\pi_\xi) + I(\pi_\eta)/\beta}{I(\sigma_\xi) + I(\sigma_\eta)/\beta} = \frac{I(\pi)}{I(\sigma)}, \tag{3}$$

where β is the relative sensitivity of the η to ξ components. The ratio $I(\pi)/I(\sigma)$ is the value without polarimeter. The sensitivity β is obtained as

$$\beta = \frac{I(\pi_\eta) - \frac{I(\pi)}{I(\sigma)} I(\sigma_\eta)}{\frac{I(\pi)}{I(\sigma)} I(\sigma_\xi) - I(\pi_\xi)}. \tag{4}$$

Though the two σ lights have equal intensities respectively in the ξ and η components, $I(\sigma_\xi)$ and $I(\sigma_\eta)$ are different. This contradicts our expectation. $I(\pi_\xi)$ and $I(\pi_\eta)$ are also different and it is confirmed that the polarization condition of the π light is also different from our expectation.

We again try to understand these results with the help of polarization ellipses. Here, the intensities of the two σ lights in the ξ component are identical. This indicates that the length of the envelope rectangle in the ξ axis direction of the two σ lights is the same. η components can be understood similarly. That is to say the two envelope rectangles corresponding to the two σ lights coincide with each other. The situation is schematically drawn in Fig. 10. The ellipses drawn in the figure are, however, again just examples and they are not uniquely determined yet.

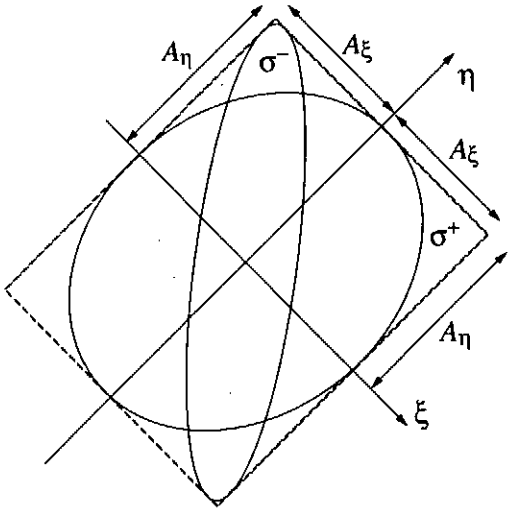

Figure 10: Similar to Fig. 7 but when the axes of the polarimeter is aligned in the ξ and η directions.

So far, for each of the π and two σ lights the shapes of two envelope rectangles for which the axes are rotated 45 degrees from each other, are determined. The relative intensity or the relative scale of the rectangles between in the x-y and ξ-η coordinates is,

however, not determined. Since both the measurements are carried out for different discharges, they cannot be compared directly. We normalize them with the total intensity for the moment and this presumes that the relative sensitivity of the system has no dependence on the rotation angle of the polarimeter. The normalization factor γ is therefore derived from a relation

$$I(\sigma_x^+) + I(\sigma_y^+) = \gamma[I(\sigma_\xi^+) + I(\sigma_\eta^+)]. \tag{5}$$

Finally, the two envelope rectangles for each of the π and two σ lights are completely determined.

The polarization ellipse which simultaneously correspond to the two envelope rectangles uniquely exists and it is determined as follows. Any elliptically polarized light is mathematically expressed in the x-y coordinate as

$$x = A_x \cos(\omega) \tag{6}$$

$$y = A_y \sin(\omega + \Delta). \tag{7}$$

Here, A_x or A_y is the the electric field amplitude of the light in the axis denoted by the subscript. The square of this value corresponds to the observed intensity. The relative phase difference Δ is the only unknown quantity in the expression at this moment and is derived as follows. The ξ component of the same light is expressed as

$$\xi = \frac{\sqrt{2}}{2}\left\{A_x \cos(\omega) + A_y \sin(\omega + \Delta)\right\} \tag{8}$$

$$\equiv A_\xi K \sin(\omega + \phi), \tag{9}$$

with

$$A_\xi = \frac{\sqrt{2}}{2}\sqrt{\left\{A_x + A_y \sin(\Delta)\right\}^2 + \left\{A_y \cos(\Delta)\right\}^2}, \tag{10}$$

and

$$\tan\phi = \frac{A_x + A_y \sin(\Delta)}{A_y \cos(\Delta)}. \tag{11}$$

From eq. (10)

$$\sin(\Delta) = \frac{A_\xi^2 - A_\eta^2}{2A_xA_y} \tag{12}$$

is obtained where

$$A_x^2 + A_y^2 = A_\xi^2 + A_\eta^2 \tag{13}$$

is used. There are two candidates for Δ even if the range is subtended from 0 to 2π. They correspond to the right-handed and left-handed elliptically polarized lights and hence the shape is at least uniquely determined. The polarization ellipses for the π and two σ lights which are determined similarly are shown in Fig. 11.

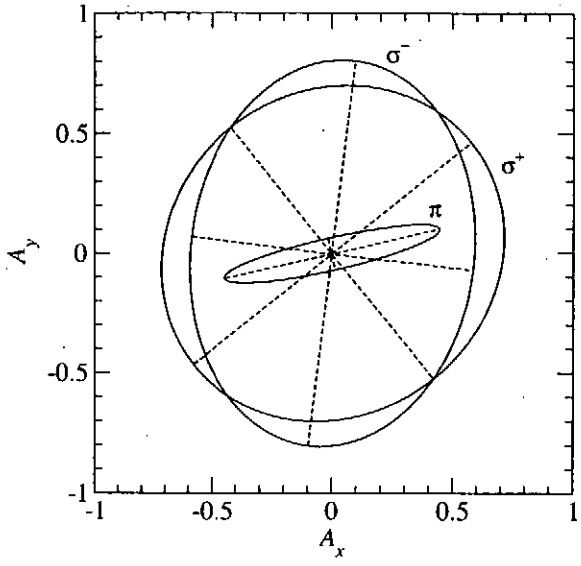

Figure 11: Polarization ellipses for the observed π and two σ lights.

4 Discussion

In the previous section we have shown how to determine the polarization ellipse of the observed light. However, it has not been confirmed whether the light is intrinsically distorted when it is emitted or the emitted light is somehow distorted in the medium. It is generally difficult to intuitively understand the transformation of polarization ellipses, and we usually resort to matrix theories such as Jones and Muller calculi [1], under which a polarization state and an affection to it are expressed as a vector and a matrix, respectively. Though in principle the operator matrix can be determined by observing a required number of transformations for different polarization states, our data is not enough for that purpose. Instead, we guess the reason of the distortion through some characteristics of the phenomena.

First, the same observation is attempted for a discharge with a reversed magnetic field, which means that the filed direction is reversed while other characteristics like the strength are intact. The result is shown in Fig. 12. As compared with Fig. 5, the normal field direction case, it is readily noticed that the asymmetry of the σ^+ and σ^- light intensities is reversed. Under the normal direction field, σ^+ and σ^- lights correspond to the right-handed and left-handed polarized lights from the observer, respectively. When the field direction is reversed, these relations are also reversed. This result implies that the observed distortion of the polarization is not an intrinsic effect on the atomic emission itself but an effect on the emitted light.

Other emission lines are also observed. Figure 13 shows the results for the Zeeman profile of the CIII 3^3S–3^3P lines. Here also shown are the expected profiles under an assumption that the same effect as on the neutral helium case works on this case. The

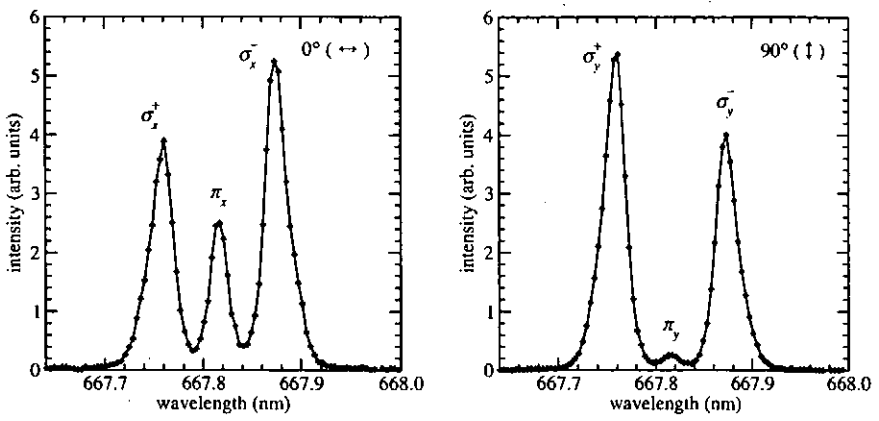

Figure 12: Similar to Fig. 6 but for a discharge of reversed magnetic field.

effect of the magnetic field, however, is not be expressed as a linear effect such as the normal or anomalous Zeeman effect. We have instead solved a problem of general cases of the Zeeman effect and have calculated all the transition components between the magnetic sublevels. We have finally had a good agreement with the experiment as seen in Fig. 13. A similar observation and simulation are carried out for the CII $2s2p(^3P^o)3s^4P^o$–$2s2p(^3P^o)3p^4P$ lines. The results are shown in Fig. 14 and a good agreement between the experiment and simulation is again obtained. It is inferred from these results that the effect on the polarization state depends on neither the angular momentum states of the energy levels nor the wavelength of the observed emission line, and this make certain our provisional conclusion that the effect works on the emitted light.

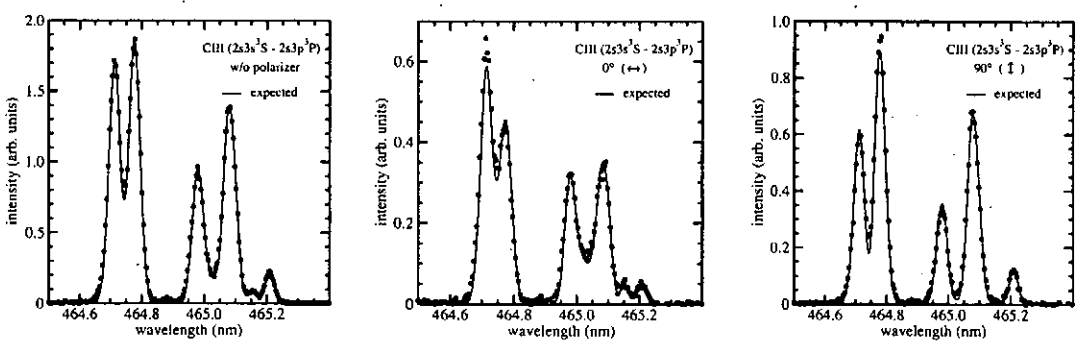

Figure 13: Spectra of the CIII 3^3S–3^3P lines measured with the polarimeter. Synthetic Zeeman spectra with B = 2.75 T and based on the same polarization states as the helium line are also shown.

Finally, the dependence of the effect on the magnetic field strength is investigated. Figure 15 shows the observed y-axis component of the Balmer-α line of neutral hydrogen for three different B_{ax} discharges and no B_{ax}-dependence is observed.

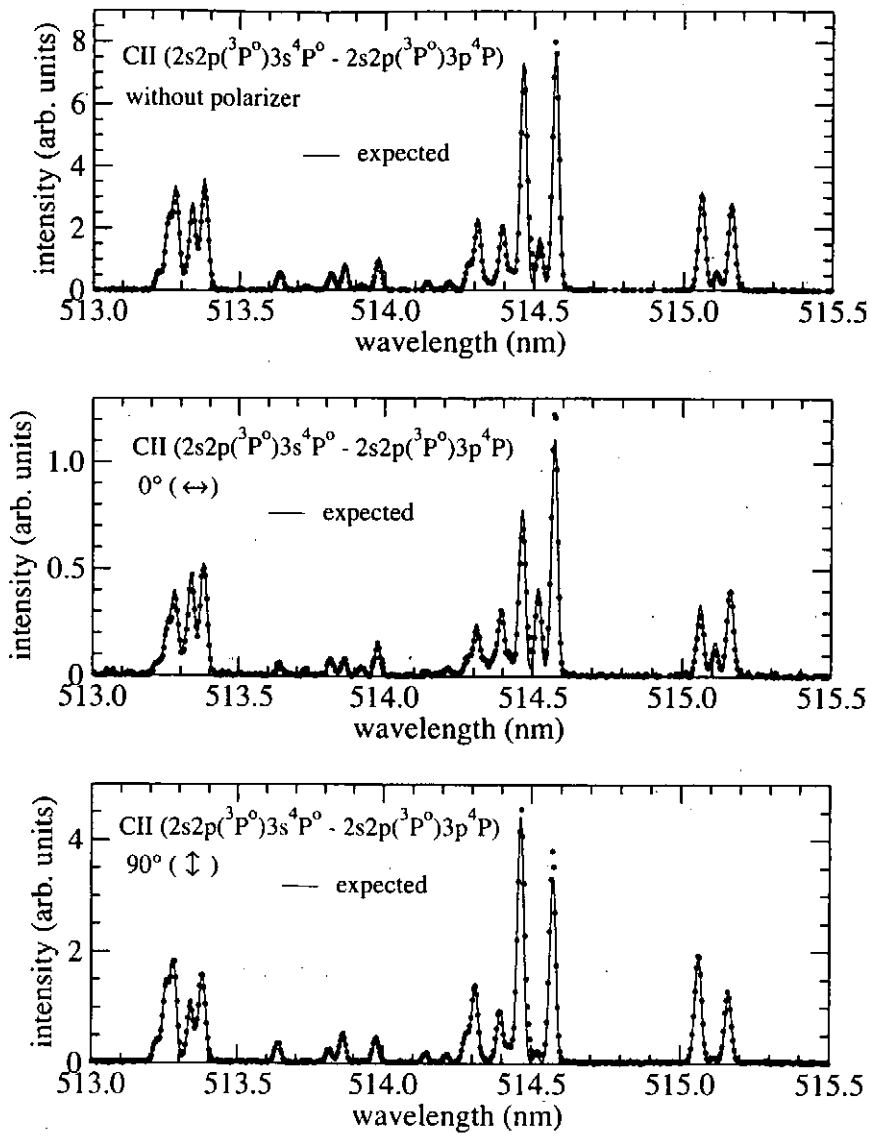

Figure 14: Similar to Fig. 13 but for the CII $2s2p(^3P^o)3s^4P^o$–$2s2p(^3P^o)3p^4P$ lines.

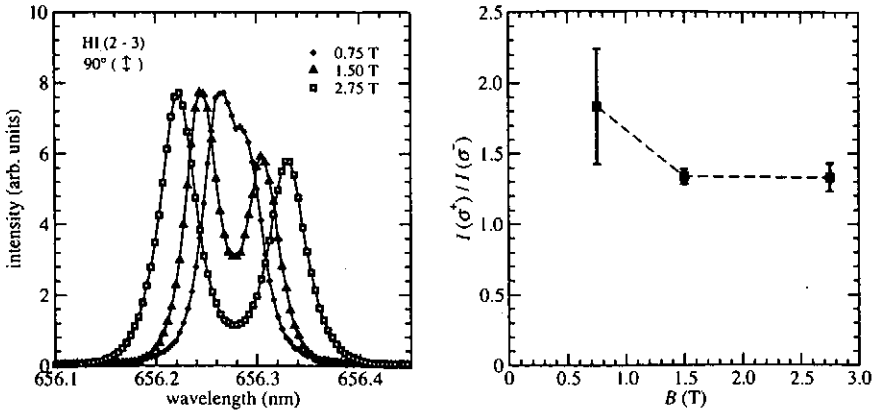

Figure 15: Dependence on the magnetic field of (a) the hydrogen Balmer-α line profile and (b) the intensity ratio of two σ lights.

The comprehensive understanding of the effect from these evidences is that the effect has nothing to do with the plasma and the magnetic field and might be appeared by the photoelasticity of the optical window.

References

[1] D. S. Kliger, J. W. Lewis, and C. E. Randall, *Polarized Light in Optics and Spectroscopy* (Academic Press, Inc., San Diego, 1990).

[2] M. Goto, S. Morita, *et al.*, Phys. Plasmas **9**, 4316 (2002).

Polarization measurement of Iron L-shell lines on EBIT-I

Hui Chen, Peter Beiersdorfer
Lawrence Livermore National Laboratory, Livermore, CA 94551
Darron Robbins, A.J. Smith
Department of Physics, Morehouse College, Atlanta, GA 30314
Ming Feng Gu
Department of Physics, Stanford University, CA94305

Abstract

We report measurements of the line polarization of Ne-like and F-like of iron n=3 to n=2 transitions in the x-ray region. We used the "two-crystal technique" developed in previous polarization measurements in our laboratory. Preliminary results from our measurements are presented together with the theoretical calculations using the Flexible Atomic Code (FAC). Our calculations show that contributions from cascades play an important role in the polarization calculations of most of the transitions. The uncertainties and difficulties of our experiments are also discussed.

1. Introduction

Fe L-shell polarizations are important to laboratory studies relevant to astrophysics. Polarization processes have been demonstrated [1] to affect the emissions of many astrophysical sources. Another aspect of the relevance of polarization studies to astrophysics is based on the fact that polarizations can change the emission intensity, and therefore it has to be properly taken into account before one can extract other information from the emission. A good example is the Fe XVII line emission studies. Fe XVII lines have been observed in the Sun as well as in numerous cosmic sources studied with the Chandra and XMM-Newton observatories. Applications of these lines include using them as diagnostics for the source parameters. A laboratory measurement of the ratios of the 3s-2p to 3d-2p lines reported by Laming et al. [2] used the NIST electron beam ion trap and determined that the ratio 3s-2p and 3d-2p line intensities differed by nearly a factor of 2 from the same ratio measured from the Sun and Capella. Their results would have had far-reaching consequences for solar and astrophysics. However, another measurement from the Livermore EBIT group [3] strongly disagrees with the NIST measurements. The difference of the two measurements is as large as a factor of 2 at some data points. Careful calculations show good agreement with the later measurements. One of the many factors that resulted in the flawed results from the former measurement was later attributed to their neglect of polarization correction to the EBIT line emission.

In this report, we made use of the fact that the line emission from the EBIT source is polarized and measured the polarization of the Ne-like and F-like Fe lines that are of particular interests to astrophysics. This study is a part of the laboratory atomic database we are building. Related work includes the comprehensive Fe L-shell 3-2 line emission measurements that were completed a few years ago [4,5]. As will be shown in this report, these line measurements are the foundations of present measurements.

2. Experimental technique and instrumental setup

A number of previous polarization studies made on Livermore EBIT have established the "two crystal technique", which literally means that two crystal spectrometers are used for the experiment. The details of these techniques have been described elsewhere [6-8]. The equations for in this technique have been explained in detail by Beiersdorfer et al. [8]. The essence of this technique is summarized as the following.

For each line intensity dispersed by the crystal, we have $I_{meas.}=I_{//}R_{//} + I_{\perp}R_{\perp}$, R is the reflectivity of crystals. Line polarization is defined as $P = (I_{//} - I_{\perp})/(I_{//} + I_{\perp})$.

$$\left(\frac{I^a}{I^b}\right)_G = \frac{I^a_{//} + R_1 I^a_{\perp}}{I^b_{//} + R_1 I^b_{\perp}} = \frac{I^a_{//} + I^a_{\perp}}{I^b_{//} + I^b_{\perp}},$$
$$\left(\frac{I^a}{I^b}\right)_{Xtal} = \frac{I^a_{//} + R_2 I^a_{\perp}}{I^b_{//} + R_2 I^b_{\perp}} \qquad (1)$$

If one has line b as a reference line, and the P_b is known, assuming $R= R_{\perp}/ R_{//}$ is constant for the lines *a* and *b*, then we can derive the polarization for line *a* as:

$$P_a = \frac{\left(\frac{I^a}{I^b}\right)_G \left(1 + R_1 \frac{1-P_b}{1+P_b}\right)(R_2+1) - \left(\frac{I^a}{I^b}\right)_{Xtal} \left(1 + R_2 \frac{1-P_b}{1+P_b}\right)(R_1+1)}{\left(\frac{I^a}{I^b}\right)_G \left(1 + R_1 \frac{1-P_b}{1+P_b}\right)(R_2-1) - \left(\frac{I^a}{I^b}\right)_{Xtal} \left(1 + R_2 \frac{1-P_b}{1+P_b}\right)(R_1-1)} \qquad (2)$$

Replacing one crystal spectrometer with a grating spectrometer, we have $R_{//} = R_{\perp} = 1$ for the grating measured intensity in Eq. (2).

The setup of the spectrometers on EBIT-I is shown in Fig 1. A flat field crystal spectrometer [9] was used. The crystal was RAP (2d=26.1Å). The grating spectrometer uses a 44.3m grazing-incidence grating which has variable line spacing of about 2400 l/mm. It features with high resolving power and larger wavelength coverage (10 - 50 Å). It used a liquid nitrogen cooled back- illuminated CCD as detector.

Our data was all taken in steady state. The electron beam energies were set so that we can maximize the population of the desired charge states. This is illustrated in Fig.2. At the beam energy of 1.3 keV, the Ne-like Fe ions are dominant, as shown by the strong Ne-like lines, compared to the spectrum at 1.4 keV where the F-like lines are very strong. At 1.5 keV, Ne-like lines have almost vanished while F-like and O-like lines take the stage. In addition to the feature of "charge state selectiveness", by applying different beam energy, one can actually "select" emission processes, such as minimizing emission from resonance excitations or dielectronic recombinations. These two "selective" features made EBIT an ideal device to quantitatively measure atomic data including the line polarization.

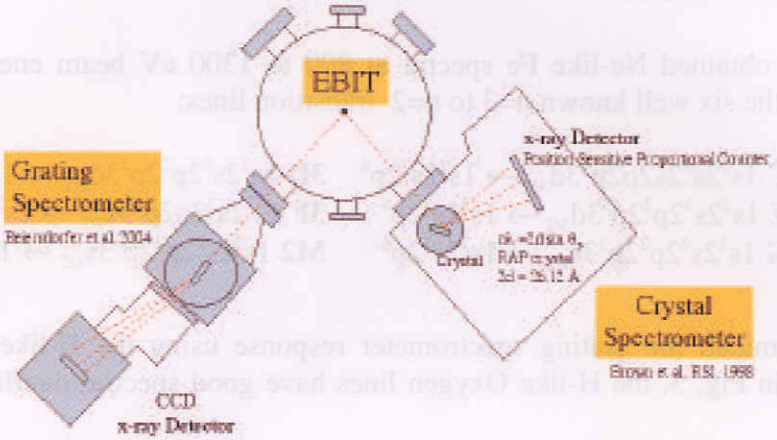

Figure 1: Diagram of the experimental setup.

In our experiment, the Ne-like Fe spectral data were taken at beam energies at 850 to 1400 eV. The F-like Fe data were taken at 1300 to1500 eV. The grating spectrometer covered the interested spectral range of 13-18Å, while we needed two crystal settings to cover the same wavelength interval.

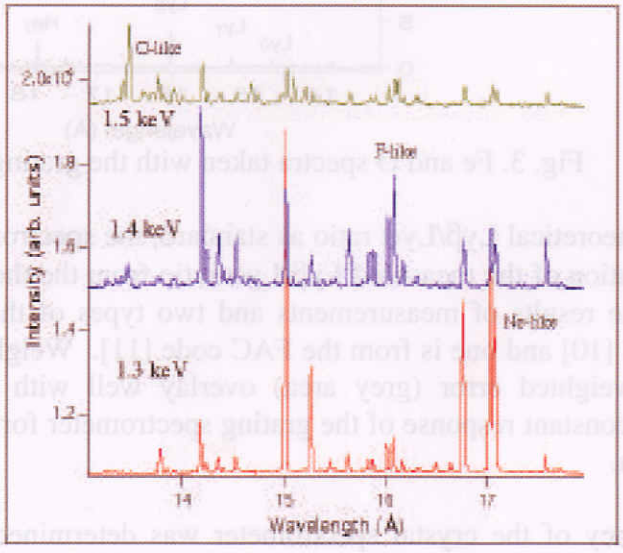

Figure 2. Fe spectra at three electron beam energies.

3. Experimental results and discussion

3.1.Ne-like Fe

We have obtained Ne-like Fe spectra at 800 to 1300 eV beam energies in the region covering the six well known n=3 to n=2 transition lines:

3C $1s^22s^22s2p2p^43d_{3/2} \rightarrow 1s^22s^22p^6$ **3D** $1s^22s^22p^22p^33d_{5/2} \rightarrow 1s^22s^22p^6$
3E $1s^22s^22p^22p^33d_{3/2} \rightarrow 1s^22s^22p^6$ **3F** $1s^22s^22p2p^43s_{1/2} \rightarrow 1s^22s^22p^6$
3G $1s^22s^22p^22p^33s_{1/2} \rightarrow 1s^22s^22p^6$ **M2** $1s^22s^22p^22p^33s_{1/2} \rightarrow 1s^22s^22p^6$

We determined the grating spectrometer response using the H-like Oxygen lines. As showing in Fig. 3, the H-like Oxygen lines have good spectral overlap with the Ne-like Fe lines.

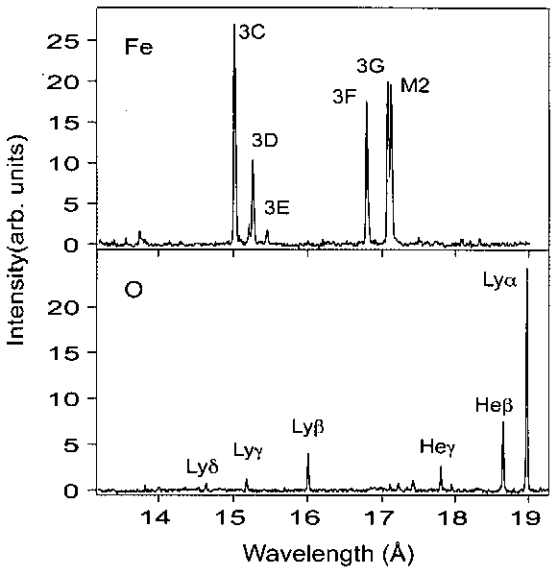

Fig. 3. Fe and O spectra taken with the grating spectrometer

Using the theoretical Lyβ/Lyα ratio as standard, the spectrometer response is determined by the deviation of the measured Lyβ/Lyα ratio from the theoretical calculations. Figure 4. shows the results of measurements and two types of theoretical calculations, one is from APEC [10] and one is from the FAC code [11]. Weighted measurements (thin blue line) and weighted error (grey area) overlay well with the FAC calculations. This indicates a constant response of the grating spectrometer for the wavelength range we are interested in.

The efficiency of the crystal spectrometer was determined by taking into account the window foils and the absorption of the detector. The result is given in Fig. 5. These response functions were then folded in the measured line intensities during analysis.

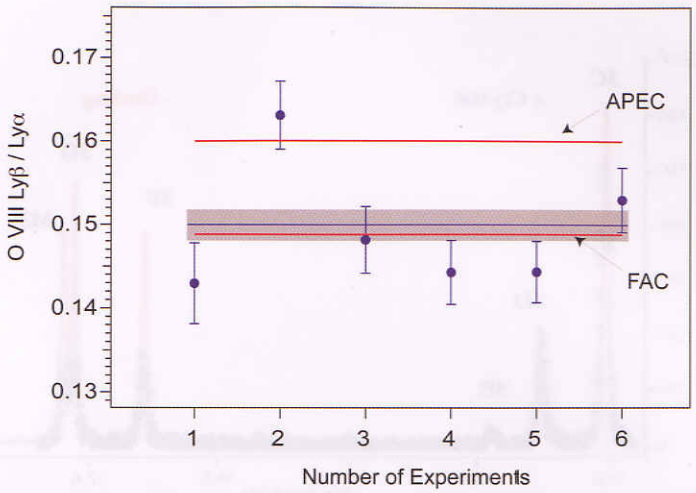

Figure 4. OVIII Lyβ/Lyα ratios from the grating spectrometer measurements (dots with error bars) and model calculations (red lines each from FAC and APEC).

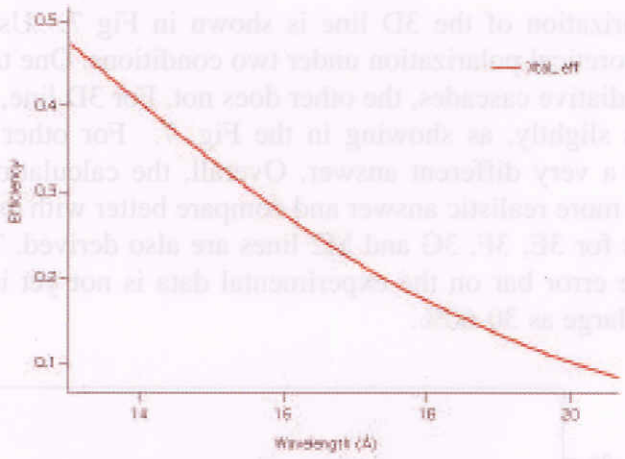

Figure 5. The efficiency of the crystal spectrometer in the wavelength range of interest.

We used the 3C line as reference/normalization P_{3C}=0.4. Figure 6 shows the overlap of two spectra taken with the grating and crystal spectrometers. It is from the difference of the line ratios of the two spectrometers that the polarization was determined, as described by equation (1) and (2).

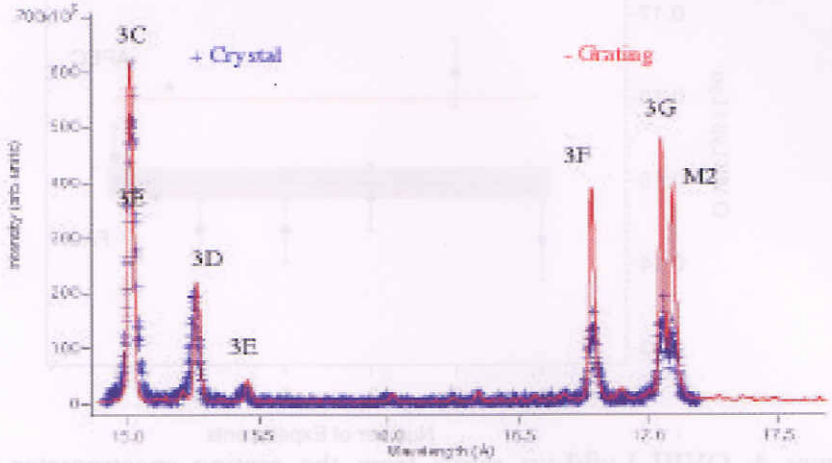

Figure 6. Ne-like Fe spectra from the grating spectrometer and from the crystal spectrometer.

The derived polarization of the 3D line is shown in Fig 7. Using the FAC code, we calculated the theoretical polarization under two conditions. One takes into account of the contribution of radiative cascades, the other does not. For 3D line, the prediction from the two cases differs slightly, as showing in the Fig. 7. For other Ne-like lines, the two calculations give a very different answer. Overall, the calculations taking the cascades into account give more realistic answer and compare better with experiments.
The Polarizations for 3E, 3F, 3G and M2 lines are also derived. The results are listed in Table 1 Ð 4. The error bar on the experimental data is not yet in its final form, but we expect it to be as large as 30-60%.

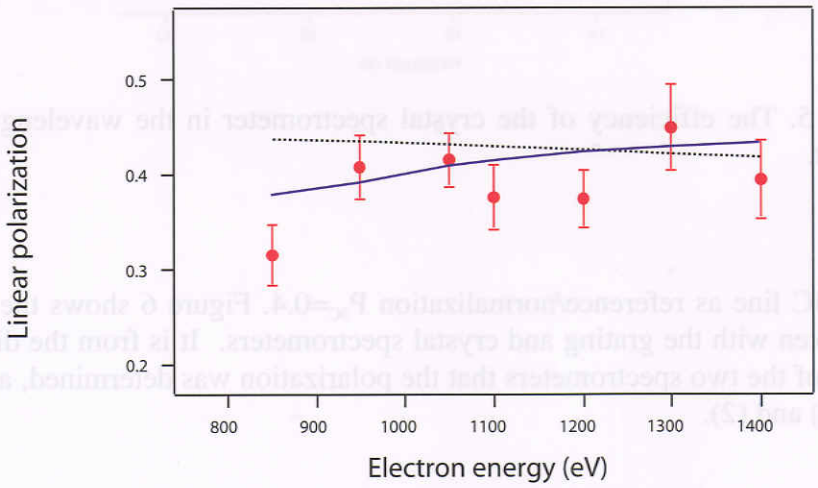

Figure 7. Comparison of the polarization of 3D from measurements (dots with error bars) and FAC calculations with the contributions from cascades taken into account (solid line) and not taken into account (dotted line).

Table 1: Polarization measurement and calculations for 3E line.

Energy (eV)	Polarization	FAC (cascades)	FAC (no cascades)
850	-0.37	-0.39	-0.19
950	-0.20	-0.34	-0.17
1050	-0.40	-0.33	-0.14
1100	-0.21	-0.32	-0.13
1200	-0.39	-0.29	-0.10

Table 2: Polarization measurement and calculations for 3F line.

Energy (eV)	Polarization	FAC (cascades)	FAC (no cascades)
850	-0.10(0.03)	0.067	0.57
950	-0.13(0.04)	0.068	0.56
1050	-0.17(0.03)	0.071	0.56
1100	-0.10(0.04)	0.072	0.56
1200	-0.12(0.03)	0.074	0.55
1300	-0.24(0.05)	0.076	0.55
1400	-0.34(0.05)	0.078	0.54

Table 3: Polarization measurement and calculations for 3G line.

Energy (eV)	Polarization	FAC (cascades)	FAC (no cascades)
850	-0.22	0.052	0.58
950	-0.18	0.051	0.57
1050	-0.22	0.056	0.57
1100	-0.19	0.058	0.56
1200	-0.27	0.061	0.56
1300	-0.30	0.065	0.55

Table 4: Polarization measurement and calculations for M2 line.

Energy (eV)	Polarization	FAC (cascades)	FAC (no cascades)
850	-0.23	-0.10	-0.24
950	-0.22	-0.13	-0.24
1050	-0.22	-0.12	-0.23
1100	-0.25	-0.12	-0.23
1200	-0.21	-0.12	-0.23
1300	-0.31	-0.11	-0.22

3.2 F-like Fe lines

F-like 3-2 Fe spectra are much more complicated. They contain many more lines in the wavelength region of 14 Å – 18 Å. Fig.8 shows three F-like Fe spectra taken with the grating and crystal spectrometers at the electron energy of 1.35 keV. The F-like Fe lines have all been identified previously [5]. The lines and their corresponding transitions are listed in Table 5.

Applying the same technique as described earlier, we have some preliminary line polarization results for some of the strong lines. Since this analysis is not yet complete, we cannot draw concrete conclusions. So far we found that the polarization analysis is very sensitive to the variation of the line intensities, and small errors in the line intensity fitting could result in amplified error in the polarization values. Also, the derived polarization appeared to be quite different if we use lines from different charge states as normalization. As an illustration, Fig. 8 shows our preliminary results for line F11. Several other F-like Fe lines seem to have a similar pattern as F11. This could due to some artifacts of our analysis, or could be caused by some new physics that is unknown to us. We are going to further investigate this issue, for which both further analysis and new experiments will be needed.

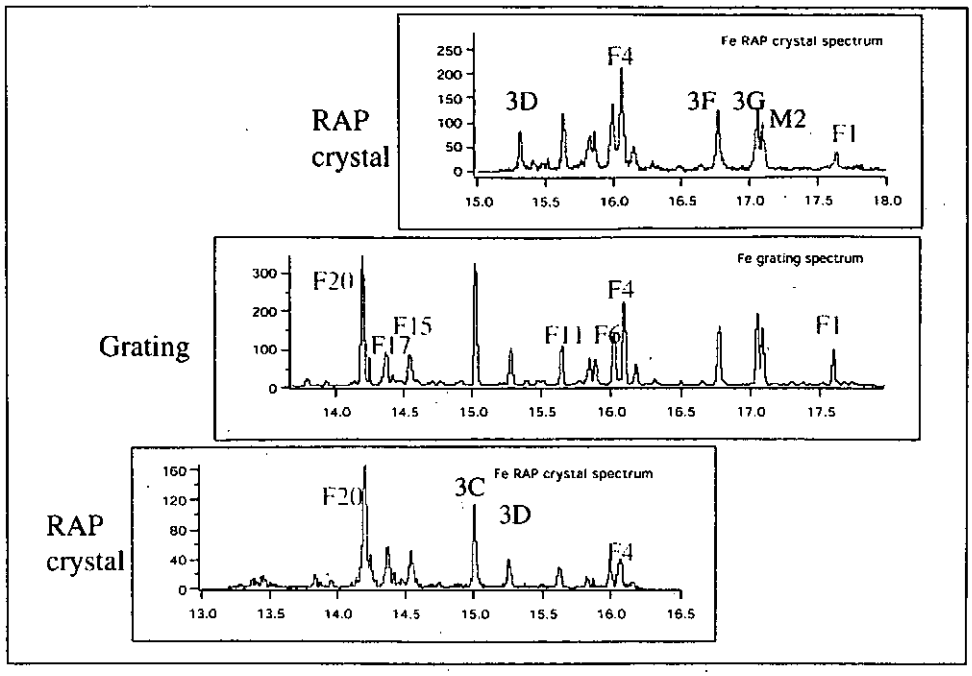

Figure 8. Fe spectra at the electron beam energy of 1.35 keV. Strong lines are marked and the labels of the F-like lines use the line labels of Brown et al.

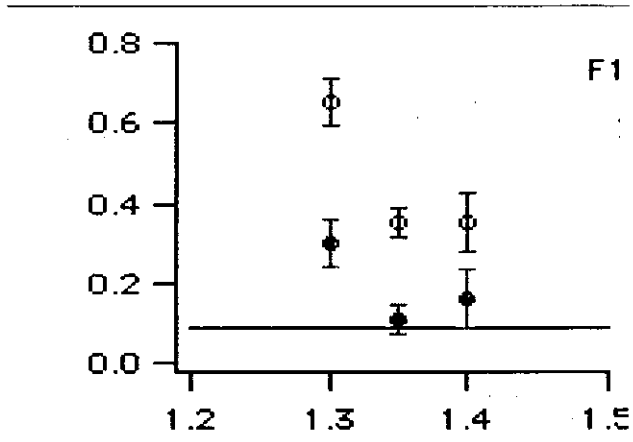

Figure 9. Polarization of the F1 line from analysis using line 3G as normalization (circles with error bar) and using line F4 as normalization (dots with error bar). The FAC calculation is shown in solid line.

In conclusion, using the "two-crystal technique", we measured the polarization of Ne-like and F-like Fe lines using the Livermore EBIT. We have achieved good Ne-like Fe measurements. The F-like Fe analysis did not yet give a consistent picture; we hope further experiments will be performed to shine more light on these puzzling results.

Table 5: F-like Fe line indentifications

Label	Upper	J	Lower	J	λ(Å)
F1[d]	$1s^2 2s^2 2p_{1/2} 2p^3_{3/2} 3p_{1/2}$	$\frac{3}{2}$	$1s^2 2s_{1/2} 2p^2 2p^4$	$\frac{1}{2}$	17.664
F2	$1s^2 2s_{1/2} 2p^2 2p^3_{3/2} 3s$	$\frac{1}{2}$	$1s^2 2s_{1/2} 2p^2 2p^4$	$\frac{1}{2}$	16.345
F3	$1s^2 2s_{1/2} 2p_{1/2} 2p^4 3s$	$\frac{1}{2}$	$1s^2 2s_{1/2} 2p^2 2p^4$	$\frac{1}{2}$	16.197
F4	$1s^2 2s^2 2p^2 2p^2_{3/2} 3s$	$\frac{5}{2}$	$1s^2 2s^2 2p^2 2p^3_{3/2}$	$\frac{3}{2}$	16.097
F5	$1s^2 2s^2 2p_{1/2} 2p^3_{3/2} 3s$	$\frac{1}{2}$	$1s^2 2s^2 2p_{1/2} 2p^4$	$\frac{1}{2}$	16.044
F6	$1s^2 2s^2 2p^2 2p^2_{3/2} 3s$	$\frac{3}{2}$	$1s^2 2s^2 2p^2 2p^3_{3/2}$	$\frac{3}{2}$	16.023
F7	$1s^2 2s^2 2p^2 2p^2_{3/2} 3s$	$\frac{1}{2}$	$1s^2 2s^2 2p^2 2p^3_{3/2}$	$\frac{3}{2}$	15.901
F8	$1s^2 2s^2 2p_{1/2} 2p^3_{3/2} 3s$	$\frac{1}{2}$	$1s^2 2s^2 2p_{1/2} 2p^4$	$\frac{1}{2}$	15.883
F9	$1s^2 2s^2 2p_{1/2} 2p^3_{3/2} 3s$	$\frac{3}{2}$	$1s^2 2s^2 2p^2 2p^3_{3/2}$	$\frac{3}{2}$	15.853
F10	$1s^2 2s^2 2p_{1/2} 2p^3_{3/2} 3s$	$\frac{1}{2}$	$1s^2 2s^2 2p^2 2p^3_{3/2}$	$\frac{1}{2}$	15.787
F11	$1s^2 2s^2 2p_{1/2} 2p^3_{3/2} 3s$	$\frac{5}{2}$	$1s^2 2s^2 2p^2 2p^3_{3/2}$	$\frac{3}{2}$	15.641
F12	$1s^2 2s_{1/2} 2p^2 2p^3_{3/2} 3s$	$\frac{3}{2}$	$1s^2 2s_{1/2} 2p^2 2p^4$	$\frac{1}{2}$	15.501
F13	$1s^2 2s^2 2p^2 2p^3_{3/2} 3d_{5/2}$	$\frac{1}{2}$	$1s^2 2s^2 2p^2 2p^3_{3/2}$	$\frac{3}{2}$	14.601
F14	$1s^2 2s^2 2p^2 2p^3_{3/2} 3d_{5/2}$	$\frac{1}{2}$	$1s^2 2s^2 2p^2 2p^3_{3/2}$	$\frac{3}{2}$	14.568
F15	$1s^2 2s^2 2p^2 2p^3_{3/2} 3d_{5/2}$	$\frac{5}{2}$	$1s^2 2s^2 2p^2 2p^3_{3/2}$	$\frac{3}{2}$	14.548
F16	$1s^2 2s^2 2p_{1/2} 2p^3_{3/2} 3d_{5/2}$	$\frac{3}{2}$	$1s^2 2s^2 2p_{1/2} 2p^4$	$\frac{1}{2}$	14.424
F17	$1s^2 2s^2 2p_{1/2} 2p^3_{3/2} 3d_{3/2}$	$\frac{5}{2}$	$1s^2 2s^2 2p^2 2p^3_{3/2}$	$\frac{3}{2}$	14.386
F18	$1s^2 2s^2 2p_{1/2} 2p^3_{3/2} 3d_{3/2}$	$\frac{1}{2}$	$1s^2 2s^2 2p_{1/2} 2p^4$	$\frac{1}{2}$	14.360
F19	$1s^2 2s^2 2p_{1/2} 2p^3_{3/2} 3d_{3/2}$	$\frac{1}{2}$	$1s^2 2s^2 2p^2 2p^3_{3/2}$	$\frac{3}{2}$	14.276
	$1s^2 2s^2 2p_{1/2} 2p^3_{3/2} 3d_{5/2}$	$\frac{5}{2}$	$1s^2 2s^2 2p^2 2p^3_{3/2}$	$\frac{3}{2}$	14.267
F20	$1s^2 2s^2 2p_{1/2} 2p^3_{3/2} 3d_{5/2}$	$\frac{3}{2}$	$1s^2 2s^2 2p^2 2p^3_{3/2}$	$\frac{3}{2}$	14.216
	$1s^2 2s^2 2p_{1/2} 2p^3_{3/2} 3d_{3/2}$	$\frac{5}{2}$	$1s^2 2s^2 2p^2 2p^3_{3/2}$	$\frac{3}{2}$	14.203

By Brown et al., Apj supp. 140, 589 (2002)

Reference

[1] Csanak, G., Review talk at this conference, (2004)
[2] Laming, J. M, et al, ApJ., 545, L161, (2000)
[3] Beiersdorfer, P. et al, ApJ, 576, L169, (2002)
[4] Brown, G, V., et al Apj, 502 1015 (1998)
[5] Brown, G.V, et al, ApJ. Sup. 140, 589, (2002)
[6] Wargelin, B. J., PhD thesis, University of California, Berkeley, (1993), UCRL-LR-115961
[7] Beiersdorfer et al. PRA, 53, 3974,(1996)
[8] Beiersdorfer, P., et al, PRA 60, 4156 (1999)
[9] Brown et at. RSI, 70, 280 (1999)
[10] APEC: Astrophysical plasma emission code
[11] Gu, M. F., ApJ, 582, 1241, 2003

X-Ray Line Polarization of the K-shell Resonance Line Emission of Heliumlike and Lithiumlike Sulfur at Relativistic Electron Impact Energies

D.L. Robbins[1], H. Chen[2], P. Beiersdorfer[2], A. Ya. Faenov[3], T.A. Pikuz[3], M.J. May[2], J. Dunn[2], K.J. Reed[2], and A.J. Smith[1]

[1]*Department of Physics, Morehouse College, Atlanta, GA 30314*

[2]*Lawrence Livermore National Laboratory, Livermore, CA 94550*

[3]*Multicharged Ions Spectra Data Center of VNIIFTRI, Mendeleevo, Moscow region, 141570 Russia*

Abstract

We have measured the polarization of the heliumlike sulfur resonance line 1s2p $^1P_1 \rightarrow 1s^2\ ^1S_0$, and of the blend of the lithiumlike sulfur resonance lines 1s2s2p $^2P_{3/2} \rightarrow 1s^22s\ ^2S_{1/2}$ and 1s2s2p $^2P_{1/2} \rightarrow 1s^22s\ ^2S_{1/2}$ as a function of electron beam energy from near threshold to 144 KeV. These lines were excited with the LLNL high-energy electron beam ion trap and measured using a newly modified two-crystal technique. Our results test polarization predictions in an energy regime where few empirical results have been reported. We also present calculations of the polarization using two different methods, and good agreement is obtained.

I. Introduction

Previous studies have highlighted the possibility of using polarization of x-ray line emissions as a plasma diagnostic tool to infer the presence of directional electrons [1,2]. This diagnostic has been successfully applied to the study of laser-produced plasmas [3], vacuum spark plasmas [4], and Z-pinches [5,6]. It also has been used to determine the electron cyclotron energy component of the electron beam in an electron beam ion trap [7]. Additional polarization affects on the K-shell line emission have also been predicted in laser-produced plasmas [8].

Theoretical studies of line polarization have been presented by Reed *et al.* [9], Itikawa *et al.* [10], Zhang *et al.* [11], and Inal *et al.* [1]. These predictions have been tested by various measurements. Henderson *et al.*, reported the first x-ray emission line polarization measurement of a highly charge ion, heliumlike Sc^{19+} [12]. Other reported polarization measurements include Fe^{23+}, Fe^{24+}, Ba^{46+}, Ti^{19+}, Ti^{20+}, and Ti^{21+} [13 - 20]. Polarization measurements of the K-shell x-ray emission lines of heliumlike ions were made near threshold of the corresponding resonance lines. The exception is He-like Fe^{24+} which was measured up to 120 KeV as reported in 1998 PPS workshop [18,19]. The polarization of the magnetic quadrupole transition in neonlike Ba^{46+} was measured at a variety of electron impact energies above the excitation threshold (but not at relativistic energies). Measurement of the polarization of the Lyman-α_1 line in hydrogenlike Ti^{21+}

was presented recently which extended well to electron impact energies of 50 KeV (10 threshold units). The results reported in reference [20], showed unexplained systematic discrepancy with the theoretical predictions. These results motivate further studies at high collision energies. In this paper we report the measurement of the polarization of both heliumlike and lithiumlike sulfur resonance lines as a function of electron impact energy up to ~ 60 threshold units. We also present calculations based on two different computer codes in this relativistic energy regime, which agree well with the measurements.

II. Experimental Measurement

The polarization measurements reported here were made using the Lawrence Livermore National Laboratory SuperEBIT electron beam ion trap [21,22]. The sulfur ions were electrostatically trapped and probed with a quasi mono-energetic electron beam ~60 μm in diameter. The electron beam was tuned to energies ranging from 3 KeV to 144 KeV for these measurements. Past measurements on the Livermore electron beam ion trap have used the "two-crystal technique" [13,14]. The main idea of this technique is to use two crystal spectrometers: one of them aligned at a Bragg angle near 45° and another one far from such an angle. Both crystal spectrometers employ a spectral dispersion plane perpendicular to the electron beam propagation. In a second approach, only one crystal spectrometer has a dispersion plane in the direction perpendicular to the electron beam propagation. The second spectrometer has a dispersion plane parallel to the electron beam propagation. Because of the extended x-ray source size in the direction parallel to the electron beam propagation (15-20 mm) it is necessary to use a focusing crystal spectrometer, as shown in Fig 1.

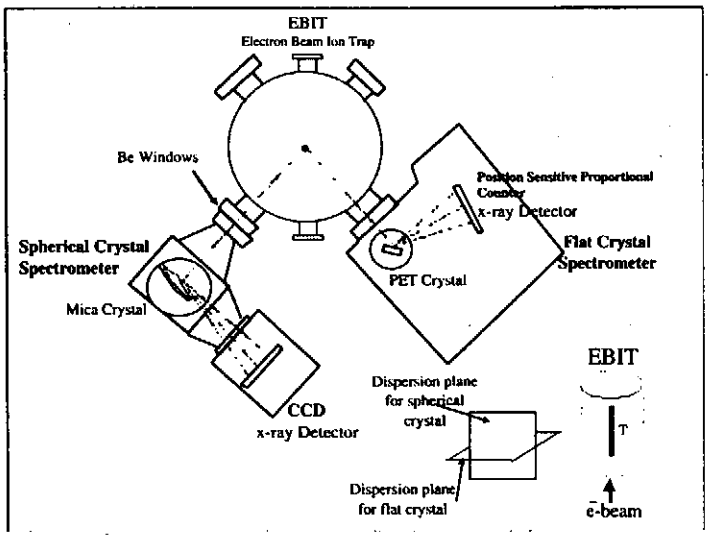

FIGURE 1. Electron beam ion trap x-ray polarization measurement set-up (modified "two-crystal technique"). FCS preferentially reflects $I_{\parallel}$, while the spherically bent crystal spectrometer reflects $I_{\perp}$ (see text).

The second approach described above has been utilized here to infer the polarization of the K-shell resonance lines of S^{13+} and S^{14+}. As illustrated in Fig. 1, two polarization sensitive crystal spectrometers which act as polarizers were installed on SuperEBIT for simultaneous spectroscopic measurements. One spectrometer, a flat crystal spectrometer (FCS) [23], was equipped with a PET (002) crystal which has a lattice spacing of 2d = 8.742 Å, resulted in a Bragg angle of $\theta_B = 35.2°$ for observing the Kα transition of heliumlike sulfur. A position sensitive proportional counter was used in connection with the FCS for x-ray detection. The second spectrometer, (a compact spherical crystal spectrometer [24,25]), employed a Mica (002) crystal bent to a radius of 30 cm. The lattice spacing of 2d = 19.942 Å resulted in a Bragg angle of $\theta_B = 49.6°$ for the transition of interest observed in third order reflection. A charged-coupled device (CCD) was used with this spectrometer for x-ray detection. Figures 2 and 3 show typical spectra obtained by each spectrometer for different electron beam energies. These figures show that the FCS produced spectra with high signal-to-noise ratio, though somewhat lower resolution than the compact focusing spectrometer. The comparatively poor quantum efficiency and high noise level of the CCD detector hampered the latter.

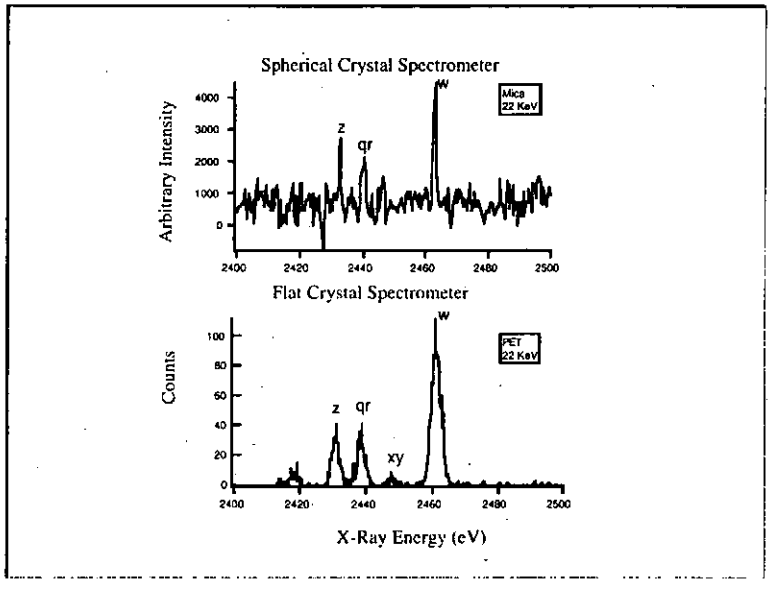

FIGURE 2. Spectra obtained with the spherically bent crystal spectrometer compared to spectra taken with the flat crystal spectrometer (electron beam energy: 22 KeV).

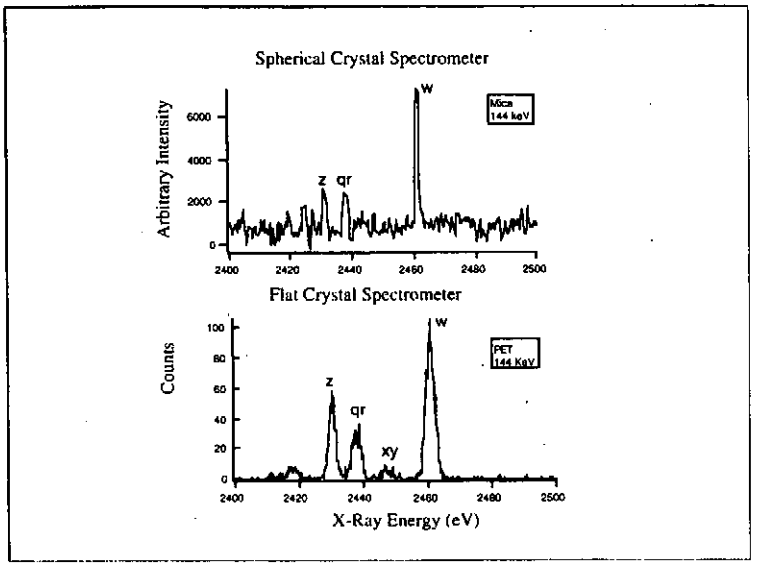

FIGURE 3. Spectra obtained with the spherically bent crystal spectrometer compared to spectra taken with the flat crystal spectrometer (electron beam energy: 144 KeV).

III. Analysis

The intensities observed by the crystal spectrometers can be expressed as,

$$I^{obs} = R_{\|} I_{\|} + R_{\perp} I_{\perp} \qquad (1),$$

where $R_{\|}$, and $R_{\perp}$ represent the integrated crystal reflectivities for x-ray emission polarized parallel and perpendicular to the plane of dispersion, respectively. $I_{\|}$ and $I_{\perp}$ denote the intensity of the emitted radiation with an electric field vector parallel and perpendicular to the electron beam direction, respectively. The integrated crystal reflectivities are commonly written as the ratio, $R \equiv R_{\perp}/R_{\|}$. This ratio varies as a function of the Bragg angle and is tabulated by Henke, Gullikson, and Davis [26] for a variety of crystals including PET (002) and Mica (002) crystals used for this experiment. The polarization of emission lines observed at an angle of $\vartheta = 90°$ from the electron beam are defined as,

$$P = \frac{I_{\|} - I_{\perp}}{I_{\|} + I_{\perp}} \qquad (2).$$

As stated earlier, the two crystal spectrometers act as polarimeters. The FCS is oriented in a geometry that preferably reflects $I_{\parallel}$, but I_{PET}^{Obs} also contains contributions from $I_{\perp}$, since the PET crystal used in the FCS was set at Bragg angle of θ_B = 35.2°, which corresponds to an integrating crystal reflectivity ratio of R_{PET} ~ 0.28. The spherical crystal spectrometer was set at a Bragg angle close to 45° corresponding to a ratio of R_{Mica} ~ 0.04. As a result, the spherical crystal spectrometer absorbs most of $I_{\parallel}$ while reflecting $I_{\perp}$. The measured intensities of the spherical crystal spectrometer in the following are approximated as,

$$I_{Mica}^{Obs} = R_{\perp} I_{\perp} \qquad (3).$$

When using the "two-crystal technique" to infer polarization of line emissions it is convenient to normalize the line intensity of interest to a line emission unaffected by polarization (or to a line emission where P is known either experimentally or theoretically). In our case, the observed line emission is normalized to the forbidden z line ($1s2s\ ^3S_1 \rightarrow 1s^2\ ^1S_0$) in heliumlike sulfur. The $1s2s\ ^3S_1 \rightarrow 1s^2\ ^1S_0$ transition is readily observed in the spectra measured with either spectrometer. Line z is intrinsically unpolarized, but can be slightly polarized due to cascades [13]. Applying this normalization, the intensity ratio of lines of interest can be written as,

$$\left(\frac{I^w}{I^z}\right)_{Mica} = \frac{I_{\perp}^w}{I_{\perp}^z} \qquad (4)$$

for intensities observed with the spherically bent crystal spectrometer. As for intensities observed with the FCS this ratio becomes,

$$\left(\frac{I^w}{I^z}\right)_{PET} = \frac{I_{\parallel}^w + R_{PET} I_{\perp}^w}{I_{\parallel}^z + R_{PET} I_{\parallel}^z} \qquad (5).$$

Combining Eqs. (2), (4), and (5) we derive an expression for the polarization of resonance line of He-like sulfur,

$$P_w = \frac{\left[\left(\frac{1+P_z}{1-P_z}\right) + R_{PET}\right]\left(\frac{I^w}{I^z}\right)_{PET} - \left(\frac{I^w}{I^z}\right)_{Mica}\left(R_{PET}+1\right)}{\left[\left(\frac{1+P_z}{1-P_z}\right) + R_{PET}\right]\left(\frac{I^w}{I^z}\right)_{PET} + \left(\frac{I^w}{I^z}\right)_{Mica}\left(R_{PET}-1\right)} \qquad (6).$$

The terms $\left(\frac{I^w}{I^z}\right)_{PET}$ and $\left(\frac{I^w}{I^z}\right)_{Mica}$ are obtain from Gaussian fits of the spectra. Since the spectra were taken concurrently, the polarization of the blended resonance line of Li-like sulfur (P_{qr}) can be calculated from Eq. (6) by simply replacing I^w with I^{qr}. Where I^{qr} denotes the line intensity blend of Li-like sulfur resonance lines $1s2s2p\ ^2P_{3/2} \rightarrow 1s^22s\ ^2S_{1/2}$ and $1s2s2p\ ^2P_{1/2} \rightarrow 1s^22s\ ^2S_{1/2}$.

The slight polarization of line z due to cascades can be determined entirely by the branching ratios of the upper levels [13]. Using the flexible atomic code (FAC) [27], we

calculated cascades contributions from $n \leq 3$ (cascades contributions from $n > 3$ are considered negligible). As for the theoretical predictions of P_w and P_{qr}, we again use FAC as well as distorted-wave (DW) computer code developed by Zhang, Sampson, and Clark [28]. Since the polarization is due to the preferential population of the magnetic sublevels, both computer codes are used to calculate the magnetic sublevel cross sections of the resonance lines of interests:

$$P_w = \frac{\sigma_0 - \sigma_1}{\sigma_0 + \sigma_1} \qquad (7),$$

$$P_q = \frac{3\sigma_{1/2} - 3\sigma_{3/2}}{5\sigma_{1/2} + 3\sigma_{3/2}} \qquad (8).$$

In Eq. 7 σ_0 and σ_1 denote the cross sections for electron impact excitation from the ground state to the m=0 and 1 magnetic sublevels for He-like ion resonance transition, $1s2p\ ^1P_1 \rightarrow 1s^2\ ^1S_0$. Similarly, in Eq. 8 $\sigma_{1/2}$ and $\sigma_{3/2}$ denote the magnetic sublevel cross sections concerning Li-like ion resonance transition, $1s2s2p\ ^2P_{3/2} \rightarrow 1s^22s\ ^2S_{1/2}$. The polarization of the blend of the Li-like sulfur resonance lines can be written as,

$$P_{rq} = \frac{\beta_r P_r \sigma_r + \beta_q P_q \sigma_q}{\beta_r \sigma_r + \beta_q \sigma_q} \qquad (9),$$

where σ_q and σ_r denote the total electron impact excitation cross sections for two transitions $1s2s2p\ ^2P_{3/2} \rightarrow 1s^22s\ ^2S_{1/2}$ and $1s2s2p\ ^2P_{1/2} \rightarrow 1s^22s\ ^2S_{1/2}$, respectively (since the latter's total angular momentum of its upper state is 1/2, $P_r = 0$ in Eq. 9). Also note that the branching ratios β_r and β_q in Eq. 9 are both approximately equal to 0.80 [27]. While the distorted-wave method uses a fully relativistic approach to calculate magnetic sublevel cross sections due to electron impact, FAC uses a quasi-relativistic approximation which give adequate results for low to mid-Z elements [27].

IV. Discussion and Conclusion

Unlike the results reported in Ref. 20, the measured polarization agrees well with our predictions made with the Flexible Atomic Code and the relativistic distorted-wave code. The measured values and predictions are also shown in Fig. 4 and Fig. 5. The error bars in both figures represent the quadrature sum of the statistical error and the high noise level of the CCD detector used with the compact spherical crystal spectrometer. Also shown in Fig. 4 are the non-relativistic predictions of Itikawa *et al.* [10]. These early predictions are limited from near threshold of the resonance line of He-like sulfur (~2.5 KeV) up to 12 KeV, but nevertheless agree well with both the predictions of FAC and DW for this limited energy region. The measured polarization for the blended resonance lines of Li-like sulfur as function of electron impact energy ($1s2s2p\ ^2P_{3/2} \rightarrow 1s^22s\ ^2S_{1/2}$ and $1s2s2p\ ^2P_{1/2} \rightarrow 1s^22s\ ^2S_{1/2}$) compared to the predictions of FAC and DW show fair agreement as well.

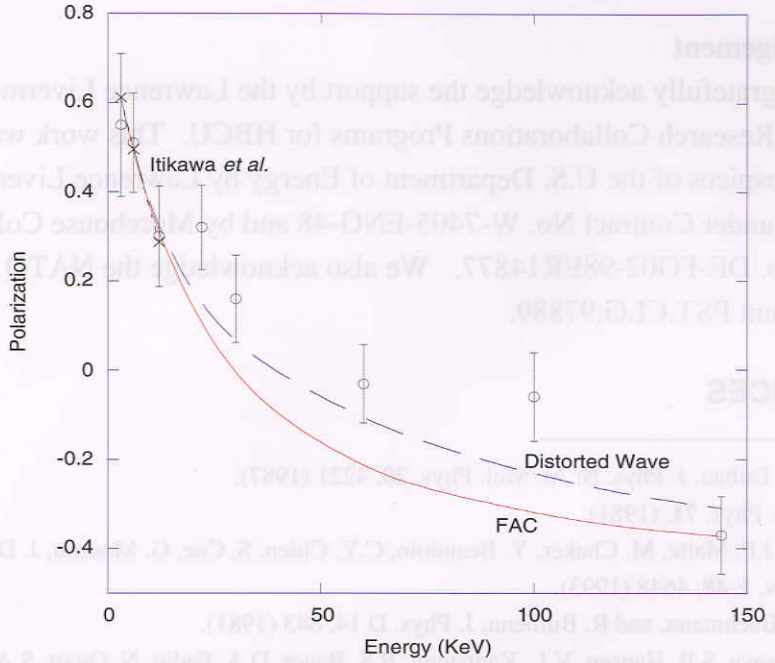

FIGURE 4. Measured polarization of the resonance line of heliumlike sulfur at electron impact energies 3, 6, 12, 22, 30, 60, 100, and 144 KeV compared to the predictions of FAC and distorted-wave. The non-relativistic predictions of Itikawa from 3 to 12 KeV are also shown.

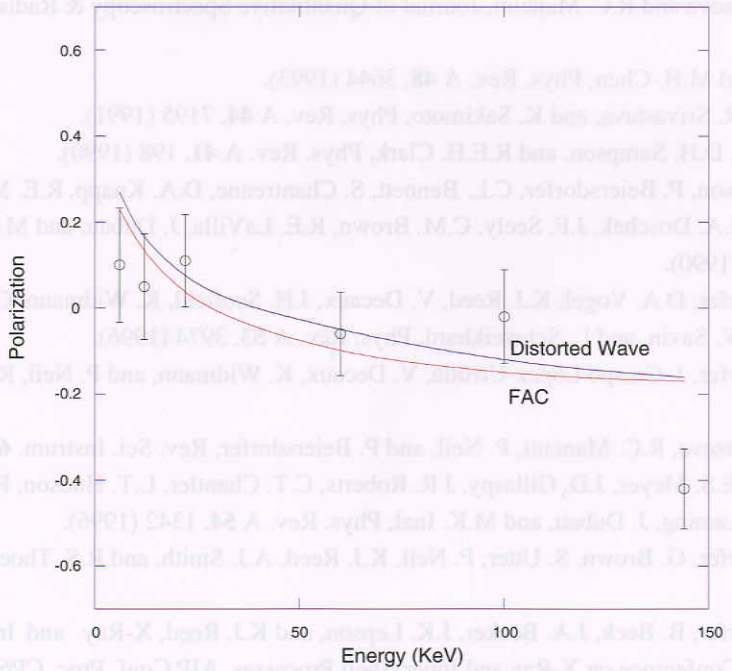

FIGURE 5. Measured polarization of the resonance line of lithiumlike sulfur at electron impact energies 6, 12, 22, 60, 100, and 144 KeV compared to the predictions of FAC and distorted-wave.

Acknowledgement

We gratefully acknowledge the support by the Lawrence Livermore National Laboratory Research Collaborations Programs for HBCU. This work was performed under the auspices of the U.S. Department of Energy by Lawrence Livermore National Laboratory under Contract No. W-7405-ENG-48 and by Morehouse College under Contract No. DE-FG02-98ER14877. We also acknowledge the NATO Collaborative Linkage Grant PST.CLG.97889.

REFERENCES

[1] M.K. Inal, J. Dubau, J. Phys. B: At. Mol. Phys. **20**, 4221 (1987).

[2] E. Haug, Sol. Phys. **71**, (1981).

[3] J.C. Kieffer, J.P. Matte, M. Chaker, Y. Beaudoin, C.Y. Chien, S. Coe, G. Mourou, J. Dubau, and M.K. Inal, Phys. Rev. E **48**, 4648 (1993).

[4] R. Beier, C. Bachmann, and R. Burhenn, J. Phys. D 14, 643 (1981).

[5] A.S. Shlyaptseva, S.B. Hansen, V.L. Kantsyrev, B.S. Bauer, D.A. Fedin, N. Ouart, S.A. Kazantsev, A.G. Petrashen, and U.I. Safronova, Rev. Sci. Instrum. **72**, 1241 (2001).

[6] A.S. Shlyaptseva, V.L. Kantsyrev, N. Ouart, D. Fedin, S. Hamasha, and S. Hansen, *Proceedings of SPIE* **5196**, Aug. 3-8, 2003, San Diego, CA, USA.

[7] P. Beiersdorfer and M. Slater, Phys. Rev. E **64**, 066408 (2001).

[8] A.S. Shlyaptseva and R.C. Mancini, Journal of Quantitative Spectroscopy & Radiative Transfer 58, 917 (1997).

[9] K.J. Reed and M.H. Chen, Phys. Rev. A **48**, 3644 (1993).

[10] Y. Itikawa, R. Srivastava, and K. Sakimoto, Phys. Rev. A **44**, 7195 (1991).

[11] H.L. Zhang, D.H. Sampson, and R.E.H. Clark, Phys. Rev. A **41**, 198 (1990).

[12] J.R. Henderson, P. Beiersdorfer, C.L. Bennett, S. Chantrenne, D.A. Knapp, R.E. Marrs, M.B. Schneider, K.L. Wong, G.A. Doschek, J.F. Seely, C.M. Brown, R.E. LaVilla, J. Dubau, and M.A. Levine, Phys. Rev. Lett. **65**, 705 (1990).

[13] P. Beiersdorfer, D.A. Vogel, K.J. Reed, V. Decaux, J.H. Scofield, K. Widmann, G. Hölzer, E. Förster, O. Wehrhan, D.W. Savin, and L. Schweikhard, Phys. Rev. A **53**, 3974 (1996).

[14] P. Beiersdorfer, J. Crespo López-Urrutia, V. Decaux, K. Widmann, and P. Neil, Rev. Sci. Instrum. **68**, 1073 (1997).

[15] A.S. Shlyaptseva, R.C. Mancini, P. Neil, and P. Beiersdorfer, Rev. Sci. Instrum. **68**, 1095 (1997).

[16] E. Takács, E.S. Meyer, J.D. Gillaspy, J.R. Roberts, C.T. Chantler, L.T. Hudson, R.D. Deslattes, C.M. Brown, J.M. Laming, J. Dubau, and M.K. Inal, Phys. Rev. A **54**, 1342 (1996).

[17] P. Beiersdorfer, G. Brown, S. Utter, P. Neil, K.J. Reed, A.J. Smith, and R.S. Thoe, Phys. Rev. A **60**, 4156 (1999).

[18] P. Beiersdorfer, B. Beck, J.A. Becker, J.K. Lepson, and K.J. Reed, X-Ray and Inner-Shell Processes: 19th International Conference on X-Ray and Inner-Shell Processes, AIP Conf. Proc. CP652, edited by A. Bianconi, A. Marcelli, and N. L. Saini (American Institute of Physics, New York, 2003), p. 131-140.

[19] P. Beiersdorfer, Linear X-Ray Line Polarization Effects on Spectal Measurements Using an Electron beam Ion Trap: 2nd US-Japan Plasma Polarization Spectroscopy Workshop, NIFS-PROC-37, edited by T.

Fujimoto and P. Beiersdorfer (National Institute For Fusion Science of Japan, Nagoya, Japan 1998), p. 67-86.

[20] N. Nakamura, D. Kato, N. Miura, T. Nakahara, and S. Ohtani, Phys. Rev. A **63**, 024501-1 (2001).

[21] M.A. Levine, R.E. Marrs, J.N. Bardsley, P. Beiersdorfer, C.L. Bennett, M.H. Chen, T. Cowan, D. Dietrich, J.R. Henderson, D.A. Knapp, A. Osterheld, B.M. Penetrante, M.B. Schneider, and J.H. Scofield, Nucl. Instrum. Methods **B43**, 431 (1989).

[22] D.A. Knapp, R.E. Marrs, S.R. Elliott, E.W. Magee, R. Zasadzinski, Nucl. Instrum. Methods **A334**, 305 (1993).

[23] G.V. Brown, P. Beiersdorfer, and K. Widmann, Rev. Sci. Instrum. **70**, 280 (1999).

[24] N. Nakamura, E. Nojikawa, H. Shiraishi, F. J. Currell, S. Ohtani, A. Ya. Faenov, and T.A. Pikuz, Rev. Sci. Instrum. **70**, 1658 (1999).

[25] B.K.F. Young, A.L. Osterheld, D.F. Price, R.Shepherd, R.E. Stewart, A.Ya. Faenov, A.I. Magunov, T.A. Pikuz, I.Yu. Skobelev, F.Flora, S. Bollanti, P.Di Lazzaro, T. Letardi,A.Grilli, L. Palladino, A. Reale, A. Scafati, and L. Reale, Rev. Sci. Instrum. **69**, 4049 (1998).

[26] B.L. Henke, E.M. Gullikson, and J.C. Davis, At. Data Nucl. Data Tables **54**, 181 (1993).

[27] M.F. Gu, private communication (Flexible Atomic Code)

[28] H.L. Zhang, D.H. Sampson, and R.E.H. Clark, Phys. Rev. A **41**, 198 (1990).

Level alignment in C III ions:

R-matrix calculations of *m*-resolved excitation cross section

I.Yu.Tolstikhina, L.A.Vainshtein

P.N.Lebedev Physical Institute, Russian Academy of Sciences
Moscow, Russia

INTRODUCTION

The polarization of emission lines from plasma in addition to their intensities is the source of data for the interpretation of the plasma characteristics. It carries information about the anisotropic velocity distribution of electrons. The population-alignment collisional-radiative (PACR) model code has been developed in the group of Professor T.Fujimoto for the interpretation of the experimental observations in terms of the anisotropic electron velocity distribution in plasma. The implementation of the PACR model for Be-like oxygen (OV) and He-like carbon (CV) has been reported recently [1, 2].

The polarization of CIII triplet emission lines for the $1s^2 2s3s\ ^3S_1 - 1s^2 2s3p\ ^3P_{0,1,2}$ (465.1473, 465.0246, 464.7418 nm) transition may also be studied with the PACR model. Assuming the ionizing plasma, which is reasonable in the main region of the magnetically confined plasma with heating modes, the alignment of the upper level ($1s^2 2s3p\ ^3P_{0,1,2}$) is produced by the collisional excitations from the ground state $1s^2 2s^2\ ^1S_0$ and metastable state $1s^2 2s2p\ ^3P_{0,1,2}$ by electrons having an anisotropic velocity distribution.

The main task of the present work is to calculate m-resolved excitation cross sections for the following transitions in Be-like CIII ion:

(i) from ground state $1s^2 2s^2\ ^1S_0$ to $1s^2 2s3p\ ^3P_{0,1,2}$

(ii) from metastable $1s^2 2s2p\ ^3P_{0,1,2}$ to $1s^2 2s3p\ ^3P_{0,1,2}$

METHOD OF CALCULATIONS

The calculation is performed by two codes: RMATRIX1 [3] (K.A.Berrington, W.B.Eissner, P.H.Norrington) and SCATTAMPREL [4] (K.Bartschat, N.S.Scott) modified by K.A.Berrington to extract m-resolved excitation cross sections. RMATRIX1 is used to calculate reactance **K**-matrix which is the input to the code SCATTAMPREL [5].

R-matrix calculations

1. **STG1**

The first stage of RMATRIX1 code is the calculation of the orbital basis and all radial integrals in the inner-region. The orbital basis includes the target basis ϕ_i and the continuum orbitals $u_{ij}(r)$.

The target basis ϕ_i is constructed from a bound orbital basis consisting of self consistent field orbitals plus some additional pseudo-orbitals included to model electron correlation effects. The orbitals $o_{nlm_l}(\vec{r}, m_s)$ form an orthonormal set

$$\left\langle o_{n_i l_i m_{l_i}} \middle| o_{n_j l_j m_{l_j}} \right\rangle = \delta_{n_i n_j} \delta_{l_i l_j} \delta_{m_{l_i} m_{l_j}} \delta_{m_{s_i} m_{s_j}}$$

and corresponding radial parts are expanded in the form

$$P_{nl}(r) = \sum_i c_i r^{p_i} \exp(-\xi_i r), \quad \left\langle P_{n_i l} \middle| P_{n_j l} \right\rangle = \delta_{n_i n_j}$$

Parameters c_i, p_i and ξ_i are the input to the first stage of RMATRIX1. In the present calculation we use six orthonormal basis orbitals 1s, 2s, 2p, 3s, 3p, 3d and two pseudo-orbitals $\overline{4s}$, $\overline{4p}$ which have been calculated with CIV3 code by Hibbert [6].

The continuum orbitals $u_{ij}(r)$ for each angular momentum l_i are obtained by solving the model single-channel scattering problem

$$\left(\frac{d^2}{dr^2} - \frac{l_i(l_i+1)}{r^2} + V_0(r) + k_{ij}^2 \right) u_{ij}(r) = \sum_n \Lambda_{ijn} P_{nl_i}(r)$$

subject to the fixed boundary conditions defined by the parameters of R-matrix calculations

$$u_{ij}(0) = 0, \qquad \left(\frac{a}{u_{ij}(a)} \right) \left(\frac{du_{ij}}{dr} \right)_{r=a} = b.$$

In our case the radius of the sphere defining the inner region is 14 a.u., the constant b is set to be zero, the maximum value of the angular momentum l is 24 and 20 continuum orbitals $u_{ij}(r)$ for each angular momentum l_i have been obtained.

2. **STG2**

The second stage of RMATRIX1 is the calculation of LS-coupling matrix elements in the inner-region. It solves the target-state problem by calculating the N-electron Hamiltonian (H^N) matrix element

$$H_{kk'} = \left\langle \phi_k(x_1 \ldots x_N) \middle| H^N \middle| \phi_{k'}(x_1 \ldots x_N) \right\rangle$$

involving the target basis

$$\phi_i(x_1 \ldots x_N) = A o_1(x_{v_1}) o_2(x_{v_2}) \ldots o_N(x_{v_N})$$

Here A is the antisymmetrisation operator. In our calculations spin-orbit interaction in the Breit-Pauli approximation was included

$$H^N = \sum_{n=1}^{N} \left(-\tfrac{1}{2}\nabla_n^2 - \frac{Z}{r_n} + \sum_{m>n}^{N} \frac{1}{r_{nm}} \right) + \frac{\alpha^2 Z}{2} \sum_{n=1}^{N} \frac{\vec{l}_n \cdot \vec{s}_n}{r_n^3}$$

and the basis configurations were generated automatically by requiring that the two of four target electrons are retained in the 1s shell and the other two electrons are distributed amongst the other seven shells in all possible ways. Thus, the number of states is 82 for 13 symmetries:

Parity	Even							Odd					
Symmetry	$^1S^e$	$^3S^e$	$^1P^e$	$^3P^e$	$^1D^e$	$^3D^e$	$^3F^e$	$^1P^o$	$^3P^o$	$^1D^o$	$^3D^o$	$^1F^o$	$^3F^o$
Number of states	13	6	3	7	10	6	1	12	12	3	3	3	3

The total *(N+1)* –electron wave function in the inner region is expanded in the form

$$\psi_k(x_1...x_N) = \mathrm{A}\sum_{ij} c_{ijk}\,\overline{\Phi_i}(x_1...x_N;\hat{r}_{N+1}\sigma_{N+1})\frac{1}{r_{N+1}}u_{ij}(r_{N+1}) + \sum_j d_{jk}\chi_j(x_1...x_N),$$

where the antisymmetrisation operator A accounts for exchange between the target electrons and the free electron. The channel function $\overline{\Phi_i}$ are obtained by coupling the target states Φ_i

$$\Phi_i(x_1...x_N) = \sum_k b_{ik}\phi_k(x_1...x_N)$$

with the angular and spin functions of the scattered electron to form states of the total angular momentum and parity. Quadratically intergrable functions χ_i formed from the bound orbitals are included to ensure completeness of the total wavefunction.

Let φ_λ denote collectively the basis functions in this expansion. Continuum-continuum, continuum-bound and bound-bound matrix elements of the inner region *(N+1)* –electron Hamiltonian

$$H_{\lambda\lambda'} = \langle\varphi_\lambda(x_1...x_{N+1}|H^{N+1}|\varphi_{\lambda'}(x_1...x_{N+1})\rangle$$

are evaluated. In our calculations the maximum value of the *(N+1)*-electron state orbital angular momentum *L* is 19

3. RECUPD

The third stage of the RMATRIX1 is diagonalization of the target Hamiltonian and definition of term-coupling coefficients as well as transformation of Hamiltonian matrices from LS- to pair-coupling. If the spin-orbit interaction in a target is included, the *(N+1)*-electron R-matrix basis functions are defined for each total angular momentum J_T and parity. A pair-coupling scheme

$$\boldsymbol{J + l = K,}\ \text{<and>}\ \boldsymbol{K + s = J_T}$$

is used, *J* is the total target angular momentum, *l, s=1/2* are the free electron orbital and spin angular momenta.

We performed calculations for the 70 lowest states of the target:

Parity	Even				Odd				
J	0	1	2	3	0	1	2	3	4
Number of states	10	12	10	3	7	14	10	3	1

In the following table the calculated target states energies of interest are presented and compared with the corresponding energies from NIST data base. There is an option in RMATRIX1 code to correct calculated energies. In our calculations we didn't use it.

Configuration	Term	Energy (Ry)	
		Present calculation	NIST data base
$1s^2 2s^2$	$^1S_0$	0	0
$1s^2 2s2p$	$^3P_0$	0.48337	0.47720
	$^3P_1$	0.48362	0.47742
	$^3P_2$	0.48412	0.47793
$1s^2 2s3p$	$^3P_0$	2.36024	2.36661
	$^3P_1$	2.36030	2.36666
	$^3P_2$	2.36042	2.36678

4. **STGH**

This module of RMATRIX1 deals with remaining inner-region tasks. It diagonalizes $(N+1)$-electron Hamiltonian in the continuum basis.

Calculation time of the energy independent part of RMARIX1 is 20 hours on PC with Pentium-4 processor (2.53 GHz) and 1 GB RAM.

5. **STGF**

In the last stage of the R-matrix calculations the total wavefunction of the inner region and the R-matrix on the boundary for all considered total $(N+1)$-electron energies E are established and the electron-target scattering problem in the external region is solved. Matching the internal and external region solutions on the boundary ($r=a$) the reactance matrix **K** is evaluated. The **K**-matrix is real and symmetric, and represents the asymptotic form of the entire wavefunction, containing information from both internal and external region. It may be used for the calculations of scattering observables.

In our calculations on this stage we used code STGF (written by N.R.Badnell [5]).

The following figures show the comparison of the total cross sections for transitions of interest calculated by RMATRIX1 code and by our code ATOM-AKM based on the K-matrix calculation in the first order perturbation theory. The comparison shows good agreement between RMATRIX1 and ATOM-AKM calculation results out of the resonance region. For the case of the excitation from excited state, K-matrix slightly overestimates cross sections.

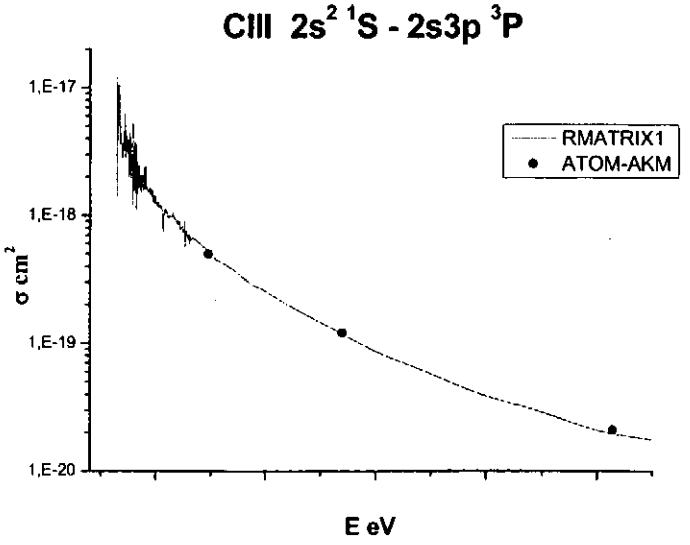

Fig.1

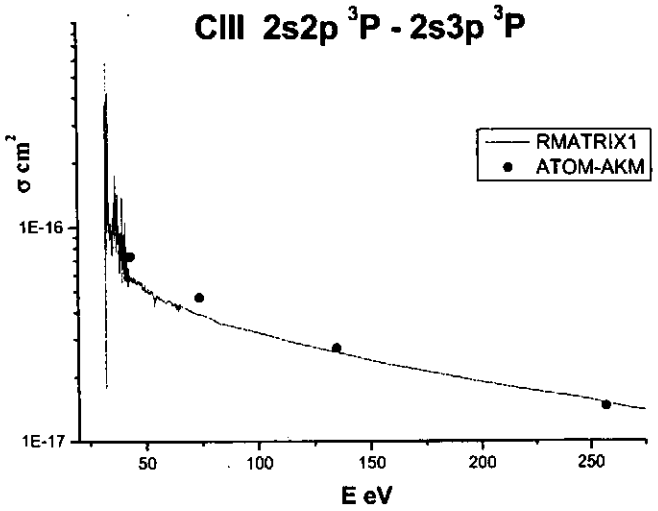

Fig.2

Calculation of *m*-resolved excitation cross sections with code SCATTAMPREL

Code SCATTAMPREL was used to calculate scattering amplitudes for inelastic scattering of electrons by C III ion for transitions

$1s^2 2s^2\ {}^1S_0$ to $1s^2 2s3p\ {}^3P_{0,1,2}$

$1s^2 2s2p\ {}^3P_{0,1,2}$ to $1s^2 2s3p\ {}^3P_{0,1,2}$

between m-components.

The input data are K-matrix elements which have been calculated in a representation diagonal in the total angular momentum J_T and parity π using the ***JlK***-coupling scheme (RMATRIX1, STGF).

The program calculates scattering amplitude $f(\theta)$ given by

$$f(n_1 J_1 M_{J_1} m_1, n_0 J_0 M_{J_0} m_0; \theta) = -i\frac{1}{2}\left[\frac{1}{k_0 k_1}\right]^{1/2} \sum_{l_1 K_1 l_0 K_0 J\pi} [(2l_1+1)(2l_0+1)]^{1/2} \left[\frac{(l_1 - m_{l_1})!}{(l_1 + m_{l_1})!}\right]^{1/2}$$

$$\times P_{l_1}^{m_{l_1}}(\cos\theta) T^{J\pi}_{n_1 J_1 K_1 l_1, n_0 J_0 K_0 l_0} (J_0 M_{J_0} l_0 0 | K_0 M_{J_0})(K_0 M_{J_0} \tfrac{1}{2} m_0 | J M_J)(J_1 M_{J_1} l_1 m_{l_1} | K_1 m_{K_1})(K_1 M_{K_1} \tfrac{1}{2} m_1 | J M_J)$$

where $P_l^{m_l}$ is an associated Legendre polynomial. T-matrix is calculated from K-matrix using the well-known formulas

$$\mathbf{T} = -2\,(\mathbf{1} + \mathbf{K}^2)^{-1}\,(\mathbf{K} - i\mathbf{K})$$

The *m*-resolved cross section is equal

$$\sigma(n_1 J_1 M_{J_1} m_1, n_0 J_0 M_{J_0} m_0) = \frac{k_1}{k_0} \int_0^{\pi} |f(\theta)|^2 \sin\theta \, d\theta$$

The data obtained by described method can be used as an input to the PARC model code.

Calculation results

Figures 3 and 4 show the cross sections for the transitions from the ground state to *m*-components of $2s3l\ ^3L$ levels. To exclude trivial dependence on energy we multiplied the cross sections by E^3 (exchange transitions). There are curves with smooth and strong dependence on energy below 100 eV which may be useful for the plasma diagnostics purposes.

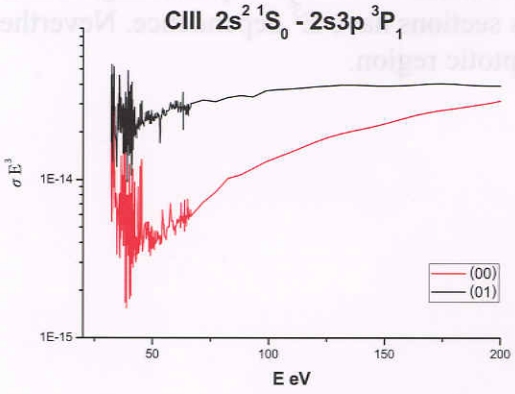

Fig.3

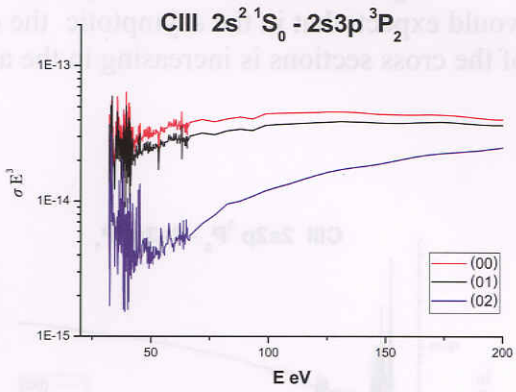

Fig.4

Figures 5-8 show the m-component excitation cross sections for the transitions from the metastable state. Transitions from the metastable state with $\Delta J=0$ (Fig.6, 7) have a common feature: the excitation cross sections between different *m*-components are divided into two groups with different cross section values in the asymptotic. The cross sections for $\Delta m=0$ are larger up to two orders of magnitude.

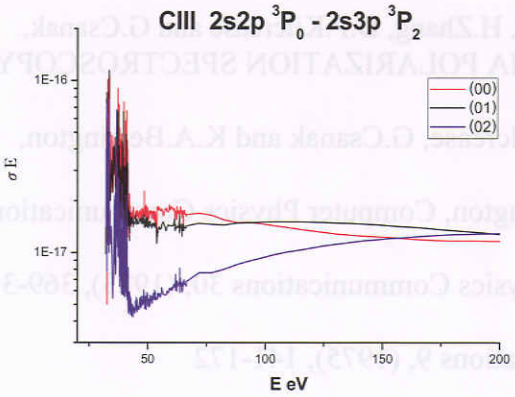

Fig.5

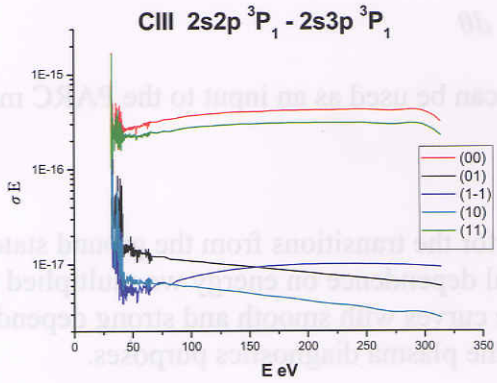

Fig.6

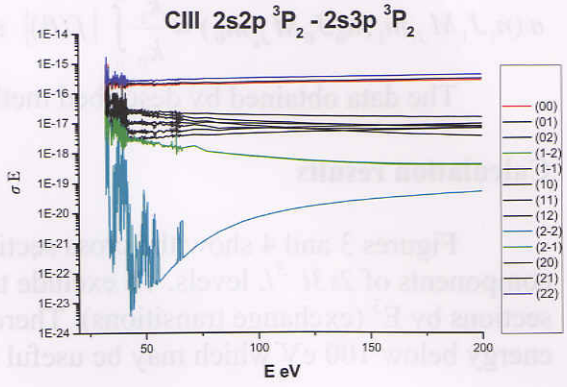

Fig.7

Figure 8 shows the *m*-component cross sections for the purely exchange transition. One would expect that in the asymptotic the cross sections have E^3 dependence. Nevertheless, one of the cross sections is increasing in the asymptotic region.

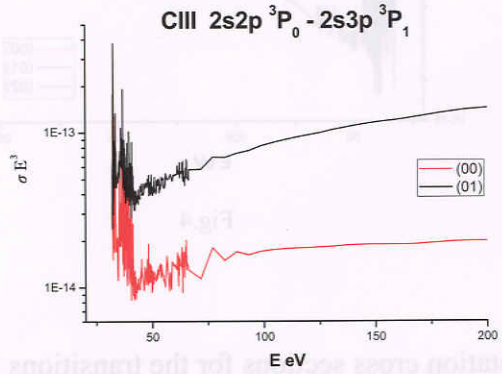

Fig.8

These results are very interesting from the point of view of both plasma diagnostics and general collision theory. We are planning to analyze the results using more simple code based on Born approximation in order to study behavior of the cross sections in the asymptotic region.

References

[1]. A.Iwamae, A.Tanaka, T.Inoue, T.Fujimoto, H.Zhang, D.P.Kilcrease and G.Csanak, Proceedings of the 3rd US-Japan PLASMA POLARIZATION SPECTROSCOPY WORKSHOP, (2002)

[2]. A.Iwamae, T.Fujimoto, H.Zhang, D.P.Kilcrease, G.Csanak and K.A.Berrington, NIFS-DATA-78, (2003)

[3]. K.A.Berrington, W.B.Eissner, P.H.Norrington, Computer Physics Communications 92, (1995), 290-420

[4]. K.Bartschat and N.S.Scott, Computer Physics Communications 30, (1983), 369-381

[5]. K.A.Berrington, privet communication

[6]. A.Hibbert, Computer Physics Communications 9, (1975), 141-172

Alignment Creation by Elastic Electron Scattering
A Quantum Treatment

G. Csanak and D. P. Kilcrease
Theoretical Division
Los Alamos National Laboratory
Los Alamos, NM 87545, USA
and
D. V. Fursa and I. Bray
School for Engineering Sciance
Murdoch University
Perth, Western Australia 6150, Australia

1. Introduction

Alignment creation by elastic heavy particle scattering has been studied for many years by Omont [1], by D'yakonov and Perel [2], and by Petrashen, Rebane, and Rebane [3-12]. The technique has been adapted for arbitrary perturbers (including electrons) by Fujimoto et al. [13] and by Fujimoto and Kazantsev [14]. In the case of heavy particle perturbers (e.g. ions) there was an argument by Petrashen, Rebane, and Rebane [7] that under certain conditions (namely only elastic scattering is possible and the semi-classical straight-line trajectory assumption holds) in the case of an isolated level, alignment can not be created by elastic scattering. This contention has been questioned by Dashevskaya and Nikitin [15] who argued that the above conclusion of Petrashen et al. [7] is due to an extra symmetry introduced into the problem by the straight-line trajectory approximation (which introduces detailed balance for magnetic sublevel to magnetic sublevel transitions) and if a more accurate approximation is made alignment creation can be obtained by elastic scattering. (See the discussion in Fujimoto et al. [13].) In the case of inelastic scattering Kazantsev et al. [16,17] gave a quantum-mechanical definition of the alignment creation cross section. In earlier works, Trajmar et al. [18] and Csanak et al. [19] adopted the inelastic alignment creation cross section definition of Kazantsev et al. [16,17] for elastic electron scattering and reported results for Ba [18] and O V ions [19] based on that formula. (Apparently Dashevskaya and Nikitin [15] used the same formula.) However, a closer inspection of the semi-classical formula of Fujimoto et al. [13] and Fujimoto and Kazantsev [14] as well as the quantum-mechanical rate equations of Ben-Reuven [20] and Nienhuis [21] and Bommier and Sahal-Brechot [22] also indicated that the inelastic scattering formula might not hold for elastic scattering. The present work reinvestigates this problem, and shows that indeed the alignment creation cross section formula is different for elastic scattering, as compared to the inelastic scattering formula.

2. Semi-classical background

Fujimoto et al. [13] and Fujimoto and Kazantsev [14] gave the following formula for the alignment creation cross section by elastic scattering (Eq. 3.15b in Fujimoto et al. [13]),

$$\sigma_0(20) = (2F+1)^{-1/2}\sum_{M'}(-1)^{F-M'}\langle FFM'-M'|20\rangle D_{\alpha FM'}$$
$$+(2F+1)^{-1/2}\sum_{M\neq M'}\left[(-1)^{F-M'}\langle FFM'-M'|20\rangle-(-1)^{F-M}\langle FFM-M|20\rangle\right]Q_{\alpha FM,\alpha FM'} \tag{1a}$$

where $D_{\alpha FM'}$ and $Q_{\alpha FM,\alpha FM'}$ were defined as (Eq. 3.14 in Fujimoto et al. [13])

$$D_{\alpha FM'} = 2\pi\int bdb\sum_{M}\left[\delta_{MM'}-\left|\langle\alpha FM|S_c|\alpha FM'\rangle\right|^2\right] \tag{1b}$$

and

$$Q_{\alpha FM,\alpha FM'} = 2\pi\int bdb\left|\langle\alpha FM|S_c|\alpha FM'\rangle\right|^2 \tag{1c}$$

(we have adopted their [13,14] notation).
These equations are somewhat involved and it is difficult to see their relationship to the inelastic scattering formulas. By simple algebraic transformation it can be shown that $\sigma_0(20)$ can be written in the form,

$$\sigma_0(20) = (2F+1)^{-1/2}\sum_{M}(-1)^{F+M}\langle FFM-M|20\rangle 2\pi\int bdb\sum_{M'}\left[\delta_{MM'}-\left|\langle\alpha FM|S_c|\alpha FM'\rangle\right|^2\right] \tag{2}$$

where (as in Fujimoto et al. [13]) S_c refers to the S-matrix (actually an operator) in the 'collision frame' whose axis is parallel to the incident electron beam.

If we now introduce the T_c operator by the definition,

$$S_c = 1 + T_c \tag{3}$$

we obtain,

$$\sigma_0(20) = (2F+1)^{-1/2}\sum_{M}(-1)^{F-M+1}\langle FFM-M|20\rangle$$
$$\times\{2\pi\int bdb\left[\langle\alpha FM|T_c|\alpha FM\rangle+\langle\alpha FM|T_c^+|\alpha FM\rangle\right]+\sum_{M'}Q_{\alpha FM,\alpha FM'}\} \tag{4}$$

The second term on the right hand side is identical in form to the expression for the alignment creation cross section in the case of inelastic processes. The first term is a linear term in the T-operator and it is an additional term for elastic scattering. Its physical meaning in this semi-classical treatment is not clear. It will become clear in the quantum mechanical analysis presented in the next section. Similar additional linear terms appear in the relaxation rate-equations of Ben-Reuven [20], Nienhuis [21] and Bommier and Sahal-Brechot [22].

3. Wave-packet formulation of alignment creation by elastic scattering

The above uncertainties prompted us to reinvestigate the quantum-mechanical problem of alignment creation by elastic scattering. In this initial investigation we

shall assume non-relativistic conditions for the scattering electron, we shall treat the electron as a distinguishable particle, the target is also treated non-relativistically, but some semi-relativistic effects in the target (e.g. spin-orbit coupling) will be allowed.

We will assume that the incident electron beam is described by the wave-packet (see e.g. Rodberg and Thaler [23], p.190),

$$\left|\Phi_{\vec{k}_{in}\alpha}\right\rangle = (2\pi)^{-3}\int d\vec{k}\; A(\vec{k})\left|\vec{k},\alpha\right\rangle e^{-(i/\hbar)E_k t} \tag{5}$$

where in spatial representation,

$$\left\langle \vec{r},\sigma\middle|\vec{k},\alpha\right\rangle = e^{i\vec{k}\cdot\vec{r}}\;\eta_\alpha(\sigma) \tag{6}$$

with $\vec{k}$ referring to the wave-vector and α referring to the spin of the incident electron; $E_k = \hbar^2 k^2/2m$. We shall assume that the $A(\vec{k})$ function is strongly peaked around the $\vec{k} = \vec{k}_{in}$ value of the wave vector with a width of $\delta k << k_{in}$ (for the wave-packet description of a collision experiment, see Chapter 2 of Rodberg and Thaler [23]).

We shall assume that the initial atomic state vector with energy E_J is given by

$$\left|J\;M\right\rangle \tag{7}$$

where J refers to the total angular momentum quantum number and M to its projection.
Thus the initial state of the electron plus target system is described by the state-vector,

$$\left|\Phi_{\mathrm{J\,M.}\vec{k}_{in}\alpha}\right\rangle = (2\pi)^{-3}\int d\vec{k}\; A(\vec{k})\left|\vec{k},\alpha\right\rangle e^{-(i/\hbar)E_k^J t}\left|J\;M\right\rangle \tag{8}$$

where,

$$E_k^J = E_k + E_J \tag{9}$$

is the total energy of the electron plus atom system.

If we now let the incident electron interact with the target and want to look at the system in the asymptotic future (i.e. for $t \to +\infty$) then we can write the state vector of the electron plus target system in the form,

$$\left|\Phi(t)\right\rangle_{out} = (2\pi)^{-6}\int d\vec{k}_1\; A(\vec{k}_1)\, e^{-(i/\hbar)E_{k_1}t}\int d\vec{k}_1{}'\sum_{M_1'\alpha_1'}\left\langle \vec{k}_1{}'\alpha_1';JM_1'\middle|S\middle|JM;\vec{k}_1\alpha\right\rangle\left|JM_1';\vec{k}_1{}'\alpha_1'\right\rangle \tag{10}$$

where,

$$\left|\vec{k}_1\alpha;JM\right\rangle = \left|\vec{k}_1\alpha\right\rangle\left|JM\right\rangle \tag{11}$$

is the state-vector of the non-interacting electron plus target system, and S is the scattering operator. In Eq.(10) we only wrote out explicitly the elastic scattering terms

while the inelastic scattering terms were suppressed since they will not appear in the final elastic subspace expression considered in the present work.

Let us assume now that electrons are scattered elastically with final wave vector $\vec{k}_0$ of arbitrary direction and spin α_0 (i.e. the magnitude of $\vec{k}_0$ is the same as that of the incident wave vector, $\vec{k}$) and we do not detect the scattered electrons. We want to obtain the reduced density matrix of the final state of the target system under these conditions. The appropriate procedure was described e.g. by Blum [24]. The reduced density matrix of the target states under the assumption that the electrons scattered elastically can be given in the form,

$$\rho_{out} = \frac{1}{2}(2\pi)^{-3}\sum_{\alpha\alpha_0}\int d\vec{k}_0 \left\langle \vec{k}_0\alpha_0 \middle| \Phi(t)\right\rangle_{out\ out}\left\langle \Phi(t)\middle|\vec{k}_0\alpha_0\right\rangle \tag{12}$$

where we have also introduced an averaging over the spin of the incident electron assuming an unpolarized incident electron beam. Using Eq. (10) in Eq (12) we obtain,

$$\begin{aligned}\rho_{out} = \frac{1}{2}(2\pi)^{-9}\sum_{\alpha\alpha_0}\int d\vec{k}_0\int d\vec{k}_1\ A(\vec{k}_1)\, e^{-(i/\hbar)E_{k_1}t}\int d\vec{k}_2\ A(\vec{k}_2)^*\, e^{+(i/\hbar)E_{k_2}t} \\ \times\sum_{M_1'M_2'}\left|JM_1'\right\rangle\left\langle JM_2'\right|\left\langle \vec{k}_0\alpha_0;JM_1'\middle|S\middle|\vec{k}_1\alpha;JM\right\rangle\left\langle \vec{k}_2\alpha;JM\middle|S^+\middle|\vec{k}_0\alpha_0;JM_2'\right\rangle\end{aligned} \tag{13}$$

For the matrix elements of this reduced density operator we obtain,

$$\begin{aligned}\left\langle JM_1\middle|\rho_{out}\middle|JM_2\right\rangle \equiv \rho^{out}_{M_1M_2} = \frac{1}{2}(2\pi)^{-9}\sum_{\alpha\alpha_0}\int d\vec{k}_0\int d\vec{k}_1\ A(\vec{k}_1)\, e^{-(i/\hbar)E_{k_1}t}\int d\vec{k}_2\ A(\vec{k}_2)^*\, e^{+(i/\hbar)E_{k_2}t} \\ \times\left\langle \vec{k}_0\alpha_0;JM_1\middle|S\middle|\vec{k}_1\alpha;JM\right\rangle\left\langle \vec{k}_2\alpha;JM\middle|S^+\middle|\vec{k}_0\alpha_0;JM_2\right\rangle\end{aligned} \tag{14}$$

If we now write the S scattering operator in the form,

$$S = 1 - 2\pi\, i\,\delta(E - H_0)\,T \tag{15}$$

(where H_0 is the Hamiltonian of the non-interacting electron plus target system) then we shall obtain four terms for $\rho^{out}_{M_1M_2}$.

We obtain the first term if we make the substitutions, $S \to 1$ and $S^+ \to 1$ in Eq.(14). Then we obtain for the first term,

$$\rho^{out(1)}_{M_1M_2} = \delta_{M_1M_2}\delta_{M_1M} \tag{16}$$

which is equal to the density matrix element of the initial state given in the form,

$$\rho^{in} = \left|JM\right\rangle\left\langle JM\right| \tag{17}$$

The second term is obtained if we make the substitution $S \to 1$ and $S^+ \to 2\pi i\delta(E - H_0)T^+$. Then we obtain,

$$\rho^{out(2)}_{M_1M_2} = (2\pi)^{-5} i\,\delta_{M_1M} \frac{1}{2}\sum_{\alpha}\left\langle \vec{k}_{in}\alpha;JM\middle|T^+\middle|\vec{k}_{in}\alpha;JM_2\right\rangle \int d\vec{k}_1 \int d\vec{k}_2\; A(\vec{k}_1)A^*(\vec{k}_2)\delta(E_{k_1} - E_{k_2}) \tag{18}$$

where we used the fact that the $A(\vec{k})$ function is strongly peaked at $\vec{k}_{in}$ (see the discussion in Rodberg and Thaler [23], p. 194).

According to Rodberg and Thaler (p. 195) [23] the probability that the incident wave-packet crosses a unit area perpendicular to the z-axis (the direction of propagation of the packet) can be given by,

$$\frac{dP}{dS} = 2\pi\hbar\, v_{in} \int \frac{d\vec{k}_1}{(2\pi)^3} \int \frac{d\vec{k}_2}{(2\pi)^3} A(\vec{k}_1)A^*(\vec{k}_2)\,\delta(E_{k_1} - E_{k_2}) \tag{19}$$

where v_{in} is the initial speed of the center of the wave packet and can be given as,

$$v_{in} = \frac{\hbar k_{in}}{m} \tag{20}$$

In fact, dP/dS represents the current created by the wave packet (see e.g. Rodberg and Thaler [23] pp 20-21, 195). Thus we obtain,

$$\rho^{out(2)}_{M_1M_2} = \frac{m}{\hbar^2 k_{in}} i \frac{dP}{dS}\delta_{M_1M} \frac{1}{2}\sum_{\alpha}\left\langle \vec{k}_{in}\alpha;JM\middle|T^+\middle|\vec{k}_{in}\alpha;JM_2\right\rangle \tag{21}$$

If we now introduce the scattering amplitude by the definition,

$$f^{\alpha\beta}_{M_1M_2}(\vartheta,\phi) = -\frac{m}{2\pi\hbar^2}\left\langle \vec{k}_2\beta;JM_2\middle|T\middle|\vec{k}_1\alpha;JM_1\right\rangle \tag{22}$$

where $|\vec{k}_1| = |\vec{k}_2|$ and ϑ and ϕ refer to the polar angles of $\vec{k}_2$ relative to $\vec{k}_1$, then we obtain,

$$\rho^{out(2)}_{M_1M_2} = -\frac{2\pi}{k_{in}} i \frac{dP}{dS}\frac{1}{2}\sum_{\alpha} f^{\alpha\alpha}_{MM_2}{}^*(\vartheta = 0,\phi = 0)\delta_{M_1M} \tag{23}$$

The third term for $\rho^{out}_{M_1M_2}$ is obtained if we make the substitutions $S \to -2\pi i\delta(E - H_0)T$, $S^+ \to 1$. A calculation analogous to that used for the second term gives the result,

$$\rho^{out(3)}_{M_1M_2} = \frac{2\pi}{k_{in}} i \frac{dP}{dS}\frac{1}{2}\sum_{\alpha} f^{\alpha\alpha}_{MM_1}(\vartheta = 0,\phi = 0)\delta_{MM_2} \tag{24}$$

Finally the fourth term contributing to $\rho^{out}_{M_1M_2}$ is obtained if the $S \to -2\pi i\delta(E - H_0)T$, $S^+ \to 2\pi i\delta(E - H_0)T^+$ substitutions are made. This gives the result,

$$\rho^{out(4)}_{M_1M_2} = \frac{dP}{dS}\frac{1}{2}\sum_{\alpha\alpha_0}\int d\Omega_0 f^{\alpha\alpha_0}_{MM_1}(\vartheta_0,\phi_0)\, f^{\alpha\alpha_0}_{MM_2}{}^*(\vartheta_0,\phi_0) \tag{25}$$

Here we are interested in the change of the reduced atomic density matrix by elastic scattering. Thus we define the quantity,

$$\Delta\rho_{M_1M_2} = \rho^{out}_{M_1M_2} - \rho^{in}_{M_1M_2} \tag{26}$$

where,

$$\rho^{in}_{M_1M_2} = \langle JM_1|\rho^{in}|JM_2\rangle \tag{27}$$

Using Eqn's (16), (17), (21), (24), and (25) in Eq. (26), we obtain,

$$\begin{aligned}\Delta\rho_{M_1M_2} = &\frac{2\pi}{k_{in}} i \frac{dP}{dS}\frac{1}{2}\sum_{\alpha}\left[f^{\alpha\alpha}_{MM_1}(\vartheta=0,\phi=0)\delta_{MM_2} - f^{\alpha\alpha}_{MM_2}{}^{*}(\vartheta=0,\phi=0)\delta_{MM_1}\right] \\ &+ \frac{dP}{dS}\frac{1}{2}\sum_{\alpha\alpha_0}\int d\Omega_0 f^{\alpha\alpha_0}_{MM_1}(\vartheta_0,\phi_0) f^{\alpha\alpha_0}_{MM_2}{}^{*}(\vartheta_0,\phi_0)\end{aligned} \tag{28}$$

This is the fully quantum mechanically obtained expression which shows the linear terms in the scattering amplitude and corresponds to the semi-classical expression given by our Eq.(4). Here we shall make an argument which is based on the assumption that the scattering electron is considered distinguishable (i.e. we neglect exchange) and is described non-relativistically. Under these assumptions the angular momentum projection quantum number of the target state and the spin-projection of the incident electron are conserved upon elastic scattering in the forward direction and they are independent of the spin projection of the incident electron. We can therefore write,

$$f^{\alpha\alpha}_{MM_1}(\vartheta=0,\phi=0) = f_{MM}(\vartheta=0,\phi=0)\delta_{MM_1} \tag{29}$$

Then we obtain for $\Delta\rho_{M_1M_2}$, the formula

$$\begin{aligned}\Delta\rho_{M_1M_2} = &\frac{2\pi}{k_{in}} i \frac{dP}{dS}\left[f_{MM}(\vartheta=0,\phi=0) - f^{*}_{MM}(\vartheta=0,\phi=0)\right]\delta_{MM_1}\delta_{MM_2} \\ &+ \frac{dP}{dS}\frac{1}{2}\sum_{\alpha\alpha_0}\int d\Omega_0 f^{\alpha\alpha_0}_{MM_1}(\vartheta_0,\phi_0) f^{\alpha\alpha_0}_{MM_2}{}^{*}(\vartheta_0,\phi_0)\end{aligned} \tag{30}$$

If we now use the mathematical identity,

$$f_{MM}(\vartheta=0,\phi=0) - f^{*}_{MM}(\vartheta=0,\phi=0) = 2i\,\mathrm{Im}\, f_{MM}(\vartheta=0,\phi=0)$$

along with the optical theorem (see e.g. Rodberg and Thaler [23] pp 183-186),

$$\mathrm{Im}\, f_{MM}(\vartheta=0,\phi=0) = \frac{k_{in}}{4\pi}\sigma_{MM}$$

where σ_{MM} is the integrated cross section defined by the formula,

$$\sigma_{MM} = \frac{1}{2}\sum_{\alpha}\int d\Omega\left|f^{\alpha\alpha}_{MM}(\vartheta,\phi)\right|^2 \tag{31}$$

we obtain for $\Delta\rho_{M_1M_1}$ the expression,

$$\Delta\rho_{M_1M_1} = -\frac{dP}{dS}\sigma_{M_1M_1}\,\delta_{MM_1}\delta_{MM_2} + \frac{dP}{dS}\frac{1}{2}\sum_{\alpha\alpha_0}\int d\Omega_0 f^{\alpha\alpha_0}_{MM_1}(\vartheta_0,\phi_0) f^{\alpha\alpha_0}_{MM_2}{}^{*}(\vartheta_0,\phi_0) \tag{32}$$

These transformations are of great physical significance as we will see below.

This expression was obtained with the assumption that the initial state was described by the density operator,

$$\rho^{in} = |JM\rangle\langle JM| \tag{17}$$

Here we are interested in alignment creation by elastic scattering from an initial isotropic state (with no alignment). The isotropic state will be described by the density operator,

$$\rho^{in}_{iso} = \frac{1}{2J+1}\sum_{M}|JM\rangle\langle JM| \tag{33}$$

giving the initial density matrix as,

$$\rho^{in,iso}_{M_1M_2} = \frac{1}{2J+1}\delta_{M_1M_2} \tag{34}$$

Since ρ^{in}_{iso} is additive from the ' ρ^{in} elements', we can simply sum Eq.(32) over M and divide by $(2J+1)$ to obtain,

$$\Delta\rho^{iso}_{M_1M_2} = -\frac{dP}{dS}\frac{1}{2J+1}\left\{\sigma_{M_1M_1}\,\delta_{M_1M_2} - \frac{1}{2}\sum_{\alpha\alpha_0}\sum_{M}\int d\Omega_0 f^{\alpha\alpha_0}_{MM_1}(\vartheta_0,\phi_0) f^{\alpha\alpha_0}_{MM_2}{}^{*}(\vartheta_0,\phi_0)\right\} \tag{35}$$

where $\Delta\rho^{iso}_{M_1M_1}$ is the change of the density matrix element of the initially isotropic state by the elastically scattered electron. The alignment created in the scattering process from the isotropic state can be given in the form (see e.g. Blum [24], p. 98),

$$\left\langle T(J)^{+}_{20}\right\rangle = \frac{5^{1/2}}{\left[(2J+3)(2J+1)J(2J-1)(J+1)\right]^{1/2}}\sum_{M}\left[3M^2 - J(J+1)\right]Q(M) \tag{36}$$

where

$$\mathrm{Q(M)} = \Delta\rho^{\mathrm{iso}}_{\mathrm{MM}} \tag{37}$$

From Eq.(35) we obtain,

$$\begin{aligned}\Delta\rho^{iso}_{MM} &= -\frac{dP}{dS}\frac{1}{2J+1}\left\{\sigma_{MM} - \frac{1}{2}\sum_{\alpha\alpha_0}\sum_{M'}\int d\Omega_0\left|f^{\alpha\alpha_0}_{M'M}(\vartheta_0,\phi_0)\right|^2\right\} \\ &\equiv \frac{dP}{dS}\frac{1}{2J+1}\left\{\frac{1}{2}\sum_{\alpha\alpha_0}\sum_{M'}\sigma^{\alpha\alpha_0}_{MM'} - \sigma_{MM}\right\} \\ &= \frac{dP}{dS}\frac{1}{2J+1}\left\{\sum_{M'}\sigma_{MM'} - \sigma_{MM}\right\}\end{aligned} \tag{38}$$

where we have defined the $\sigma_{MM'}$ cross section by the formula,

$$\sigma_{MM'} \equiv \frac{1}{2}\sum_{\alpha\alpha_0}\sigma_{MM'}^{\alpha\alpha_0} \tag{39}$$

We can define the alignment creation cross section by the formula,

$$Q_{20} = \left(\frac{dP}{dS}\right)^{-1}\left\langle T(J)_{20}^{+}\right\rangle \tag{40}$$

which gives,

$$Q_{20} = \frac{5^{1/2}}{\left[(2J+3)(2J+1)J(2J-1)(J+1)\right]^{1/2}}\sum_{M}\left[3M^2 - J(J+1)\right]q(M) \tag{41}$$

where

$$q(M) = \frac{1}{2J+1}\left\{\frac{1}{2}\sum_{\alpha\alpha_0}\sum_{M'}\sigma_{MM'}^{\alpha\alpha_0} - \sigma_{MM}\right\} = \frac{1}{2J+1}\left\{\sum_{M'}\sigma_{MM'} - \sigma_{MM}\right\} \tag{42}$$

For the $J = 1$ case which is relevant to the experiment of Trajmar et al. [18],

$$Q_{20} = \left(\frac{2}{3}\right)^{1/2}\left(q(1) - q(0)\right) = \left(\frac{2}{3}\right)^{1/2}\frac{1}{3}\left(\sigma_{10} + \sigma_{1-1} - 2\sigma_{01}\right) \tag{43}$$

For electron scattering from laser excited neutral Barium, we have from converged close coupling (CCC) calculations (Trajmar et al. [18]):

Table 1. Magnetic Sublevel Cross Sections and Alignment Creation Cross Section The Magnetic sublevel cross sections $\sigma_{MM'}$, alignment creation cross section Q_{20}, and the total cross section Q (all in units of 10^{-16} cm^2) for differing incident electron energies.

E_k^{in}(eV):	2.8	20.0	97.8
σ_{10}	1.16	0.59	0.054
σ_{1-1}	4.52	1.57	0.360
σ_{01}	1.97	0.70	0.054
Q_{20}	0.47	0.21	0.310
Q	114.30	36.36	17.26

The earlier calculation by Trajmar et al. [18] that used the inelastic formula for Q_{20} gave the respective values of 8.70, 2.33 and 1.00 for the above energies.

4. Discussion and Conclusions

Here we have obtained a formula by quantum-mechanical methods for the alignment creation cross section by elastic electron scattering. The formula obtained differs from the analogous formula relevant for inelastic electron scattering. In the case of a $J = 1$

to $J=1$ transition according to the inelastic formula the alignment created is proportional to the quantity $\sigma(1)-\sigma(0)$ where $\sigma(M)$ is the excitation cross section of the M magnetic sublevel and thus $\sigma(1)=(\sigma_{1-1}+\sigma_{10}+\sigma_{11})/3$ and $\sigma(0)=(\sigma_{0-1}+\sigma_{00}+\sigma_{01})/3$ where $\sigma_{MM'}$ refers to the cross section of the electron impact induced M' to M transition. In the elastic scattering alignment creation formula obtained by us in the case of a $J=1$ to $J=1$ elastic scattering, the alignment created is proportional to the quantity $q(1)-q(0)$ where $q(1)=\sigma(1)-\sigma_{11}/3$ and $q(0)=\sigma(0)-\sigma_{00}/3$. Thus in obtaining $q(M)$, the elastic scattering cross section by the M magnetic sublevel, σ_{MM}, is subtracted. Indeed it was intuitively felt for some time by us that such a cross section (i.e. σ_{MM}) should not contribute to the alignment creation cross section by elastic scattering. Thus we can conclude that the 'linear terms' that were missing in the earlier expression have clear physical meaning in the quantum mechanical case while their meaning in the semi-classical case was not clear [27]. Our derivation considered only direct scattering, i.e. the incident electron was considered distinguishable from the target electrons. The wave packet treatment of exchange was discussed by Goldberger and Watson [25], by Rodberg and Thaler [23], and by Kelly [26].These works indicate that the major part of our results carry over when exchange scattering is also considered. However when both exchange and spin-orbit coupling are incorporated into the treatment the final formula might not be correct. However as long as the spin-flip cross section is small in the forward direction compared to the spin-conserved cross section (no spin-flip) our formula derived here will be valid and the essential physical interpretation discussed above will still obtain. Future work will be directed toward the treatment of exchange and spin-orbit coupling effects quantitatively.

Acknowledgements

The authors want to thank Professor T. Fujimoto for suggesting this problem and for his collaboration throughout the years. This work was partially conducted under the auspices of the U.S. Department of Energy. Support of the Australian Research Council is also acknowledged.

References

[1] A. Omont, Jour. de Phys. **26**, 26 (1965).

[2] M.I. D'yakonov and V.I. Perel, JETP (USSR) **48**, 345 (1965) (English translation: Soviet Physics JETP, **21**, 227 (1965)).

[3] V.N. Rebane and T.K. Rebane, Opt. i Spektrosk. **20**, 185 (1966) (English translation: Optics and Spectroscopy, 20, 101 (1966)).

[4] V.N. Rebane, Opt. i Spektrosk., **21**, 405 (1966) (English translation: Optics and Spectroscopy, **21**, 229 (1966)).

[5] V.N. Rebane, Opt. i Spektrosk. , **24**, 296 (1968) (English translation: Optics and Spectroscopy, **24**, 155 (1968)).

[6] V.N. Rebane, Opt. i. Spektrosk. , **24**, 309 (1968) (English translation: Optics and Spectroscopy, **24**, 163 (1968)).

[7] A.G. Petrashen, V.N. Rebane, and T.K. Rebane, Opt. i Spektrosk., **55**, 819 (1983) (English translation: Optics and Spectroscopy, **55**, 492 (1984)).

[8] A.G. Petrashen, V.N. Rebane, and T.K. Rebane, Opt. i Spektrosk. **56**, 376 (1984) (English translation: Optics and Spectroscopy, **56**, 230 (1984)).

[9] A.G. Petrashen, V.N. Rebane, T.K. Rebane Zh. Eksp. Teor. Fiz. **87**, 147 (1984) (English translation: Sov.Phys. JETP, **60**, 84 (1984)).

[10] A.G. Petrashen, V.N. Rebane, and T.K. Rebane, Zh.Eksp.Teor.Fiz. **94**, 46 (1988) (English translation: Sov.Phys.JETP, **67**, 2202 (1989)).

[11] A.G. Petrashen, V.N. Rebane, Opt. i Spektrosk., **67**, 6 (1989) (English translation: Optics and Spectroscopy, **67**, 3 (1990)).

[12] S.A. Kazantsev, A.G. Petrashen, V.N. Rebane, Zh.Eksp.Teor.Fiz **106**, 698 (1994) (English translation: Sov.Phys. JETP **79**, 384 (1994)).

[13] T. Fujimoto, H. Sahara, G. Csanak, and S. Grabbe, Atomic States and Collisional Relaxation in Plasma Polarization Spectroscopy, Research Report NIFS-DATA Series, NIFS-DATA-38, Oct. 1996, Nagoya, Japan.

[14] T. Fujimoto and S.A. Kazantsev, Plasma Phys. Control.Fusion **39**, 1267 (1997).

[15] E.I. Dashevskaya and E.E. Nikitin, Sov. J. Cem. Phys. **4**, 1934 (1987).

[16] S.A. Kazantsev, N.Ya. Plynovskaya, L.N. Pyatnitskii, and S.A. Edel'man, Usp.Fiz.Nauk **156**, 3 (1988) (English translation: Sov.Phys.Usp. **31**, 785 (1988)).

[17] S.A. Kazantsev and J.-C. Henoux, Polarization Spectroscopy of Ionized Gases, Kluwer Academic Publishers, Dordecht, 1995, p. 33.

[18] S. Trajmar, I. Kanik, M.A. Khakoo, L.R. LeClair, I. Bray, D. Fursa, and G. Csanak, J. Phys. B: At. Mol. Opt. Phys. **32**, 2801 (1999).

[19] G. Csanak, D.P. Kilcrease, H. Zhang, D.V. Fursa, I. Bray, T. Fujimoto, and A. Iwamae, Plasma Polarization Spectroscopy for the OV Ion: Relevant Collision Cross Sections for Kinetic Modeling, in Proceedings of the 3rd US-Japan Plasma Polarization Spectroscopy Workshop, June 18-21, 2001 (P. Beiersdorfer and T. Fujimoto, Editors) University of California Lawrence Livermore National Laboratory Report UCRL-ID-146907.

[20] A. Ben-Reuven, Phys. Rev. **145**, 7 (1966).

[21] G. Nienhuis, J. Phys. B: At. Mol. Phys. **9**, 167 (1976).

[22] V. Bommier and S. Sahal-Brechot, Ann. Phys. Fr. **16**, 555 (1991).

[23] L.S. Rodberg and R.M. Thaler, Introduction to the Quantum Theory of Scattering, Academic Press, New York, 1967.

[24] K. Blum, Density Matrix Theory and Applications, Plenum, New York, 1981.

[25] M.L. Goldberger and K.M. Watson, Collision Theory, Krieger Publishing Co., New York, 1975.

[26] R.L. Kelly, Phys. Rev. **147,** 376 (1966).

[27] P. Paradoksov, Usp. Fiz. Nauk **89**, 707 (1996) (English translation: Sov. Phys. Uspekhi **9**, 618 (1967)).

A short demonstration of using the Flexible Atomic Code (FAC)

Hui Chen
Lawrence Livermore National Laboratory, Livermore, CA 94551, USA

1. Basic information on the FAC code

FAC stands for Flexible Atomic Code. It was written and maintained by Ming-Feng Gu. Gu is at the Physics department, Stanford University at the present. The code was written when Gu was at MIT as a Chandra Fellow, a prestigious award given to young talented astrophysicists.

The FAC code is distributed free of charge. Anyone who is interested can download the code from website:
http://kipac-tree.stanford.edu/fac
Ming Feng Gu, Stanford University, mfgu@stanford.edu Tel: 650-724-3431

One of the greatest virtues of the FAC code is that it is easy to use. It uses simple python scripts to carry out complex functions. It is ideal for people who do not want to get too deep into the complicated atomic calculation theories and numerical techniqes but want to gain decent atomic predictions.

The tasks the FAC can perform are vast in number and range. Details can be obtained from the manuals included with the free code package. One cannot only use the already built-in capacities to obtain the desired atomic calculations, but also use the easy-to-apply output (such as cross-sections) as input for ones own models (such as a kinetic atomic model). Both aspects have been tested and put to actual applications by many with great successes.

However, as the author's "disclaimer" from the manual states:

"*FAC is freely distributed in the hope that it will be useful. The author makes every effort to ensure its correctness. However, he does not guarantee its fitness to any specific purpose. The author is not responsible for any damage resulting from the use of this program, including failure to obtain or loss of tenure.*"

2. Atomic physics embedded in the FAC code

The FAC code is an integrated software package to calculate various atomic radiative and collisional processes, including energy levels, radiative transition rates, collisional excitation and ionization by electron impact, photoionization, autoionization, radiative recombination and dielectronic capture. The package also includes a collisional radiative model to construct synthetic spectra for plasmas under different physical conditions. It also calculates the degree of linear polarizations. Gu has compared the FAC calculations with those from other codes. Two examples are shown in the Table 1 and Figure 1.

Table 1

Comparison with Sampson & Zhang Code

	Level	FAC ΔE	FAC gf	SZ ΔE	SZ gf
2	$(2p_{3/2}3s_{1/2})_1$	726.99	0.1214	727.22	0.1102
4	$(2p_{1/2}3s_{1/2})_1$	739.24	0.1049	739.50	0.0937
16	$(2p_{3/2}3d_{3/2})_1$	802.42	0.0103	802.64	0.0099
22	$(2p_{3/2}3d_{5/2})_1$	812.88	0.6333	813.15	0.6095
26	$(2p_{1/2}3d_{3/2})_1$	827.32	2.6120	827.69	2.5514
30	$(2s_{1/2}3p_{1/2})_1$	894.81	0.0338	894.83	0.0358
32	$(2s_{1/2}3p_{3/2})_1$	899.18	0.2767	899.18	0.2868

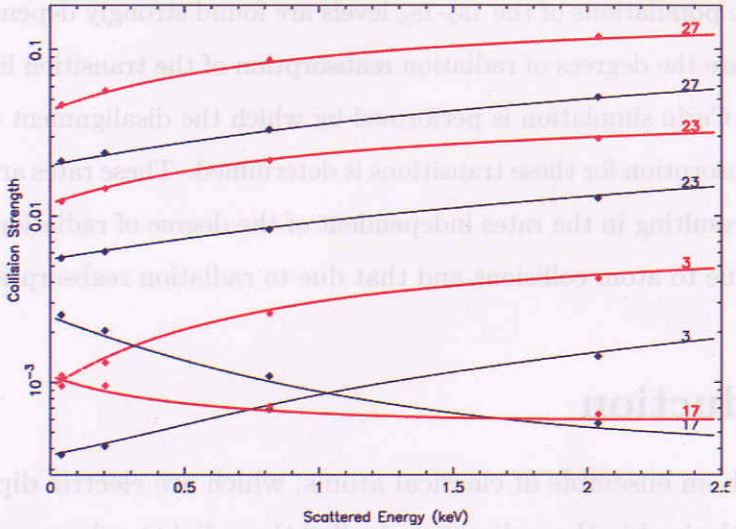

Figure 1: Comparison of M sublevel collision strength of Ne-like Iron from FAC calculation and Zhang and Sampson's calculations. Solid lines are FAC results; diamonds are from Zhang and Sampson (PRA 41, 198, 1990). Thinner lines for M=1 states, thicker lines for M=0 states. Levels 27,23,17,3 correspond to 3C, 3D, 3E and 3G lines.

Gu provides users with a number of documents. They are included in the doc folder of the package. Besides 76 pages manual (which explains the usages and the functions of the code), Gu has 5 papers on the following topics that describe the detailed atomic physics model of the code:

The Flexible Atomic Code: I. Atomic Structure
The Flexible Atomic Code: II. Electron Impact Excitation
The Flexible Atomic Code: III. Photoionization and Radiative ecombination
The Flexible Atomic Code: IV. Autoionization and Dielectronic Recombination
The Flexible Atomic Code: V. Electron Impact Ionization

The published reference for the FAC code is:
Gu, M. F., Astrophysical Journal, 582, 1241, (2003)

Relaxation of atomic polarization by radiation re-absorption

Masanori Nimura, Masahiro Hasuo, and Takashi Fujimoto

Department of Engineering Physics and Mechanics, Graduate School of Engineering, Kyoto University, Kyoto 606-8501, Japan

Abstract

In a positive column of a glow discharge, a polarized laser pulse produces polarized neon atoms in the $2p_2$ (Paschen notation) level, and the subsequent fluorescence is observed with its polarized components resolved. The disalignment rate and the disorientation rate are thus determined. The populations of the $1s_2$-$1s_5$ levels are found strongly dependent on the discharge current, and so are the degrees of radiation reabsorption of the transition lines from $2p_2$ to these levels. A Monte Carlo simulation is performed by which the disalignment or disorientation rate by radiation reabsorption for these transitions is determined. These rates are subtracted from the observed rates, resulting in the rates independent of the degree of radiation reabsorption. Thus, depolarization due to atom collisions and that due to radiation reabsorption are separated.

1 Introduction

We start with an ensemble of classical atoms, which are electric dipoles, excited by the light linearly polarized in the z-direction (called the π-light), where we define the direction of polarization as the direction of the oscillating electric field. The electric dipoles begin to oscillate along the z-direction. The anisotropy of atomic states produced by such a directional excitation is called the *alignment*.

Both the population and the alignment subsequently decay with time. We call the relaxation of the alignment the *disalignment*. If this excitation-decay process occurs in an atomic vapor, the fluorescence radiation emitted by an atom may be absorbed by another atom in the vapor. In this study, we performed the Monte Carlo simulation on radiation re-absorption, and determined the disalignment rate due to radiation re-absorption quantitatively.

2 Experiment: disalignment

Figure 1 shows the block diagram of our experimental set-up. The excitation light source is the dye laser pumped by the frequency-doubled pulsed YAG laser. The laser light is tuned to the λ616.4 nm ($1s_3 - 2p_2$). Before entering into the cell, the laser light passes through an aperture of 1 mm diameter and the Glan-Thompson prism, by which the laser light is linearly polarized in the direction perpendicular to the paper of this figure. We choose this direction as the quantization axis, so the laser light is π polarized. The laser light pulse is incident on the discharge plasma and excites one of the upper levels. The analyzing polarizer selects one of the two polarized components, *i.e.*, the π-light or the σ-light which is polarized parallel to the paper in figure 1. The fluorescence of the λ659.9 nm ($1s_2 - 2p_2$) transition is selected and its intensity is measured with the photomultiplier. The discharge cell consists of three layers. The central discharge channel has an inner diameter of 5 mm. The surrounding layer is for the purpose of controlling the temperature of the discharge channel. In the present experiment, this space is filled with liquid nitrogen, and the temperature of the discharge gas is 77 K. The outer layer is vacuum for thermal insulation.

Figure 2(a) shows the partial energy level diagram of neutral neon atoms relevant to the experiment described in this paper. The upper level is one of the ten $2p^5 3p$ configuration levels, *i.e.*, $2p_2$ in the Paschen notation. The total angular momentum quantum number is J'=1. Lower levels connected by electric dipole transitions are of the $2p^5 3s$ configuration, *i.e.*,$1s_2$ (J=1), $1s_3$ (J=0), $1s_4$ (J=1) and $1s_5$ (J=2). Since, in figure 2(b), we excite the (J=0 $\rightarrow$ J'=1) transition with the π-component only the magnetic sublevel with $m_{J'}$=0 is populated among the three magnetic sublevels of the upper level $2p_2$ (J'=1). Since we observe the fluorescence of the (J=1 $\leftarrow$ J'=1) transition, this magnetic sublevel emits only the σ-light, as understood in figure 2(c). Figure 3 shows an example of the observed fluorescence intensities of this component. This figure also contains the π-component. It is seen that the π-component is observed with substantial intensities. In this figure, we recognize that the relative intensity of the π-component to the σ-component increases with time; *i.e.*, the degree of polarization decreases. The degree of polarization is quantified in

terms of the longitudinal alignment

$$A_{\mathrm{L}} = \frac{I_\pi - I_\sigma}{I_\pi + 2I_\sigma}, \tag{2.1}$$

It is noted that this quantity is proportional to $[(n_0 - n_1)/(n_0 + 2n_1)]$, and decays exponentially with time. Here n_0 and n_1 are the populations of the magnetic sublevels of the upper level. We define this decay rate as the disalignment rate. Figure 4 shows the time dependence of the longitudinal alignment (with the sign reversed) as deduced from the data of figure 3. From the fitted line in figure 4, we determine the disalignment rate to be $(8.9\pm0.3) \times 10^6$ s^{-1} as given by the closed circle in figure 5. This figure shows the disalignment rates observed for various discharge currents. It is obvious that the apparent rate increases with the increase in the discharge current. Under our experimental conditions the disalignment can be brought about by three mechanisms: *i.e.*, by atom collisions, by electron collisions and by radiation reabsorption. Throughout the condition of Figure 5 the atom temperature is virtually 77 K[2] and the atom density is constant. Thus, the disalignment rate by atom collisions should be constant in this figure. It is known that electron density is approximately proportional to the discharge current, which is confirmed quantitatively by the microwave resonance method on similar discharges[3]. In our present case, electron density is estimated from [3] to be about 2×10^{16} m^{-3} at the highest discharge current. From the measured disalignment rate coefficient of $(4.1\pm1.0) \times 10^{-13}$ m^3/s [4], we obtain the disalignment rate of less than 10^4 s^{-1} under our discharge conditions. This rate is smaller than the observed disalignment rates by about three orders of magnitude and is well neglected. The third mechanism, disalignment by radiation reabsorption is the subject of this study. The increase can be attributed to the effect of an increase in radiation reabsorption: with the increase in the discharge current the populations of the lower levels, $1s_2$ – $1s_5$, may increase, and, since these levels are connected by the radiative transitions with the upper level $2p_2$, as seen in figure 2(a), radiation reabsorption of these transitions may accordingly increase, and thereby increasing the disalignment rate of the $2p_2$ level atoms.

3 Experiment: lower-level populations

In figure 1, on the opposite side of the discharge cell to the observation direction, a concave mirror with the radius of 150 mm is placed, and the light from the discharge plasma through the slit of the discharge channel wall is reflected back and focused by this mirror on the plasma itself. The laser beam is absent, and we observe the emission lines from the dc discharge plasma with the same monochromator and the photomultiplier as in the previous section. The output current from the photomultiplier is measured with the digital electrometer (Advantest, R8340). We observe the intensities of an emission line with and without the mirror. As a measure of the strength of absorption, or of the optical thickness, of this plasma to this transition line, we define the *line absorption* as

$$\alpha = 1 - (I_2 - I_1)/I_1, \tag{3.2}$$

where I_1 is the observed emission line intensity without the mirror and I_2 is that with the mirror. In the optically thin limit, α tends to zero, while for completely optically thick case, it tends to 1. We determine the line absorption of the four lines in figure 2 under all the discharge conditions in figure 5. The maximum line absorption is about 0.5 for the λ616.4 nm line at the current of 2 mA. The optical thickness was calculated from the experimental line absorption values. The maximum optical thickness at the line center was 1.37. This indicates that the plasma is not necessarily optically thin and, thus, the effect of radiation reabsorption may be substantial. We thus determined the lower level populations averaged over the discharge channel diameter[6]. Figure 6 shows the result. It is actually seen that, with the increase in the discharge current, the lower-level populations increase. We easily recognize the similarities between these current dependences and that of the observed disalignment rate.

4 Monte Carlo simulation

We simulate the disalignment process due to the radiation reabsorption. We perform the Monte Carlo simulation on the following assumptions:

1. The spatial population density distribution of the lower level atoms over the discharge channel is given by the zero-th order Bessel function[7].

2. The initial excitation takes place in the axial region of 1 mm diameter in the plasma of 5 mm diameter cylinder with infinite length.
3. The atoms in the lower level and the upper level have the same Maxwell distribution with 77 K. This assumption is equivalent to the assumption of complete frequency redistribution[8, 9].

The steps of the simulation is as follows:

1. The initial state is the $m_{J'}$=0 magnetic sublevel of $2p_2(J'=1)$, and we follow the light emission-absorption process for the four transitions given in figure 2(a). If this step is in the second or later cycle of this simulation in which this atom is produced by photoabsorption, its state is the coherent superposition of the states of the three magnetic sublevels.
2. We choose one of the transitions according to the transition probability as given in figure 2(a). In this transition, we treat transitions of $(m_J \leftarrow m_{J'})$ to different lower sublevels separately. We choose one lower sublevel m_J.
3. Each of the transitions of $(m_J \leftarrow m_{J'})$ is characterized by the 3-j symbol. The radiation field from each transition is regarded as that from a classical electric dipole.
4. For this particular m_J, the radiation field is produced by the classical oscillator, the state of which is determined from the states of the upper sublevels. We choose the direction of the emitted radiation or a photon. Then, the electric field vector in space, or the polarization state of the photon, in this direction is determined.
5. This photon travels over a certain distance and may be absorbed by an atom in the lower level according to the absorption coefficient. Here the magnetic sublevels are assumed incoherent and equally populated.
6. An atom in one of the magnetic sublevels absorbs this photon and is excited into the coherent superposition of the sublevels $m_{J'}$ in the upper level, according to the polarization state of the photon.
7. We return to step (1).
8. We repeat the above procedure until the last photon reaches the wall or the slits. We register the photons which emanate from the slit of 1 mm width and record the time and the polarization state of each of them.

We repeat this chain of procedures about 10^7 times under each discharge condition.

The result is given with the open circles in figure 5. On the assumption that disalignment by atom collisions and that by radiation reabsorption are additive, we subtract this contribution from the observed disalignment rates. The solid squares show the result. It is seen that the resulting disalignment rate is virtually independent of the discharge current, so that this rate, 4.6×10^6 s^{-1}, is regarded as the disalignment rate solely by atom collisions.

5 Measurements of the disorientation rates

We can create the oriented state easily using the same experimental setup described in figure 1. We set the Soleil-Babinet compensator, and made the laser light circularley polarized. If we take the traveling direction of the laser light as the quantization axis, the excited atoms are said to be oriented. The definition of the oriented states and the aligned states can be seen in many papers. For example, see [10]. We measured the disorientation rates in a similar way as the measurement of the disalignment rates. The closed circles in figure 7 show the results. This figure also includes the open circles and solid squares which represent the simulation results, and the disorientation rates by atom collisions respectively. We obtained the disorientation rate by atom collisions to be 8.80×10^6 s^{-1}. This value is larger than the disalignment rate by atom collisions by nearly factor 2. We do not have any model that account for this difference.

reference

[1] M.Seo, M.Nimura, M.Hasuo, and T.Fujimoto, *J.Phys.B* **36** 1869 (2003)

[2] Holt H K 1976 *Phys.Rev.A* **13** 1442

[3] Wakabayashi T, Yamamoto A, Yaneda T, Furutani T, Hishikawa A and Fujimoto T 1998 *J.Phys.B* **31** 341 (1998)

[4] Takaishi T and Sensui Y 1963 Trans. Farad. Soc. **59** 2953

[5] Hirabayashi A, Nambu Y, Hasuo M and Fujimoto T 1988 *Phys.Rev.A* **37** 83

[6] Kazantsev S A, Luchinkina V V, Mezentsev A P, Mustafaev A S, Rebane V N, Rys A G and Stepanov Yu L 1994 *Opt.Spectrosc.* **76** 809

[7] Fujimoto T, Goto C and Fukuda K 1982 *PhysicaScripta* **26** 443

[8] Hishikawa A, Fujimoto T and Erman P 1995 *Phys.Rev.A* **52** 189

[9] Holstein T 1947 *Phys.Rev.* **72** 1212; 1951 *Phys.Rev.* **83** 1159

[10] A. Fischer and I.V. Hertel, Z. Phys. A-Atoms and Nuclei **304**, 103 (1982)

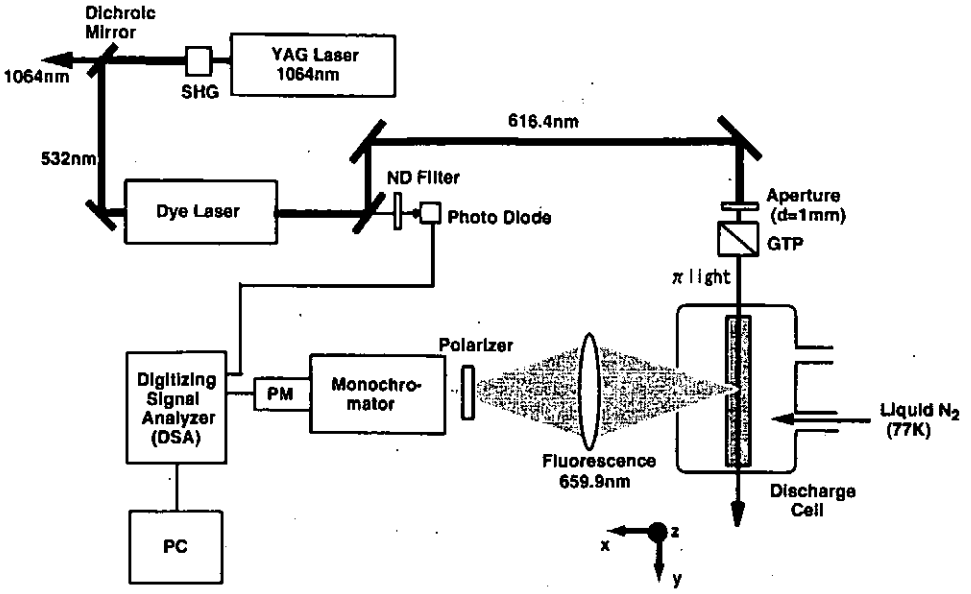

Figure 1: A schematic diagramof the experimental set-up. SHG: second harmonic generator, ND filter: neutral density filter, PM: photomultiplier.

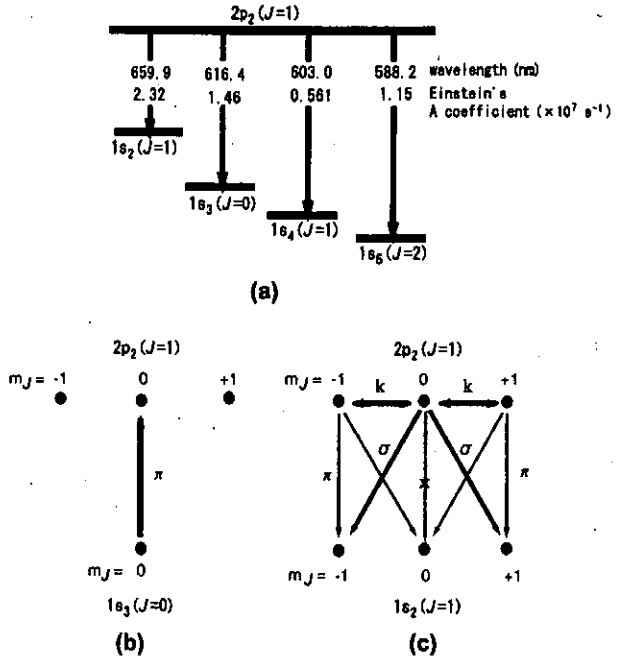

Figure 2: (a)The partial energy level diagram relevant to the present (b)The Kastler diagram for the emission of the $1s_3 - 2p_2$ transition showing the π-light excitation (c)The Kastler diagram for the emission of the $1s_2 - 2p_2$ transition and population transfer between the magnetic sublevels.

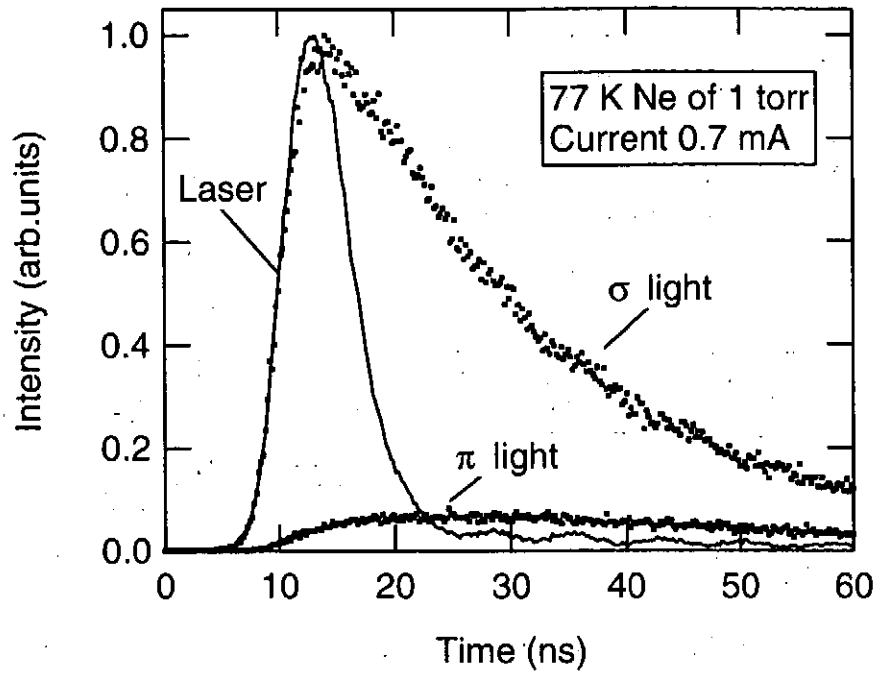

Figure 3: An example of the observed fluorescence line $(1s_2 - 2p_2)$ intensities with the polarized components resolved subsequent to the π-light excitation of the $1s_3 - 2p_2$ transition.

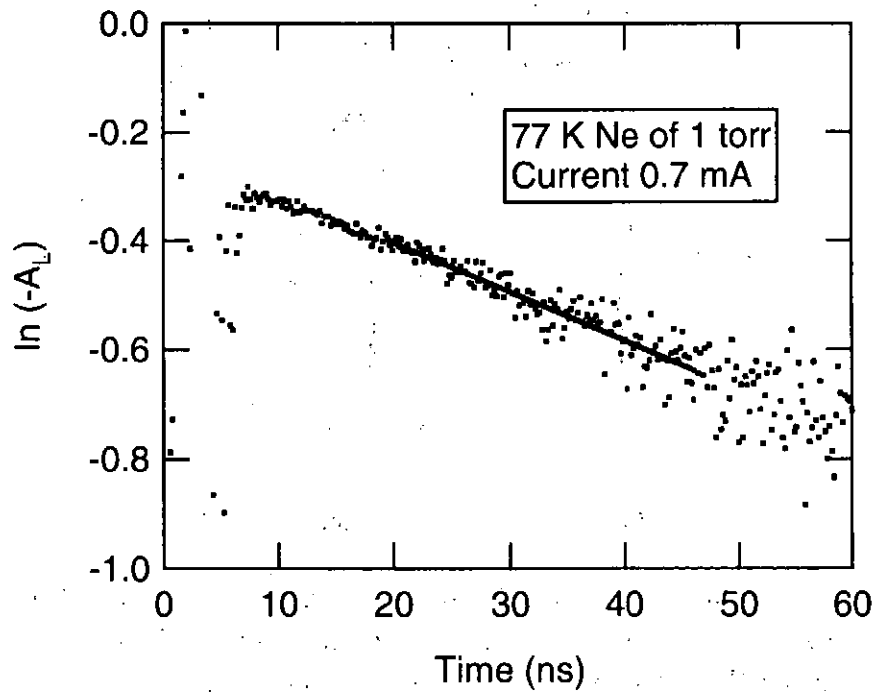

Figure 4: The longitudinal alignment (with sign reversed) deduced from the data in figure 3.The slope of the decay is the disalignment rate.

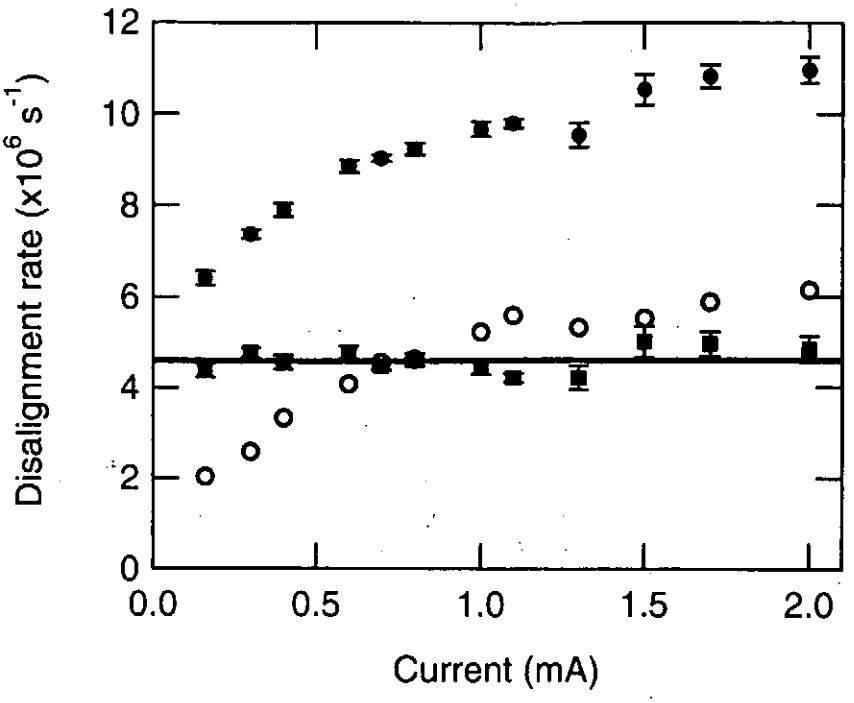

Figure 5: Disalignment rate against the discharge current. 77 K neon of 1 Torr. The closed circles: experiment, the open circles: simulation, the closed squares: experimental rate minus the simulated rate.

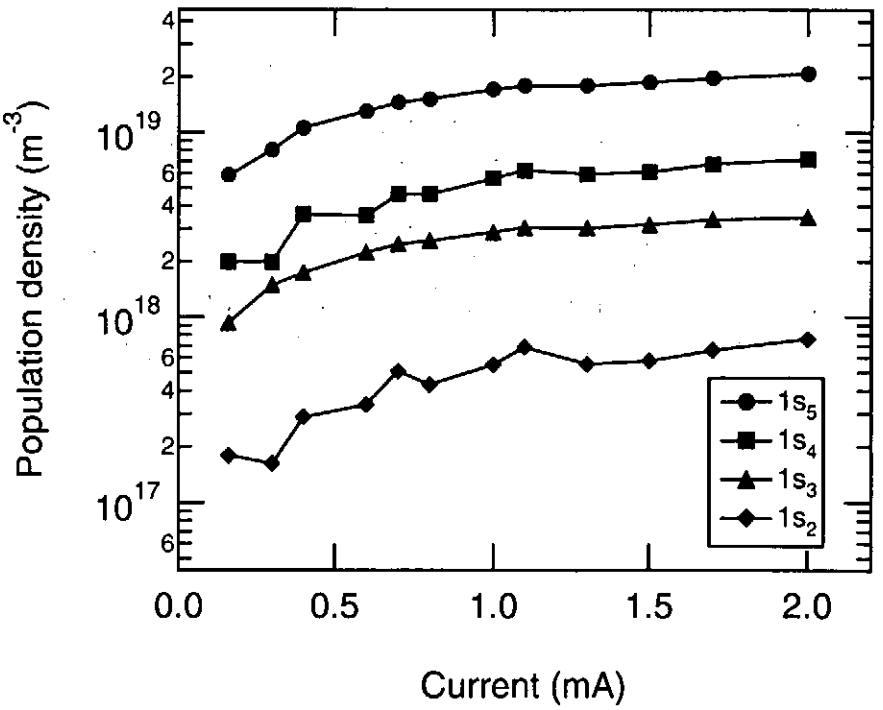

Figure 6: The population of the $1s_2 - 1p_5$ level atoms as determined from the self-absorption experiment.

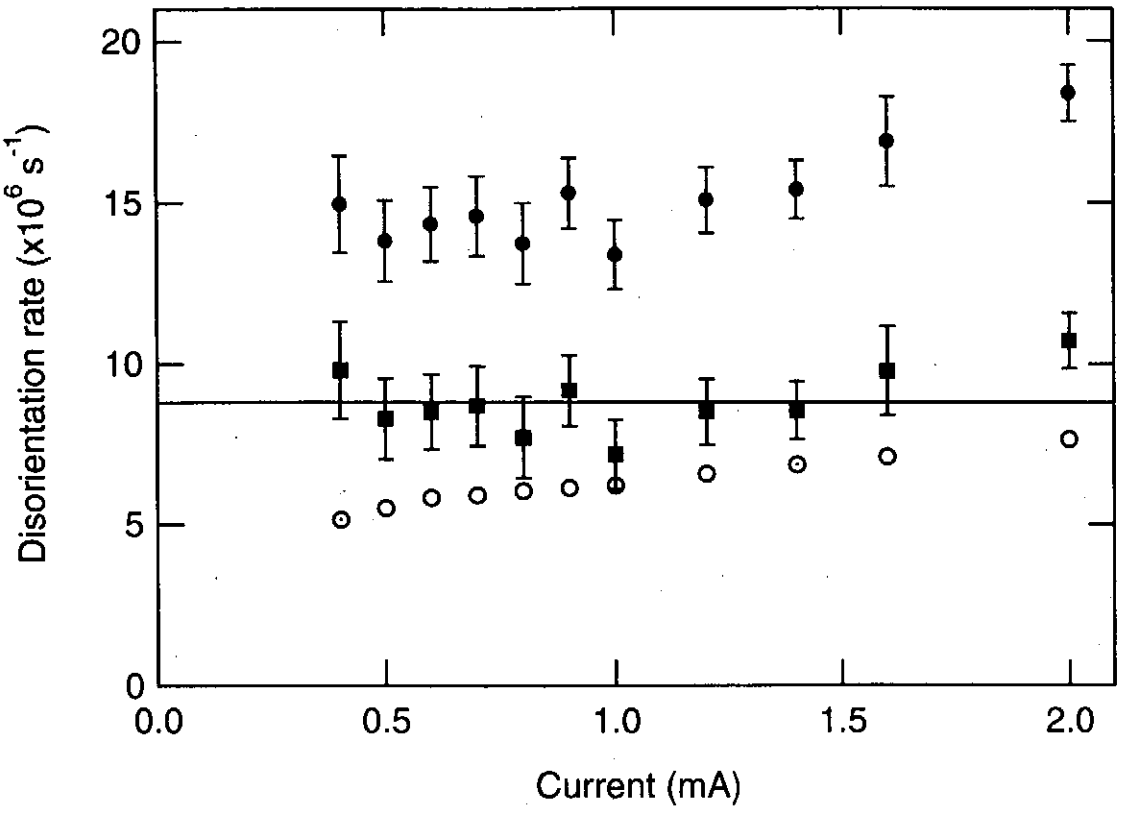

Figure 7: Disorientation rate against the discharge current. 77 K neon of 1 Torr. The closed circles: experiment, the open circles: simulation, the closed squares: experimental rate minus the simulated rate.

Observation of Interference between Stark and Electric Quadrupole Transitions in LIF from He Atoms in Plasmas

K. Takiyama, S. Namba, S. Furukawa,
Graduate School of Engineering, Hiroshima University, Higashi-Hiroshima 739-8527, Japan

T. Oda
Faculty of Engineering, Hiroshima Kokusai Gakuin University, Hiroshima 739-0321, Japan

B. W. James and D. Andruczyk
School of Physics, the University of Sydney, NSW 2006, Australia

Interference between Stark-induced dipole and electric quadrupole amplitudes was observed in a He hollow cathode plasma with axial magnetic field perpendicular to the sheath electric field E by laser-induced fluorescence (LIF) method. Circularly polarized LIF signals were observed in the sheath region. Spatial profile of the degree of polarization P_C showed characteristic features of the interference. Using theoretically calculated P_C-E relationship, E-profile was successfully obtained from the measured P_C.

1. Introduction

The importance of measuring the electric field E induced in plasma edges which plays an essential roll in plasma confinement and plasma processing has been well recognised. Laser-induced fluorescence (LIF) methods utilizing the Stark effect have been extensively developed to directly measure electric field distributions because of their high sensitivity and high spatial resolution [1-3]. There have been, however, few methods applicable to plasmas in a magnetic field B. We have developed a sensitive method to directly measure the electric field in plasmas by using LIF of helium atoms [2]. In this technique the electric field can be determined from the linear polarization of LIF (He I: $n^1D \rightarrow 2^1P$) subsequent to the excitation of forbidden transitions (He I: $2^1S \rightarrow n^1D$). This method has been extended for the plasma in a magnetic field, such as ECR plasma, by considering the influence of the magnetic field on the LIF observation [4, 5]. In $E \perp B$ geometry, as in Fig. 1, the applicability has been demonstrated by previous experiments using a cylindrical hollow cathode plasma in the axial B [6].

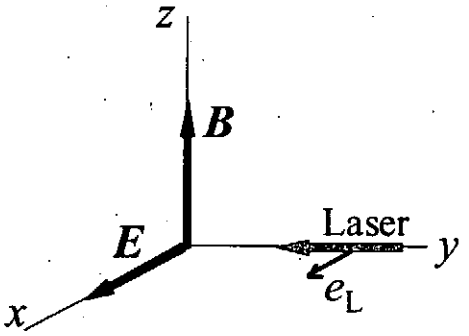

Fig. 1 Geometry for laser-induced fluorescence. e_L: laser polarization

When E is perpendicular to B (Fig. 1), the atomic interference can take place between the Stark-induced electric dipole and the electric quadrupole (QDP) transition amplitudes [6, 7], as shown in Fig. 2. This makes possible a new higher-sensitive LIF measurement. The laser excitation generates anisotropic populations among magnetic sublevels with opposite sign, e.g. m= +1 and −1. The anisotropy can be observed as the circular dichroism of LIF along the magnetic field, which is expected to be an order of magnitude higher than the linear one in sensitivity with respect to the electric field.

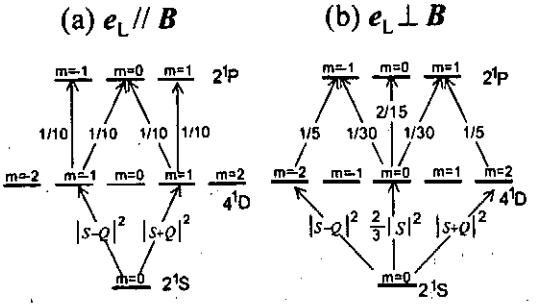

Fig. 2 Relative excitation and fluorescence transition probabilities for the various magnetic sublevels of He I when $E \perp B$. S and Q represent the Stark and quadrupole amplitudes.

The aim of this work is to show the existence of the interference in the laser absorption process and the possibility of higher sensitive electric field measurements by a model-type experiment using a cylindrical hollow cathode discharge with the magnetic field applied perpendicularly to the radial electric field in the plasma sheath.

2. Experimental

The structure of the cylindrical hollow cathode is depicted in Fig. 3 (a). The He plasma was produced in a cylindrical hollow cathode (inner diameter of 30 mm and length of 60 mm) made of aluminium, with a discharge current of 20 mA at a He gas pressure of 0.53 Torr. A magnetic field of 55 G was applied to the plasma by setting a permanent magnet disk on the central axis (z-axis) of the hollow cathode. The cathode-fall potential was observed by an electric probe to be 220 V. The cathode has two rectangular slits (28x0.8 mm^2) to introduce a laser beam into the cylinder and then LIF can be observed in a region between −14mm and +14mm along x-axis.

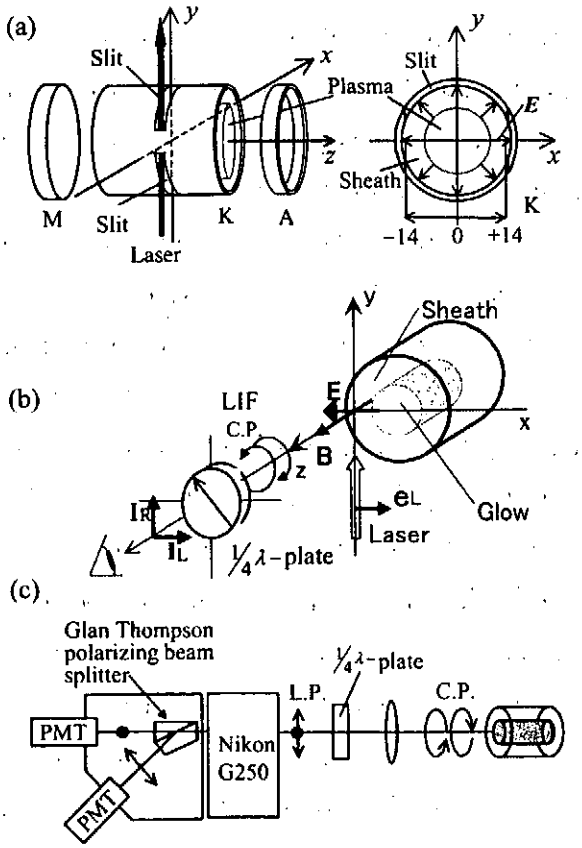

Fig. 3 (a) Schematic view of cylindrical hollow cathode. (b) Geometry for LIF observation. (c) Detection system of circular polarisation.

The excitation of forbidden transition (2^1S-4^1D, 397.2 nm) was made by a YAG pumped dye laser (397.2 nm) with pulse width of 5 ns. The polarization direction of laser e_L was chosen to be parallel e_z or perpendicular e_x to z (B). The intensities of circularly polarized LIF (4^1D-2^1P, 492.2 nm) were observed in the z-direction, as in Fig. 3 (b). The σ-light was separated into left hand I_L and right hand I_R circular polarization components by a 1/4λ plate and a Glan Thompson polarizing beam splitter (Fig. 3 (c)). Sensitivity of the detection system for both polarization components was *in situ* calibrated by using circularly unpolarized LIF. The degree of circular polarization P_C is defined as follows;

$$P_C = \frac{I_L - I_R}{I_L + I_R}. \qquad (1)$$

The spatial distribution was measured by scanning the plasma vessel in the x direction.

3. Results and Discussion

Figure 4 shows temporal circular polarization components of LIF, I_L and I_R, observed with an axial magnetic field (B=55G) for e_x-excitation at the negative glow (x=+6 mm). The observed σ-light was unpolarized in the negative glow, where only the QDP transition was excited, since the electric field is negligibly small.

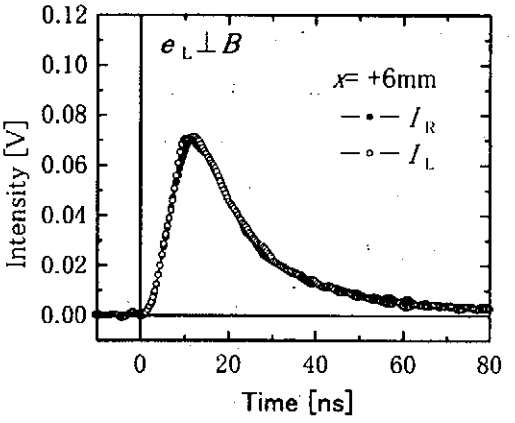

Fig. 4 Time evolutions of polarization components, I_L and I_R of 492.2 nm fluorescence excited by laser polarized in the x direction, observed in the negative glow.

On the other hand strongly polarized LIF was observed in the sheath (x=+12 mm) for (a) e_x-excitation and (b) e_z-excitation, as in Fig. 5. I_L is much stronger than I_R. This clearly shows a difference in population among the magnetic sublevels with opposite sign in the final state of the laser absorption transition, 4^1D. This is due to the Stark-QDP interference. The pulse shapes also differ from each other. For I_R pulse the width is broader and the peak is delayed with respect to I_L pulse. The value of P_C is very close to unity at the onset of the pulse and then rapidly decreases toward zero with time. The decay of polarization is caused by collision of the excited atoms with plasma particles, mainly He ground state atoms in this plasma: I_R predominantly originates from the population created due to the collisional transfer from m=+1 for (a) and m=+2 for (b). The intensity of LIF observed for e_x-excitation is strong compared with that for e_z-excitation. This is reasonably explained to be mainly due to the difference in the excitation rate by laser as shown in Fig. 2. There is a

difference in the decay profile of P_C. The decay in case (b) seems to begin with a time delay compared with case (a). In case (b) laser excitation creates the population in a sublevel with +2 in 4^1D to emit I_L. Subsequent collisional transfer from m=+2 to m=0, -1 or -2 causes depolarisation. The collisional transfer m=+2 to 0 might take longer time than the transfer +1 to 0 in case (a).

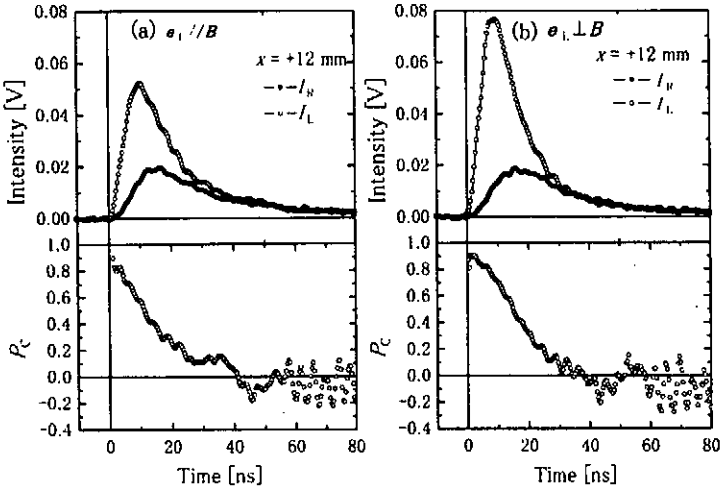

Fig. 5 Time evolutions of polarization components, I_L and I_R, and of polarization degree of LIF (492.2 nm) observed in the sheath for (a) e_z-excitation and (b) e_x-excitation.

The spatial distribution of P_C is represented in Fig. 6. Values of P_C are almost 0 in the negative glow region between x = -9 and +9 mm, where the macroscopic electric field can be considered to be zero. On the other hand in the sheath region P_C shows an increase for x>0 and oppositely a decrease for x<0 towards the cathode surface. It is noted that the P_C-profile has a positive peak for x>0 and a negative peak for x<0 in the middle of the sheath where the electric field increases linearly.

The observed P_C-profile can be explained by the following theoretical consideration on the basis of the atomic interference mentioned in Sect. 1. In the case of e_z-excitation, for example, using the relative amplitudes of the transitions described in Fig. 2, the relative intensities of polarization components are given as,

$$I_L = |S+Q|^2, \qquad (2)$$

$$I_R = |S-Q|^2, \qquad (3)$$

Substituting eqs (2-3) into eq. (1), P_C is written as a function of S/Q,

$$P_C = \frac{2S/Q}{[1+(S/Q)^2]}. \qquad (4)$$

In a similar way P_C in the case of e_x-excitation can be obtained as follows,

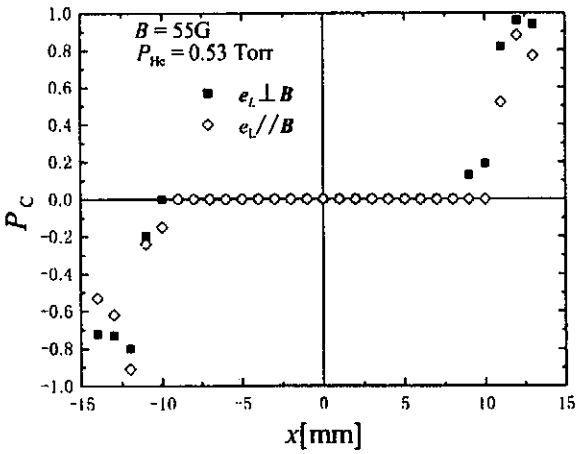

Fig. 6 Radial distribution of degree of polarization of LIF. The cathode surface is situated at x = ±15 mm.

$$P_C = \frac{2S/Q}{\left[1+\frac{10}{9}(S/Q)^2\right]}. \qquad (4')$$

Here, S is the Stark-induced electric dipole transition (2^1S - 4^1D) amplitude, which involves a matrix element of the Stark mixing between 4^1P and 4^1D. Since the matrix element has a linear dependence on E, the signs of numerators, S/Q, in equations (4) and (4') are changed when the electric field vector is reversed. Then, P_C becomes positive (negative) when $x > 0$ ($x < 0$).

The ratio S/Q can be related to E as follows,

$$S/Q = \sqrt{\frac{3}{4C^2}} \cdot E \ , \quad \cdots(5)$$

where C=0.24 kV/cm for n=4 [6]. Putting eq. (5) into eqs. (4) and (4'), the degree of circular polarization, P_C, is obtained as a function of E. Values of P_C calculated for e_x- and e_z-excitation are plotted versus E in the upper part of Fig. 7. A peak in each P_C curve is situated at an electric field where S/Q approximately equals 1. Similarly, it can be considered that peaks in P_C-profiles shown in Fig. 6 correspond to the positions where $|S/Q| \approx 1$. P_C has high sensitivity and wide dynamic range compared with the case of linear polarization method as shown in the lower part of Fig. 7 [6]. Circular polarization method is higher in sensitivity by one order of magnitude. In the present case of n=4 it will be possible to measure very weak electric fields of the order of 10 V/cm.

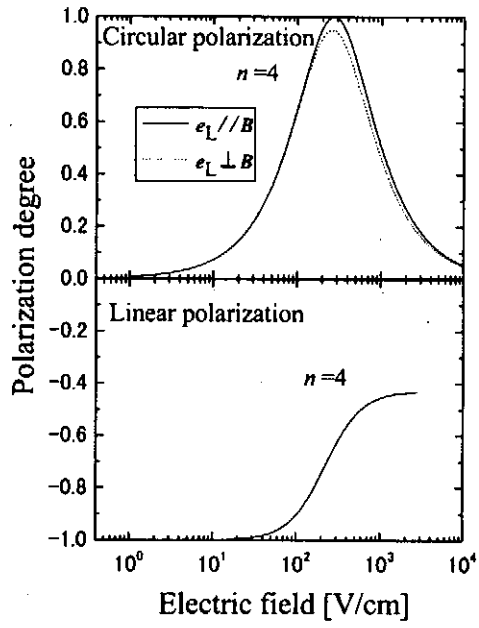

Fig. 7 Calculated sensitivity of circular polarization.

Figure 8 shows the radial distribution of E obtained from the observed P_C profile using the theoretically calculated P_C–E relationship (Fig. 7). Here, values obtained from P_C observed at x<0 are also plotted. In the sheath region the distribution shows a linear dependence against x. By extrapolating E the cathode-fall potential and the sheath thickness were estimated to be 200±20 V and 4 mm, respectively. The obtained potential agrees

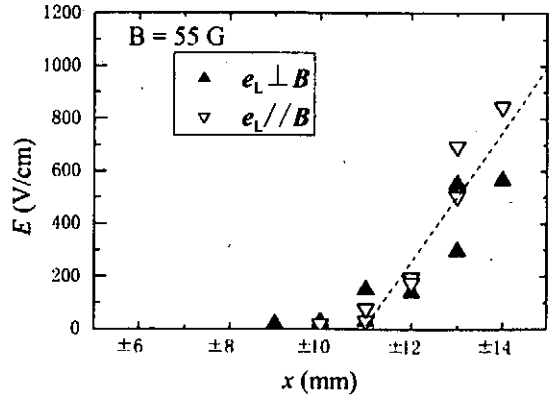

Fig. 8 Radial distribution of electric field

with that obtained by a cylindrical electric probe within the experimental errors.

4. Concluding remarks

The interference effect between the Stark-induced electric dipole and the electric quadrupole amplitudes involved in laser absorption processes has been observed for the first time in a cylindrical hollow cathode He plasma with the magnetic field applied perpendicularly to the sheath electric field ($E \perp B$). In the middle of the sheath the LIF observed in the direction of magnetic field was strongly polarized, which was obviously due to anisotropic population created by laser excitation between magnetic sublevels with different sign, ± 1 for e_Z-excitation or ± 2 for e_X-excitation. The observed radial profile of the degree of circular polarization P_C also showed characteristic features of the interference. A positive and a negative peak in the P_C profile were observed in the sheaths located in $x>0$ and $x<0$, respectively. The theoretical consideration showed that the peaks corresponded to the boundary between $S<Q$ and $S>Q$ and the sign of P_C means the direction of electric fields. The radial profile of E was obtained from the observed P_C using the theoretical P_C-E relationship calculated according to our model. Sheath potential estimated from the resulting profile of E was in good agreement with probe measurements.

It was demonstrated that our new LIF technique using interference of atomic transition amplitudes had high sensitivity to measure the weak electric field of the order of 10 V/cm for $n=4$ and a wide dynamic range of 3 orders of magnitude. It should be noted that the new technique enables us to measure the direction of the electric field vector in plasmas. In plasmas with higher particle density (electrons, ions and atoms), however, the decay of polarization becomes faster and the LIF waveform is considerably modified by the frequent collisions of n^1D atoms with the plasma particles. In such cases it will become difficult to estimate E straightforwardly from the experimental P_C. To evaluate E accurately, we will need to simulate the temporal evolution of polarized LIF by using a rate-equation model involving the depolarisation process of oriented atoms

Acknowledgments

This work was partially supported by Japan-Australia Research Cooperative Program of Japan Society for Promotion of Science and a Grant-in-Aid for Scientific Research from the Japanese Ministry of Education, Culture, Sports, Science and Technology.

References

[1] C. A. Moore, G.P. Davis and R.A. Gottscho *Phys. Rev. Lett.* **52** (1984) 538.

[2] T. Oda and K. Takiyama, *Proc. 7th International Symposium on Laser-Aided Plasma Diagnostics*, Fukuoka, Japan, (1995) p. 227.

[3] U. Czarnetskii, D. Luggenhölscher and H.F. Döbele, *Phys. Rev. Lett.* **81** (1998) 4592.

[4] M. Watanabe, K. Takiyama and T. Oda, *Rev. Sci. Instrum.* **70** (1999) 903.

[5] K. Takiyama, T. Oda, K. Sato, J. Nucl. Mater. **290-293** (2001) 976.

[6] K. Takiyama, M. Watanabe, T. Oda, J. Nucl. Mater. **266-269** (1999) 953.

[7] L.R. Hunter, W.A. Walker, and D.S. Weiss, Phys. Rev. Lett. **56** (1986) 823.

Plasma Polarization Spectroscopy on the ECR helium plasma in a cusp magnetic field

T. Sato, A. Iwamae, T. Fujimoto, M. Uchida*, and T. Maekawa*,
Graduate School of Engineering, Kyoto University
**Graduate School of Energy Science, Kyoto University*

Abstract

Helium emission lines have been observed on the ECR plasma in a cusp field with the polarized components resolved. The polarization map is constructed for the 501.6 nm (2^1S-3^1P) line emission. Lines from n^1P and n^1D levels are strongly polarized and those from n^3D levels are weakly polarized. As the helium pressure increases the polarization degree decreases.

1. Introduction

In plasma, electron heating which accelerates electrons to a particular direction together with a trapping of electrons in a magnetic field may make the electron velocity distribution function (EVDF) anisotropic. Intensity and polarization of emission lines from excited levels, which are produced by electron-atom collisions, are the result of the EVDF. Especially the polarization strongly reflects the anisotropy of the EVDF.

Since the propagation of errors from measured intensities to the polarization degree tend to make its error large, it is difficult to measure a polarization degree less than 0.1. In the following we report our first observation on a reproducible and stable plasma and determination of polarization degrees with relatively small errors.

2. Experiment

Figure1 shows the cusp plasma generator. Helium gas pressure is from 1.7×10^{-4} to 2.0×10^{-3} torr. Two coils (900 A) generate a cusp field. The magnetic field is strong in the outer regions of the plasma. The field strength of the chamber wall near the coils is about 3000 G. The electrons tend to be trapped in the central part of the plasma. Microwaves (2.45 GHz, 800 W) enter through the upper quartz window into the chamber and generate virtually stationary plasma for four seconds. The electron cyclotron resonance (ECR) surface is a spheroid. The stuffer conductor is not used in our present experiment. We have a probe in the camber and it gives plasma parameters. When helium pressure is 1.7×10^{-4} torr the electron temperature and the electron density are 20 eV and 1×10^{17} m^{-3}, respectively, in the middle.

In front of the lens of a digital camera, we placed a band pass filter (center wavelength

501.8 nm, bandwidth 1.5 nm, transmitting He I 501.6nm (2^1S-3^1P) line) and took a photograph of the area marked (a) in Fig.1. Figure 2(a) shows the photograph. Figure 2(b) shows the magnetic field lines and the ECR surface. It is seen that the plasma is formed along the magnetic field lines. We then placed a linear polarizer in front of the camera system and took photographs by changing the polarization direction of the transmitted light. Thus, we obtained the spatial distribution of the intensity of four linearly polarized components I_0, I_{45}, I_{90}, I_{135}, the polarization direction of which are 0, 45, 90, 135 degrees from the vertical direction. We thus determined the linear polarization components of the Stokes parameters $Q = I_0$-I_{90} and $U = I_{45}$-I_{135}. We assume the circular polarization components to be $V = 0$. From these distributions we determined the distribution of the polarization direction and degree as shown in Fig. 2(c). The polarization direction is perpendicular to the magnetic field. This result suggests that the electron velocity distribution is anisotropic: the velocity component perpendicular to the magnetic field is stronger.

In order to investigate the polarization characteristics of our plasma quantitatively, we observe several emission lines on the four areas shown in Fig. 2(b) by using an optical system with a Glan-Thompson prism and optical fibers. Figure 3 shows the side view of the chamber and the optical system. We observe the plasma by four lines of sights (LOS 1, 2, 3 and 4). The LOS 4 is near the ECR surface. The emission radiation transmitted through the quartz window is resolved into two linearly polarized components (π component parallel to the magnetic field and σ component perpendicular to the magnetic field) by the Glan-Thompson prism and focused on the four pairs of optical fibers (core diameter ϕ400 μm, length 8 m) by a lens (f = 50 mm). The exit light from the fibers enters through the entrance slit of the spectrograph, (Nikon G500, f 500 mm, grating 1200 grooves/mm, F/8.5) resolved and recorded by the ICCD.

Figure 4 shows an examples of the spectra for the helium pressure of 1.7×10^{-4} torr. The left panel is for LOS 1 and the right one is for LOS 4. The π components are displaced to the right. The lines included are 492.2 nm (2^1P-4^1D), 501.6 nm (2^1S-3^1P) and 504.8 nm (2^1P-4^1S). The upper level of the 504.8 nm line is a ^1S level, so that the emission is never polarized. Apparent different intensities for this line are due to different sensitivities of our detection system for the polarized components. We calibrated our system by using a calibrated standard irradiance lamp and a white reflectance standard. It is seen that other two lines are polarized.

3. Analysis

The spectra shown in the left-side panels of Fig. 5 are LOS 2 observed at different helium pressures. In the lower graph the helium pressure is higher. From these spectra we determine the longitudinal alignment $A_L = (I_\pi - I_\sigma)/(I_\pi + 2I_\sigma)$ to quantify the polarization degree.

We repeated the measurement several hundred times and obtained the histograms shown in the right-side panels of Fig.5. The unpolarized line is used to determine the zero point of the A_L scale. As the helium pressure increases the polarization degree decreases.

We now examine these distributions in detail. The histograms follow quite well the normal statistical distribution, and the dispersion depends on the line intensity. Intensity of the 501.6 nm line is higher than others, and the dispersion of this line is smaller. This is consistent with statistical fluctuations of photon numbers. Since we have enough numbers of experimental data, the statistical uncertainty is quite small. If the polarization itself fluctuates, the central value should fluctuate, and the dispersion should be wider. In our experiment, intensities of the polarized 492.2 nm line and unpolarized 504.8 nm line are almost equal and the dispersions of their distributions are essentially the same. We can conclude that the polarization degree is quite reproducible, which means that the anisotropic distribution of electrons is quite stable.

In Fig. 6 we plot the pressure dependence of A_L for all the LOSs. Statistical uncertainty is smaller than the size of the symbols. Here we note the three points. First, with an increase in the helium pressure A_L comes close to zero. Second, A_L of the 492.2 nm line is almost the same for all the line of sights. Third, A_L of the 501.6 nm line is larger outside than close to the ECR surface.

Figure 7 shows the energy level diagram of neutral helium and emission lines for which we determined intensities and A_Ls. The emission lines represented by the broken line are those the A_L of which is calibrated with an unpolarized line from a ^{1}S level. The A_L comes from the alignment, or the population imbalance among the magnetic sublevels, of the upper level population. Figure 7(a) shows A_L with bar originating from the position of the upper levels of the emission lines. All values are negative. Emission lines from ^{1}P and ^{1}D levels are strongly polarized and those from triplet levels, especially from higher excited levels, are only weakly polarized. The line intensity itself is another important quantity. The intensity comes from the population of the upper level. We determine the population, n, with $I_\pi+2I_\sigma = n(p)\,\chi_{pq}\,A_{pq}$. Here χ_{pq} is the photon energy and A_{pq} is Einstein's A coefficient. Figure 7(b) shows the distribution of populations in the log scale. Population has been divided by the statistical weight.

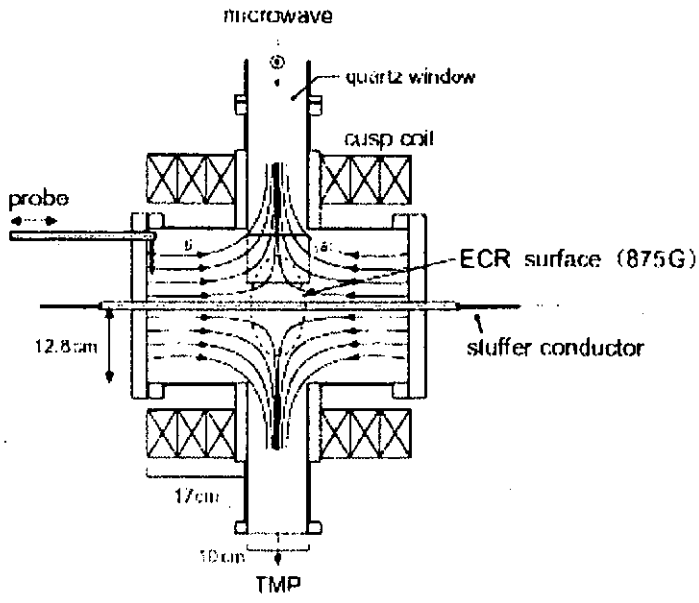

Fig. 1. The front view of the plasma generator.

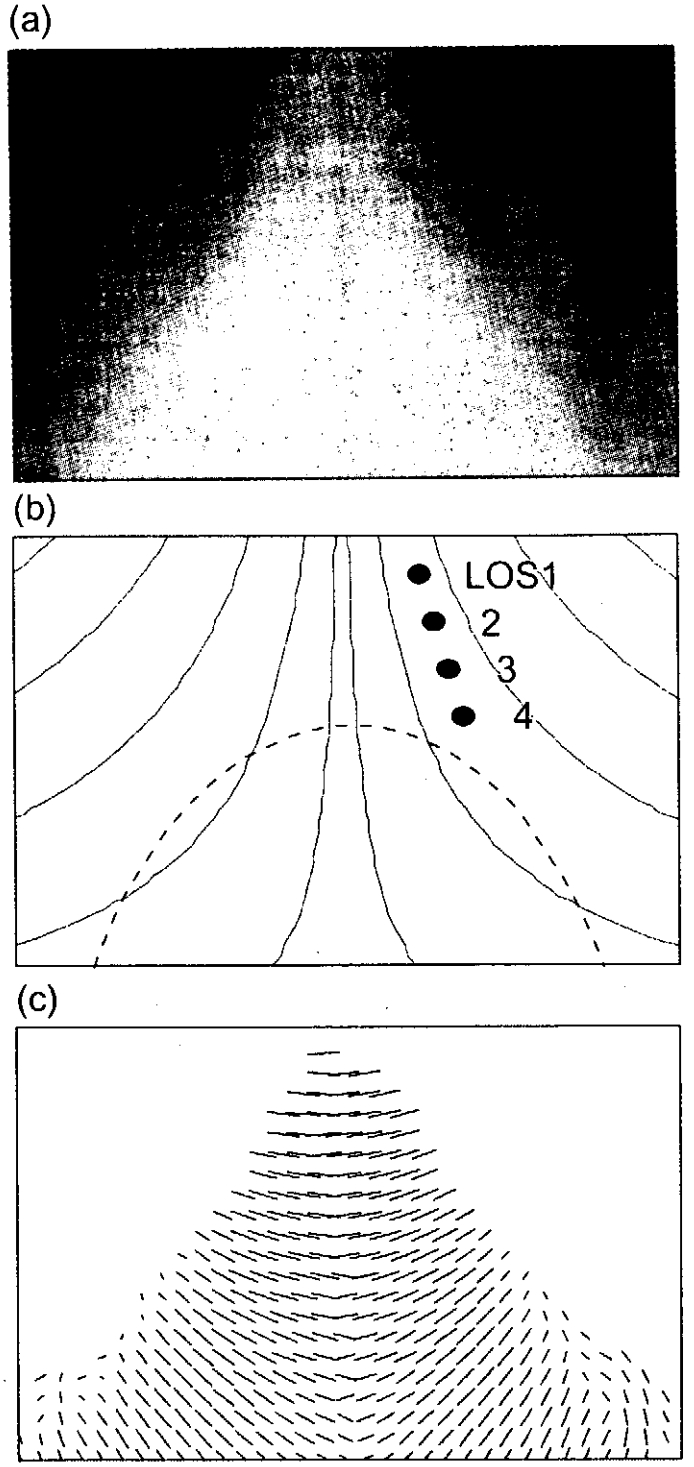

Fig. 2. (a) An example of He I 501.6nm (2^1S-3^1P) line images of area (a) in Fig.1. (b) The magnetic field lines (solid lines), the ECR surface (broken line) and the line of sights (LOS) of the optical system with the Glan-Thompson prism and optical fibers in the area. (c) Polarization map for the 501.6 nm line. The lines indicate the polarization direction and the length of the lines are proportional to the square root of the polarization degree.

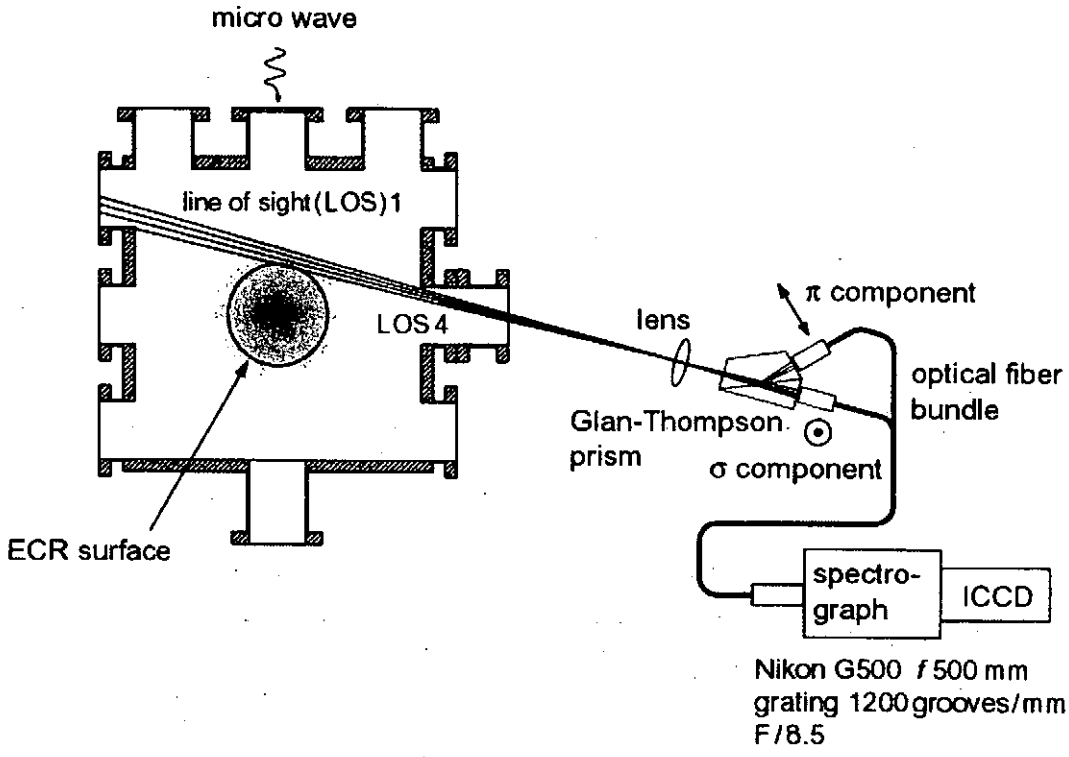

Fig. 3. The side view of the chamber and the optical system.

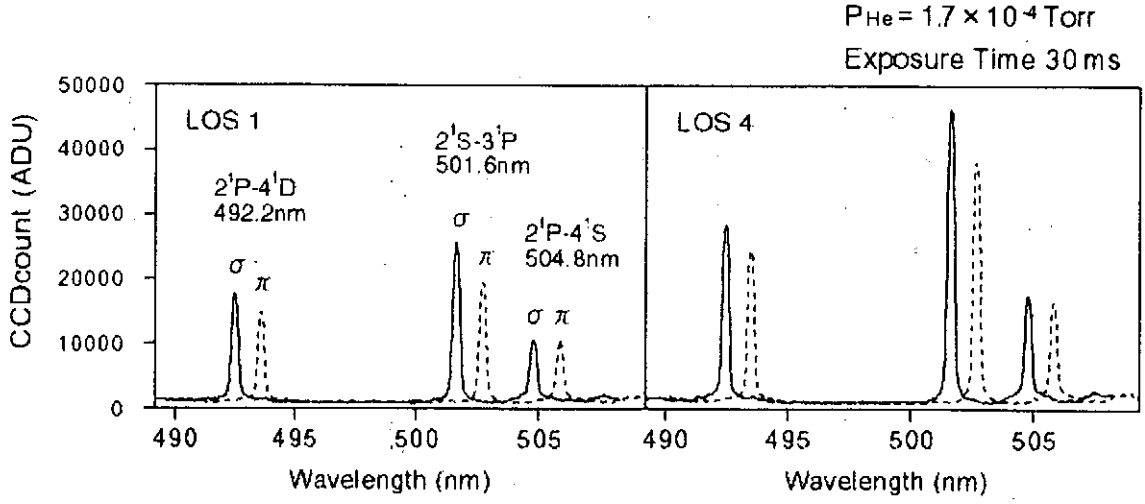

Fig. 4. An example of the spectra of the σ component (solid line) and the π component (broken line) when helium pressure is 1.7×10^{-4} torr. The left panel is for LOS 1 and the right one is for LOS 4. These indicate 492.2 nm (2^1P-4^1D), 501.6 nm (2^1S-3^1P) and 504.8 nm (2^1P-4^1S) lines. The π components are displaced to the right.

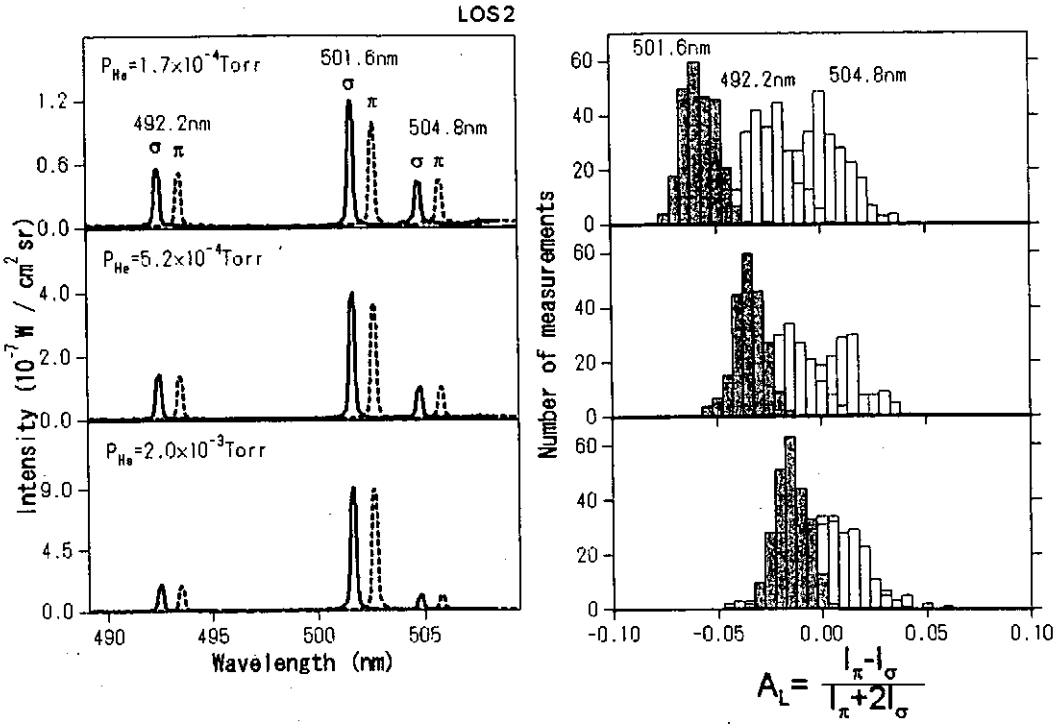

Fig. 5. The spectra for the line of sight 2 observed at different helium pressures and the corresponding histograms of the longitudinal alignment $A_L = (I_\pi - I_\sigma)/(I_\pi + 2I_\sigma)$.

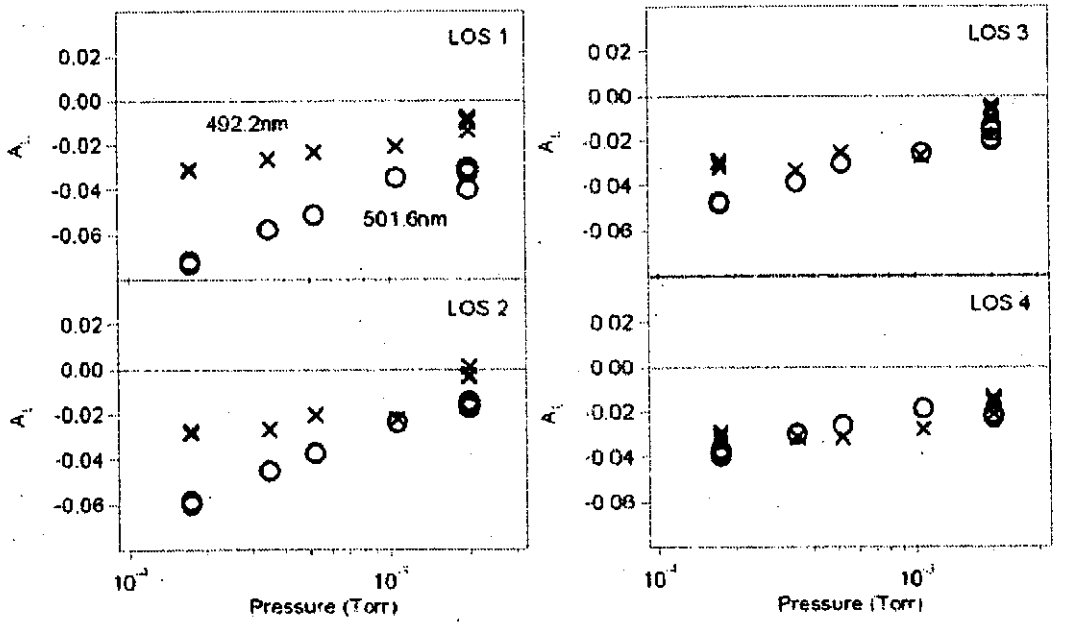

Fig. 6. The pressure dependence of the A_L of 492.2 nm line (cross) and 501.6 nm line (circle) for all the LOSs.

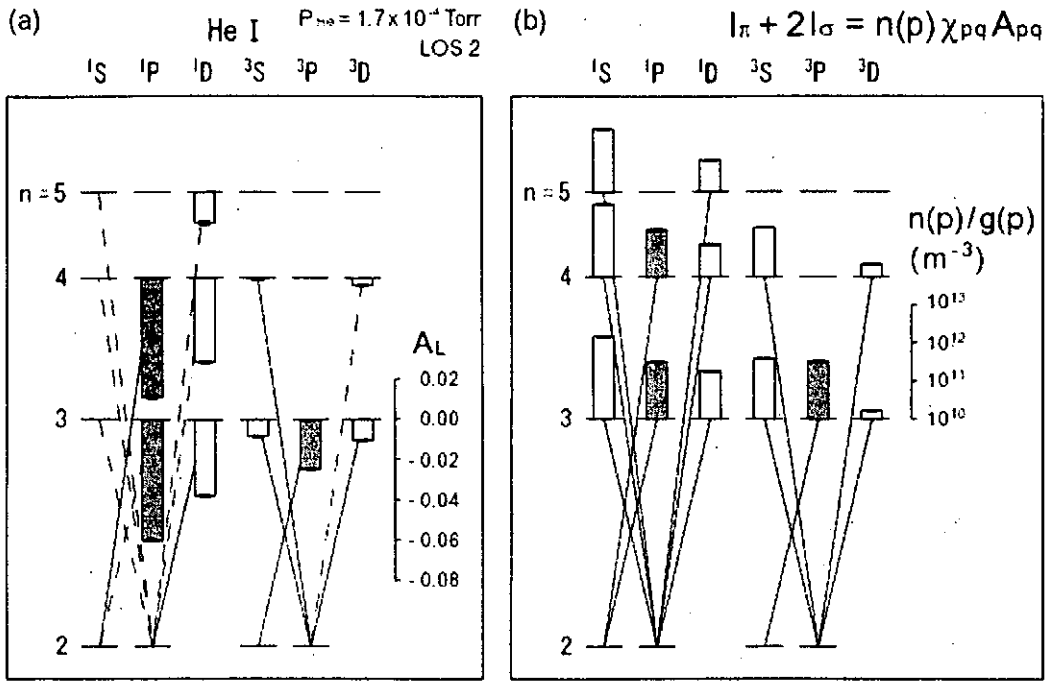

Fig. 7. The energy level diagram of neutral helium and emission lines for which we determined intensities and A_Ls. The emission lines represented by the broken line are calibrated by unpolarized line from a ^1S level. (a) A_L expressed with a bar originating from the position of the upper levels of the emission lines. (b) The distribution of populations in the log scale.

Polarization of ECR Helium Plasma and Population-Alignment Collisional-Radiative Model

Atsushi Iwamae, Takeshi Sato, Yasuhiro Horimoto and Takashi Fujimoto
Department of Engineering Physics and Mechanics,
Graduate School of Engineering, Kyoto University, Kyoto 606-8501, Japan

Abstract

A population-alignment collisional-radiative (PACR) model for neutral helium, He I, atoms has been developed. The PACR model correlates quantitatively the intensity and the polarization of emission lines from atoms and ions in a plasma with an anisotropy of the electron velocity distribution function (EVDF). The alignment production from the ground state, $1s^2\ ^1S_1$, and metastable levels, 1s2s $^1S_1$ and 1s2s, $^3S_1$, is considered. An EVDF of electron cyclotron gyration around the magnetic field lines is represented by a Saturn-type anisotropic EVDF which has higher values in the perpendicular direction to the magnetic field lines than in the parallel direction. An oblate Saturn-type EVDF explains negative longitudinal alignment of the emission lines with respect to the magnetic field lines.

Introduction

We have measured the absolute intensity and the polarization degree of emission lines for various transitions on a cusp plasma[1]. In the plasma, helium atoms are excited by electron impact. Intensity of emission lines is proportional to the upper level population, $n(p)$. Polarization degree of emission lines, or the longitudinal alignment, A_L, which we employ to quantify the polarization, is proportional to the upper level alignment divided by the population, $a(p)/n(p)$. If electrons with a thermal or Maxwell distribution excite the atoms, in other words, electron collisions are spatially isotropic, we will have no polarization, i.e., $A_L=0$. Anisotropic excitation, on the other hand, would produce alignment $a(p)$ on the level. The intensity and the polarization tell us how the upper level population and alignment are created by electron impact. The Population-Alignment Collisional-Radiative (PACR) model is a theoretical framework which relates the experimental observation to the anisotropic EVDF in the plasma. We consider an ensemble of atoms in the following situation. (i) Axial symmetry is present around the z-axis, the quantization axis. (ii) There is no coherence among different Zeeman multiplets. (iii) Electric and magnetic fields are absent. The magnetic field strength of the cusp field is 3000 gauss at most. The Zeeman splitting of the level of He is 1.2 GHz at 875 gauss of the 2.45 GHz microwave ECR spheroid. These magnetic fields play the role of realizing the axial symmetry of EVDF and defining the quantization axis in this model.

For quantitative evaluation, we need extensive cross section data for various transitions which are beyond the standard cross section data. Fortunately, a couple of theorists provided us with cross sections for some essential transitions in our model.

Population-Alignment Collisional-Radiative model

Excitation cross sections by electron impact and the polarization degree of radiative transitions on He I are examined experimentally and theoretically[2-6]. Csanak and Cartwright presented on the basis the relativistic distorted wave approximation (DWA) the polarization degree[4] or the alignment production cross sections, Q_0^{20}, [6] for various transitions: i.e., from the ground state, 2^1S and 2^3S metastable states to upper singlet and triplet, P and D states of principle quantum number n up to 5 or 6. It is shown that the polarization degree depends weakly on principle quantum number n[5].

Figure 1 shows an example of the experimental observations of polarization on helium atoms; the atoms in the ground state are excited by a beam of electrons. The polarization degree, P, of the 1^1S - n^1P emission lines in the VUV region is determined. At the threshold energy, just above 21.2 eV for 2^1P, the polarization degree tends to 1. It gradually decreases with the increase of electron impact energy. Then the

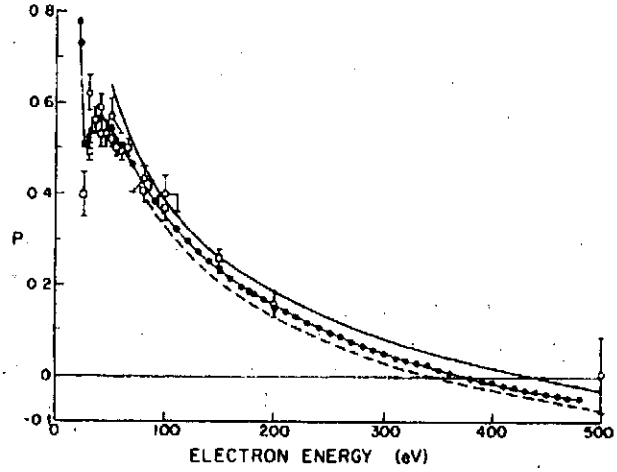

Fig. 1. Polarization of the He I (1 1S0 – 1P1) line excited by a beam of electrons. Experimental data by several workers and compared with theoretical calculations (Quoted from [3]).

polarization degree crosses the zero line at 380 eV. The solid line is the result presented by Ref. [5], which reproduces well the experiment. From the polarization degree P or longitudinal alignment, $A_L = 2P/(3-P)$, the alignment production cross-section Q_0^{20} is obtained from the Q_0^{00} and A_L substituted into the equation[8]

$$Q_0^{20}(r,p) = (-1)^{L_p+L_s}\sqrt{\frac{2}{3}}(2L_p+1)\begin{Bmatrix} L_p & L_p & 2 \\ 1 & 1 & L_s \end{Bmatrix}^{-1} A_L(p,s)Q_0^{00}(r,p), \qquad (1.1)$$

where {} is the 6-j symbol. For $n^1S \leftarrow m^1P$ emission line, Eq. (1.1) is simplified to

$$Q_0^{20} = -\sqrt{\frac{2}{3}}A_L(r,p)Q_0^{00}. \qquad (1.2)$$

We use the excitation cross section, Q_0^{00}, data presented by Ralchenko et. al.[9]. For n=2, 3, 4, 5, and 6, Q_0^{20} cross sections are calculated from[5] as shown in Fig. 2.

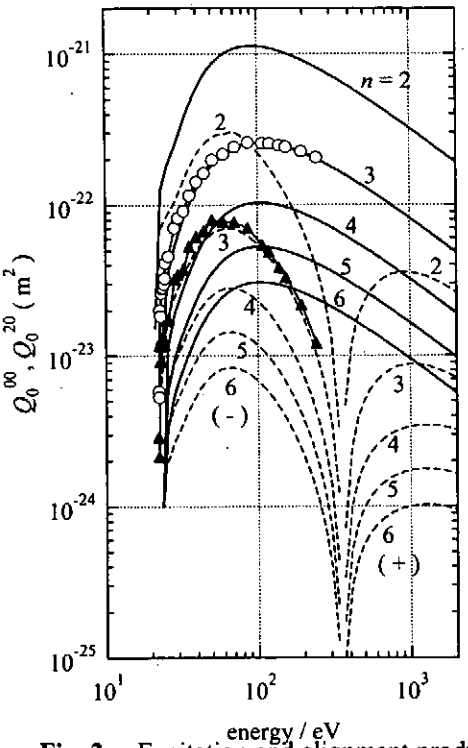

Fig. 2. Excitation and alignment production cross sections, Q_0^{00} and Q_0^{20}, from the 1 ^{1}S level to n^1P levels. Thick solid curves: Q_0^{00} Ralchenko el. al.[9] ,. Thin dashed curves: Q_0^{20} Csanak and Cartwright[5]. Marks ○ and ▲: Q_0^{00} and Q_0^{20} Bray[7].

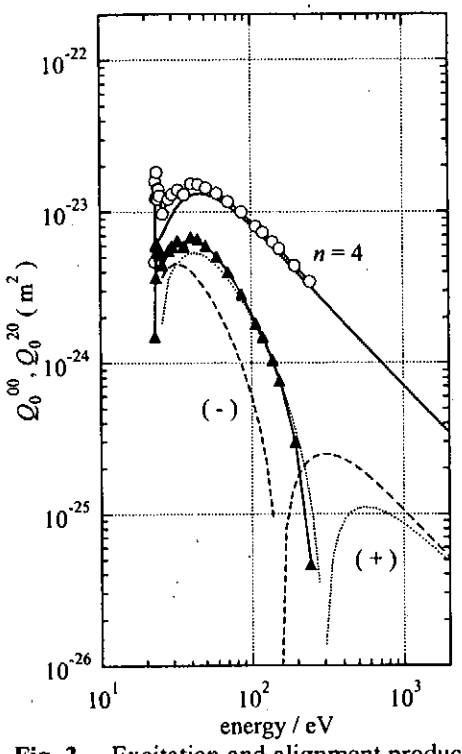

Fig. 3. Excitation and alignment production cross sections, Q_0^{00} Q_0^{20}, from the 1^{1}S level to 4 ^{1}D level. Thick solid curve: Q_0^{00} Ralchenko el. al.[9], Thin dashed curves: Q_0^{20} Csanak and Cartwright[5], Dotted curves: Q_0^{20} McFarland [2]. Marks ○and ▲: Q_0^{00} and Q_0^{20} Bray[7].

The dashed curves represent the alignment production cross sections, Q_0^{20}, which change their sign from negative to positive. Recently, Bray provided magnetic-sublevel-resolved cross section data for excitation from the ground state to 3^1P, 4^1P, 3^3P and 4^3D, from the 2^1S metastable level to 3^1P, 4^1P, 3^3P and 4^3D, and from the 2^3S level to 3^1P, 4^1P, 3^3P and 4^3D [7] calculated by the Convergent Closed Coupling (CCC) method. In Fig. 2, circles and triangles represent Q_0^{00} and Q_0^{20} which are

deduced from the CCC sublevel-resolved cross sections $Q_{\alpha LM,\alpha'L'M'}$ [8] for transition $\alpha J \leftarrow \alpha' J'$ or $r \rightarrow p$

$$Q_0^{00}(r,p) = \frac{1}{(2L'+1)} \sum_{MM'} Q_{\alpha LM,\alpha'L'M'} , \tag{1.3}$$

$$Q_0^{20}(r,p) = \frac{1}{(2L'+1)} \sum_{MM'} (-1)^{L-M} \langle L\,L\,M\,-M|20\rangle Q_{\alpha LM,\alpha'L'M'} , \tag{1.4}$$

where $\langle L\,L\,M\,-M|20\rangle$ is the Clebsch-Gordan coefficient. For electron impact excitation on an electric dipole transition, $1^1S \rightarrow n^1P$, no significant difference is observed between the results of DWA and CCC. We now look at $1^1S \rightarrow n^1D$ excitation cross sections as shown in Fig. 3. From the theoretical polarization degree calculated by DWA [5], the alignment production cross sections Q_0^{20} are obtained as shown by the dashed curves. The experimentally observed polarization leads to Q_0^{20} shown as dotted curves[2]. The cross sections Q_0^{00} and Q_0^{20} calculated by CCC are plotted on the same graph as circles and triangles, respectively. The experimental polarization agrees well with the CCC calculation. For other n^1D states, we assume that the polarization degree, or A_L, is independent of the principle quantum number n and then we use the polarization[2] and the Q_0^{00} function proposed by Ralchenko et. al.[9].

We consider the second element of PACR model, the electron velocity distribution function (EVDF) in plasma; an anisotropic EVDF on the assumption of axial symmetry is expressed by $f(v,\theta)$. We expand the EVDF in terms of Legendre polynomials,

$$f(v,\theta) = \sum_K f_K(v) P_K(\cos\theta) \tag{1.5}$$

with

$$f_K(v) = \left[(2K+1)/2\right] \int f(v,\theta) P_K(\cos\theta) \sin\theta \, d\theta \ . \tag{1.6}$$

As a model of the EVDF accelerated by the ECR microwave, we adopt the Saturn-type distribution expressed as

$$\begin{aligned} f(v,\theta) = {} & 2\pi \frac{1}{1+\delta} \left(\frac{m}{2\pi k_B T_{eth}} \right)^{3/2} \exp\left(-\frac{m}{2k_B T_{eth}} v^2 \right) \\ & + 2\pi \frac{\delta}{1+\delta} A_r \exp\left[-\frac{m}{2k_B T_{er}} \left(v^2 - 2vV_r \sin\theta + V_r^2 \right) \right] \end{aligned} \tag{1.7}$$

where A_r is the normalization factor for $\int_0^\infty \int_0^\pi f(v,\theta) v^2 \sin\theta \, d\theta dv = 1$, m is the electron mass and k_B is the Boltzman constant;

$$\frac{1}{A_r}=\left(\frac{2\pi k_B T_{er}}{m}\right)^{3/2}\exp\left(-\frac{mV_r^2}{2\pi k_B}\right)+\left(\frac{2\pi k_B T_{er}}{m}\right)\pi V_r\left\{1+\mathrm{Erf}\left(\sqrt{\frac{m}{2\pi k_B T_{er}}}V_r\right)\right\}. \quad (1.8)$$

The first line of Eq. (1.7) represents the thermal bulk component and the second line represents the cyclotron gyrating electrons, which may be called the ring component of the Saturn-type EVDF. The variable electron temperature parameters T_{eth} and T_{er} are for the thermal and ring components, respectively. The ratio of number density of these components is δ. The displacement of the ring component is given by V_r. Exmaples of the EVDF are plotted in Fig. 4.

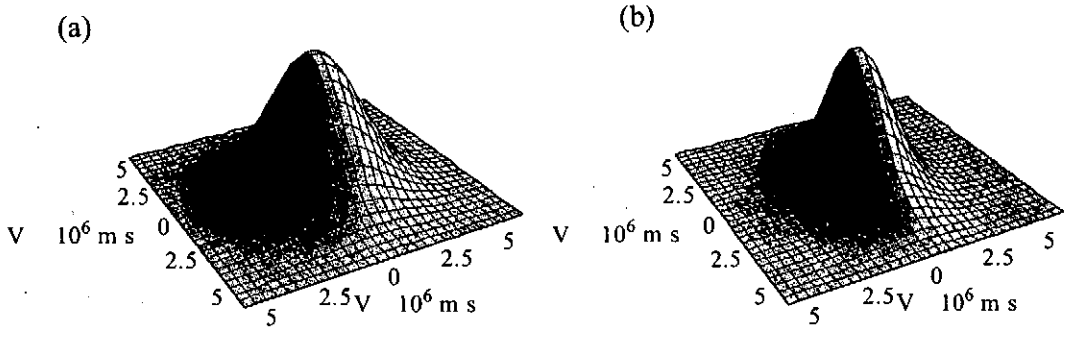

Fig. 4 Examples of 3D plot of EVDF $f(v,\theta)$ (a) Maxwell: T_{eth}=20 eV, no ring component δ=0 (b) Anisotropic Saturn-type: T_{eth}=10 eV, T_{er}=10 eV, V_r=2.6×10^6 m/s, δ= 1.

The rate coefficients $C^{kk'}$ are defined for transition $r \rightarrow p$ as,

$$C^{00}(r,p)=\int Q_0^{00}(r,p)2f_0(v)v^3\,dv \quad (1.9a)$$

$$C^{20}(r,p)=\int Q_0^{20}(r,p)\frac{2}{5}f_2(v)v^3\,dv \quad (1.9b)$$

$$C^{02}(r,p)=\int Q_0^{02}(r,p)\frac{2}{5}f_2(v)v^3\,dv \quad (1.9c)$$

$$C^{22}(r,p) = \int\left[Q_0^{22}(r,p)+Q_1^{22}(r,p)+Q_2^{22}(r,p)\right]\frac{2}{5}f_0(v)v^3\,dv$$
$$+\int\left[2Q_0^{22}(r,p)+Q_1^{22}(r,p)-2Q_2^{22}(r,p)\right]\frac{2}{35}f_2(v)v^3\,dv \quad . \qquad (1.9d)$$
$$+\int\left[6Q_0^{22}(r,p)-4Q_1^{22}(r,p)+Q_2^{22}(r,p)\right]\frac{2}{105}f_4(v)v^3\,dv$$

When the excitation originates from an S state, there are no Q_0^{02}, Q_0^{22} cross sections. Thus neither C^{02} nor C^{22} component appears from the S level. The Legendre expansion coefficients of EVDF, $f_k(v,\theta)v^3$ (k=0, 2), are plotted in Fig. 5(a) for parameters; T_{eth} =10 eV, T_{er} =10 eV, δ= 1 and three different values in V_r . The peak position of $v^3 f_0(v)$ moves with the increase of V_r. The shape $v^3 f_0(v)$ of V_r= 2.6×10^6 m/s is quite similar to that of the Maxwell distribution of 20 eV. The $v^3 f_2(v)$ contribution to the alignment production rate coefficient C^{20} increases with the increase in V_r. Fig. 5 (b) and (c) shows Q_0^{00}, Q_0^{20} for $1^1S \rightarrow 3^1P$ and for $1S \rightarrow 4^1D$, respectively. We can see that dependence on EVDF is different for individual transitions.

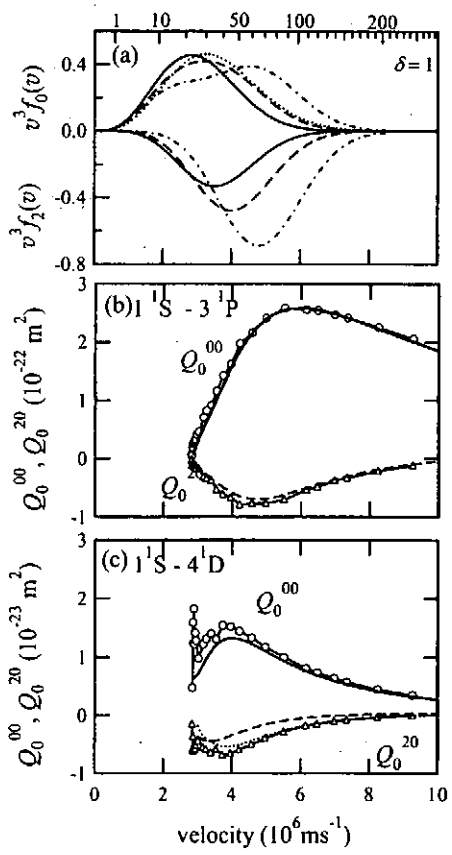

Fig. 5. (a) Legendre expansion terms of the EVDF, $f_k(v,\theta)v^3$ (k = 0, 2) for three different values of V_r, and T_{eth} = T_{er} = 10 eV δ= 1. Solid curves: V_r = 1.8×10^6 m/s, 10 eV. Dashed curves: V_r = 2.6×10^6 m/s, 20 eV. Dash-dotted curves: V_r = 3.8×10^6 m/s, 40 eV. Dotted curve: Maxwellian (20 eV) for comparison.

Cross sections for (b) $1^1S \rightarrow 3^1P$ and for (c) $1S \rightarrow 4^1D$. Bray[7] Q_0^{00} (○) and Q_0^{20} (▲). Solid curves: Q_0^{00} Ralchenko et. al.[9], Dashed curves: Q_0^{20} Csanak and Cartwright[5], Dotted curve: Q_0^{20} McFarland[2].

We allocated two quantities, population $n(p)$ and alignment $a(p)$ to each level p. We have a set of rate equations for the population and for the alignment,

$$\begin{aligned} dn(p)/dt = & \sum_{r\neq p}\left[C^{00}(r,p)n_e + A(r,p)\right]n(r) \\ & -\left[\left\{\sum_{r\neq p}C^{00}(p,r)+S(p)\right\}n_e + \sum_{r\neq p}A(p,r)\right]n(p), \\ & +\sum_{r\neq p}C^{02}(r,p)n_e a(r) \\ & -C^{02}(p,p)n_e a(p) \end{aligned} \tag{1.10a}$$

$$\begin{aligned} da(p)/dt = & \sum_{r\neq p}C^{20}(r,p)n_e n(r) \\ & -C^{20}(p,p)n_e n(p) \\ & +\sum_{r\neq p}\left[C^{22}(r,p)n_e + A^{22}(r,p)\right]a(r). \\ & -\left[C^{22}(p,p)n_e + \sum_{r\neq p}A(p,r)\right]a(p) \end{aligned} \tag{1.10b}$$

The first two lines on right hand side (rhs) of Eq. (1.10a) are the conventional rate equation for population. We have no cross section data Q_0^{02} for the rest of two terms in Eq. (1.10a), so that we neglect $C^{02}(r, p)$ and $C^{02}(p, p)$. Concerning the rate equation of the alignment, the first line on the rhs of Eq. (1.10b) represents the production of alignment in this level p from population in other levels r. The second line, the alignment production by elastic collision $C^{20}(p, p)$ is not included in the present calculation. A quantum-mechanical formula for the alignment creation cross section has been derived by Csanak et al.[10]. It is expected to be small. On the third line the alignment transfer $C^{22}(r, p)$ by electron collisions is not included. Alignment transfer by radiative decay and decay of alignment are included.

Under the steady state conditions, the population and alignment are determined by solving the two sets of rate equations. The intensity I_0 of the emission line for $p \rightarrow s$ is proportional to the population

$$I_0 = \frac{1}{4\pi l^2}n(p)A(p,s)\hbar\omega. \tag{1.11}$$

When we observe the emission line from the direction perpendicular to the quantization axis, it is also given as

$$I_0 = \frac{2}{3}(I_\pi + 2I_\sigma), \tag{1.12}$$

where I_π and I_σ are the intensities of the polarized components of the line [11]. We

employ the longitudinal alignment

$$A_L = \frac{I_\pi - I_\sigma}{I_\pi + 2I_\sigma}. \tag{1.13}$$

This quantity is related to alignment $a(p)$ and population $n(p)$ by

$$A_L(p,s) = (-1)^{L_p+L_s}\sqrt{\frac{3}{2}}(2L_p+1)\begin{Bmatrix} L_p & L_p & 2 \\ 1 & 1 & L_s \end{Bmatrix}\frac{a(p)}{n(p)}. \tag{1.14}$$

For the triplet state, the fine structure causes depolarization effects. When radiative decay rate is much smaller than the fine-structure splitting, which is the case for the $2^3S \leftarrow n^3P$ transitions observed in the cusp experiment, the longitudinal alignment is given[12] as

$$A_L(p,s) = \gamma G\left(L_p\right)_2 (-1)^{L_p+L_s}\sqrt{\frac{3}{2}}(2L_p+1)\begin{Bmatrix} L_p & L_p & 2 \\ 1 & 1 & L_s \end{Bmatrix}\frac{a(p)}{n(p)}, \tag{1.15a}$$

where

$$G\left(L_p\right)_K = \frac{1}{\gamma}\frac{1}{2S_p+1}\sum_{J_p}(2J_p+1)^2\begin{Bmatrix} L_p & J_p & S_p \\ J_p & L_p & K \end{Bmatrix}^2. \tag{1.15b}$$

Figure 6(a) and (b) shows the alignment over population, $a(p)/n(p)$ and population density, $n(p)/g(p)$ plot assuming Saturn-type EVDF for the parameters; T_{eth} = 10 eV, T_{er} = 10 eV, V_r = 1.88×10^6 m/s , δ= 1. The population distribution is normalized at the 3^1S level to the observed one. From the experimentally observed intensity I_0 and longitudinal alignment A_L on the cusp plasma, we plotted the alignment over population, $a(p)/n(p)$ and the population density, $n(p)/g(p)$, distributions in Fig. 6(c) and (d), respectively against the effective quantum number n^* of the level. Two additional factors are included in our PACR model for the population distribution. The first is the diffusion of metastable atoms out of the plasma and the second is the radiation trapping or radiation re-absorption of the 1^1S-n^1P emission lines. We find from the collision mean free path and the diffusion coefficient that the 2^3S metastable atoms diffuse out of the plasma. In order to take this effect into account we reduce the metastable population by a factor of ten. Then the triplet S, P, D populations decrease as shown in Fig. 6(b). The population distribution becomes close to that observed.

Since the Zeeman level splitting of 2^1P level at 875 gauss at the ECR resonance is smaller than the FWHM of Doppler line broadening, emitted photons from the 2^1P and 3^1P to 1^1S may be re-absorbed by ground state atoms. Then this atom emits another photon. This emission-absorption process may be repeated several times. As a result of this chain of processes, the effective A coefficient is reduced. We approximate this

reduction by introducing the escape factor g_0. The population and emitted radiation intensity decay with g_0A. The 2^1P and 3^1P level populations are increased. The population distribution obtained in Fig. 6(b) is found similar to that of the Maxwell distribution of $T_e = 20$ eV.

We have taken into account the radiation trapping for population. For the alignment, we also consider relaxation of atomic polarization by radiation re-absorption. We use D'yaconov and Perel's formula [13] to estimate the γ_2 for 2^1P and 3^1P levels and $0.87R$ are used in the formula according to the result of numerical simulation by Nimura [14] where R is the radius of the plasma. The alignment destruction rate γ_{ad} is the sum of the disalignment rate γ_2 and the depopulation rate γ_0: $\gamma_{ad} = \gamma_2 + \gamma_0$. We thus add the rate coefficients of alignment destruction as $C^{22}(p,p)n_e + \sum_{r\neq p} A(p,r) + \gamma_2$ in the fourth line of rate equation, Eq. (1.10b). This relaxation effect of atomic polarization by radiation re-absorption reduces $a(p)/n(p)$ of both the 2^1P and 3^1P levels.

Figure 6(a) and (b) is the result of the PACR simulation where we use a combination of the cross sections of DWA and CCC. We used CCC cross section data for transitions Q_0^{00} and Q_0^{20} from 1^1S, 2^1S or 2^3S to 3^1P, 4^1D, 3^3P or 4^3D levels.

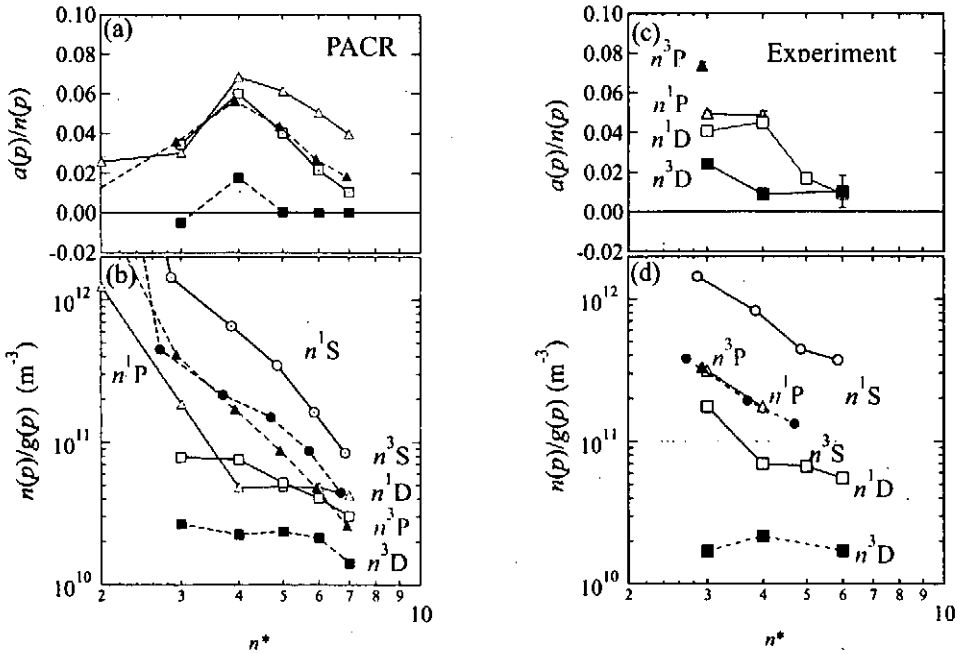

Fig. 6 (a) Observed alignment over population, $a(p)/n(p)$, distribution derived from longitudinal alignment. Abscissa is effective principle quantum number, n^*. (b) Observed population density, $n(p)/g(p)$, distribution. (c) Simulated alignment over population distribution by PACR model. The EVDF is Saturn-type defined by eq. (1.7). (d) Simulated population density, $n(p)/g(p)$, distribution.

The alignment over population $a(p)/n(p)$ of n^3D obtained by PACR model simulation is negative or close to zero except for 4^3D, only for which we use the CCC cross section. Production of the population and the alignment in the n^3D level has two dominant contributions, i.e., from the ground state, and from the 2^3S metastable state. We compare Q_0^{00} and Q_0^{20} from CCC and DWA from the 1^1S and the 2^3S to 4^3D as shown in Fig. 7. For the 1^3S-4^3D transition, the absolute value of CCC Q_0^{20} is two times larger than that of DWA, and both DWA and CCC give Q_0^{20} negative values. The Legendre expansion term $v^3 f_2(v)$ of the Saturn-type EVDF is negative. Then the rate coefficient C^{20} which is the integration of the product of Q_0^{20} and $v^3 f_2(v)$ over the velocities gives a positive alignment on the 4^3D level from the 1^1S level. On the other hand 2^3S-4^3D transition, DWA cross section gives positive alignment and CCC cross section is negative near the threshold. If we adopt the CCC cross section, the rate coefficient C^{20} gives a positive alignment on the 4^3D level from the 2^3S level. So the alignment production from both the 1^1S and 2^3S levels is positive. On the other hand, if we employ the DWA Q_0^{20}, which is positive, the rate coefficient C^{20} gives negative alignment on the 4^3D level from the 2^3S level that is opposite to the contribution from the 1^1S level. The alignment production from the 2^3S level is larger than that from 1^1S level, and then the alignment of 4^3D level becomes negative. In order to be consistent with the experimental observation and the assumed EVDF is the CCC Q_0^{20} cross section is preferable. In order to be more quantitative, we need many cross sections which are of high quality.

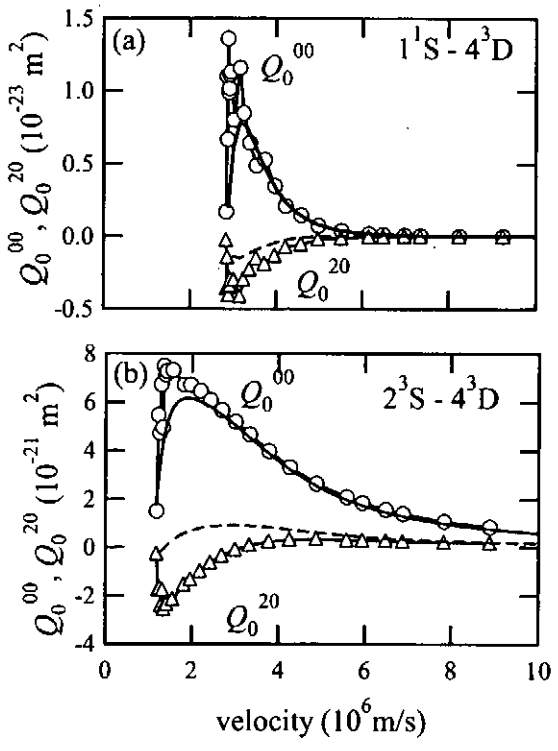

Fig. 7. Cross sections for (a) $1^1S \rightarrow 4^3D$ and for (c) $2^3S \rightarrow 4^3D$. Marks (○ and ▲): Q_0^{00} and Q_0^{20} CCC by Bray[7]. Solid curves: Q_0^{00} Ralchenko et. al.[9]. Dashed curves: Q_0^{20} Csanak and Cartwright[5].

Reference

[1] T. Sato, K. Inoue, A. Iwamae and T. Fujimoto, *Plasma polarization spectroscopy on the ECR helium plasma in a CUSP fileld* (This Workshop, 2004).

[2] R. H. McFarland Phys. Rev. **156**, 55 (1967)

[3] P. Hammond, W. Karras, W. A.G. McKonkey and J. W. McKonkey, Phys Rev. **A40**, 1804 (1989).

[4] D. W. O. Heddle and J. W. Gallagher, Rev. Mod. Phys. **61**, 221 (1989)

[5] G. Csanak and D.C. Cartwright, *J. Phys.* **B22** (1989) 2769

[6] G. Csanak and D.C. Cartwright, S. A. Kazantsev and I. Bray, Proceedings of the Japan-US workshop on PPS (Kyoto), NIFS-PROC-37.

[7] I. Bray, Private Communication.

[8] T. Fujimoto and S. A. Kazantsev, Plasma Phys. Control. Fusion **39**, 1267 (1997).

[9] Yu. V. Ralchenko, R. K. Janev, T. Kato, D. V. Fursa, I. Bray and F. J. de Heer, NIFS-DATA-59 (2000).

[10] G. Csanak, Alignment creation by elastic electron scattering: a review and new developments (This Workshop, 2004).

[11] A. Omont, Prog. Quantum, Electron. **5**, 69 (1977).

[12] K. Blum, Density Matrix Theory and Applications 2nd ed., Plenum Press, New York.

[13] M. I. D'yakonov and V. I. Perel'. Sov. Phys. JETP **20**, 997 (1966).

[14] M. Nimura, M. Hasuo and T. Fujimoto, Relaxation of atomic polarization by radiation re-absorption (This Workshop, 2004)

Progress report on the polarization of J=0-1 x-ray laser line of germanium Ne-like ion

J. Dubau*, M.K. Inal†, M.Cornille‡
C. Möller* and D. Benredjem*

*L.I.X.A.M., Université Paris-Sud,
91405 Orsay, France
†Institut de Physique, Université A. Belkaid,
BP 119, 13000 Tlemcen, Algeria
‡Observatoire de Paris,
92195 Meudon, France

Abstract.

The 19.6 nm x-ray laser line due to a 3p - 3s, J=0−1 transition in Ne-like Ge ions was found to be polarized parallel to the target plane with a degree of polarization of -53 % by Kawachi et al. (1995). They interpret it as a consequence of an unbalanced population of the 3s magnetic sublevels. Kieffer et al. (1993) have shown that, during plasma heating, some electrons could be accelerated preferentially in the same direction as the pump laser. In the present work, we shall show that such anisotropic electrons can give a small difference in populations of the 3s sublevels. The 3s level spontaneous emission to the ground level is linearly polarized and can be reabsorbed by the Ne-like ion ground state which amplifies the population of the 3s levels, as well as it increases the different sublevel populations. The 3p-3s laser amplification depending on the 3s level population starts unpolarized but becomes progressively polarized when the difference between the upper and lower level populations decreases up to the laser saturation.

1. Introduction

From linear polarization measurements, Kieffer et al. [1] have shown, that some electrons could be accelerated in the same direction as the pump laser, during plasma heating. Later on, Kawachi et al. [2] have found, for Ne-like germanium, that the 3p - 3s J=0−1 x-ray laser line was strongly linear polarized with a - 53 % polarization degree (the sign corresponding to the direction of the electric field : +100 % for the direction of the pumping laser, -100 % for the perpendicular direction). They interpreted it as due the Doppler effect which could play a role on the radiation trapping of the line from the $2p^5 3s$ level to the $2p^6$ ground level, this trapping increasing the 3s sublevel populations as well as unbalancing them. Since these populations are far from being negligible compared to the 3p sublevel population, the amplification of the 3p - 3s lasing line depends on them and it is polarized due to the unbalance population of 3s sublevels. Using a simple formula,

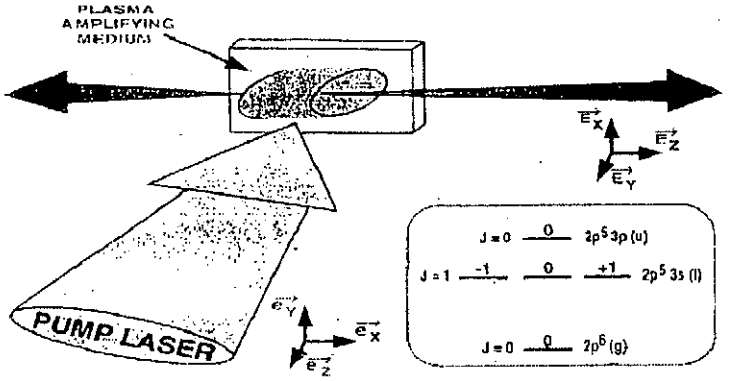

Figure 1: *Schematic diagram showing the geometry of the system.*

Benredjem et al.[3] estimated the elastic cross-sections between 3s sublevels and found it so large that the sublevel populations differences should be destroyed by electron collisions. Later on, Dubau et al. [4], did some quantum calculations which gave smaller elastic collisional rates (see Tab. 1).

Meanwhile, Cornille, Dubau and Jacquemot [5] have calculated several atomic data for the excitation of Ne-like ions for x-ray laser studies, in particular for Ge. In their calculations the projectile electron was assumed to be isotropic. Later on, Benredjem, Sureau, Cornille and Dubau [6] have used these data to model the Ge x-ray laser, using the Bloch-Maxwell code developed by Sureau and Holden [7].

2. Geometry of the experiment

Fig. 1. illustrates the geometry of the experiment. The pump laser is incident perpendicularly to the Ge-slab, and the x-ray laser is observed parallel to the slab. We suppose free electrons are heated by the pump laser by inverse bremsstrahlung, a few percents of them being anisotropic. In the plasma, at any point, we suppose that the electron distribution has some axial symmetry, around the pump laser direction, keeping in mind that most electrons are isotropic and thermalized.

In the present study, we consider a very simple collisional radiative-model including only 3 levels : the ground level (g), $2p^6$ J=0, the lower level of the lasing line (l) $2p^5 3s$ J=1 and the upper level of the lasing line (u) $2p^5 3p$ J=0. At the beginning of the plasma heating, there are not enough emitted photons to be

either absorbed by the ground level or to induce emission of the lasing transition. At that time, the photons are therefore only produced by spontaneous emission. To model electrons accelerated by the pump laser, the best reference axes are $\vec{e}_x$, $\vec{e}_y$, $\vec{e}_z$, the ones with z axis perpendicular to the Ge slab. Indeed, as long as photon absorptions or inducing emissions are negligible, the density matrix is diagonal in this referential, denotated by $\perp$:

$$\rho^{\perp}_{M'_J M_J} = \delta_{M'_J M_J} N_{M_J}, \tag{1}$$

N_{M_J} being the population of the sublevel M_J and $\delta_{M'_J M_J}$ the Kronecker symbol. Futhermore, the population does not depend on the sign of M_J:

$$\rho^{\perp}_{+1\,+1} = \rho^{\perp}_{-1\,-1}. \tag{2}$$

T_1 (keV)	0.2	0.3	0.4	0.5
C_{ug}	1.60(-2)	1.24(-1)	3.31(-1)	5.84(-1)
C_{lg}	3.36(-4)	2.43(-3)	6.38(-3)	1.13(-2)
C_{lu}	5.82(1)	4.93(1)	4.41(1)	4.06(1)
C_{0+}	9.99(-1)	7.73(-1)	6.07(-1)	5.14(-1)

Table I. Rate coefficients (in units of 10^{-11} cm^3/s) for excitation ($g \to u$, $g \to l$), i.e. C_{ug}, C_{lg}, de-excitation ($u \to l$), C_{lu} and "elastic" ($l, M_J = +1 \to l, M_J = 0$), C_{0+}, transitions for thermal electrons of temperature T_1

3. Collisional radiative model (CRM) at the beginning of the x-ray laser process

If we neglect ionization and recombination, the CRM includes only level transitions inside Ge Ne-like ion, due to electron excitation (de-excitation) and spontaneous radiative decay. In a given plasma point, we also assume the electron distribution, heated by the laser by inverse bremsstrahlung, is axially symetric around the pump laser direction. As already pointed out, the most convenient quantization axis z is then the direction of the pump laser ($\vec{e}_x, \vec{e}_y, \vec{e}_z$) The CRM can be directly applied to the sublevels, as it is usually done for levels. We shall use the 3 levels approximation shown in Fig. 1: the ground level (g), $J = 0$, the lower level of the lasing line (l), $J = 1$, the upper level of the lasing line (u), $J = 0$. They are 5 sublevels : "u", i.e (u) $M_J = 0$; "+", i.e (l) $M_J = 1$; "0", i.e (l) $M_J = 0$; "$-$", i.e (l) $M_J = -1$; and "g", i.e (g) $M_J = 0$.

$$\frac{d\rho^{\perp}_{m\,m}}{dt} = \sum_n B_{m\,n}\, \rho^{\perp}_{n\,n}. \tag{3}$$

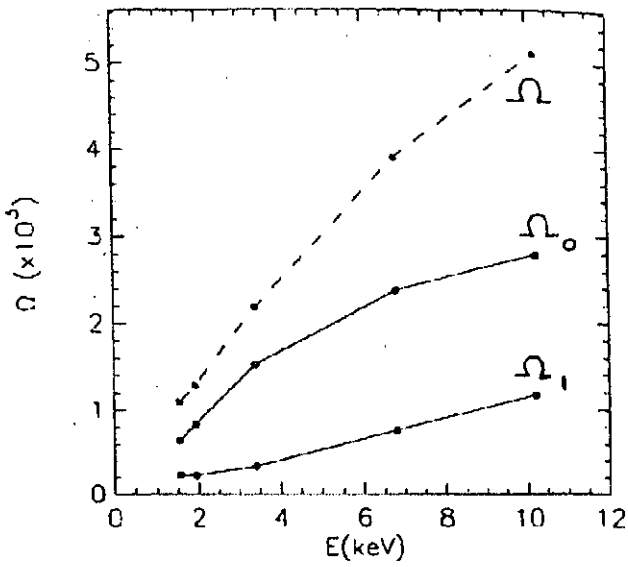

Figure 2: *Collision strengths, Ω_0 Ω_1, from the ground level (g), $J = 0$, to the sublevels, $|M_j| = 0, 1$, of the lasing line lower level, (l), $J = 1$, for beam electron along $\vec{e}_z$. The total collision strength is $\Omega = \Omega_0 + 2\,\Omega_1$*

In Fig. 2, are presented the collision strengths for beam electron along the z axis, to be used to calculate $C_{+g} = C_{-g}$ and C_{0g}. We see that these collision strengths can be very different, i.e. $\Omega_0 \neq \Omega_1$. The spontaneous decay rates are respectively : $A^r_{gl} = 1.653\,10^{12}\,\mathrm{s}^{-1}$ and $A^r_{lu} = 2.015\,10^{10}\ \mathrm{s}^{-1}$. In Table 1, for isotropic Maxwellian electrons, are given excitation/de-excitation rates, as well as "elastic" transition rates between l sublevels [4] : $C_{0+} = C_{+0} = C_{0-} = C_{-0}$. Due to a small energy difference, excitation/de-excitation between excited states u and l are dominated by low energy electrons which are thermalized electrons, whereas excitations from the ground level require larger energy electron which can still be non-thermalized. Including these data in Eq. (3) we get : $(\rho^\perp_{--} = \rho^\perp_{++})$

$$\frac{d\rho^\perp_{uu}}{dt} = N_e\,C_{ug}\,\rho^\perp_{gg} - (A^r_{lu} + N_e C_{lu})\,\rho^\perp_{uu}, \tag{3.1}$$

$$\frac{d\rho^\perp_{++}}{dt} = N_e\,C_{+g}\,\rho^\perp_{gg} + N_e\,C_{+0}\,\rho^\perp_{00} + \frac{1}{3}\,(A^r_{lu} + N_e C_{lu})\,\rho^\perp_{uu} - (A^r_{gl} + N_e\,C_{0+})\rho^\perp_{++}, \tag{3.2}$$

$$\frac{d\rho^\perp_{00}}{dt} = N_e\,C_{0g}\,\rho^\perp_{gg} + 2\,N_e\,C_{0+}\,\rho^\perp_{++} + \frac{1}{3}\,(A^r_{lu} + N_e C_{lu})\,\rho^\perp_{uu} - (A^r_{gl} + 2\,N_e\,C_{+0})\,\rho^\perp_{00}, \tag{3.3}$$

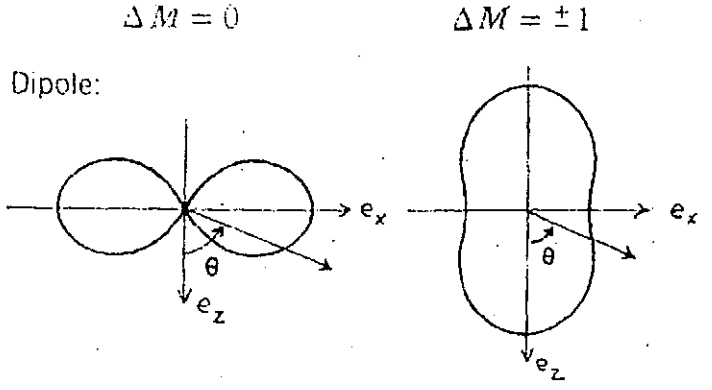

Figure 3: *Angular distribution of the emissivity* $\Delta M = 0$, $\phi_{\Delta M}(\theta) = 3\sin^2(\theta)/8\pi$, *and* $\Delta M = \pm 1$, $\phi_{\Delta M}(\theta) = 3(1+\cos^2(\theta))/16\pi$, *between the levels* $J = 0$ *and* $J = 1$

$$\frac{d\rho^{\perp}_{gg}}{dt} = A^{r}_{gl}\,(2\,\rho^{\perp}_{++} + \rho^{\perp}_{00}) - N_e\,(C_{ug} + 2\,C_{+g} + C_{0g})\,\rho^{\perp}_{gg}. \tag{3.4}$$

4. Emissivity

We are interested by the emissivities of 2 lines : (u) to (l), and (l) to (g). The angular distribution of the emissivity is not isotropic. It depends on the ΔM transition, either $\Delta M = 0$ or $|\Delta M| = 1$:

$$\epsilon_{(\alpha' J' M'_J)(\alpha J M_J)}(\theta) = A^{r}_{(\alpha' J')(\alpha J)} \left| C^{J'\,1\,J}_{M'_J M_J - M'_J - M_J} \right|^2 N^{(\alpha J)}_{M_J}\,\phi_{\Delta M}(\theta). \tag{4}$$

$C^{j_1 j_2 J}_{m_1 m_2 M}$ is a Clebsch-Gordan coefficient. For the present model :

$$(u \to +\,(\mathrm{ou}\,-)) \qquad \epsilon_{+u} = \frac{1}{3}\,A^{r}_{lu}\,\rho^{\perp}_{uu}\,\phi_{|\Delta M|=1}(\theta), \tag{4.1}$$

$$(+\,(\mathrm{ou}\,-) \to g) \qquad \epsilon_{g+} = A^{r}_{gl}\,\rho^{\perp}_{++}\,\phi_{|\Delta M|=1}(\theta), \tag{4.2}$$

$$(u \to 0) \qquad \epsilon_{0u} = \frac{1}{3}\,A^{r}_{lu}\,\rho^{\perp}_{uu}\,\phi_{\Delta M=0}(\theta), \tag{4.3}$$

$$(0 \to g) \qquad \epsilon_{g0} = A^{r}_{gl}\,\rho^{\perp}_{uu}\,\phi_{\Delta M=0}(\theta). \tag{4.4}$$

In Fig 3., are shown the 2 angular distributions $\phi_{\Delta M}(\theta)$, for $|\Delta M| = 0\,,1$

From now on, we shall only consider the radiation parallel to the Ge-slab, i.e. along $\vec{e}_x = \vec{E}_z$, For convenience, we define $z = ct$. During x-ray laser amplification, the radiation from (l) to (g) is absorbed by (g), and the radiation from (u) to (l) is amplified by (u). But, at the beginning, photon absorptions or inducing emissions being negligible, only the emissivities contribute to the Stokes parameters of a line. In the present case, it can be proved that only 2 Stokes parameters are non-zero : the intensity $I(\nu, z)$ and the (first) linear polarization $Q(\nu, z)$, where ν is the photon frequency. Usually in hot plasma, the most important line broadening effect is Doppler effect. The line profile function $\xi(\nu)$ is taken normalized ($\int \xi(\nu)d\nu = 1$). $\Delta\Omega$ is a small solid angle ($\approx$ 10 millisteradian) [6]:

$$\frac{\partial}{\partial z} I_{lu}(\nu, z) = \epsilon^I_{lu}(\nu, z) = \frac{\Delta\Omega}{4\pi} A^r_{lu}\, \rho^{\perp}_{uu}\, h\nu_{lu}\, \xi(\nu - \nu_{lu}), \tag{5.1}$$

$$\frac{\partial}{\partial z} Q_{lu}(\nu, z) = \epsilon^Q_{lu}(\nu, z) = 0, \tag{5.2}$$

$$\frac{\partial}{\partial z} I_{gl}(\nu, z) = \epsilon^I_{gl}(\nu, z) = \frac{3\,\Delta\Omega}{8\pi} A^r_{gl}\, (\rho^{\perp}_{00} + \rho^{\perp}_{++})\, h\nu_{gl}\, \xi(\nu - \nu_{gl}), \tag{5.3}$$

$$\frac{\partial}{\partial z} Q_{gl}(\nu, z) = \epsilon^Q_{gl}(\nu, z) = \frac{3\,\Delta\Omega}{8\pi} A^r_{gl}\, (\rho^{\perp}_{00} - \rho^{\perp}_{++})\, h\nu_{gl}\, \xi(\nu - \nu_{gl}). \tag{5.4}$$

The linear polarization degree is defined as:

$$P(\nu, z) = \frac{Q(\nu, z)}{I(\nu, z)}. \tag{6}$$

From Eq. (5.2), we see that, at the beginning of the laser amplification, the x-ray laser line ($l\,u$) is not polarized. But, if $\rho^{\perp}_{00} \neq \rho^{\perp}_{++}$, the resonance line ($l \rightarrow g$) is linearly polarized.

5. Change of reference axes

The definition of the sublevels depends on the choice of the quantization axis, z. These sublevels are therefore different if the axes are rotated. ($\perp$: $\vec{e}_x, \vec{e}_y, \vec{e}_z$) $\rightarrow$($\parallel$: $\vec{E}_x, \vec{E}_y, \vec{E}_z$). The sublevels of, $J = 1$, $M_J = -1,\ 0,\ +1$ are therefore different in the 2 sets of axes. It is possible to pass from one set to the other by 2 successive rotations of 90°: the first one around $\vec{e}_y$, $\vec{e}_z \rightarrow \vec{E}_z$; the second one around $\vec{E}_z$. The new sublevels are a linear combination of the old ones [8]:

$$(l) \begin{Bmatrix} (u) \\ (-1) \\ (0) \\ (+1) \\ (g) \end{Bmatrix} \quad R = \begin{pmatrix} 1 & 0 & 0 & 0 & 0 \\ 0 & \frac{1}{2} & +\frac{1}{\sqrt{2}} & \frac{1}{2} & 0 \\ 0 & -\frac{1}{\sqrt{2}} & 0 & +\frac{1}{\sqrt{2}} & 0 \\ 0 & \frac{1}{2} & -\frac{1}{\sqrt{2}} & \frac{1}{2} & 0 \\ 0 & 0 & 0 & 0 & 1 \end{pmatrix} \begin{pmatrix} 1 & 0 & 0 & 0 & 0 \\ 0 & \exp\left(i\frac{\pi}{2}\right) & 0 & 0 & 0 \\ 0 & 0 & 1 & 0 & 0 \\ 0 & 0 & 0 & \exp\left(-i\frac{\pi}{2}\right) & 0 \\ 0 & 0 & 0 & 0 & 1 \end{pmatrix}$$

$$\rho^{\perp} = \begin{pmatrix} d & 0 & 0 & 0 & 0 \\ 0 & a & 0 & 0 & 0 \\ 0 & 0 & b & 0 & 0 \\ 0 & 0 & 0 & a & 0 \\ 0 & 0 & 0 & 0 & f \end{pmatrix} \quad \Rightarrow \quad \rho^{\parallel} = \begin{pmatrix} d & 0 & 0 & 0 & 0 \\ 0 & \frac{b+a}{2} & 0 & \frac{b-a}{2} & 0 \\ 0 & 0 & a & 0 & 0 \\ 0 & \frac{b-a}{2} & 0 & \frac{b+a}{2} & 0 \\ 0 & 0 & 0 & 0 & f \end{pmatrix}$$

where: $d = \rho^{\perp}_{u\,u}$; $f = \rho^{\perp}_{g\,g}$; $a = \rho^{\perp}_{+\,+} = \rho^{\perp}_{-\,-}$; $b = \rho^{\perp}_{0\,0}$.

$$\rho^{\parallel} = R\,\rho^{\perp}\,R^{+} \quad \Rightarrow \quad \frac{d\rho^{\parallel}}{dt} = R\,\frac{d\rho^{\perp}}{dt}\,R^{+} \tag{7}$$

We see that :

$$\rho^{\parallel}_{-\,-} = \rho^{\parallel}_{+\,+};\ \rho^{\parallel}_{-\,+} = \rho^{\parallel}_{+\,-}$$

Using (3.1-4) and (7), we obtain:

$$\frac{d\rho^{\parallel}_{u\,u}}{dt} = N_e\,C_{u\,g}\,\rho^{\parallel}_{g\,g} - (A^{r}_{l\,u} + N_e C_{l\,u})\,\rho^{\parallel}_{u\,u}, \tag{8.1}$$

$$\frac{d\rho^{\parallel}_{+\,+}}{dt} = N_e\,\frac{(C_{0\,g} + C_{+\,g})}{2}\,\rho^{\parallel}_{g\,g} + \frac{1}{3}\,(A^{r}_{l\,u} + N_e C_{l\,u})\,\rho^{\parallel}_{u\,u} - A^{r}_{g\,l}\,\rho^{\parallel}_{+\,+} - N_e\,C_{0+}\rho^{\parallel}_{+\,-}, \tag{8.2}$$

$$\frac{d\rho^{\parallel}_{+\,-}}{dt} = N_e\,\frac{(C_{0\,g} - C_{+\,g})}{2}\,\rho^{\parallel}_{g\,g} - A^{r}_{g\,l}\,\rho^{\parallel}_{+\,-} - 3\,N_e\,C_{0+}\rho^{\parallel}_{+\,-}, \tag{8.3}$$

$$\frac{d\rho^{\parallel}_{0\,0}}{dt} = N_e\,C_{+\,g}\,\rho^{\parallel}_{g\,g} + 2\,N_e\,C_{0+}\rho^{\parallel}_{+\,-} + \frac{1}{3}\,(A^{r}_{l\,u} + N_e C_{l\,u})\,\rho^{\parallel}_{u\,u} - A^{r}_{g\,l}\,\rho^{\parallel}_{0\,0}, \tag{8.4}$$

$$\frac{d\rho^{\parallel}_{g\,g}}{dt} = A^{r}_{g\,l}\,(\,\rho^{\parallel}_{0\,0} + 2\,\rho^{\parallel}_{+\,+}) - N_e\,(C_{u\,g} + 2\,C_{+\,g} + C_{0\,g})\,\rho^{\parallel}_{g\,g}. \tag{8.5}$$

6. Radiative transfer

In this section, we suppose the photons can be absorbed or can stimulate emissions. The equations (4.1-4) are replaced (see [9]) by:

$$\frac{\partial}{\partial \mathrm{z}} I_{lu}(\nu, \mathrm{z}) = \epsilon^{I}_{lu}(\nu, \mathrm{z}) - K^{I}_{lu}(\nu, \mathrm{z})\,I_{lu}(\nu, \mathrm{z}) - K^{Q}_{lu}(\nu, \mathrm{z})\,Q_{lu}(\nu, \mathrm{z}), \tag{9.1}$$

$$\frac{\partial}{\partial \mathrm{z}} Q_{lu}(\nu, \mathrm{z}) = \epsilon^{Q}_{lu}(\nu, \mathrm{z}) - K^{I}_{lu}(\nu, \mathrm{z})\,Q_{lu}(\nu, \mathrm{z}) - K^{Q}_{lu}(\nu, \mathrm{z})\,I_{lu}(\nu, \mathrm{z}), \tag{9.2}$$

$$\frac{\partial}{\partial z} I_{gl}(\nu, z) = \epsilon^I_{gl}(\nu, z) - K^I_{gl}(\nu, z)\, I_{gl}(\nu, z) - K^Q_{gl}(\nu, z)\, Q_{gl}(\nu, z), \tag{9.3}$$

$$\frac{\partial}{\partial z} Q_{gl}(\nu, z) = \epsilon^Q_{gl}(\nu, z) - K^I_{gl}(\nu, z)\, Q_{gl}(\nu, z) - K^Q_{gl}(\nu, z)\, I_{gl}(\nu, z). \tag{9.4}$$

The emissivities have already been defined in (5.1-4). In [9], the expressions of the opacities K^I and K^Q are given:

$$K^I_{lu} = \frac{c^2}{4\pi} \frac{A^r_{lu}}{\nu^2_{lu}} (\rho^{\|}_{++} - \rho^{\|}_{uu})\, \xi(\nu - \nu_{lu}), \tag{10.1}$$

$$K^Q_{lu} = \frac{c^2}{4\pi} \frac{A^r_{lu}}{\nu^2_{lu}} \rho^{\|}_{+-}\, \xi(\nu - \nu_{lu}), \tag{10.2}$$

$$K^I_{gl} = \frac{3\,c^2}{4\pi} \frac{A^r_{gl}}{\nu^2_{gl}} (\rho^{\|}_{gg} - \rho^{\|}_{++})\, \xi(\nu - \nu_{gl}), \tag{10.3}$$

$$K^Q_{gl} = -\frac{3\,c^2}{4\pi} \frac{A^r_{gl}}{\nu^2_{gl}} \rho^{\|}_{+-}\, \xi(\nu - \nu_{gl}). \tag{10.4}$$

Now we include the effect of radiation in the right hand side of equations (8.1), (8.2), (8.3), and (8.5).

$$\frac{d\rho^{\|}_{uu}}{dt} = \cdots + (\rho^{\|}_{++} - \rho^{\|}_{uu}) A^r_{lu} \int \frac{I_{lu}(\nu, z)}{2\,c\,h\,\nu_{lu}}\, \xi(\nu - \nu_{lu})\, d\nu + (\rho^{\|}_{+-} - \rho^{\|}_{uu}) A^r_{lu} \int \frac{Q_{lu}(\nu, z)}{2\,c\,h\,\nu_{lu}}\, \xi(\nu - \nu_{lu})\, d\nu, \tag{8.1b}$$

$$\frac{d\rho^{\|}_{++}}{dt} = \cdots + (\rho^{\|}_{uu} - \rho^{\|}_{++}) \frac{A^r_{lu}}{3} \int \frac{I_{lu}(\nu, z)}{2\,c\,h\,\nu_{lu}}\, \xi(\nu - \nu_{lu})\, d\nu - (\rho^{\|}_{++} - \rho^{\|}_{gg}) A^r_{gl} \int \frac{I_{gl}(\nu, z)}{2\,c\,h\,\nu_{gl}}\, \xi(\nu - \nu_{gl})\, d\nu, \tag{8.2b}$$

$$\frac{d\rho^{\|}_{+-}}{dt} = \cdots + (\rho^{\|}_{uu} - \rho^{\|}_{+-}) \frac{A^r_{lu}}{3} \int \frac{Q_{lu}(\nu, z)}{2\,c\,h\,\nu_{lu}}\, \xi(\nu - \nu_{lu})\, d\nu - (\rho^{\|}_{+-} - \rho^{\|}_{gg}) A^r_{gl} \int \frac{Q_{gl}(\nu, z)}{2\,c\,h\,\nu_{gl}}\, \xi(\nu - \nu_{gl})\, d\nu, \tag{8.3b}$$

$$\frac{d\rho^{\|}_{gg}}{dt} = \cdots + (\rho^{\|}_{++} - \rho^{\|}_{gg})\, A^r_{gl} \int \frac{I_{gl}(\nu, z)}{2\,c\,h\,\nu_{gl}}\, \xi(\nu - \nu_{gl})\, d\nu + (\rho^{\|}_{+-} - \rho^{\|}_{gg})\, A^r_{gl} \int \frac{Q_{gl}(\nu, z)}{2\,c\,h\,\nu_{gl}}\, \xi(\nu - \nu_{gl})\, d\nu, \tag{8.5b}$$

Eq. (8.4) is not modified because the radiation is transverse to E_z.

Eq. (5.2) shows that $\epsilon^Q_{lu}(\nu, z) = 0$ but, Eq (9.2) shows that, due to

$$-K^I_{lu}(\nu, z)\, Q_{lu}(\nu, z) - K^Q_{lu}(\nu, z)\, I_{lu}(\nu, z),$$

it is possible that $Q_{lu}(\nu, z) \neq 0$. Then, as for the x-ray laser intensity, this polarization parameter can grow exponentially up to a saturation.

6. Conclusion

We have shown qualitatively that it is possible to have a strong polarization of the x-ray lasing line J=0 − J=1 in Germanium Ne-like ions, if there are some electrons accelerated by the pump laser during the period of amplification of the x-ray laser. Even if the polarization due to electrons is very small, as long as the plasma column is long enough, it is possible to have both intensity and polarization amplifications of the x-ray laser until saturation is reached. In [6], we have run some simulations but with an isotropic thermal electron distribution. These calculations have shown the importance to include a large number of levels to simulate correctly the x-ray laser. Of course, since electrons were isotropic, no polarization was obtained. In a near future, we wish both to include a few percents of non-thermal electrons and more sublevels in the present model.

Acknowledgements

The authors are grateful to O. Zabaydullin (Institute of Nuclear Fusion, Kurchatov Institute, Moscow, Russia) for useful discussions.

References

[1] Kieffer J.C., Matte J.P., Pepin H., Chaker M., Beaudoin Y., Johnston T.W., Chien C.Y., Coe S., Mourou G., and Dubau J., *Phys. Rev. Lett.* **68** (1992) 480.
[2] Kawachi T., Murai K., Yuan G., Ninomiya S., Kodama R., Daido H., Kato Y., and Fujimoto T., *Phys. Rev. Lett.* **75** (1995) 3826.
[3] Benredjem D., Sureau A., Rus B., and Möller C., *Phys. Rev.* **A56** (1997) 5152.
[4] Inal M.K. and Dubau J., Cornille M., *International Conference on Plasma Polarization Spectroscopy* NIFS-PROCS-37 (1998) 164.
[5] Cornille M., Dubau J., and Jacquemot S., *Atom. Data Nucl. Data Tables* **58** (1994) 1.
[6] Benredjem D., Sureau A., Cornille M. and Dubau J., *J.Q.S.R.T.* **65** (2000) 751.
[7] Sureau A. and Holden P.B., *Phys. Rev.* **A52** (1995) 3110.
[8] Blum K., *Density Matrix Theory and Applications* (New York: Plenum) (1981).
[9] Landi Degl'Innocenti E., *Solar Phys.* **85** (1983) 3.

Recent Issues of NIFS-PROC Series

NIFS-PROC-37 (Eds.)T. Fujimoto, P. Beiersdorfer,
Proceedings of the Japan-US Workshop on Plasma Polarization Spectroscopy and The International Seminar on Plasma Polarization Spectroscopy January 26-28, 1998, Kyoto: June 1998

NIFS-PROC-38 (Eds.) Y. Tomita, Y. Nakamura and T. Hayashi,
Proceedings of the Second Asian Pacific Plasma Theory Conference APPTC '97, January 26-28, 1998, Kyoto: Aug. 1998

NIFS-PROC-39 (Ed.) K. Hirano,
Production, Diagnostics and Application of High Energy Density Plasmas: Dec. 1998

NIFS-PROC-40 研究代表者 加古 孝（電気通信大学）
所内世話人 渡辺 二太
平成 10 年度核融合科学研究所共同研究 研究会「プラズマ閉じ込めに関連する数値計算手法の研究」
Ed. by T. Kako and T. Watanabe
Proceeding of 1998-Workshop on MHD Computations "Study on Numerical Methods Related to Plasma Confinement Apr. 1999

NIFS-PROC-41 (Eds.) S. Goto and S. Yoshimura,
Proceedings of The US-Japan Workshop and The Satellite Meeting of ITC-9 on Physics of High Beta Plasma Confinement in Innovative Fusion System, Dec. 14-15, 1998, NIFS, Toki: Apr. 1999

NIFS-PROC-42 (Eds.) H. Akiyama and S. Katsuki,
Physics and Applications of High Temperature and Dense Plasmas Produced by Pulsed Power: Aug. 1999

NIFS-PROC-43 (Ed.) M. Tanaka,
Structure Formation and Function of Gaseous, Biological and Strongly Coupled Plasmas: Sep. 1999

NIFS-PROC-44 (Ed.) T. Kato and I. Murakami,
Proceedings of the International Seminar on Atomic Processes in Plasmas, July 29-30, 1999, Toki, Japan: Jan. 2000

NIFS-PROC-45 (Eds.) K. Yatsui and W. Jiang,
Physics and Applications of Extreme Energy-Density State, Nov. 25-26, 1999, NIFS: Mar. 2000

NIFS-PROC-46 研究代表者 加古 孝（電気通信大学）
所内世話人 渡辺 二太
平成 11年度核融合科学研究所共同研究 研究会「プラズマ閉じ込めに関連する数値計算手法の研究」
Ed. by T. Kako and T. Watanabe
Proceeding of 1999-Workshop on MHD Computations "Study on Numerical Methods Related to Plasma Confinement June. 2000

NIFS-PROC-47 岡本正雄、村上定義、中島徳嘉、汪衛生
プラズマ物理におけるモンテカルロシミュレーション
WatanabeM. Okamoto, S. Murakami, N. Nakajima, W.X. Wang.
Monte Carlo Simulations for Plasma Physics: July 2000

NIFS-PROC-48 K. Miyamoto,
Fundamentals of Plasma Physics and Controlled Fusion: Oct. 2000

NIFS-PROC-49 (Ed.) K. Kawahata,
Proceeding of the 5th International Workshop on Reflectometry, 5-7 march, 2001: May 2001

NIFS-PROC-50 (Ed.) S. Ishii Workshop on Extremely High Energy Density Plasmas and Their Diagnostics, Mar. 8-9, 2001, National Institute for Fusion Science, Toki, Japan: Sep. 2001

NIFS-PROC-51 (Ed.) K. Horioka,
Physics and Applications of High Energy Density Plasmas -Extreme state driven by pulsed electromagnetic energy, Dec.20-21, 2001, National Institute for Fusion Science: June 2002

NIFS-PROC-52 第６回「シミュレーション・サイエンス・シンポジウム」及び核融合科学研究所共同研究「大型シミュレーション研究」合同研究会 集録
Proceedings of Joint Meeting of the 6th Simulation Science Symposium and the NIFS Collaboration Research "Large Scale Computer Simulation": Mar. 2003

NIFS-PROC-53 研究代表者 渡邉二太 LHD型磁場配位を用いたICRF支援 水素・硼素核融合炉の理論的研究ー平成14年度核融合科学研究所共同研究ー
(Ed.) T. Watanabe
Theoretical Study for ICRF Sustained LHD Type p-^{11}B Reactor: Apr. 2003

NIFS-PROC-54 (Ed.) K. Masugata
Physics and Applications of Micro and Fast Z-Pinch Plasmas (Dec. 5-6, 2002, NIFS): July 2003

NIFS-PROC-55 シミュレーション科学教育講座 2003 テキスト
Text of Simulation Science Open Lecture 2003: Apr. 2004

NIFS-PROC-56 第６回「シミュレーション・サイエンス・シンポジウム」及び 核融合科学研究所共同研究「大型シミュレーション研究」合同研究会集録
Proceedings of Joing Meeting of the 6th Simulation Science Symposium and the NIFS Collaboration Research "Large Scale Computer Simulation": Apr. 2004

NIFS-PROC-57 (Eds.)T. Fujimoto, P. Beiersdorfer
Proceedings of The Japan-US Workshop on Plasma Polarization Spectroscopy and The Fourth International Symposium on Plasma Polarization Spectroscopy: July 2004